Title

Kinetic Modeling of Halogen-Based Plasma Etching of Complex Oxide Films and its Application to Predictive Feature Profile Simulation

Author

Marchack, Nathan

Publication Date

2012

Peer reviewed|Thesis/dissertation

UNIVERSITY OF CALIFORNIA

Los Angeles

Kinetic Modeling of Halogen-Based Plasma Etching of Complex Oxide Films and its Application to Predictive Feature Profile Simulation

A dissertation submitted in partial satisfaction of the

requirements for the degree Doctor of Philosophy

in Chemical Engineering

by

Nathan Philip Marchack

2012

ABSTRACT OF THE DISSERTATION

Kinetic Modeling of Halogen-Based Plasma Etching of Complex Oxide Films

and its Application to Predictive Feature Profile Simulation

by

Nathan Philip Marchack

Doctor of Philosophy in Chemical Engineering

University of California, Los Angeles, 2012

Professor Jane P. Chang, Chair

In this work, a comprehensive framework for predicting etching behavior is developed using the test case of hafnium lanthanate ($Hf_xLa_yO_z$) in Cl_2/BCl_3 chemistry, starting from detailed thermodynamic analysis in the form of volatility diagrams. Through these calculations, it was predicted that at typical plasma reactor operating pressures, the reactions of molecular Cl_2 and Cl radicals with La_2O_3 and HfO_2 could generate sufficiently high partial pressures of O_xCl_y for measurable material removal to occur.

The etch rate of $Hf_{0.25}La_{0.12}O_{0.63}$ as a function of ion energy was characterized *in situ* using a quartz crystal microbalance. The etch rate data was found to exhibit a dual ion energy dependence with a maximum etch rate of ~27 Å/min at E_{ion} = 175 eV. The overall etch rate was found to be approximately half that of a pure HfO_2 film etched at the same conditions, due to the formation of non-volatile $LaCl_x$ compounds.

QMS measurements of HfLaO in Cl_2 chemistry showed LaOCl and LaCl as the primary La-containing etch products. XPS analysis of pure La_2O_3 films provided further evidence of this hypothesis, showing significant Cl retention (~10%) compared to HfLaO and also revealing the presence of Cl-O-La bonding. A kinetics-based bulk scale (TML) model was fit to the aforementioned experimental data and good agreement was shown between the TML model's simulated results and etch rate data. An additional degree of validation was provided through a comparison of the model's predicted composition of the surface mixing layer and the XPS-measured film compositions after plasma exposure.

The final validation of this approach was to assess the fitted kinetic parameters for complex oxide etching in Cl-based chemistry (such as reaction rate coefficients, threshold energies and sticking probabilities) at feature scale levels. The results from the TML model were coupled to a Monte Carlo based feature profile simulator and used to predict the variation of the etched feature profiles of $Hf_{0.25}La_{0.12}O_{0.63}$ films for varying aspect ratios (1.5, 3 and 6) and ion energies (75, 100 and 175 eV). In order to compare to experimental results, features of varying aspect ratio were achieved using an e-beam tool to pattern a ZEP520A photoresist mask on HfLaO followed by etching in Cl_2. Good agreement was achieved with the etched profile at 100 eV and AR = 5. As a test of the model's ability to handle variations in gas chemistry with a material system besides that of high-k dielectrics, this methodology was also applied to the shallow trench isolation process (Si etching in Cl_2/O_2 chemistry). The model showed good fitting of the major process parameters (etch rate, etch product ratios and surface composition) and showed an ability to predict the profile variation with 0, 2, 6 and 8% oxygen addition to a pure Cl_2 plasma for the etching of Si.

The dissertation of Nathan Philip Marchack is approved.

Puneet Gupta

Robert F. Hicks

Yunfeng Lu

Jane P. Chang, Committee Chair

University of California, Los Angeles

2012

TABLE OF CONTENTS

LIST OF FIGURES

LIST OF TABLES

ACKNOWLEDGEMENTS

There are many people whose support was invaluable during this undertaking - unfortunately, mentioning them all is impossible due to space constraints, and thus I must apologize in advance for anyone whose name is not explicitly mentioned here. Please rest assured that you have not been forgotten.

First and foremost, I would like to thank Professor Jane P. Chang for serving as my research advisor. Her incredible work ethic, analytical mind and meticulous attention to detail have truly inspired me and influenced the way I approached my research tasks, be it in the laboratory or at my desk. After every instance in which I sought her counsel, I felt a heightened sense of determination with regards to the ensuring course of action. In all of my future endeavors, I hope to continue upholding the high academic and professional standards that I learnt under her tutelage. She also gave me several opportunities to contribute to invited works beyond the scope of my primary project; prospects that I recognize were not lightly afforded. As such I am truly thankful for those chances to expand my knowledge, as well as her trust in assigning me such tasks. I would also like to thank the members of my thesis committee, Professors Puneet Gupta, Yunfeng Lu and Robert Hicks, as well as the funding support from the UC Discovery Grant, the IMPACT consortium and the UCLA Dean's Fellowship for my research.

I must also thank my lab mentor, Dr. Ryan Martin, for his dedication and patience in teaching me the ways of a plasma experimentalist. He undoubtedly maintained a truly lofty set of values with regards to diligence and scholastic achievement, and I genuinely aspired to those ideals during the training of the next member of the lineage, Jack Chen. Time will tell how successful those

efforts were, but given Jack's willingness to learn and dedication to completing his assigned work, I have high hopes for his success.

I would also like to thank other members of the Chang Lab, past and present, for their guidance and company during the journey – namely Drs. John Hoang and Sandy Perng, as well as Vladan Jankovic, Calvin Pham, Leo Li and Carissa Eisler. My fellow members of the Class of 2012 also deserve mention, but especially Talar Tokatlian and John Thompson for their camaraderie over the last five years. Additionally, having friends outside of the world of engineering was essential to maintaining some semblance of sanity and so I would like to thank the following individuals: Chris Eisert, Risa Garza, Bryan Lee, Felicia Lee, Vicki Lung, Ashfaque Siddiqui, Alex Stein, Yuriko Tamura, Zenia Wei and Zarina Zainul. I also need to mention the UCLA Brazilian Jiu-Jitsu Community, specifically Sang Bae, John Czorny, Peter Felton, Genny Ki, Dohun Kim, Julia Kim, Toshiya Miyatsu, Jonathan Nakashima, Jimmy Rivera, Jimmy Tang, Duc Tran, Kevin Willenson, Will Wong and Rose Zarcone for being the best training partners one could ask for, as well as teaching me lessons about myself that I would never have realized otherwise.

Last but not least, I would like to thank my family – my mother, father, sister, grandparents, uncles, aunts and cousins – for their continual love, patience and encouragement throughout the last five years, through the ups and downs. Without them I would not have had the means or will to persevere.

VITA

2007	B. Sc. (Hons), Chemical Engineering Stanford University Stanford, CA
2007-2012	Graduate Student Researcher Department of Chemical Engineering University of California, Los Angeles
2009	Teaching Assistant Department of Chemical Engineering University of California, Los Angeles
2011	UCLA Dean's Fellowship Department of Chemical Engineering University of California, Los Angeles
2011	AVS Coburn and Winters Award Finalist 58th AVS International Symposium

PUBLICATIONS AND PRESENTATIONS

Marchack, N., and Chang J.P. "Chemical Processing of Materials on Silicon: More Functionality, Smaller Features and Larger Wafers", Annual Reviews in Chemical and Biomolecular Engineering, 3, 235-262, July 2012.

Marchack, N., Blom, H-O. and Chang, J.P. "Kinetic Modeling of Complex Oxide Etching and Its Application to Predictive Feature Scale Simulation", November 2011, Nashville, TN. (Oral Presentation - Nominated for Coburn and Winters Award)

Marchack, N., and Chang, J.P. "Nanoscale Etching and Deposition: Top Down Methods", in *Plasma Processing of Nanomaterials*, ed. Mohan Sankaran, CRC Press, Boca Raton, FL, USA, 1-34, December 2011.

Marchack, N., and Chang, J.P. "Perspectives in Nanoscale Plasma Etching: What are the ultimate limits?", Journal of Physics D: Applied Physics (Special Cluster Issue on Perspectives and Challenges in Plasma Nanoscience), 44 170411, April 2011. (Invited Progress Article).

Mullings, M.N., Lee, H.B.R., Marchack, N., Jiang, X., Chen, Z., Gorlin, Y., Lin, K.P., Bent, S.F. "Area Selective Atomic Layer Deposition by Microcontact Printing with a Water-Soluble Polymer", Journal of the Electrochemical Society, 157 (12), D600-D604, October 2010.

Marchack, N., Pham, C., Hoang, J., Chang, J.P., "Predicting the Surface Response Upon Simultaneous Etching and Deposition", 57th AVS International Symposium, October 2010, Albuquerque, NM. (Oral Presentation)

Hoang, J., Marchack, N., Pham, C., Chang, J.P., "Feature Profile Evolution: From Plasma Etching and Deposition to Surface Roughness Propagation", 56th AVS International Symposium, November 2009, San Jose, CA. (Oral Presentation)

Marchack, N., King, J.S., Bent, S.F. "Printing of Fluorocarbon Self-Assembled Monolayers as Atomic Layer Deposition Resists", MRS Spring Meeting, April 2007, San Francisco, CA. (Poster Presentation).

CHAPTER 1: INTRODUCTION

Top-down patterning methods which involve a combination of optical lithography and plasma etching have provided high-fidelity, reproducible pattern transfer capabilities in the semiconductor processing industry for decades. However, the emergence of complex multifunctional materials and three-dimensional architectures as cornerstones of the next generation of integrated circuit (IC) devices poses several major challenges to established processing techniques. The key to navigating this uncharted territory is in cultivating a fundamental understanding of the surface reaction kinetics between the plasma and materials involved, as insight into the complexities of the process mechanics allow predictions to be made about the etch behavior of novel material systems. Vast disparities in both length and time scales exist between various aspects of the plasma etch process (e.g. the size of processing reactors (cm) compared to individual transistors (nm) and impinging reactive species (Å), and overall processing times (minutes) compared to bond breakage (milliseconds) and photo-stimulated excitation (<nanoseconds)), dictating a combination of theoretical and experimental techniques to properly address the scope of this endeavor. This work aims to develop such a framework, beginning with initial assessments and selection of suitable etch chemistries using fundamental thermodynamic data. Next, experimental measurements of the macroscopic etch rate, surface composition and etch products are obtained, serving as the foundation for a kinetics-based modeling approach. Although established upon a base system of complex oxide materials and chlorine-based etchant chemistry, this methodology is sufficiently versatile to be applied in instances featuring the inverse scenario (i.e. a simpler substrate with a more complex plasma environment), such as the shallow trench isolation (STI) process – silicon etching in Cl_2

chemistry with oxygen addition. Finally, the nature of this approach allows it to be used as the input for modeling at the feature scale, which is a tremendous asset for optimizing future patterning processes.

1.1 Motivation

The basic building block of the electronic industry is a metal-oxide semiconductor (MOS) field-effect transistor, as depicted in Figure 1.1. (Marchack and Chang 2012) The metal modulates the conductivity of the silicon (semiconductor) through a dielectric (oxide), and the on-off of this device is used as the 1 and 0 binary codes for computation. The physical dimensions of this device have been aggressively downscaled over the past few decades to improve speed and packing density. One classic scaling methodology is constant-field scaling (Dennard, Gaenssle.Fh et al. 1974), which keeps the electric field in the transistor unchanged by reducing the supply voltage and the transistor length, oxide thickness, and junction depth while increasing the doping level in the channel by the same factor. However, as device dimensions were further reduced below 90 nm, the inherent physical limits of the conventional materials started to limit the attainable performance. For example, at thicknesses below 10 Å the SiO_2 dielectric layer would become susceptible to direct quantum-mechanical tunneling, thus resulting in unacceptably high leakage current, as well as dielectric breakdown at intolerably low voltages. This quandary threatened to hinder the continuation of Moore's Law, which states that the number of transistors that can be placed inexpensively on an integrated circuit doubles every two years.

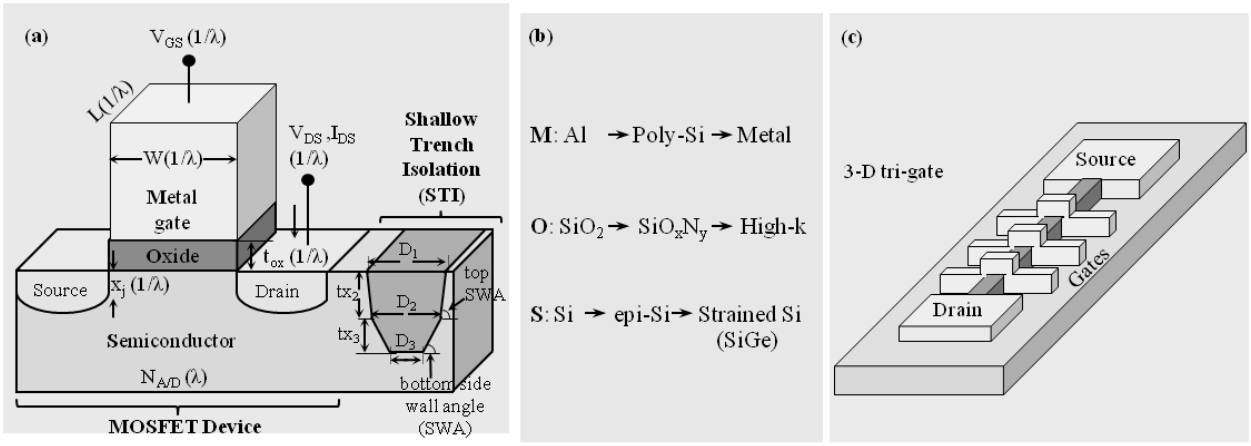

Figure 1.1 (*a*) A simplified cross-sectional view of a metal-oxide semiconductor field-effect transistor (MOSFET); key parameters are labeled along with their constant-field scaling factor (λ). *L*, *W*, t_{ox}, and x_j are the gate length, width, dielectric thickness, and junction depth, respectively. V_{GS}, V_{DS}, and I_{DS} are the gate voltage, drain voltage, and drain current, respectively, and $N_{(A/D)}$ is dopant concentration. A shallow trench isolation (STI) is also shown with labeled features: top and bottom sidewall angles (SWA), trench width (D) and trench depth (t_x) . (*b*) The material evolution and (*c*) the geometric advancement of a 3D tri-gate structure to further enable device scaling.

As a consequence, much research in recent years has focused on both designing new materials with multiple functionalities as well as engineering novel, complex device architectures, in order to achieve increased device functionality and speed while reducing weight and energy consumption. On the architectural front, the recent introduction of a tri-gate structure provided one additional degree of freedom in device scaling by changing the core structure of the transistor from a planar one into a 3D one (also shown in Figure 1.1), thereby enabling further device scaling based on Moore's law while achieving significant energy savings. (Doyle, Datta et al. 2003) Other notable three-dimensional architectures proposed for logic and memory applications include charge traps (Lee, Hur et al. 2005), cross point devices (Chen, Liu et al. 2006) and FinFETs. (Hisamoto, Lee et al. 2000) Prominent examples of new materials incorporated over the past decade include strained silicon (Thompson, Armstrong et al. 2004; Thompson, Chau et al. 2005), high-*k* dielectrics (Wilk, Wallace et al. 2001), and metal gates

(Mistry, Allen et al. 2007), all of which have enabled both channel mobility improvement and the scaling of gate capacitance; essentially redefining the building blocks of future MOS devices. The future appears to hold even further expansion into hitherto unutilized regions of the periodic table; as transition and noble metals for their application in magnetic random access memory, (Slaughter 2009) and multiferroic materials with strong coupling between magnetic and electronic order parameters have gained attention recently for their application in new devices such as spin-field-effect transistors (Chu, Martin et al. 2008; Jia and Berakdar 2009) and advanced memory devices (Scott 2007; Ahn, Lee et al. 2008) that could offer fast and low-power electrical write operation and nondestructive magnetic read operation.

However, if these novel materials are unable to be patterned successfully at the requisite length scales, their outstanding properties are limited in large scale integration. Bottom-up methods have several key advantages that give them great potential for material patterning, namely the potential for self-organization (which allows for simplicity and reduced cost), independence from optical lithography limitations and the low induced damage from minimizing the need for material removal. Yet despite these benefits, there are currently many obstacles that must be addressed if such methods are to become truly viable for high throughput and industrial integration. Directing and organizing the base units for these structures are divided between two extremes: delivery of the molecules to the surface via a neutral gas can lead to disordered arrays with virtually non-existent control over the final product (Ostrikov 2007), but manipulation of individual molecules via techniques such as scanning probe/dip pen lithography is an extremely tedious and time-consuming endeavor. Additionally, the difficulty of aligning and layering several patterns over each other poses a serious barrier to creating more complex features. Finally, the potential cost of significantly altering or completely replacing the equipment

infrastructure utilized in fabrication facilities to accommodate new processing techniques is likely to be prohibitively expensive and not feasible in the near future. Thus, although there have been reports on bottom-up and self-assembly-based approaches to generate nanoscale patterns, such as by area-selective ALD (Chen and Bent 2006; Liu, Mao et al. 2008), the most successful method of patterning materials so far has been top down processing (a combination of optical lithography and plasma etching), which has been demonstrated successfully for a wide variety of materials such as semiconductors, oxides, and metals (Flamm, Donnelly et al. 1983; Ventzek, Hoekstra et al. 1994).

Applying plasma etching to the aforementioned novel architectures and materials does not come without challenges. Increasingly demanding geometrical requirements, e.g. aspect ratios in excess of 100:1 have been presented for dynamic random access memory (DRAM) applications (Kiihamaki and Franssila 1999), meaning a sufficiently fast etch rate must be achieved without compromising anisotropy, selectivity and low damage - an example is illustrated in Figure 1.2(a). (Lill and Joubert 2008) The situation is only further complicated when one considers a multi-component device, as understanding the etch behavior of a single material layer is insufficient when placed in the context of several others. For example, the chemistries that are required to etch an organic polymer compound (such as photoresist) as opposed to a crystalline oxide are markedly different. Such etch disparities dictate a delicate balance between the desired outcome and the viable etch chemistries, as evidenced in state-of-the-art memory devices. (Jung, Cho et al. 1999) Figure 1.2(b) shows a schematic diagram of such a device and possible profile defects such as tapered sidewalls, undercutting and notches caused by preferential etching of certain layers.

Other problems associated with high aspect ratio etching include notching, reactive ion etching, etch stop, and aspect ratio-dependent charging. (Matsui, Nakano et al. 2001) Such deviations from perfect anisotropic etch cannot be attributed solely to underlying chemical causes: physics-based effects also play a large role. Since neutral species have an isotropic distribution but ions an anisotropic one, the neutral-to-ion (n/I) flux ratio at the bottom of the feature decreases as the aspect ratio increases. Similarly, ions normally impinge upon the feature bottom at the onset of etching, but could arrive at an off-normal angle due to scattering from the sidewalls as the feature evolves and its aspect ratio increases. The variation in etch yield (a dimensionless quantity describing the number of atoms removed per impinging etchant specie) as a function of n/I flux ratio, ion energy, and angular dependence for both physical and chemical etch processes is depicted graphically in Figure 1.2(c). As the etch yield dictates the removal of all materials within the feature and its evolution, it is evident that the aforementioned parameters play a significant role in defining the attainable etch profiles. It is thus clear that realizing aspect ratio independent etch (ARIE) is a significant challenge in creating complex 3-D nano-scaled architectures.

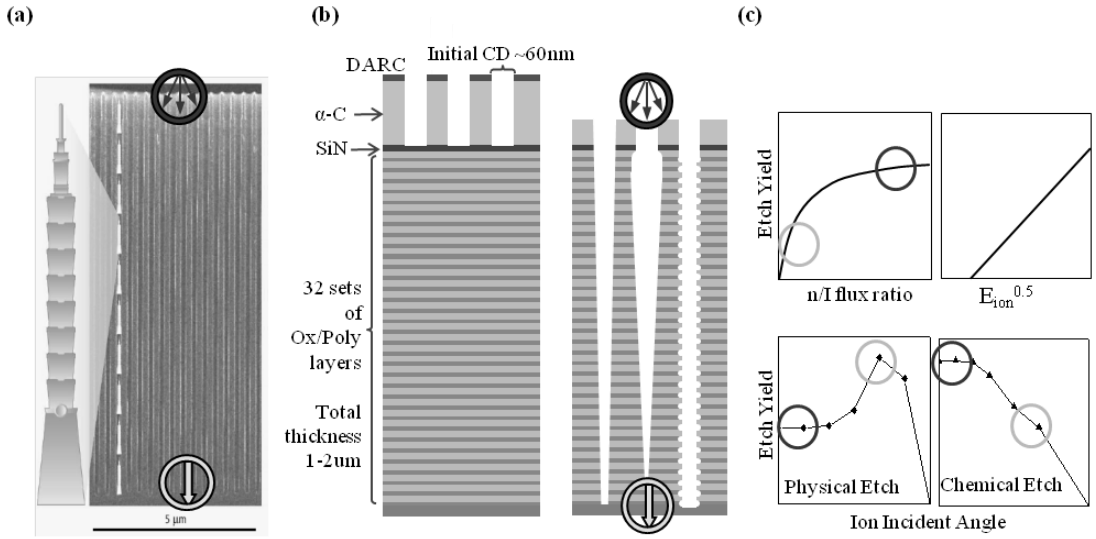

Figure 1.2 (a) High aspect ratio trenches in relation to one of the world's tallest freestanding structures, Taipei 101, (b) a schematic of high-aspect ratio holes for 3D flash memory technology showing the complexity of multi-layer and material stacks and (c) an illustration of the effect of neutral to ion flux ratios, ion energy and ion incident angles on the etch yield, defining the variation in patterning features as the aspect ratio increases during pattering transfer. (a) reprinted from Science Vol. 319, Lill and Joubert, "Materials Science: The Cutting Edge of Plasma Etching", pp. 1050-1051, Copyright (2008) with permission from AAAS.

In seeking solutions to ARIE, it is perhaps judicious to focus on the other end of the spectrum, i.e. the challenge of maintaining control over design specifications in the face of near-atomic level downscaling. Given upcoming critical dimensions (CD) of less than 14 nm, a few atomic layers of thickness can be all that separates a functional device from a catastrophically impaired one. Plasma etching is an inherently chaotic process in which a large variety of species are generated: ions, neutrals, radicals, electrons, and photons. In isolation, each of these species is usually insufficient to achieve the desired reactions, but when they are supplied simultaneously to a surface with sufficient fluxes and desirable ratios, a wealth of reactions becomes attainable owing to various synergistic mechanisms (Marchack and Chang 2011), albeit resulting in a partially uncontrollable, non-conformal process. (Kota, Coburn et al. 1998) Thus the question arises: is it possible to separate and control these synergisms in order to achieve atomic level

control of the material removal? The experimental concept that perhaps best explores this dynamic is atomic layer etching (ALE) (Athavale and Economou 1995), a schematic of which is provided in Figure 1.3 below.

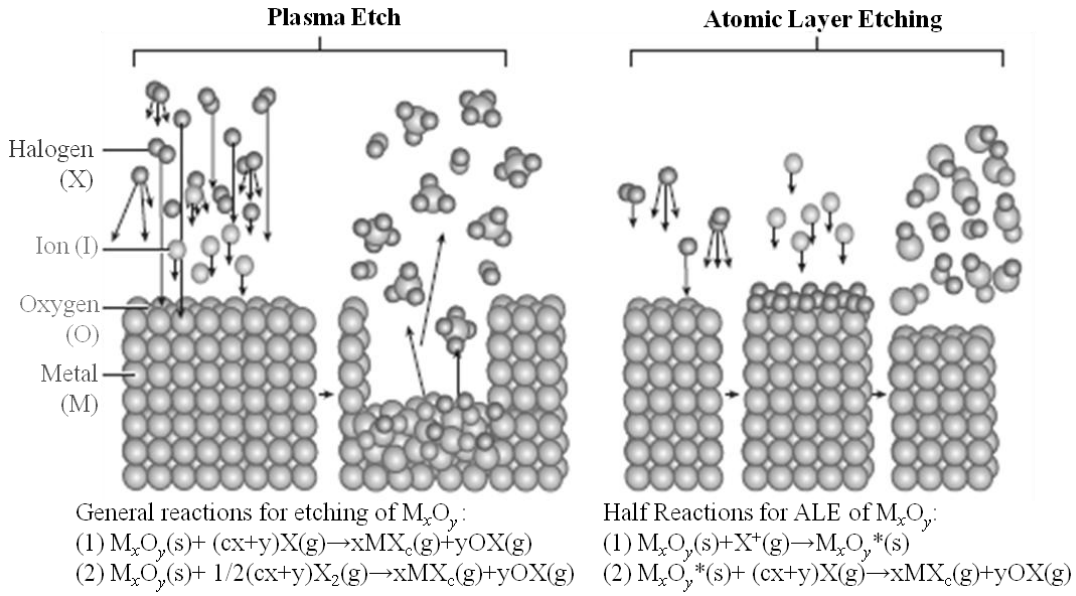

Figure 1.3 Comparison between a traditional plasma etch process and an atomic layer etching (ALE) process, illustrating the conceptual differences.

The four main steps in an ALE process can be thought of as: (i) adsorption (chemisorption) of one species onto the surface which self-terminates upon consumption of the available surface site, (ii) evacuation of the reactor to prevent reaction in the gas-phase, (iii) exposure of the surface to a second species to induce chemical reaction with the adsorbed species, leading to atomic layer etch or deposition, and (iv) evacuation of the reactor to remove the reaction products. It is important to note that the most important factor in achieving atomic scale control is that at least one of the steps, (i) or (iii), should be self-limiting. In a plausible ALE process, ions can be the enabling species to form and remove a volatile product. The energy of the ions should be low enough to prevent excessive sputtering but high enough compared to the etching threshold energy to facilitate the etching process. This general concept has been

demonstrated for etching silicon (Athavale and Economou 1996), germanium (Sugiyama, Matsuura et al. 1997), and gallium arsenide (Lim, Park et al. 2008), with only a few minor differences between the three cases. Namely, Ne^+ was used as the inert ion beam for etching GaAs (vs. Ar^+ for Si and Ge), and for ALE of Ge, only Cl_2 molecules were allowed to reach the surface for the initial reaction as Ge spontaneously reacts with Cl radicals. In other words, while ALE of Si is limited by etchant adsorption, ALE of Ge is limited by ion induced reaction. Adaptation of this technique to future complex material systems would prove useful as the technique allows for study of etch processes on a fundamental basis. There has also been some simulation work done on this research topic (Agarwal and Kushner 2009) but more thorough experimental work, particularly with regards to different material systems is in great need.

The final issue to address is that many of the potential material candidates for next generation devices are also intrinsically etch resistant, implying a need to consider more aggressive chemistries. Figure 1.4 shows the increased use of elements in the periodic table such as lanthanides and post-transition metals over the last two decades. Though fluorine-based plasmas such as CF_4, XeF_2 and SF_6 are known to be more reactive than other halogen-based chemistries, environmental concerns over potential ozone depletion and enhancement of the greenhouse effect have placed a barrier upon expanding their use. It should be noted that the usage of such gases solely for patterning these materials on wafers is potentially not that high. Rather, the fact that the deposition process of these materials affects not only the wafer surface but also the walls of the reactor means that the quantity of gas required becomes significant, as the entire chamber requires treatment in order to minimize process drift. It therefore becomes imperative to seek alternate chemistries that can be used to etch these materials.

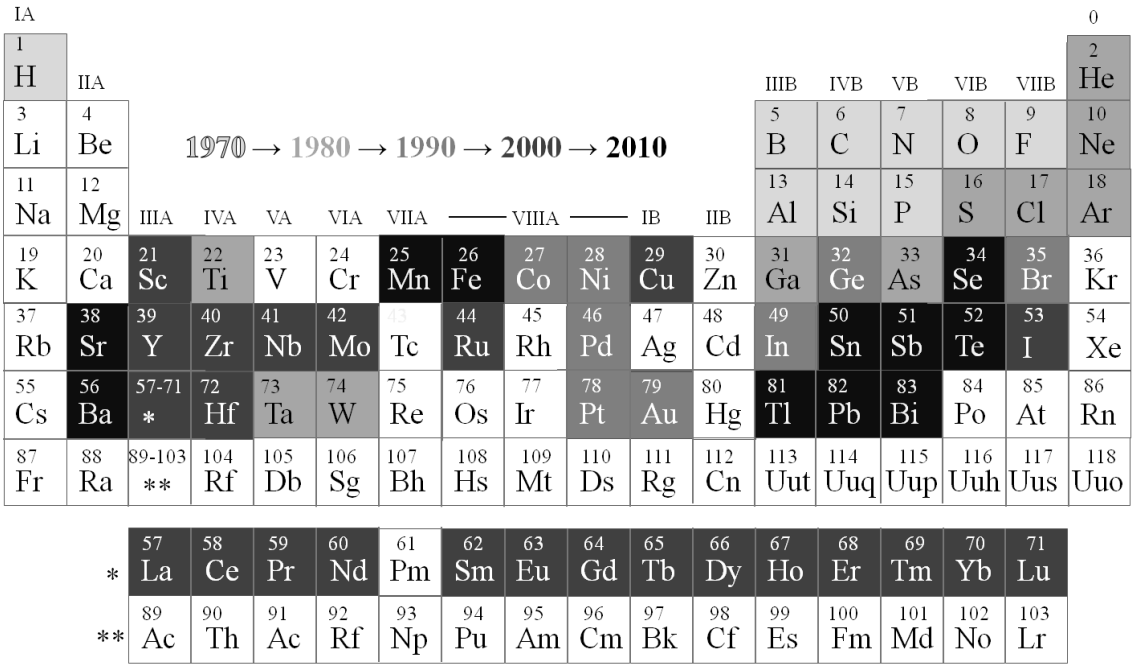

Figure 1.4 Expansion of the elements used in the periodic table as semiconductor devices have progressed through the decades.

The common thread that links these aforementioned challenges is a need for a comprehensive and fundamental understanding the reactions occurring at an atomic level (Cardinaud, Peignon et al. 2000) and competing mechanisms involved when a surface is exposed to plasma. (Abrams and Graves 1999) Despite much progress, there is still relatively little known about the exact minutiae of plasma-surface interactions at these length scales. This is in large part due to the large discrepancies in length (Cavallotti, Pantano et al. 2005) and time scales (Veprek 1972; Lymberopoulos and Economou 1993; Barone and Graves 1996; Frenklach 1998) of the plethora of reactive species involved, both in terms of how they are generated and how they interact with the surface. It becomes evident that approaching this highly complex problem cannot be solely handled by experimental work. To that effect, computation-based modeling has substantially complemented experimental work, contributing tremendously to the understanding of elementary reaction mechanisms involving plasma species that are difficult to

examine via physical probes. It also holds promises to help reduce the time and effort associated with time consuming and expensive design of experiments, by allowing prediction of the process outcome. This study aims to show the development of a robust, versatile framework with which to approach the plasma patterning of current and future materials. By utilizing in-situ diagnostics such as optical emission enabled actinometry (OES), electrical probes (e.g. Langmuir Probe), mass sensitive analysis (quadrupole mass spectrometry (QMS) (Martin and Chang 2009), quartz crystal microbalance (QCM), and surface-related analytical tools such as x-ray photoelectron spectroscopy (XPS) (Layadi, Donnelly et al. 1997), information regarding the density, flux, energy and angular distributions of impinging plasma species and etch products, as well as the composition and morphology of the evolving surface (Simpson and Yarmoff 1996) can be obtained. This data then forms the foundation upon which a kinetics-based surface model can be established. Fitting the model to the experimental results yields proper parameterization of the rate coefficients of reaction kinetics. Such a model uses a defined set of reaction equations to take into account the effect of variety of species present in the plasma, as well as different material removal pathways such as sputtering and ion enhanced etching. Predictions about the etch yield of a process, the surface composition of the material after plasma exposure, and the ratio of etch products can also be made. This approach was previously applied to the etching of SiO_2 in fluorocarbon chemistry, demonstrating good agreement with experimental data. (Kwon, Bai et al. 2006) In this work, its expansion to the test case of complex oxide materials in chlorine-based chemistry is demonstrated, thereby establishing the efficacy of the framework for use with future materials.

1.2 Complex Materials and Architecture

Continued device scaling can be enabled through the realization of multifunctional materials. For example, in complex oxide systems, the coupling and interplay among the charge, spin, orbital, and lattice degrees of freedom (Izyumskaya, Alivov et al. 2009) can be influenced by controlling the composition and atomic arrangement of the bulk material and interfaces. This leads to novel ground states for the system that can be manipulated by external perturbations (Martin, Chu et al. 2010), ultimately allowing for tuning the thermal, electric, magnetic and mechanical properties of the materials over a wide spectrum. In this section the discussion is focused on the application of complex metal oxides as high-*k* materials.

1.2.1 High-κ Dielectrics

The engineering of complex oxide thin films at an atomic level has gained prominence recently with the utilization of high-κ oxides as the gate dielectric layer in the MOSFET structure. High-κ materials are superior to SiO_2 in terms of their higher dielectric constants, which means that for a given capacitance value, a high-κ layer is thicker than the corresponding SiO_2 layer according to the capacitance equation:

$$C = \frac{\kappa \varepsilon_0 A}{t_{ox}} \tag{1.1}$$

where κ is the dielectric constant, ε_0 is the permittivity of free space, A is the interfacial area, and t_{ox} is the oxide thickness (from the previous equation, it can be derived that $t_{high-k} = \frac{\kappa_{high-k}}{\kappa_{SiO_2}} t_{SiO_2}$). (Wallace and Wilk 2003) Thus, these materials can supply heightened capacitance while

simultaneously providing a physically thicker layer to suppress quantum mechanical tunneling and dielectric breakdown. (Lo, Buchanan et al. 1997) However, merely identifying materials with high dielectric constants only accounts for a small component of the selection criteria; the successful implementation of this material into the existing MOSFET manufacturing process entails meeting many other standards such as thermodynamic stability with the underlying substrate, resistance to the high temperature (~1000°C) processing conditions currently used in industry, insulating properties (e.g. having a large enough band offset with the substrate to reduce leakage current from carrier injection), good electrical interface with the substrate, threshold voltage control and stability, and minimal mobility degradation.(Murto, Gardner et al. 2003; Robertson 2006) The interconnected nature of these various factors further complicates the choice of material. The two examples that perhaps best illustrate this are leakage current and threshold voltage control. For example, the leakage current in the direct tunneling regime is given by the equation:

$$J = t^{'} \exp\left(-\left(2m^{*}\phi\right)^{1/2}\left(\kappa / \kappa_{SiO_2}\right)\right) \tag{1.2}$$

where $t^{'}$ is the equivalent oxide thickness (EOT), m^{*} is the tunneling mass, κ and κ_{SiO_2} are the dielectric constants of the high-k material and SiO_2, respectively, and ϕ is the band offset. Hence, the figure of merit for the gate oxide is a combination of both the dielectric constant and the band offset (Yeo, King et al. 2002). In order to minimize the leakage current, both band offsets of the material candidate against the Si substrate should be at least 1 eV. However, as the conduction band offset (CBO) is usually smaller than that of the valence band, the CBO value is considered more critical. A requirement for a CBO value > 1 eV necessitates oxides with a large band gap but medium dielectric constant. (Robertson 2006).

For high-κ oxides, the band gap is between the valence band of filled oxygen p states and the conduction band of the empty transition metal (TM) d states. Thus the band gap can be increased by raising the TM d levels. Selecting 4d or 5d transition metals or utilizing transition metals from Column III of the periodic table can contribute to raising the TM d levels and thus increase the band gap. This directly affects the attainable barrier heights with respect to both electron and hole transport, thereby dictating the performance of the CMOSFET devices.(Robertson 2000) The obvious implication of this effect is that a material with a very large κ value is more susceptible to current leakage, thereby crippling device efficiency. Thus, a compromise has to be made in terms of a more moderate κ value. A graph showing this trend is reproduced in Figure 1.5.

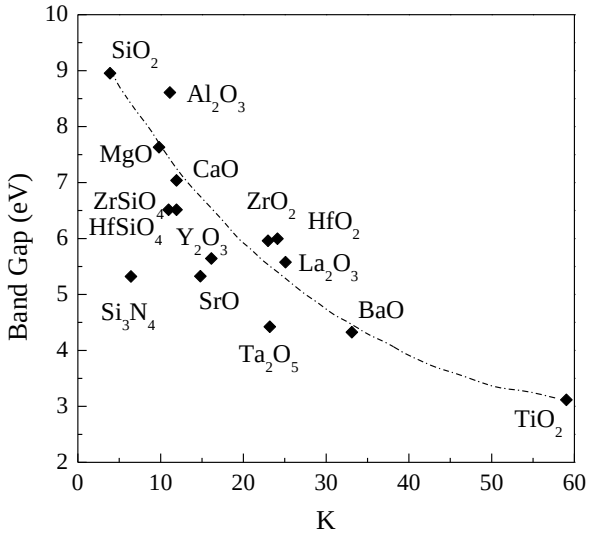

Figure 1.5 Relation between κ and band gap for several potential high-κ candidates (adapted from Robertson, Rep. Prog. Phys, 2006).

The issue of threshold voltage demonstrates how oxide selection influences other materials in the gate stack. For power dissipation in FET devices to be curtailed, a threshold voltage (V_t) of near zero is necessitated. Achieving this requires that the effective work function

(EWF) of the metal gate/stack combination be tuned to match the silicon conduction or valence band energy for both n and pFETs. Unfortunately, the phenomenon known as Fermi level pinning complicates this issue for high-k oxides. (Lee, Oh et al. 2006) This effect occurs when the Fermi level of the metal gate electrode is far beneath that of oxygen vacancies typically present in the upper band gap of the oxide. This allows the electrons from the vacancy to fall to the metal Fermi level, thus distorting the band structure and effectively reducing the EWF of the gate electrode. A graphical depiction is provided below in Figure 1.6.

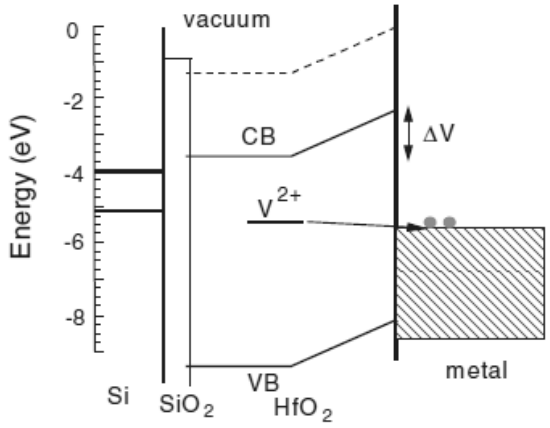

Figure 1.6 An illustration of Fermi-level pinning (Robertson, J. App. Phys., 2008).

This constrains the possible options for gate electrodes as this effect tends to be more pronounced in metals with large work functions. In order to compensate for this, metal oxide capping layers are used to shift the flatband voltage towards more adequate values, but as the magnitude of the shift is proportional to the oxide thickness, this practice increases the EOT (Alshareef, Quevedo-Lopez et al. 2006; Ragnarsson, Chang et al. 2007).

With these considerations taken into account, hafnium-based materials have emerged and have been implanted as the designated dielectrics in nanoelectronics with a gate length less than 45 nm, and the implementation of a non-silicon-based gate dielectric means a paradigm shift from diffusion-based thermal processes to ones based on ALD. Complex metal oxides are needed in high-*k* applications because a simple binary metal oxide does not have a better interface with Si compared with SiO_2. The chemical potential difference across the interface drives chemical reactions (Hubbard and Schlom 1996), and the lack of an oxygen diffusion barrier typically results in the formation of a SiO_2-rich layer at the interfaces of the oxide with both the Si substrate and the polysilicon gate. These interfacial layers degrade the attainable capacitance of the gate dielectric layer, which often results in an increased interface state density. The other issue with simple binary oxides is that they crystallize at relatively low temperatures, 500--700°C, and thus undergo thermally induced crystallization at typical post-deposition annealing temperatures. This leads to increased leakage current and dopant diffusion across the dielectric grain boundaries as well as threshold voltage instability owing to charge trapping. (Liu, Martin et al. 2008) Although crystalline phases are typically known to be more thermodynamically stable than amorphous ones, the lower surface and interfacial energies of amorphous phases can lead to stability in thin films below some critical film thickness (Molodetsky, Navrotsky et al. 2000).

To alleviate these concerns, complex metal oxides based on hafnium have been explored in an attempt to synthesize a material that combines the desired characteristics of each constituent binary oxide. For example, hafnium silicate (based on HfO_2 and SiO_2) has been proposed to improve the interfacial quality, with the inclusion of SiO_2 providing a reduced chemical potential difference to the Si substrate and thus significantly increasing the

thermochemical stability. (Wilk, Wallace et al. 2000; Robertson 2006) Hafnium aluminate (based on HfO_2 and Al_2O_3) is another promising material, as Al_2O_3 is a well-known oxygen diffusion barrier that protects the Si surface from oxidation and is thermodynamically stable in contact with Si. (Ho, Gong et al. 2002; Yu, Wu et al. 2002) Both SiO_2 and Al_2O_3 are good glass formers and thus form amorphous microstructures when alloyed with HfO_2 that can be stabilized at high temperatures. This results in enhanced phase stability and lower trap densities compared with their binary oxide counterparts. However, given that the dielectric constants of SiO_2 and Al_2O_3 are both lower than that of HfO_2 (~3.9 and 11 compared to 24), approaches involving these materials results in composite films with noticeably lower overall dielectric constants, thus limiting their ability to serve as a long term replacements.

In light of this issue, one material that has attracted attention is La_2O_3. While pure La_2O_3 possesses a similar dielectric constant (~25) to HfO_2 and a CBO of ~2 eV, characterization of its performance as a dielectric barrier revealed several of the deficiencies associated with binary oxides outlined earlier, namely high leakage current and a large negative shift in the flatband voltage. While the utility of La_2O_3 as a capping layer for engineering the work functions of HfSiO dielectric films has been documented in literature (Guha, Paruchuri et al. 2007), its incorporation in the composite hafnium lanthanate (Dimoulas, Vellianitis et al. 2004) has shown several promising results, including low defect densities and reduced Fermi level pinning compared to HfO_2. (Wang, Li et al. 2006) La_2O_3 possesses a similar κ value to HfO_2 and thus its incorporation in a composite film should not compromise the permittivity. A study showed that doping amorphous HfO_2 with La resulted in a composite oxide with a crystallization temperature of over 900°C, as illustrated in Figure 1.7.

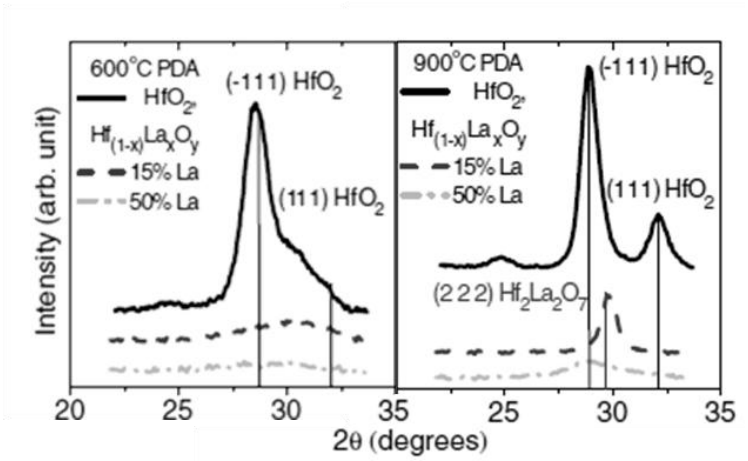

Figure 1.7 XRD data showing the increased crystallization temperature of HfO_2 upon addition of La_2O_3, from Wang et al., Solid-State Electronics, 2006.

The postulated reason for the increase in crystallization temperature was the discrepancy in ionic radius between La and Hf (1.16 vs. 0.83 Å), which promoted the formation of the $Hf_2La_2O_7$ pyrochlore structure over fluorite type solid solutions. (Ushakov, Brown et al. 2004) While this work was conducted on HfO_2 precipitated from aqueous solution, similar results regarding the crystallization temperature were observed for HfLaO films formed via magnetron sputtering. (Yamamoto, Kita et al. 2006) In that work, dielectric constants of 22-27 were reported for the composite films, which were either calculated from the slope of a capacitance equivalent thickness (CET) vs. physical thickness plot, or measured through a metal insulator metal (MIM) structure. Additionally, the C-V curves of MOS capacitor devices exhibited negligible hysteresis and no frequency dispersion, which indicated minimal degradation of the bulk and interface properties. Another possible advantage is the fact that $Hf_2La_2O_7$ possesses a lattice constant of ~2 times that of silicon, which allows it to be grown directly on the substrate via molecular beam epitaxy (MBE). HfLaO films deposited via this method exhibited low leakage currents ($< 10^{-7}$ A cm^{-2}) at a flatband voltage of -1 V, and an effective mobility of 140 cm^2 V^{-1} s^{-1} in an electric field of 1 MV cm^{-1} (compared to 170 cm^2 V^{-1} s^{-1} for MBE-deposited

HfO_2 films). (Rittersma, Hooker et al. 2006) Finally, the nitridation of HfLaO was reported to further increase the crystallization temperature (Wu, Hung et al. 2007) and reduce Fermi level pinning, thus allowing full EWF control without the need for capping layers which would increase the EOT (Wang, Yu et al. 2007).

The properties of several hafnium-based multicomponent oxides including their permittivities, bandgaps, thermal/chemical stability, and band offsets to silicon (Choi, Mao et al. 2011) are summarized in Figure 1.8.

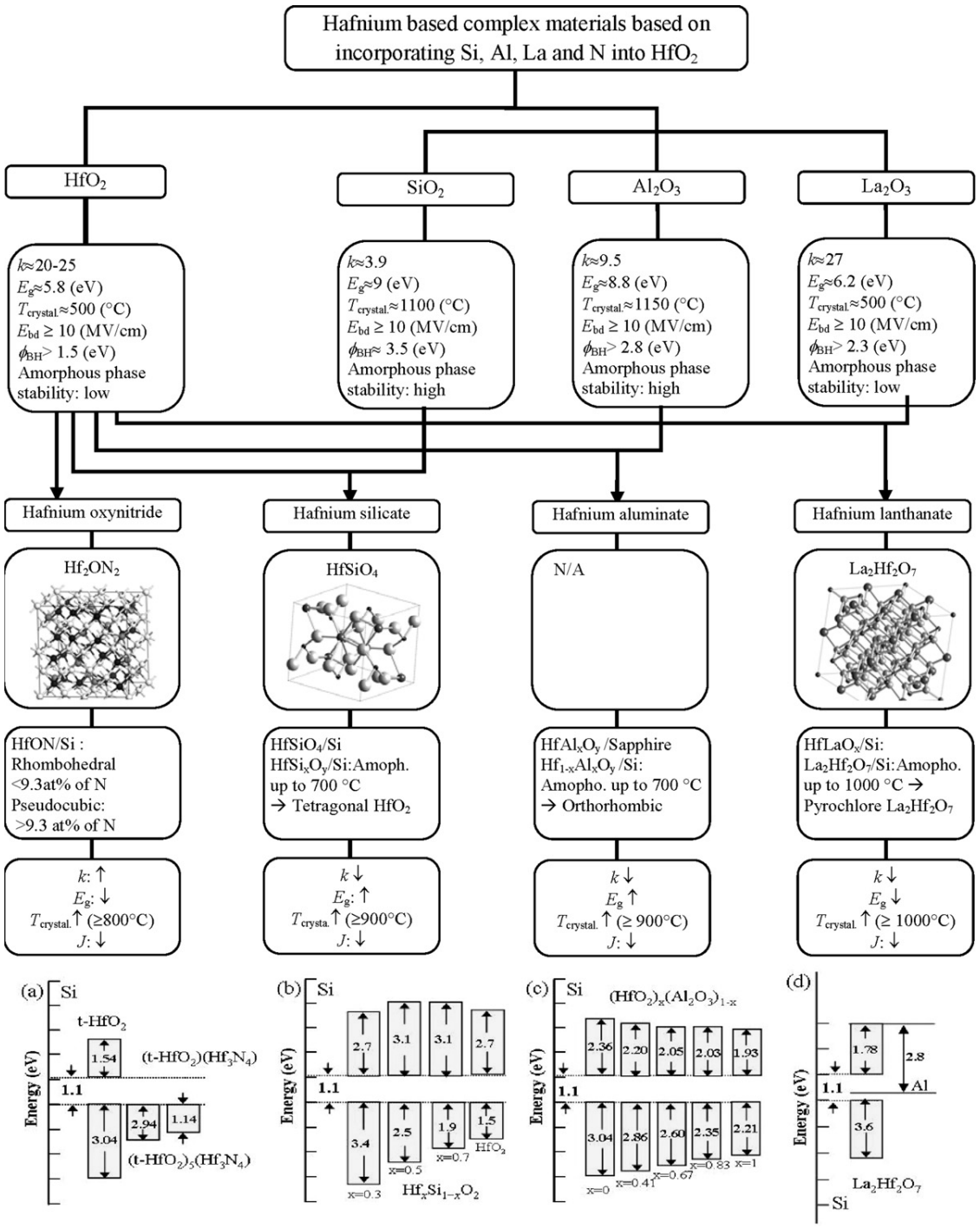

Figure 1.8 A summary of Hf-based complex oxides that illustrates material tunability and design approaches. (Choi, Mao et al. 2011)

While it is expected that the ability to etch these materials can also influence their selection, it is important to note that the creation of multiple development paths in constructing

MOSFETs, e.g. gate first and gate last processes, also exhibits significant influence on research direction. As NMOS and PMOS structures can be manufactured by a variety of paths, it can be expected that a process may be tailored to control variables such as which materials need to be subjected to etching, the extent of material to be removed, and the required selectivity between materials. A work published by Byoung Hun et al. compared electrical characteristics of MOSFET devices produced by both a conventional self aligned process path and a "gate last" approach whereby the source and drain regions are defined prior to the gate patterning. Also, in the gate last approach a dummy poly-Si gate was removed and eventually replaced with the desired metal gate/high-κ combination.(Byoung Hun, Choi et al. 2000) The results of this comparison are shown below in Figure 1.9. It can be seen that the two process paths yield comparable C-V curves and gate leakage values, with the devices manufactured using the gate last process displaying slightly better electrical properties such as lower current leakage.

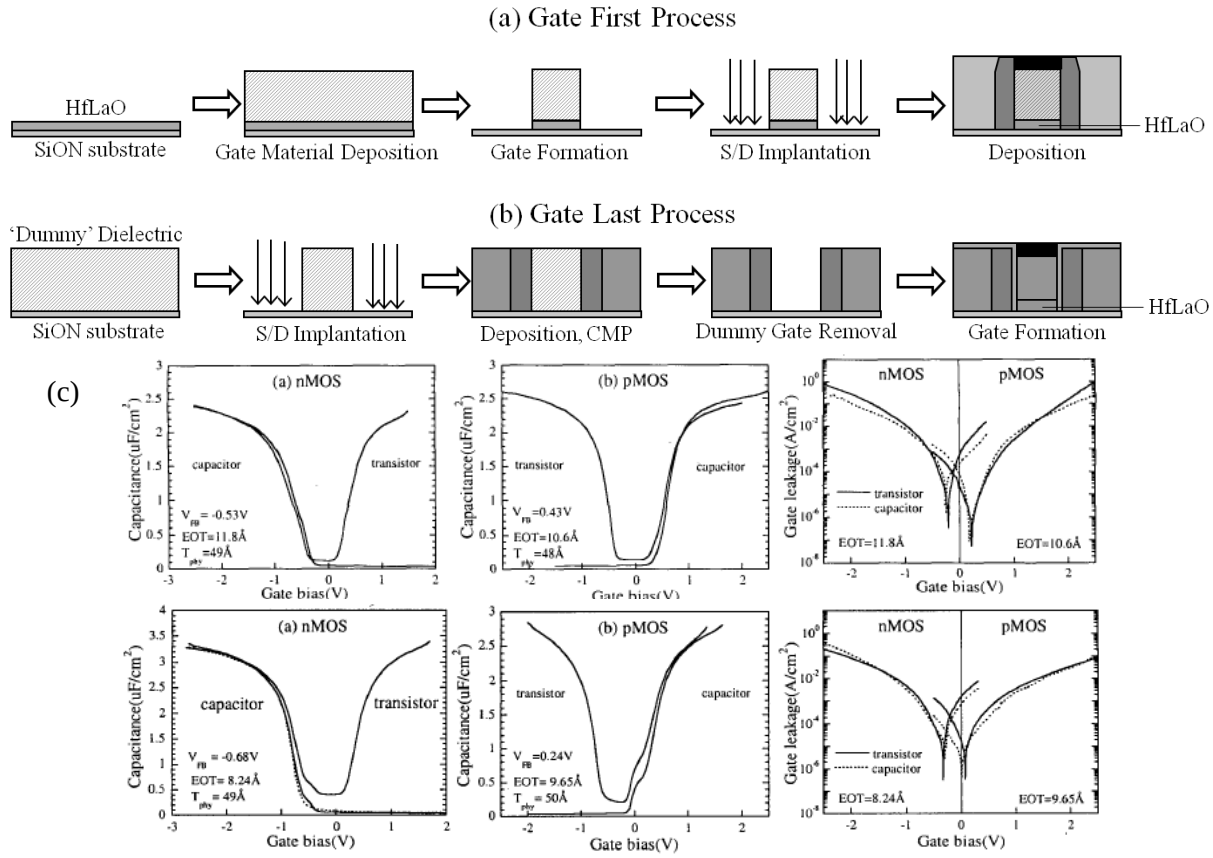

Figure 1.9 A possible example of (a) gate first and (b) gate last process paths, adapted from Hung, Hi-κ/MG Gate Stack Issues and Landscape, NCC AVS TFUG Proceedings, 2009. (c) Electrical characteristics of CMOS devices manufactured using alternate process paths (top row is data from a conventional self-aligned process; bottom row is data from a gate-last process). From Byoung Hun et al., IEDM Technical Digest, 2000.

1.3 Halogen-Based Plasma Etching of Oxide Materials

Plasma-surface interactions have found significant renown in the field of microelectronics processing, particularly in pattern transfer applications due to its high selectivity, anisotropy and reproducibility compared to wet etch processes. (Heinecke 1975)

While wet etch processes have been demonstrated as feasible for patterning of III-V semiconductor devices (the "digital etch" process) (Lee, Kim et al. 2001; Buttari, Heikman et al. 2002), significantly more mechanistic work has been published on studying "dry" plasma etching, with the possibility of combining the two approaches in gate dielectric etch (Shamiryan, Baklanov et al. 2009) and addressing selectivity discrepancy in a high mobility channel over silicon.(Shang, Campbell et al. 1994) While semiconductors, nitrides, metals and polymers have all been etched using various plasma chemistries (Kastenmeier, Matsuo et al. 1996; Shenton and Stevens 2001), this section focuses on the application of plasma etching to oxide materials. The removal of both oxygen and non-oxygen elements in an oxide etch process dictates simultaneous yet different reactions, a need that is fulfilled in a non-equilibrium plasma environment through the synergism and balance between ionic/radical induced etching and neutral stimulated deposition. (Mogab, Adams et al. 1978; Dagostino, Cramarossa et al. 1981; Steinbruchel 1983) The earliest and perhaps best known example is SiO_2 etching in a fluorocarbon chemistry, in which silicon reacts with fluorine species while the oxygen reacts with carbon species to produce volatile SiF_x and CO_x, respectively. It was noted in a study by Oehrlein et al. that these plasmas were responsible for the deposition of a fluorinated polymer film on the exposed surface. This polymeric film serves to control the etch rate and as such plays a critical role in regard to achieving the desired etching characteristics.(Oehrlein and Williams 1987) More recent studies involving the same general principle have been conducted regarding the etching of metal oxides in BCl_3 chemistries, using the specific example of high-k dielectrics (HfO_2, ZrO_2). (Sha, Cho et al. 2002; Sha, Puthenkovilakam et al. 2003) In all of these oxide systems, there is a delicate balance between deposition and etching as halogenated polymer layers are deposited on the surface during the etching process. These layers react slowly with incoming halogen species to

generate volatile products, which are predominantly removed by sufficiently energetic ion bombardment. This type of mechanism allows for the anisotropic etching of various oxides (Donnelly, Flamm et al. 1984), however, below a certain ion energy threshold, net deposition of the halogenated polymer layers occur. The deposited layers can pose an additional advantage in the context of a multi-material system: selectivity is enhanced by the preferential passivation of certain layers of a film, e.g. in a Si/oxide system polymer formation (C- or B- based) on Si far exceeds that on the oxide and as a result selective etching can be achieved.(Oehrlein, Zhang et al. 1994)

Recently, Martin published work on the etching of complex oxide $Hf_xAl_{1-x}O_y$ films of varying compositions in Cl_2 and BCl_3 plasmas. The results generally agreed with the collision cascade model of etching yield initially proposed by Steinbrüchel, whereby there is a linear dependence on the square root of ion energy ($E_{ion}^{1/2}$), signifying an ion-induced etch mechanism.(Steinbruchel 1989) However it was noted that above a certain value of energy there exists a transition point where a significant increase in etching rate occurs, which was postulated as being caused by the increased removal rate of incompletely chlorinated etching products at higher ion energy values. (Martin, Blom et al. 2009) A comparison with the etch rate data of metal nitride films such as TiN, TaN and HfN is shown in Figure 1.10, where chlorine plasmas demonstrated good etch selectivity and anisotropic profiles compared to fluorine based plasmas. (Hwang, Chen et al. 2005) In this set of experiments a transition point (as observed by Martin) was not readily apparent, however due to the lack of data presented for bias voltages under -100 V, it cannot be conclusively stated whether such a point exists or not. It should also be noted that the two studies were carried out at different power and pressure conditions – 500 W, 3 mTorr and 400 W, 10 mTorr by Martin and Hwang respectively.

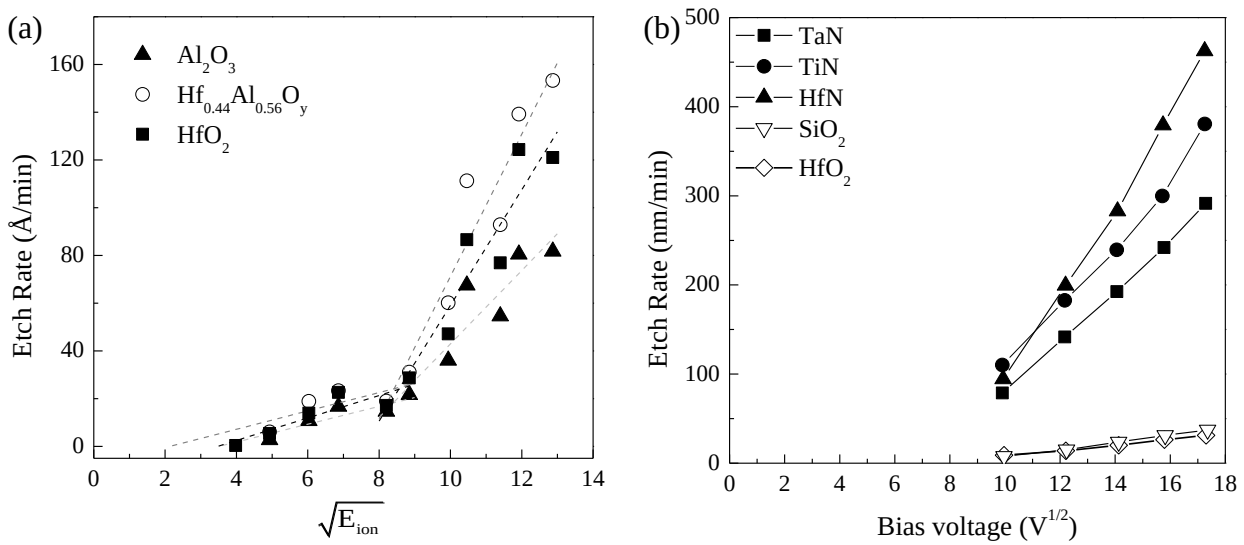

Figure 1.10 E_{ion} dependence in Cl_2 etching of various materials: (a) $Hf_xAl_{1-x}O_y$ films at 500 W, 3 mTorr and (b) metal nitride, SiO_2 and HfO_2 films at 400 W, 10 mTorr . (From Martin, JVST A 2009 and Hwang et. al, JVST A 2005).

By using Cl_2 as a base and adding selected chemistries to the gas feed, the etch selectivity can be tailored to suit the desired outcome e.g. the addition of a small amount of O_2 can improve the selectivity of poly-Si over SiO_2 and HfO_2. (Zau and Sawin 1992; Chen, Yoo et al. 2004) However oxygen addition can also lead to formation of passivation layers on the sidewalls of etched features – while these layers can serve to protect the feature from lateral etching (undercutting), they must later be removed by an appropriate chemistry to avoid compromising device performance and maintain the exact specifications of the manufacturing process. (Park, Ju et al. 2009) It has been shown that a Cl_2/CO combination can be used to achieve an anisotropic etched profile of an HfO_2 dielectric layer, while maintaining high selectivity to the underlying Si substrate, as illustrated in Figure 1.11.(Helot, Chevolleau et al. 2006)

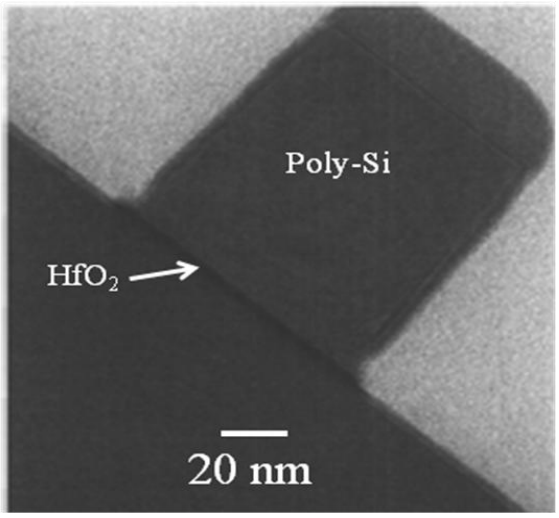

Figure 1.11 Effect of Cl_2/CO etch at 800W source power, 4 mTorr pressure, 40 sccm of each gas, and 0 V bias on a 100 nm poly-Si/3,5 nm HfO_2 gate stack. From Hélot et al. JVST A, 2006.

These and other issues associated with the etching become much more difficult to resolve when one factors the entire gate stack into the equation. For instance, a possible solution for the successful implementation of a metal gate system involves introducing two metals into the stack, one with a n^+ poly-Si-like work function and the other with a p^+ poly-Si-like work function, in order to ensure that the threshold voltages for the *n*- and *p*-channel transistors are complementary and small enough to achieve high drive currents for the supplied voltage. In this case, the selectivity of the etch chemistry towards the two different metals used in the gate stack would have to be considered when developing the process, as well as the ability to maintain the desired anisotropic profiles in all materials involved.

Another chlorine containing chemistry that has demonstrated favorable properties in the etching of novel material systems (such as metal gates and high-κ dielectrics) is BCl_3. (Sha and Chang 2004) BCl_3 has the ability to etch metal oxides (unlike Cl_2) through the formation of volatile $BOCl_x$ compounds (Iwakawa, Nagaoka et al. 2008) and also form passivating B-Si bonds that contribute to increased selectivity over the substrate in etching processes (Ohta,

Iwakawa et al. 2008). In the aforementioned paper by Martin et al. (Martin, Blom et al. 2009), BCl_3 plasma etching of the same Hf-based complex oxide films also showed a linear dependence on $E_{ion}^{1/2}$, with two main differences. Firstly, at sufficiently low E_{ion} values it was shown that there is actually a net deposition rate due to the heightened formation of a BCl_x containing film. Secondly, there was no transition region as observed in the Cl_2 etching. Both phenomena are illustrated in Figure 1.12.

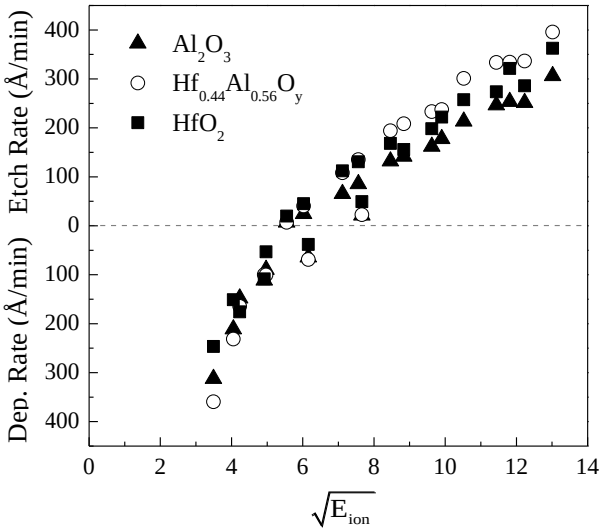

Figure 1.12 Dependence of etch rate on E_{ion} in the BCl_3 etching of various $Hf_xAl_{1-x}O_y$ films at 500 W, and 3 mTorr. From Martin, JVST A 2009.

1.4 Shallow Trench Isolation (STI)

In conjunction with the introduction of high-k materials to enable smaller and faster transistors, the method of isolating the transistors also evolved to accommodate higher packing density. The STI process involves the creation of spacer trenches filled with insulating material (typically an oxide) to electrically isolate individual transistor devices from each other. It was originally introduced as a replacement for local oxidation of silicon (LOCOS)-based techniques, owing to its superior scalability and planarity. (Badenes, Rooyackers et al. 2000) Successful STI

implementation requires stringent control over the etched trench profiles, quality of oxide deposition and the uniformity of planarization by chemical mechanical polishing (CMP). (Yeon and You 1998) Plasma etching has been utilized to provide the trench depth uniformity, sidewall tapering and high aspect ratios necessary for effective isolation as device sizes continue to shrink. (Werbaneth and Almerico 2000) However, as critical dimensions are reduced beyond 45 nm, the need to precisely and consistently control patterned features such as STI trenches becomes absolutely imperative. Previous work has examined the effects of center to edge variations in reactor flux conditions on the etched feature profiles (Hsu, Hoang et al. 2008), demonstrating the interplay between the macro- and microscopic scales. Figure 1.13 shows the etched profiles obtained in a cylindrical ICP system at the center (r = 0 cm) and the edge (r = 14.5 cm) of the reactor. The ratio of the current flow through the inner and outer components of the reactor's induction coil assembly (DC ratio = I_{outer}/I_{inner}) was varied from 11 to 30 and the operating pressure was varied from 45 to 25 mTorr in (a) and (b) respectively. The source and bias power were maintained at constant values of 350 and 150 W, and the chemistry used was Cl_2: O_2: N_2 at a ratio of 0.62: 0.11: 0.27.

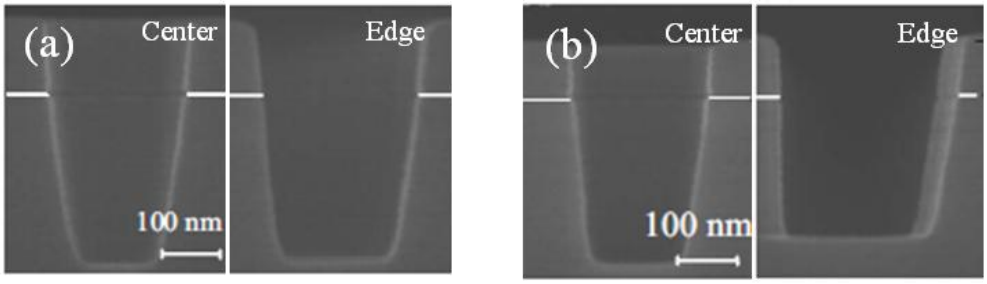

Figure 1.13 Variation in trench etch profiles at different locations within a reactor for Si in Cl_2:O_2:N_2 chemistry (0.62: 0.11: 0.27) at 350 W source power, and 150 W bias. DC ratio = 11, pressure = 45 mTorr for (a), DC ratio = 30, pressure = 25 mTorr for (b). From Hsu et al., JVST A, 2008.

The study outlined above focused primarily on the influence of physical parameters (e.g. variation in flux ratios due to manipulation of current supplied to the induction coil) while maintaining a constant etch chemistry environment. An investigation of the plasma-surface reaction kinetics in the STI process can thus supplement the existing work by extending the knowledge base to chemical considerations. Chemistries discussed in the literature cited above for STI patterning include Cl_2 + HBr with additives such as N_2, and He-O_2. STI as a case study also inherently provides a testing ground for the extension of the kinetics to both bulk and feature scales, characterizing the effects of chemistry variation on both macroscopic etch rates and feature profile variation.

1.5 Thermodynamic Assessment

Due to the factors discussed in the preceding sections, it is apparent that patterning complex materials via plasma etching is an enormously complicated process. In order to eliminate trial and error, a systematic approach to determining the feasibility of specific etch chemistries is highly desirable. Methodologies based on fundamental thermodynamic data are particularly useful as they allow initial assessments to be made without the need to perform costly and time-intensive experiments. Examples of such methods include the Ellingham diagram (plot of the Gibbs free energy change (ΔG) as a function of reaction temperature - used to predict the equilibrium temperature for reactions between a metal and non-metal reactants, e.g. O, S, N) (Ellingham 1944) and the Pourbaix diagram (plot of voltage potential with respect to the standard hydrogen electrode as a function of pH, which maps out possible equilibrium phases of an aqueous electrochemical system). (Pourbaix 1976) However, for the purpose of plasma

etching, which deals with vapor and solid phase reactants with practically no constraints on identity, the volatility diagram is the most useful of these techniques. First utilized to analyze the reactions of ceramics (Gulbrans.Ea and Jansson 1972) and metals (Gulbrans.Ea 1970) the volatility diagram is constructed using ΔG data and provides a graphical representation of the partial pressures of volatile etch products at a given temperature as a function of the partial pressure of the etchant gas being used. Such diagrams serve as a means of examining the dominant condensed and vapor phase species and can thus lead to a greater understanding of the reaction mechanisms of a process. The probability of a particular reaction pathway can be estimated by determining whether the vapor pressure of the gaseous etch product is above the threshold for substantial mass removal ($\sim 10^{-8}$ atm). This technique can potentially be applied to any materials for which the Gibbs free energy is available - resources such as the CRC Handbook of Chemistry and Physics, NIST-JANAF Database and Philips Research Journal are ample sources of information, with simulation tools such as MOPAC providing reasonable approximations for compounds whose data is not readily available.

The case study that is most relevant to this project involves the use of this method to propose a chemistry scheme for the etching of copper (Kulkarni and DeHoff 2002), which is a known etch-resistant material. Reactions of copper with molecular and atomic chlorine were considered. The overall mechanism was separated into two steps: formation of chlorinated copper compounds in the condensed (solid) phase, followed by the conversion of these products from the condensed phase to the gaseous form. While it is true that a non-equilibrium plasma environment drives reactions that would not otherwise occur without unacceptable amounts of heating, the diagrams reinforced the experimental observation that neither molecular or atomic

Cl reacts rapidly enough to be considered a viable etchant species. This driving equation in this case was:

$$3CuCl_2(c) = Cu_3Cl_3(g) + 3/2\,Cl_2(g) \tag{1.3}$$

However, the constraint placed upon this reaction by the mass balance criterion (shown in Equation 1.4) severely limited the access to the metastable portion of the $CuCl_2$-Cu_3Cl_3(g) equilibrium line.

$$\log P_{Cl_2} = \log P_{Cu_3Cl_3} + \log \frac{3}{2} \tag{1.4}$$

To overcome this barrier, the addition of molecular hydrogen gas (H_2) was considered, which shifted the dominant reaction to Equation 1.5.

$$3CuCl_2(c) + \frac{3}{2} H_2(g) = Cu_3Cl_3(g) + 3HCl(g) \tag{1.5}$$

This scenario resulted in the following mass balance criterion:

$$\log P_{HCl} = \log P_{Cu_3Cl_3} + \log 3 \tag{1.4}$$

which allowed much greater pressures of Cu_3Cl_3 over $CuCl_2$ to be generated. Substituting atomic hydrogen into the calculations revealed an even more significant change as the reaction environment changed from endothermic to exothermic. The results are shown in Figure 1.14.

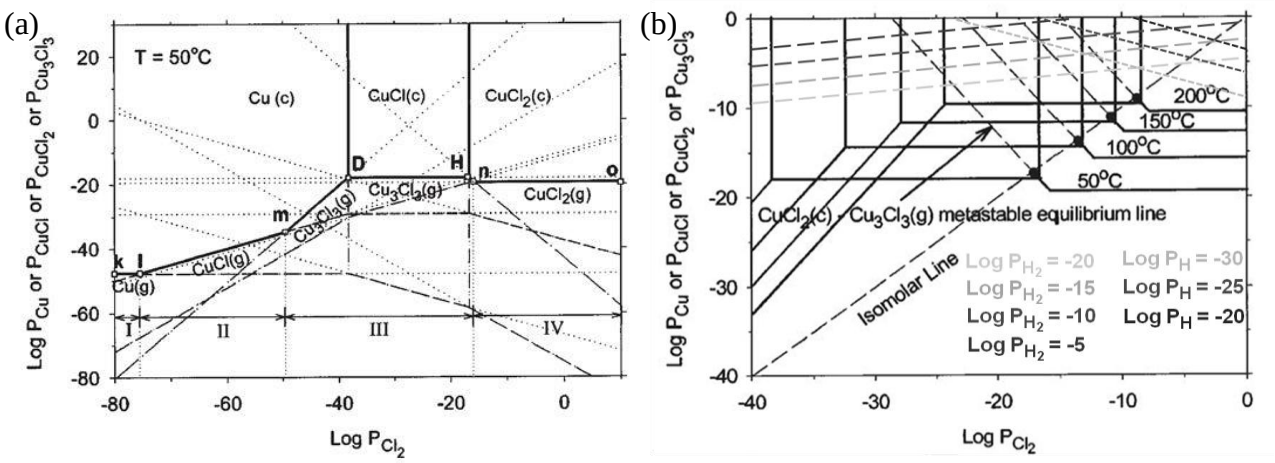

Figure 1.14 Volatility diagrams for (a) the Cu/Cl_2 system at 50°C and (b) the Cu-Cl_2-H/H_2 system at varying pressures of H/H_2 and varying temperatures. From Kulkarni and DeHoff, J. Electrochem. Soc., 2002.

Figure 1.14 (a) solely considers reactions with Cl_2. The vertical solid lines represent the equilibrium transitions between condensed states of Cu with various degrees of chlorination. Horizontal solid lines represent the vapor pressure at which transitions occur between the condensed and gas phase forms of the same chlorinated species. The sloped solid lines signify the maximum equilibrium vapor pressures of the gas phase etch products formed, while stable portions below the maxima are indicated by dashed lines. Metastable extensions are shown as dotted lines and represent theoretically achievable vapor pressures according to the thermodynamics of the reactions; however, these states are subject to a mass balance constraint, signified in the plot on the right as the isomolar line. For reactions which only involve copper and chlorine, states above the isomolar line are in violation of the principle of mass conservation even if they satisfy conditions of thermodynamic equilibrium and thus are not permissible. In the right plot, the addition of reactive hydrogen species, both molecular and atomic, is considered. With this new chemistry, separate maximum vapor pressure states can be calculated in the form of isobaric lines (shown as dashed lines for H_2 and dotted line for H), which represent the

maximum pressure of Cu_xCl_y species for a given pressure of H_2/H. It can be seen that utilizing this chemistry leads to much higher attainable vapor pressures than those from pure Cl_2.

The proposed two-step reaction scheme from this volatility diagram analysis was subsequently verified experimentally (Tamirisa, Levitin et al. 2007). The plasma reactor used was an ICP system at 500 W source power, 150 W substrate, with gas flows of Cl_2 and H_2 at 10 sccm each for a system operating pressure of 20 mTorr, thus signifying the viability of this approach in determining feasible etch chemistries for practical etching applications without the need for special equipment. The process comprised a low temperature Cl_2 exposure (to form $CuCl_2$ preferentially over CuCl), followed by a H_2 plasma to volatilize $CuCl_2$ in the trimer form, Cu_3Cl_3. In the study, Cu temperatures were maintained between 12 and 15°C, thus verifying the low temperature capability of the process. Additionally, XPS analysis showed the ability to control the desired halogenated state (in this case $CuCl_2$ over CuCl) in accordance with the thermodynamic analysis. In Chapter 2, volatility diagram analysis is expanded to a multicomponent high-k dielectric material by application to its constituent oxides.

1.6 Plasma Modeling

Shrinking IC device dimensions and increasing incorporation of novel materials have severely complicated the process of maintaining the desired feature geometry. It is thus highly desirable to have a model capable of predicting the etching behavior of these materials at both the bulk material and the feature scale. However, there are many challenges to realizing this goal. Plasmas are inherently complex environments which can feature numerous species (ions, radicals, neutrals, electrons, and photon/VUV radiation) and hundreds of reactions. Additionally,

vast disparities exist in both the length and time scales involved in modeling an etch process – from the reactor dimensions (cm) to feature profiles (nm), and processing time (minutes) to photo-stimulated excitation (<nanoseconds). These considerations have led to a multitude of modeling approaches, e.g. fluid models (Hsu, Coburn et al. 2006; Hsu, Titus et al. 2007), Monte Carlo (MC) (Hoang, Hsu et al. 2008; Hsu, Hoang et al. 2008), active site modeling (Chang and Sawin 1997; Greer, Coburn et al. 2000; Levinson, Shaqfeh et al. 2000), translating mixed layer (TML) kinetics (Kwon, Bai et al. 2006; Kwon and Sawin 2006) molecular dynamics (MD) (Barone, Robinson et al. 1996; Helmer and Graves 1998; Rauf, Sparks et al. 2007), and a hybrid plasma equipment model (HPEM), (Zhang and Kushner 2000) as no single method is adequate to address the overall scope of etching kinetics. A representation of these different length and time scales is shown in Figure 1.15. In the following sections the background behind the two major modeling tools used in this study is discussed: the bulk-scale translating mixed layer kinetics model, and the Monte Carlo-based feature profile simulator.

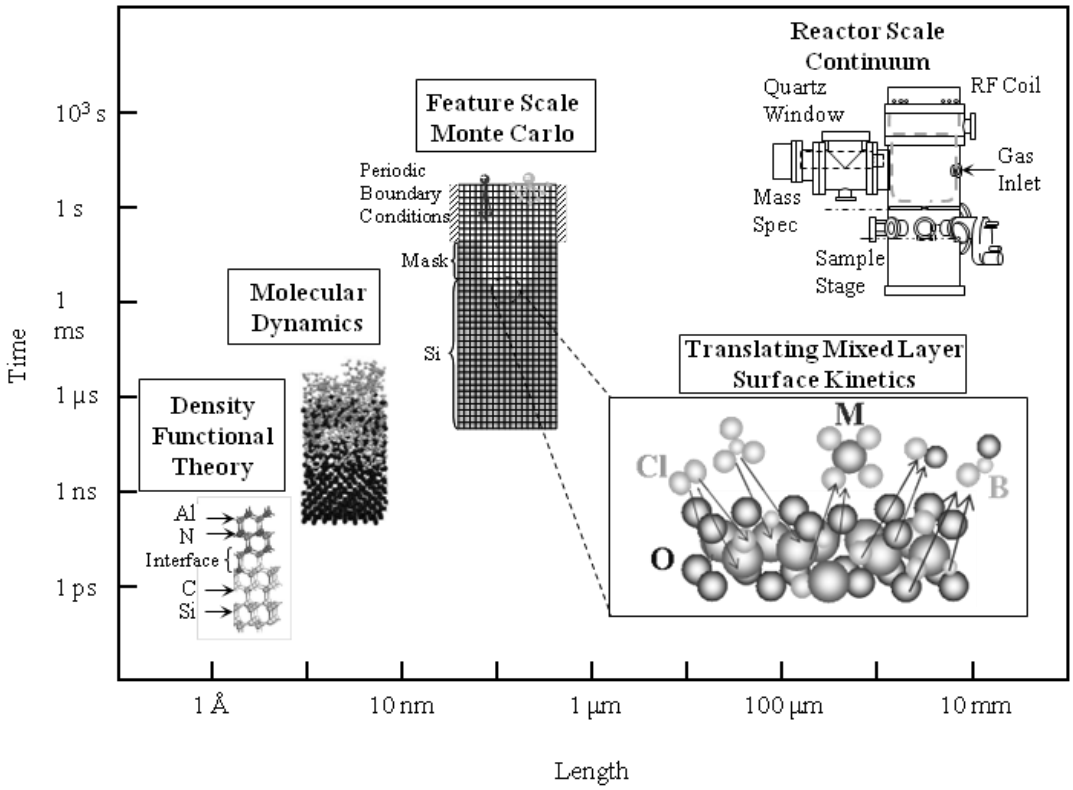

Figure 1.15 An illustration of the length and time scales addressed by several modeling techniques. The magnified inset shows a representation of a metal oxide surface being etched in a BCl_3 plasma.

1.7 Kinetic-Based Modeling of the Plasma/Surface Interactions

Previous work done by Martin established the feasibility of a surface site-based phenomenological model for predicting the etch behavior of high-k dielectric films in chlorine containing plasmas. A brief description of the model follows, with further details available in the literature.(Martin and Chang 2009) Thermodynamic properties such as the volatility of etch products, metal-oxygen and metal-chlorine bond strengths, and heat of enthalpy of reactions are used to provide initial estimates for the relative etching favorability of the different films. The model simplified the etching process into four major pathways and explained the etch-rate

dependence on key plasma parameters including plasma chemistry/condition, neutral-to-ion flux ratio, and ion energy, as well as the film composition. This model was able to fit experimentally obtained data of etch rate vs. ion energy for HfO_2, Al_2O_3 and HfAlO films in Cl_2 and BCl_3 plasmas, showing good agreement in both the etching and deposition regimes. However, the nature of the model made it unsuitable for incorporation into the final goal of this project: feature profile simulation using a Monte Carlo-based method. It is thus necessary for this model to be adapted into a kinetics-based form in order to make predictions about etch behavior at the smaller scale of device features and not solely in the bulk phase.

The translating mixed layer model was first utilized by Kwon et al. for the purpose of modeling Si etching in Cl_2 (Kwon and Sawin 2006) and SiO_2 etching in CF_4. (Kwon, Bai et al. 2006) The model assumes that all reactions take place within a 25Å layer known as the translating mixed layer, experimentally observed through x-ray photoelectron spectroscopy (XPS) measurements by Mahorawala et al. (Mahorowala and Sawin 2002), as well as the work of Layadi and Donnelly. (Layadi, Donnelly et al. 1997) The results of molecular dynamics simulations by Barone and Graves also supported these findings. (Barone and Graves 1995) The general framework of the model is depicted in Figure 1.16.

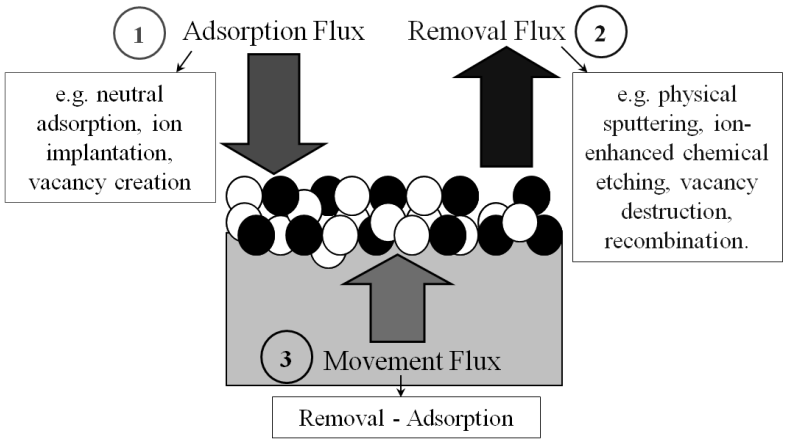

Figure 1.16 An illustration of the TML model showing the three major fluxes and listing some representative reactions.

Three major fluxes are assumed: ①adsorption - arrival of species to the surface from the gas phase, ② removal - desorption of species from the surface to the gas phase, and ③ movement from the underlying surface to the mixing layer to compensate for the difference between ① and ②. The addition of this movement flux allows for a greater degree of accuracy in modeling variations in the composition of the material being etched. (Kwon and Sawin 2006) Other key assumptions include conservation of the total number of atoms in the mixing layer and that above a certain energy threshold, all ions are implanted in the mixing layer (the sticking coefficients for all ionic species are unity). Further details about other fundamental assumptions governing the TML model have been discussed in the previous work by Guo et al. (Guo, Bai et al. 2009).

The adsorption and removal fluxes comprise several different reaction types. Examples include neutral and ion adsorption onto different surface atoms, physical sputtering, ion-enhanced chemical etching, dangling bond annihilation, vacancy creation and densification. This represents a significant evolution beyond the phenomenological model, which simplified the reaction pathways into "lumped" single reactions for deposition on and removal of substrate

atoms. The rates of reactions in the TML model are dependent on factors such as the concentration of each element present (x), ion energy (E), neutral/ion fluxes (G), angular dependence (φ), sticking probabilities (S), and reaction rate coefficients (β). A set of differential mass balance equations can then be formulated for each element in the system, and these equations are integrated to a steady state solution under the initial condition of a defined surface composition (e.g. for a pure silicon substrate the initial value of x_{Si} is 1). The result of this integration is a prediction of not only the etching yield, but also the concentration of each element in the surface mixed layer. This latter capability provides a second layer of validation that is not available in the phenomenological model.

A thorough description of the various reaction types utilized in the TML model for the system of HfLaO etching in Cl_2-based chemistry is provided in Chapter 2, however for the purpose of illustrating the model's fundamental construction, a simplified equation set for simulating the etching of SiO_2 in a F_2 plasma is shown in Table 1-1 as an example. (Kwon and Sawin 2006) The adsorption and etching reactions are separated by a double lined border. In this reaction set it is assumed that F^+ and F are the single dominant ionic and neutral species, respectively. There are a total of three adsorption reactions and five etching reactions.

Table 1-1 Adsorption reactions for the etching of SiO_2 in a F_2 plasma. (Adapted from Kwon et al., JVST A 2006)

	Reaction	Rate Expression	Reaction Type
(1)	$F_{(g)} \rightarrow F_{(s)}$	$r_{A1} = s_{F\_on\_Si} G_F J_{Si\_V}$	F neutral adsorption on Si
(2)	$F_{(g)} \rightarrow F_{(s)}$	$r_{A2} = s_{F\_on\_O} G_F J_{O\_V}$	F neutral adsorption on O
(3)	$F^+_{(g)} \rightarrow F_{(s)}$	$r_{A3} = s_{F^+} G_{F^+} f_{threshold}$	F ion adsorption
(4)	$Si_{(s)} \rightarrow Si_{(g)}$	$r_{S1} = Y_{Si} G_{F^+} x_{Si}$	Physical sputtering of Si
(5)	$F_{(s)} \rightarrow F_{(g)}$	$r_{S2} = Y_F G_{F^+} x_F$	Physical sputtering of F
(6)	$O_{(s)} \rightarrow O_{(g)}$	$r_{S3} = Y_O G_{F^+} x_O$	Physical sputtering of O
(7)	$Si_{(s)} + 2F_{(s)} \rightarrow SiF_{2(g)}$	$r_{E1} = \beta_{SiF_2} \left(J_{Si\_F}\right)^2$	Ion-induced SiF_2 production
(8)	$O_{(s)} + F_{(s)} \rightarrow OF_{(g)}$	$r_{E2} = \beta_{oF} \left(J_{O\_F}\right)$	Ion-induced OF production

The first two adsorption reactions (labeled (1) and (2)) involve F neutrals adsorbing on Si and O atoms. The third corresponds to ion implantation of F^+. The first three etching reactions (labeled (4) - (6)) represent physical sputtering of Si, F and O atoms. The other two are related to chemical etch processes, specifically the removal of Si and O through SiF_2(g) and OF(g) formation respectively. Definitions of the parameters used in the rate expressions are provided in Table 1-2.

Table 1-2 Examples of parameters used in the TML etch model for F_2 etching of SiO_2 (Adapted from Kwon et al., JVST A 2006)

Symbol	Unit	Comment
r_i	Conc./ion	Reaction rate in yield unit (reaction rate divided by total ion flux)
S	-	Sticking coefficient
G_i	Conc./ion	Flux of species *i* divided by total ion flux
J_{i_j}	Conc.	Concentration of species *i* bonded to species *j* in the mixing layer
$f_{threshold}$	eV	Threshold energy for ion implantation
Y_i	-	Sputtering yield coefficient of species *i*
x_i	Conc.	Total concentration of species i in the mixing layer
β	-	Reaction rate coefficient of ion-induced etching

The movement flux for this system is defined as:

$$r_{movement} = \frac{1}{3}\left(-r_{A1} - r_{A2} - r_{A3} + r_{S1} + r_{S2} + r_{S3} + 3r_{E1} + 2r_{E2}\right)$$

which is the sum of the atoms removed by the etching terms minus the atoms added by the deposition terms, normalized by the number of atoms in an SiO_2 molecular unit. The differential mass balance equations for this system are defined as:

$$\frac{dx_{Si}}{dt} = -r_{E1} - r_{S1} + r_{movement}$$

$$\frac{dx_{F}}{dt} = r_{A1} + r_{A2} + r_{A3} - r_{S2} - 2r_{E1} - r_{E2}$$

$$\frac{dx_{O}}{dt} = -r_{S2} - r_{E2} + 2r_{movement}$$

A comparison of the simulated model results with experimental data for the experimentally measured etch yield of SiO_2 in F_2/Ar chemistry as a function of neutral/ion flux ratio at a constant ion energy of 350 eV is shown in Figure 1.17, demonstrating a good fit.

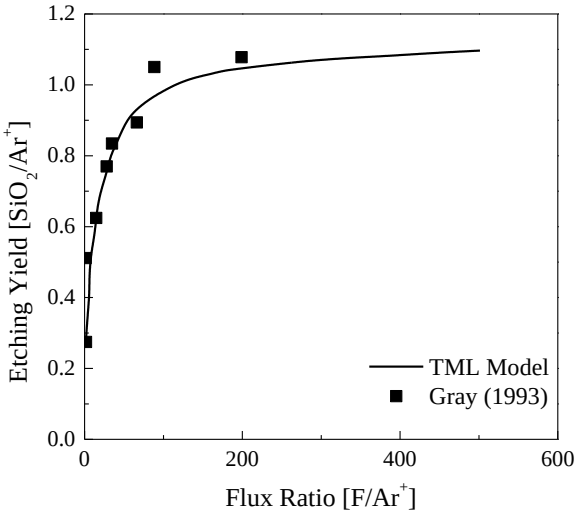

Figure 1.17 The TML model applied to SiO_2 etching in F_2/Ar chemistry as a function of neutral/ion flux ratio for E_{ion} = 350 eV. From Kwon et al., JVST A 2006.

In order to reasonably represent the etching process through the equation set detailed within the model, attempts are made to utilize as many experimentally observable parameters as possible. For example, quadrupole mass spectrometry (QMS) data can provide the identity and relative quantities of etch products, and sticking coefficients can be measured from beam experiments in simpler systems, e.g. Si in Cl_2. (Chang, Mahorowala et al. 1998) However for more complex plasma chemistries and material surfaces, it may be substantially more difficult, if not impossible, to measure some of these parameters, such as comparative reaction probabilities and scattering angles. These can potentially be calculated through tools such as molecular dynamics (MD) simulations. Finally, those parameters that cannot be calculated directly are obtained by fitting the model to experimental data. In these cases, extraction of the sticking coefficients (S) and reaction rate constants (β) can be done by fitting the model to plots of etch yield vs. neutral/ion flux ratio under a broad range of conditions. Comparison with data reported by publications from other authors, if any is available, can also serve as a means of testing the

efficacy and robustness of the model. The primary advantage of the TML model format is its ability to provide input parameters for a feature profile simulator, e.g. a Monte Carlo based cellular method (discussed in the following section). The ability to compare feature profiles is essentially the ultimate validation of the model's ability, and in turn can provide predictive capabilities for complex variations in both the material being etched and the selected etchant chemistry. A diagram illustrating these capabilities and the interconnected nature of the two models is shown in Figure 1.18.

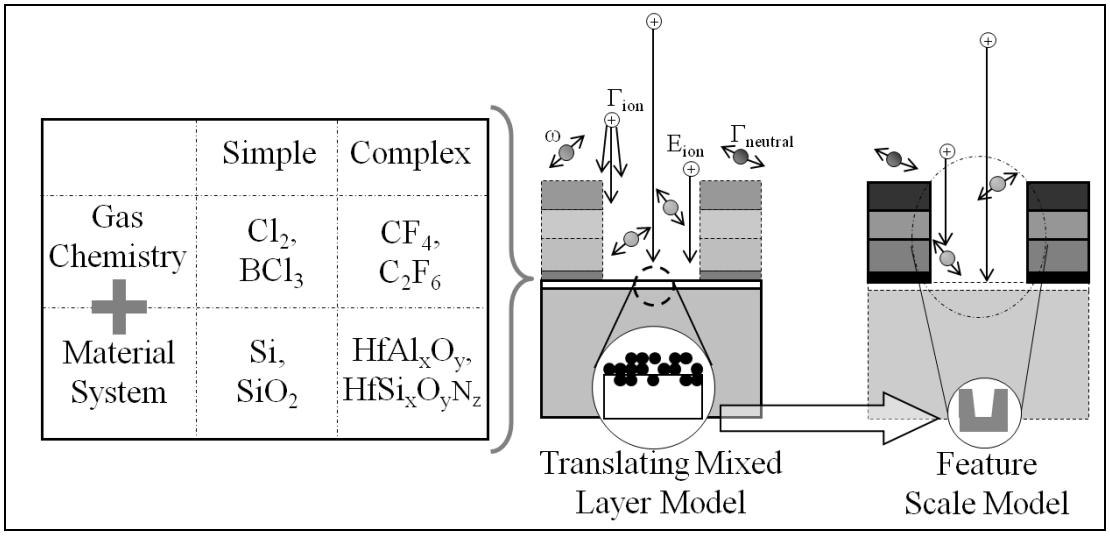

Figure 1.18 Diagram of coupling between the TML and Feature Scale Modeling Components.

1.8 Cell-Based Monte Carlo Feature Profile Simulation

Increasing the fidelity of pattern transfer across increasing wafer diameters even as the individual feature sizes continue to shrink remains a critical standard in IC manufacturing, but the financial and temporal cost associated with having to perform diagnostic experiments can be significant. Feature scale profile simulation can thus serve as an extremely useful complementary

tool to assist in determining the plasma parameters which could serve as the origin of deviations from ideal etch profiles. While a variety of methods including the marker and string (Oldham, Neureuther et al. 1980), characteristic method (Jurgensen and Shaqfeh 1989), and level set (Osher and Sethian 1988) have been used to simulate feature profile evolution, the cell-based Monte Carlo approach remains the best option for incorporating physical, chemical and compositional dependencies, which are crucial for plasma processing.

Monte Carlo-based (MC) simulation methods have been used from as early as 1978 to model spatial distributions and compositions on atomistic scales. (Donnelly and King 1978) The technique was extended to modeling the evolution of surface topography during ion bombardment-induced sputtering (Rossnagel and Robinson 1983), and subsequently applied to predicting the implantation profiles of poly(methyl methacrylate) exposed to ion beams of H^+ and Ga^+. (Karapiperis, Dubreuil et al. 1985) MC simulations generate species populations as a collection of particles followed in space and time. Events involving the particles take place at random times, but with an average frequency close to that of the real (measured) frequency. This method utilizes relatively elementary concepts such as Newton's laws of motion and reaction probabilities. A large number of particles are sampled in order to obtain a decent representation of the configuration and velocity space being studied. The MC method has subsequently been combined with other modeling techniques such as fluid models or particle-in-cell methods in a "hybrid approach" to obtain the best possible results in systems which contain physical properties that differ by orders of magnitude, such as plasmas containing ionic and electronic transport. (van Dijk, Kroesen et al. 2009)

For profile evolution of a solid surface being exposed to gas phase reactants (such as plasma etching), a computation domain is utilized that is separated into intervals or cells, the size

of which can range from that of individual atoms to tens of nanometers. These cells in turn comprise a finite number of particles, the composition of which is then varied to represent either the gas phase (empty) or the substrate (filled). Feature geometry can be defined by manipulating the cell placement. Using the generated flux calculations from the MC model as an input, incoming particles from the gas phase strike cells and are either scattered or incorporated based on factors including reaction probabilities, particle incidence angle and cell composition. Surface reaction outcomes are calculated based on parameters such as rate coefficients, sticking probabilities, and threshold energies. The paths of any scattered particles and generated etch products are monitored to the point at which they are incorporated or escape the simulation domain. With the capability and flexibility to include large amounts of kinetic data (such as chemical reaction sets) that improve the accuracy of the model in characterizing specific plasma processes, MC methods have been used to simulate profile evolution in applications as diverse as photoresist mask faceting (Mahorowala and Sawin 2002), ionized physical vapor deposition of copper (Arunachalam, Rauf et al. 2001) and via and trench etching in SiO_2. (Stout, Rauf et al. 2006)

A recent application of MC modeling to successfully capture the variations in etched profiles was demonstrated by Hsu and Hoang in the case of shallow trench isolation (STI). (Hsu, Hoang et al. 2008)The work demonstrated the coupling of a reactor and feature scale model to simulate the variations in physical conditions such as total gas pressure and coil current. The species fluxes in the MC model were calibrated using observations from the reactor scale model, such as reductions in the neutral to ion ratio and depositing species fluxes from center to edge. The results of the simulations compared to the experimental profiles are shown in Figure 1.19.

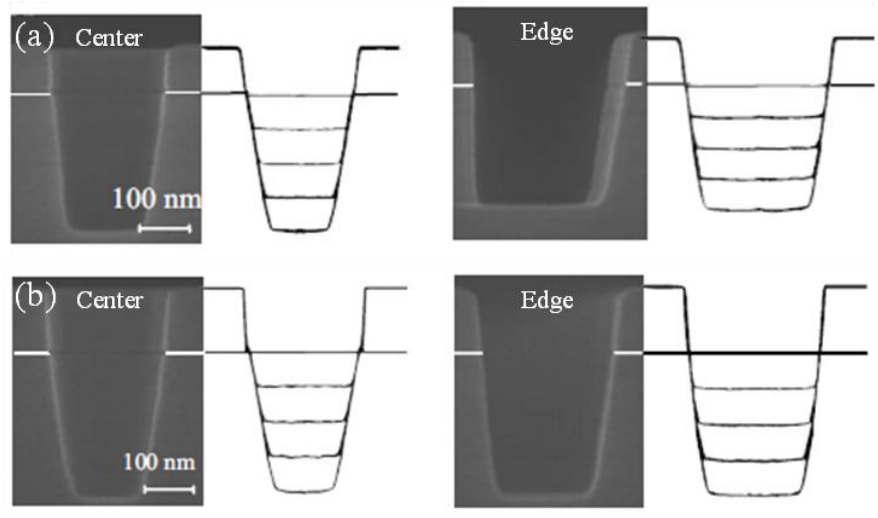

Figure 1.19 Use of an MC model to fitting of variations in trench etch profiles at different locations within an ICP reactor for Si etched in Cl_2:O_2:N_2 chemistry (0.62: 0.11: 0.27) at 350 W source power, and 150 W bias. (a) DC ratio = 11, pressure = 45 mTorr and (b) DC ratio = 30, pressure = 25 mTorr. From Hsu et al., JVST A, 2008.

The accuracy of the MC model predictions is largely based on the quality and specificity of inputs it receives. While work such as the literature cited above relied on separate sources to perform experimentation, thus running the risk of losing information through transfer, this study aims to utilize the TML modeling approach as a means of bridging the gap between bulk scale observations and individual feature geometry for novel complex oxide materials. By conducting as many *in situ* measurements as possible and performing carefully controlled experimentation, it is hoped that a powerful framework for predicting the behavior of future material candidates can be established.

1.9 Scope and Organization

The emergence of novel, complex materials as a driving force for increased functionality of IC devices brings new challenges for high-fidelity plasma patterning. It is therefore highly desirable for a universal methodology to be established that can potentially supply predictive capabilities about the etching characteristics of hitherto unused materials or compounds, combining both theoretical assessments and experimental measurements. The following chapters lay out the development of such a framework, primarily applied to the base system of $Hf_{0.25}La_{0.12}O_{0.63}$ in chlorine-containing chemistries.

Chapter 2 describes the apparatus used to conduct the experimental work in this study, focusing primarily on the inductively coupled plasma (ICP) reactor and the *in situ* diagnostic probes equipped for the purpose of characterizing the plasma, etch products and macroscopic etch rate of the complex oxide films. An ultra high vacuum transfer system and quasi *in situ* surface characterization techniques are also discussed. In addition, theoretical methods such as volatility diagram analysis, the TML model and the feature profile simulator are described in more detail using specific model systems.

Chapter 3 discusses the use of *in situ* experimental measurements to build a foundation for the construction of the aforementioned TML model, with emphasis on the macroscopic etch rate, etch product identification and quantification, and post-plasma exposure surface composition as measured by QCM, QMS and XPS respectively. Variations in etch behavior as a function of the chemistry selected (Cl_2 vs. BCl_3) and plasma properties of the ICP reactor are also examined.

Chapter 4 demonstrates the development of the TML model for multicomponent oxide films, starting with the foundation of the surface-site based phenomenological model. The etch rate data for the $Hf_{0.25}La_{0.12}O_{0.63}$ and La_2O_3 film system is fitted, with the results compared to previously acquired data for HfAlO films etched in Cl_2 and BCl_3 chemistries. Variations in the extracted parameters between the different material systems are analyzed in terms of the thermodynamic volatility diagram analysis conducted in Chapter 2 as well as the experimental results from Chapter 3. The TML model was then used to fit the etch rates, with additional validation provided through fitting to the QMS etch product measurements and XPS surface analysis.

Chapter 5 addresses feature profile simulation predictions based on extracted kinetic parameters for the HfLaO/Cl_2 system. Comparisons to experimentally patterned features were made and good agreement was found. The ability of this methodology to handle variations in etchant chemistry as well as material substrate is demonstrated through its successful application to the etching of Si in Cl_2/O_2 chemistry for shallow trench isolation (STI).

CHAPTER 2: EXPERIMENTAL SETUP

Contained in this section is a description of the systems that were used for the experimental etching work of this study, including various analytical tools that are used to characterize the plasma environment, study the in-situ reactions of the etching process, and analyze the etched material samples. Details regarding the theoretical methods used in this study, namely volatility diagram analysis, surface-sited based phenomenological modeling, bulk-layer translating mixed layer modeling, and feature scale Monte Carlo cell-based simulation are also discussed.

2.1 UHV Transfer Tube and Load Lock

An ultra high vacuum transfer system provides capability for processing and analysis in a variety of chambers without having to expose samples to ambient conditions. Each chamber is separated from the main transfer system by a gate valve. Figure 2.1 shows the relevant chambers to this experimental work attached to the tube: an inductively coupled plasma reactor, an X-Ray photoelectron spectroscopy system and a load lock.

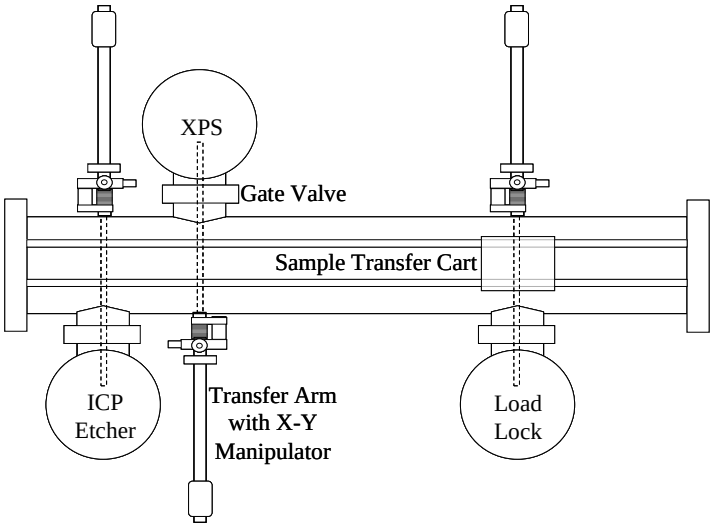

Figure 2.1 A schematic illustration of the UHV Transfer Tube Setup.

The main tube is connected to three pumps, each one for bringing the system to a different pressure regime: an Edwards E2M-18 mechanical pump, a Leybold 360 turbomolecular pump, and a CTI CT-8 croygenic pump. Pressure is monitored by a cold cathode gauge. Samples are introduced to the tube via a load lock pumped by another Leybold 360 turbomolecular pump (base pressure ~10^{-6} Torr), which is in turn backed by the same E2M-18 mechanical pump connected to the tube. A linear transfer arm on the other side of load lock allows the sample to be transferred to a cart which is utilized to ferry samples along the tube to the various chambers. The cart runs along a metal track secured to the floor of the transfer tube and is towed by a motorized pulley system. Magnetically coupled linear transfer arms connected to the tube allow samples to be loaded from the cart into the various chambers. More detailed information about this setup, including dimensions, is provided in Appendix A.

2.2 ICP Plasma Etcher

The main experimental system used in this study was a custom-built inductively coupled plasma etcher. The system can be operated in both capacitively coupled (E) and inductively coupled (H) modes based on the magnitude of the RF power supplied as observed and described by numerous authors.(Amorim, Maciel et al. 1991; Hopwood 1992; Kortshagen, Gibson et al. 1996) At low rf powers the E mode (driven by an electrostatic field) dominates and as the rf power is increased there is a transition to the H mode (driven by electromagnetic induction) which is marked by a dramatic increase in the plasma density. However, it is possible for the H mode to be sustained at lower power values owing to its more efficient sustaining mechanism. (Miyoshi, Petrovic et al. 2002) This reactor's main chamber is constructed from stainless steel and is divided into two areas, as depicted in Figure 2.2.

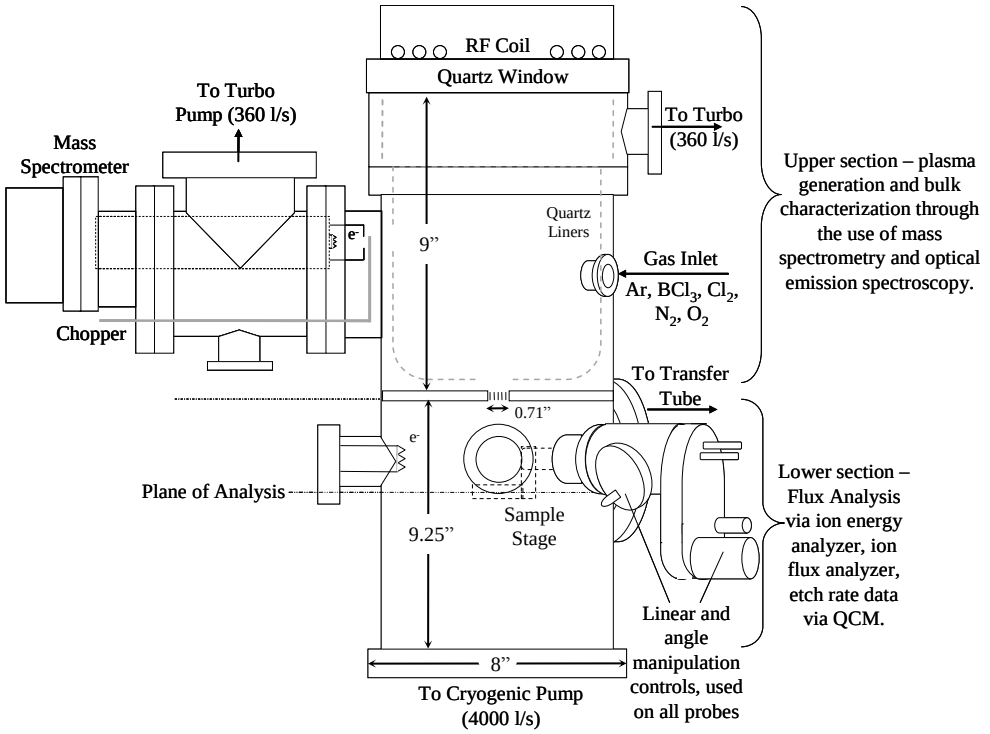

Figure 2.2 A schematic illustration of the ICP etcher showing divisions in chamber.

The upper section is capped by a quartz window upon which rests a coil connected to a 13.56 MHz RF power source. Plasma is generated via inductive coupling through the top quartz window, while a quartz liner serves to isolate the plasma from the metal walls of the chamber. A metal electrode located in the interior of the beam source allows DC biasing of up to 500 V.

A roughing valve connected to this section allows for pumping via a Leybold D25B mechanical pump. This mechanical pump also backs a Leybold Turbovac 361C turbomolecular pump directly connected to the upper section, which allows a base pressure of 4.0×10^{-7} Torr to be achieved. This section also contains the gas inlet through which the process gases – Ar, BCl_3, Cl_2, N_2 and O_2 – are introduced. The gas flow rates are controlled by MKS mass flow controllers of ranges varying from 10 to 500 sccm. The upper section can be accessed by a UTI 100C quadrupole line of sight mass spectrometer, and the specific schematic and function of this system is discussed in a later section. The lower boundary of this section is a metal barrier with a

grounded, gridded orifice of diameter 0.71 inches opened in it. This design allows a plasma beam to be extracted from the upper section and directed into the lower area, which is discussed in the subsequent paragraph.

For a 13.56 MHz RF ICP system using Cl_2 as the feed gas (with 1% each of He, Ne, Ar, Kr, and Xe) with an incident power of 400 W and operating pressure of 2 mTorr, typical ion density (n_i) and electron density (n_e) values are 6 x 10^{10} cm^{-3} (Malyshev and Donnelly 2001) with an average electron temperature (T_e) of 3 eV(Malyshev and Donnelly 2000). In a similar system utilizing CF_4 as the feed gas, with an incident power of 300 W and operating pressure of 10 mTorr, n_i and n_e were 2.75 and 1.6 x 10^{11} cm^{-3}, with T_e ~ 6.2 eV. The mean free path of particles in the chamber is given by the equation:

$$\lambda = \frac{KT}{\sqrt{2}\, p \pi d_o^2} \tag{2.1}$$

Where p = pressure, and d_0 = collision diameter of the gas molecule. For diatomic Cl_2 with a collision diameter of 4.11 Å (Ono and Tuda 1997), the mean free path at the given operating pressure of 2 mTorr and a neutral gas temperature of 590 K (Donnelly and Malyshev 2000) is therefore estimated as 4.07 cm. For CF_4 with a collision diameter of 4.1Å (Cui, He et al. 2000) at 10 mTorr and an estimated neutral gas temperature of 750 K, (Cruden, Rao et al. 2002) the mean free path is calculated to be 1.04 cm. However, it should be noted that at the pressure of the extracted beam chamber (~1 x 10^{-4} Torr) the mean free paths is larger: 81 cm for the Cl_2 plasma and 104 cm for the CF_4 plasma.

The lower area of this system is connected to a CTI CT-8 cryogenic pump with a pumping speed of 4000 l/s which maintains a base pressure of 10^{-8} Torr and a processing pressure of ~1.0 x 10^{-4} Torr. The cryo pump is necessary in this reactor as the small conductance

of the extraction grid hole prevents the turbo pump in the upper chamber from evacuating the entire reactor to a sufficient extent. An ion gauge connected to this area provides the current pressure inside the chamber, and viewports allow for visual confirmation of the plasma generation. A 0.004 inch diameter tungsten filament emits low energy electrons to minimize spreading of the aforementioned plasma beam and also to prevent charge accumulation on insulated samples. This section houses a rotatable, grounded sample stage which can hold wafer chips roughly 1.5 cm^2 in area. The lack of biasing means that ions are accelerated towards the substrate solely by the bias potential applied to the extraction grid. The sample holder is physically mounted on a pin protruding from the stage, without electrostatic chucking. The rotational capability of the stage allows for variation in the beam impingement angle relative to the substrate surface. A Langmuir Probe and optical emission spectrometer can be mounted in either section of the reactor to study selected properties of the bulk plasma or extracted beam, respectively. These diagnostic tools are discussed in more detail in Section 2.5.

2.3 Material Systems For Logic Applications

At length scales approaching that of devices manufactured today, conducting studies of the etching of patterned surfaces is difficult, e.g. etch product identification and quantification is made more feasible when a larger amount of material is available to be etched. Thus, for the purpose of this work it is important to obtain blanket films of the materials of interest in such devices as a MOSFET gate stack, specifically the complex gate dielectric and silicon substrate, to aid in the study of etch behavior - a listing of the materials is provided in Table 2-1. Ultimately, the etching behavior of materials in the context of the stack is of great importance for

the goal of modeling feature profile evolution, as achieving the desired profile for all of the components involved is largely dependent on the relative selectivity of the chemistries chosen. However, intellectual property and proprietary technology claims make the publication of etched profiles in cutting edge devices a rare occurrence, and when such profiles are available, the complete details of the process parameters used are often withheld.

Table 2-1 Detailed listing of the material blanket films investigated in this work

Material	**Application**	**Synthesis Method**	**Film Thickness (Å)**	**Density (g/cm^3)**
Si	MOSFET Substrate	Chemical Vapor Deposition	~5000	2.33
$Hf_{0.25}La_{0.12}O_{0.63}$	MOSFET High-k Gate Dielectric	Sputter Deposition	~1000 - 2000	Stoichiometry dependent HfO_2 - 9.68 La_2O_3 - 6.51

2.3.1 Hafnium Lanthanate ($Hf_xLa_yO_z$)

The $Hf_xLa_yO_z$ films used in this study were synthesized at Uppsala University, Sweden, using a Kurt J. Lesker CMS-18 sputtering system equipped with a source cluster comprising two 4" magnetrons and two 2" magnetrons in a confocal configuration, powered by Advanced Energy Pinnacle Plus supply units. The distance between the metal targets (Hf and La) and the substrate was ~18 cm. The magnetrons were operated at a constant power in pulsed DC mode at 250 kHz and 350 kHz for the Hf and La targets, respectively. An operating pressure of 4 mTorr was maintained with gas flow rates of 40 sccm Ar and 25 sccm O_2. The silicon substrate wafers were treated in HF prior to deposition to remove the native oxide layer. Films were also deposited on Maxtek SC-101 AT-cut quartz sensor crystals for use in the quartz crystal microbalance (QCM) technique. Pure HfO_2 and La_2O_3 films, as well as mixed compositions of $Hf_xLa_yO_z$, were obtained by varying the ratio of the power supplied to the magnetrons. The

primary film composition used in this study was $Hf_{0.25}La_{0.12}O_{0.63}$. Film thicknesses of ~1000 - 2000 Å were obtained by varying the deposition time between ~25 - 60 minutes.

XPS analyses of pure HfO_2 and La_2O_3 films were performed to determine the FWHM for fitting of the Hf 4f and La 3d peaks. Detailed scans of Hf 4f, La 3d, O 1s and C 1s are shown in the top row of Figure 2.3 for the HfO_2 (▲) , La_2O_3 (∆), $Hf_{0.25}La_{0.12}O_{0.63}$ (●) and $Hf_{0.11}La_{0.23}O_{0.66}$ (○) films.

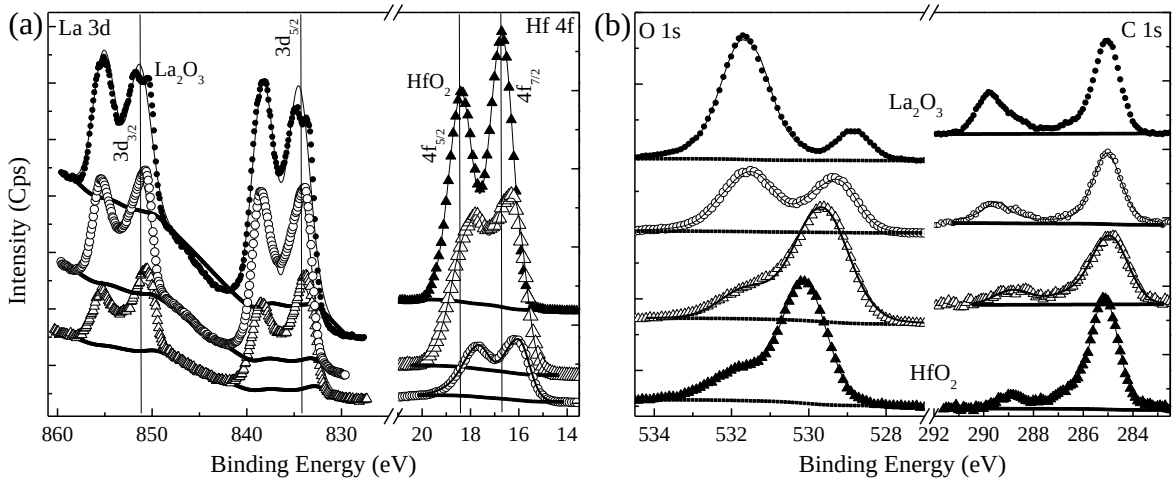

Figure 2.3 (a) La 3d and Hf 4f and (b) O 1s and C 1s XPS spectra for HfO_2 (▲), La_2O_3 (●), $Hf_{0.25}La_{0.12}O_{0.63}$ (Δ) and $Hf_{0.11}La_{0.23}O_{0.66}$ (○).

Deconvoluted spectra of the O 1s region for the primary film composition utilized in this study ($Hf_{0.25}La_{0.12}O_{0.63}$) are provided separately in Figure 2.4.

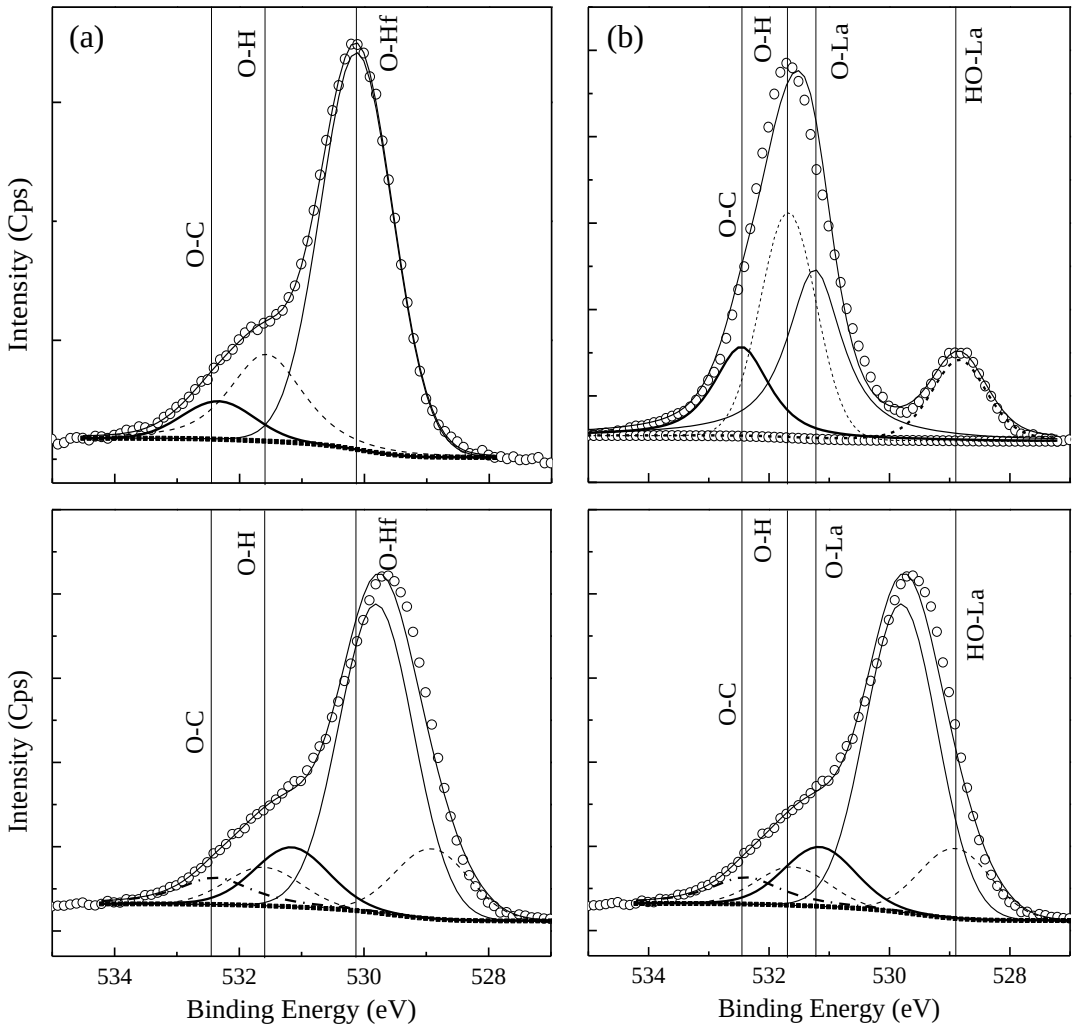

Figure 2.4 Deconvoluted O 1 s spectra showing the alignment between the pure constituent oxides (a) HfO_2 and (b) La_2O_3 and the $Hf_{0.25}La_{0.12}O_{0.63}$ film (bottom row).

The overall atomic composition and the relative bonding fractions from the deconvoluted spectra are shown in Figure 2.5. For the pure HfO_2 and La_2O_3 films, the metal : oxygen bonding ratios were 1.0 : 1.7 and 1.0 : 1.4 respectively, slightly lower than the 1 : 2 and 2 : 3 ideal stoichiometry. For the $Hf_{0.25}La_{0.12}O_{0.63}$ films, the ratios for Hf and La to O were 1.0 : 1.4 and 1.0 : 1.6 respectively, which were marginally higher than that of the $Hf_{0.11}La_{0.23}O_{0.66}$ composition (1.0 : 1.3 and 1.0 : 1.5). In all films, the ratio of the O-La peak in the O 1s spectra to the La-O peak in the La 3d spectra was ~ 2 : 1, while the ratio for HO-La/La-OH was ~1 : 1. Increasing La

content of the films appeared to be correlated with a greater observed degree of the bonding peak assigned to O-H. It should be noted that while hydrogen is not directly observable by XPS, it can be assigned peak locations based on its relative electronegativity to other elements in the surface layer. Additionally, higher La content was correlated to a larger ratio of La=O bonding compared to La-O.

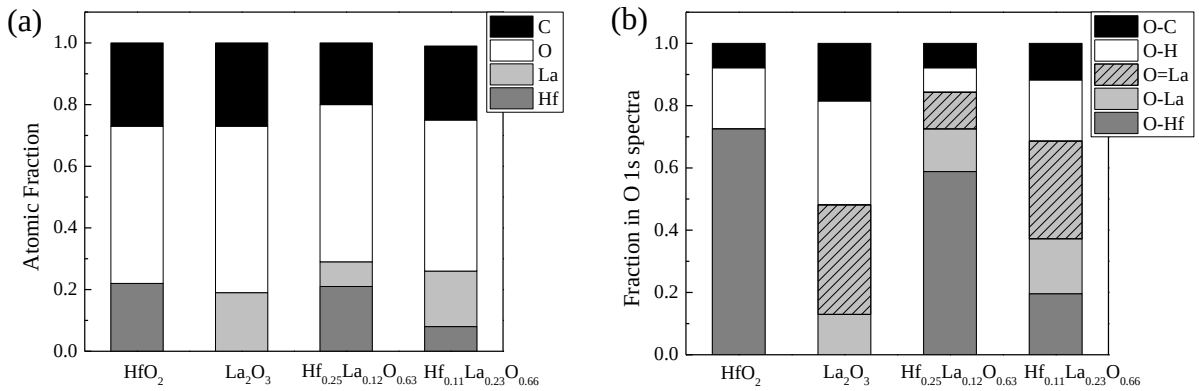

Figure 2.5 (a) Bar graphs illustrating the atomic compositions and (b) bonding fractions in the O 1s spectra for HfO_2, La_2O_3, $Hf_{0.25}La_{0.12}O_{0.63}$ and $Hf_{0.11}La_{0.23}O_{0.66}$ films.

2.4 Plasma Diagnostics

2.4.1 Langmuir Probe

The Langmuir probe is essentially a small electrode and is one of the first plasma diagnostic devices. By performing a voltage sweep over the tip of the probe a current can be measured owing to the charged species (electrons and ions) in the plasma environment. From the resulting I-V curve it is possible to derive plasma properties such as the space potential (V_s), electron temperature (T_{eV}), ion density (n_i), electron density (n_e) and the electron energy

distribution function (EEDF). A detailed discussion of the device can be found in the paper by Mott-Smith and Langmuir. (Mott-Smth and Langmuir 1926) In this study, an ESPIon Langmuir Probe from Hiden Inc. was used, with a 3 mm long cylindrical tungsten tip of radius 0.075 mm. The probe voltage range was -200 to +100 V, while the current range was -100 mA to 1000 mA. While typically a voltage step of -0.1 V was used, the resolution of voltage and current data obtained by the system was 10^{-4} V and 10^{-8} A respectively. A diagram of this setup and a typical I-V curve from a Cl_2 plasma are shown in Figure 2.6.

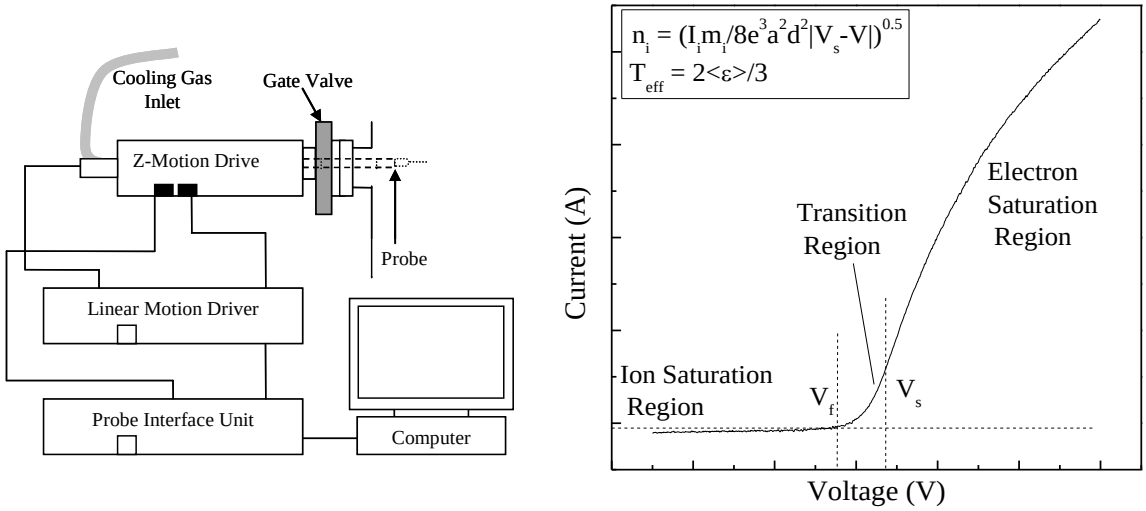

Figure 2.6 Schematic of Langmuir Probe Setup and sample I-V curve for Cl_2 plasma taken in the ICP reactor at 400W, 5mT.

The sum of the ion current and electron current to the probe tip is equal to the total current collected ($I = I_i + I_e$). The I-V curve is composed of three primary areas: (1) the ion saturation region, (2) the transition region and (3) the electron saturation region. In Area (1) most of the electrons are repelled from the probe tip due to the sufficiently large negative potential applied, thus most of the current results from the positive ions in the plasma. In Area (3) a large positive potential results in the opposite effect: ions are repelled so the majority of the current

results from electrons. In Area (2) the applied potential allows for both electrons and ions to contribute to the measured current.

The plasma floating (V_f) and space (V_s) potentials are the first parameters that can be extracted from the I-V curve. V_f is the voltage at which the total current to the probe is zero, i.e. $I(V_f) = 0$. This is the potential that an insulated object would assume when placed inside the plasma. V_s is the potential at which the plasma exists above grounded surfaces, and is typically found at the "knee" of the I-V curve, where the probe voltage is high enough that all electrons have sufficient energy to pass through the sheath. At this potential, the exponential increase in electron current plateaus, and any further increase in electron current is only due to an increase in the sheath thickness around the probe tip (resulting in a larger collection area). However, due to the variation of current with voltage in the electron saturation region, finding the precise location of the "knee" of the I-V curve can be difficult. Thus we define V_s as the point where I_c begins to deviate from exponential growth, i.e. the second derivative of I_c is equal to zero.

The density of positive ions (n_i) in the plasma can be determined for a cylindrical probe by orbital motion limited theory (OML). If we assume a collisionless sheath, Maxwellian distribution of ions, and probe tip radius-to-sheath thickness << 1, the ion saturation current can be expressed by the following equation:

$$I_i = 2en_i ad\left(\frac{2e|V_s - V|}{m_i}\right)^{1/2} \tag{2.2}$$

where I_i is the current in the ion saturation region, a and d are probe tip radius and length respectively, and m_i is the ion mass. Therefore, if an I^2-V curve is plotted it should be linear in

the ion saturation region, and the ion density can then be calculated by the slope of the curve. Under the principle of quasineutrality, n_i and the electron density (n_e) are assumed to be equal and therefore the plasma density can be expressed as $n = n_i = n_e$. However, it should be noted that the presence of negative ions (such as in halogen plasmas) negates the absolute validity of this statement. Using the I-V characteristic for a Cl_2 plasma at 400 W, 5 mTorr displayed in Figure 2.4 with an averaged ion mass of 50 amu or 8.3×10^{-26} kg (based on measured intensities using the QMS), the calculated ion density is 2.9×10^{11} cm^{-3} .

The next parameter that may be determined is the electron temperature, T_e. A Maxwellian distribution of electrons is commonly assumed, but since this is not necessarily true. Auseful concept to implement is the electron energy distribution function (EEDF) – $g_e(\varepsilon)$ from which both n_e and an effective electron temperature T_{eff} can be calculated. The EEDF is defined as:

$$g_e(\varepsilon)d\varepsilon = 4\pi v^2 f_e(v)dv \tag{2.3}$$

where v is the electron velocity and f_e is the electron distribution function. In terms of energy (ε = ½ mv^2/e) this equation takes the form:

$$g_e(\varepsilon) = 2\pi\left(\frac{2e}{m}\right)^{3/2} \varepsilon^{1/2} f_e[v(\varepsilon)] \tag{2.4}$$

which can then be expressed in terms of I_e and probe potential V as:

$$g_e(V) = \frac{2m}{e^2 A}\left(\frac{2eV}{m}\right)^{1/2} \frac{d^2 I_e}{dV^2} \tag{2.5}$$

where *m* is the electron mass, *e* is the electron charge and A is the area of the probe tip. For a Maxwellian distribution of electrons, the electron energy distribution function, expressed as the electron energy probability function (EEPF) $g_p(\varepsilon) = \varepsilon^{-1/2} g_e(\varepsilon)$ then can be expressed as:

$$g_p(\varepsilon) = \frac{2}{\sqrt{\pi}} n_e T_e^{-3/2} e^{-\varepsilon / T_e} \tag{2.6}$$

When $\ln[g_p(V_p - V_s)]$ is plotted versus $V_p - V_s$, T_e can be determined from the slope of the linear region. However in the case of a non-Maxwellian distribution, the slope is not linear and thus the effective electron temperature is more suitable, defined as:

$$T_{eff} = \frac{2}{3}\langle \varepsilon \rangle = \frac{2}{3n_e} \int_0^\infty \varepsilon g_e(\varepsilon) d\varepsilon \text{, where } n_e = \int_0^\infty g_e(\varepsilon) d\varepsilon \tag{2.7}$$

Thus, by integrating the curves of both $g_e(V_p - V_s)$ and $(V_p - V_s)g_e(V_p - V_s)$ vs. $(V_p - V_s)$, n_e and T_{eff} can be calculated. For the I-V characteristic from Figure 2.4 the calculated n_e and T_{eff} using this method were 3.5 x 10^{16} m^{-3} and4.17 eV respectively. Once the plasma density and electron temperature are known, the Debye length of the plasma (the characteristic distance scale over which significant charge densities can spontaneously exist) can be calculated by the following equation:

$$\lambda_{De} = \left(\frac{\varepsilon_0 T_e}{n_e e} \right)^{1/2} \tag{2.8}$$

where ε_0 is the permittivity of free space, and e is the fundamental charge of an electron. Based on the values of T_e and n_e above, the calculated Debye length for the ICP system was 0.08 mm.

2.4.2 Optical Emission Spectroscopy

The Ocean Optics S2000 system used in this study comprises five fiber optic cables (designated as Master and Slaves 1-4) with a total wavelength range of 200-1000 nm. These are connected to an analyzer which interfaces with a computer workstation so that data can be collected. The fiber optic cables are attached to a viewport in the ECR reactor through a machined cover held in place by screws. The described system and a sample OES spectrum are shown in Figure 2.7.

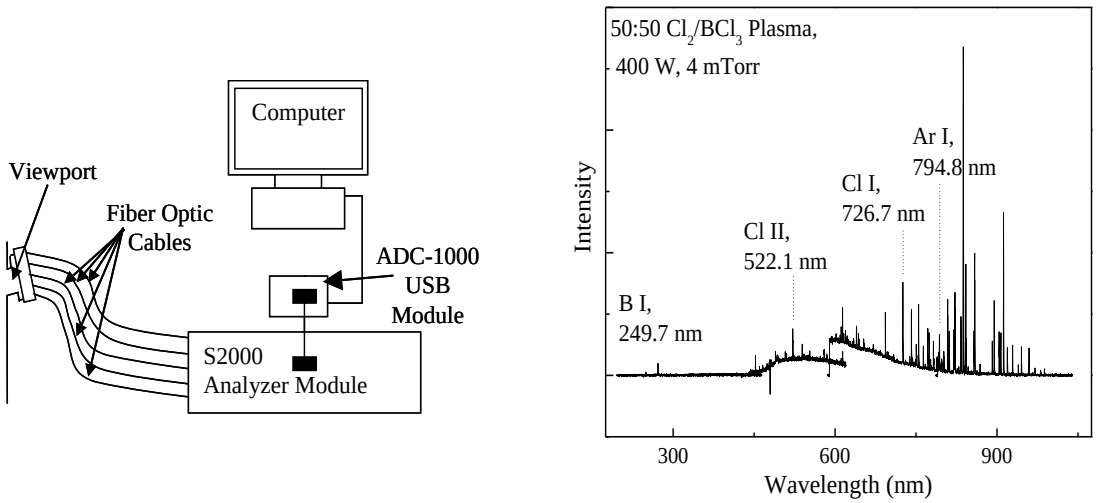

Figure 2.7 Schematic of OES setup, and sample spectrum of 50:50 Cl_2/BCl_3 plasma at 400 W, 4 mT.

The interaction between plasma species such as electrons, ions and neutrals results in the creation of particles with excited electronic states. These excited species can subsequently undergo electric dipole radiation to emit photons, returning to a relaxed state. The energy of these photons is characteristic of a particular transition in the plasma species, corresponding to

the difference between initial and final quantum energy states of the relaxed electron. The use of this measured energy to ascertain the identity of species present in the plasma is known as optical emission spectroscopy (OES). Among the primary advantages of OES is its non-intrusive nature. OES has been utilized to monitor the endpoints of plasma etching experiments (Litvak 1996), quantify the relative percentages of plasma species present and also calculate the reaction kinetics of said species through actinometry (Booth, Joubert et al. 1991; Booth and Sadeghi 1991), and obtain bulk plasma information such as T_e, n_e and EEDF using Trace Rare Gases OES (Donnelly and Schabel 2002).

As OES spectra are gathered periodically during the time span of an experiment, the endpoint of etching can be estimated by the appearance of certain lines (e.g. atomic Si when etching a thin film over silicon) in the spectra. Additionally the species can be quantified using the principle of actinometry, which is described as follows. For an electron impact excitation from the ground state to an excited state, the equation for relating the measured emission intensity to the concentration of the free radical species is as follows:

$$I_\lambda = \alpha_{\lambda A} n_A \tag{2.9}$$

where $\alpha_{\lambda A}$ is defined by the following equation:

$$\alpha_{\lambda A} = k_D(\lambda) \int_0^\infty 4\pi v^2 dv Q_{A^*}(p, n_e) \sigma_{\lambda A}(v) v f_e(v) \tag{2.10}$$

In the above equations I_λ is the optical emission intensity, n_A is the concentration of the free radical A, $\sigma_{\lambda A}$ is the cross section for the emission of a photon having wavelength λ due to electron impact excitation of A to A^*, k_d is the detector response constant, Q_{A*} is the quantum yield for photon emission from the excited state, and f_e is the electron distribution function.

However, since the aforementioned variables are not normally obtainable, it is impossible to solve for n_A and thus the measured intensities can only provide qualitative information. To circumvent this problem, a trace amount (generally < 5% of the inlet flow) of a known concentration of inert gas (the actinometer) is fed into the plasma. An emission line (T) with an excited state that possesses excitation threshold energy close to that of the chosen radical A is then selected so that the cross sections for the radical and the actinometer are similar near the excitation energy. The intensity of the emission line from the actinometer can then be described in a manner analogous to equations (2.9) and (2.10):

$$I_{\lambda'} = \alpha_{\lambda' T} n_T \tag{2.11}$$

where

$$\alpha_{\lambda' T} = k_D(\lambda') \int_0^\infty 4\pi v^2 dv Q_{T^*}(p, n_e) \sigma_{\lambda' T}(v) v f_e(v) \tag{2.12}$$

On an energy scale, only the energetic tail end of the electron distribution is above the threshold energy for the photon emission cross sections, which allows the cross sections near the threshold energy to be approximated as linear functions of electron velocity:

$$\sigma_{\lambda A} \approx C_{\lambda A}(v - v_{thr}) \tag{2.13}$$

and

$$\sigma_{\lambda' T} \approx C_{\lambda' T}(v - v_{thr}) \tag{2.14}$$

where $C_{\lambda A}$ and $C_{\lambda' T}$ are proportionality constants. The ratio of intensities of the two emission lines can then be taken to yield the radical density:

$$n_\lambda = C_{AT} n_T \frac{I_\lambda}{I_{\lambda'}} \tag{2.15}$$

where

$$C_{AT} = \frac{k_D(\lambda) Q_{A*} C_{\lambda A}}{k_D(\lambda') Q_{T*} C_{\lambda' T}} \tag{2.16}$$

If the chosen emission wavelengths are similar to each other, i.e. $\lambda' \sim \lambda$ and $Q_{A*} \sim Q_{T*}$, then $C_{AT} \sim C_{\lambda A}/C_{\lambda' T}$ can be determined and an absolute value of the radical density n_A can be calculated.(Coburn and Chen 1980) In general, for the experimental section of this work, the actinometer used is five percent of argon in the inlet gas feed. The normalized intensities of the BCl (272 nm), Cl (738.62 nm) and Cl (792.54 nm) lines to Ar (750.42 nm) in BCl_3 plasma with 5% Ar addition are shown in Figure 2.8.

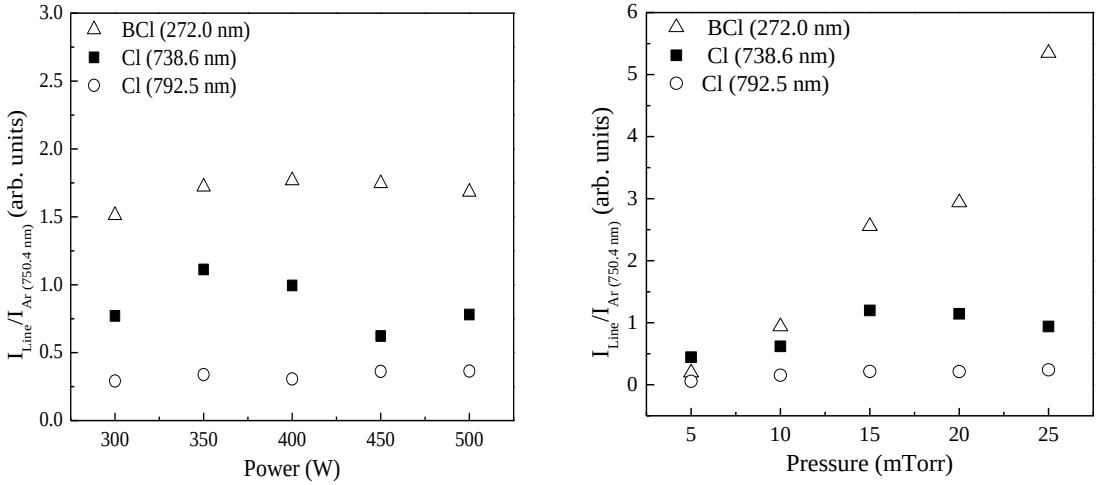

Figure 2.8 OES intensity ratio of Cl (738.62 nm), BCl (272 nm) and Cl (792.54 nm) to Ar (750.42 nm) as a function of the power at 15 mTorr (left) and chamber pressure (right) at 400 W in a BCl_3 plasma with 5% Ar addition in the ICP reactor.

2.4.3 Quadrupole Mass Spectrometry

A UTI 100C line of sight quadrupole mass spectrometer (QMS) is set up on this reactor in order to analyze the ion and neutral compositions of the plasma in the ICP chamber. The mass range of the unit was 1 to 300 atomic mass units (AMUs), with a minimum detectable partial pressure of 0.1 parts per million (ppm). The mass spectrometer assembly is housed within a stainless steel manifold which is evacuated by a Leybold 361C turbomolecular pump. An orifice 0.065 inches in diameter and 0.0625 inches deep allows the passage of ions from the plasma in the upper section of the ICP reactor to the QMS. For ionization of neutral species, energy of -50.0 V at a current of approximately 2.0 mA is applied to the filament electrons. A quadrupole - a precise square array of four parallel metal rods between which a combined rf/dc field is maintained serves as a mass filter and also increases the sensitivity and speed of analysis. (Yinon and Klein 1971). Figure 2.9 shows a simple schematic of the QMS used in this study, as well as a sample spectrum of a BCl_3 plasma with 5% Ar addition.

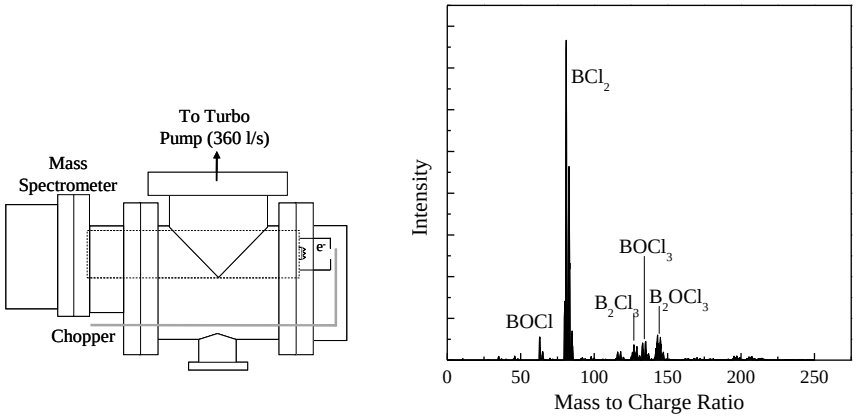

Figure 2.9 Schematic of UTI 100C Mass Spectrometer and mass spectrum for a BCl_3 plasma with 5% Ar addition at 500 W, 3 mTorr.

Since its inception, mass spectrometry has become an important tool in physics, chemistry and biology.(Mayne 1952) In the context of this study, it is a versatile analytical technique that allows for identification of individual species in the plasma environment through their isotope mass cracking patterns. Unlike OES, mass spectrometry allows for the identification of complicated molecules over a wide range of masses, rather than simple atomic and diatomic species. The basic principle of mass spectrometry lies in the fact that when a beam of charged species is passed through a variable magnetic field, species with a fixed mass to charge ratio can be focused onto a collector and spectra dependent only on mass can be obtained. (Aston 1920) By comparing these spectra to calculated isotope patterns of the various molecules that may be present in the plasma, the composition of the plasma can be verified. Figure 2.10 depicts the isotope composition patterns of the elements that are encountered in this study, and also shows how an isotope pattern can be superimposed on the QMS spectra in order to make a positive identification.

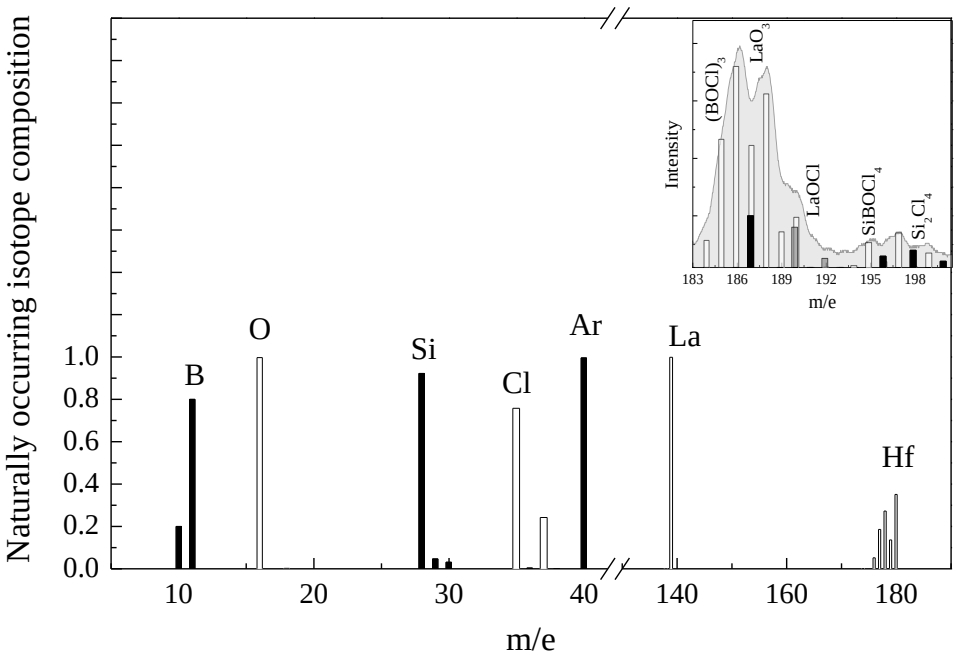

Figure 2.10 Naturally occurring isotope composition patterns of the elements encountered in this study (bar graphs). Inset shows an excerpt from a QMS spectrum taken during etching of La_2O_3 in BCl_3 plasma with 5% Ar addition at 400 W, 15 mTorr and -100V bias, with bar graphs for $BOCl_3$ (white), LaO_3 (black), LaOCl (grey), $SiBOCl_4$ (white) and Si_2Cl_4 (black) superimposed.

For QMS systems, there is an inverse relationship between the mass to charge ratio of species and the sensitivity of the spectrometer. It is important to determine this sensitivity change as a function of mass to charge ratio in order for quantitative analysis to be considered accurate. For this particular QMS, the relationship is as follows:

$$I \propto \frac{1}{m_c^k} \tag{2.17}$$

where I is the signal intensity and m_c is the mass to charge ratio. The constant k varies between 1.0 and 1.2. (Chae, Vitale et al. 2003) To determine the relative quantities of detected species, the area under each spectra is determined via integration and then multiplied by the appropriate mass correction factor.

2.5 Surface Characterization

2.5.1 X-Ray Photoelectron Spectrometer

X-Ray Photoelectron Spectroscopy (XPS) is a surface analysis technique that is used to determine the chemical composition of a thin surface layer. A sample survey spectrum of a 1000 Å thick $Hf_{0.25}La_{0.12}O_{0.63}$ film before and after exposure to a 400W, 5 mT, BCl_3 plasma at -100 V bias voltage for 5 minutes, as well as a magnified view of the Hf 4f peak are shown in Figure 2.11.

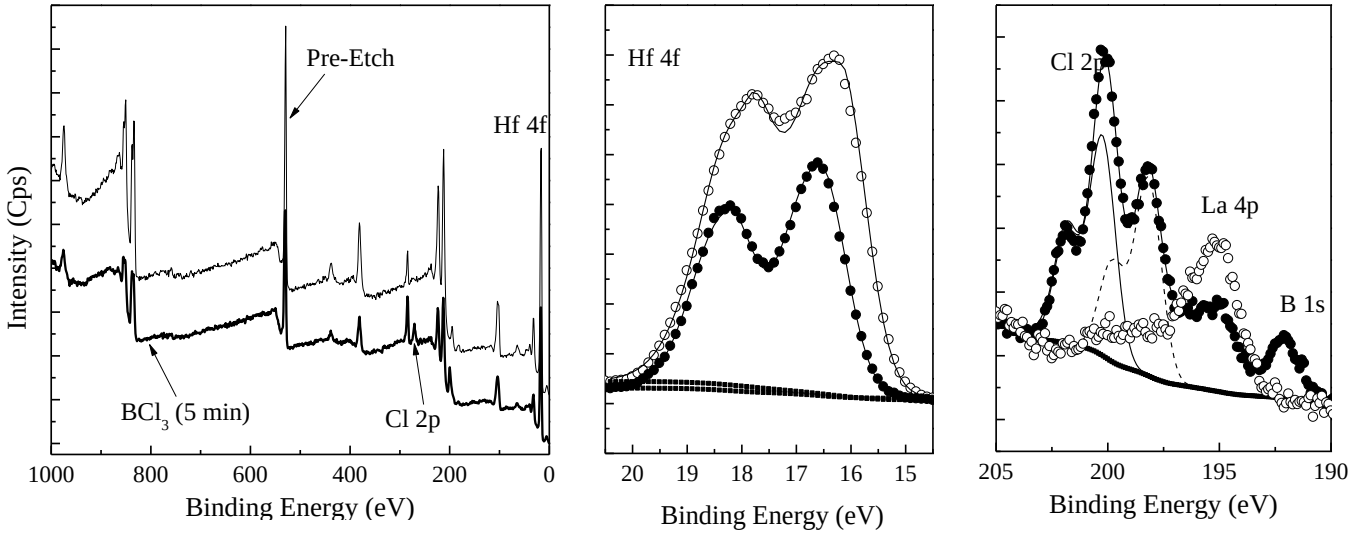

Figure 2.11 (a) Survey spectrum for a 1000 Å thick $Hf_{0.25}La_{0.12}O_{0.63}$ film before and after etching in a BCl_3 plasma at 400 W, 5 mT, -100 V bias, (b) the Hf 4f and (c) the Cl 2p detailed spectra of the sample before (○) and after etching (●) at the specified conditions.

Originally known as Electron Spectroscopy for Chemical Analysis (ESCA), the technique is based on the fact that when a material is bombarded with ionizing radiation or high

energy particles, electrons from each element can be emitted from either inner or outer valence shells. By measuring the kinetic energy of these electrons, the ionization potential or binding energy can be derived using the equation:

$$E_k = h\upsilon - E_b - \Phi \qquad (2.18)$$

where E_k = Kinetic Energy of the electron, hν = energy of the incident radiation, E_b = Binding Energy of the electron, and Φ = Work function of the spectrometer. (Hagström, Nordling et al. 1964) When the radiation source used is an X-ray source (Mg Kα, 1254 eV or Al Kα, 1487 eV), this technique is known as XPS. Use of a crystal monochromator can further enhance the resolution of the electron spectra and increase the accuracy in interpretation of results by reducing some of the uncertainty associated with inherent linewidths and degree of chemical shifts. (Siegbahn, Barnett et al. 1972)

XPS can also be used to obtain information about the local structure of solid surfaces. The immediate environment, charge and oxidation state of a particular atom can all have effects on the binding energies of its electrons, so by comparing the shift in energy of an atom relative to a standard value, specific details about the aforementioned parameters can be deduced. The integrated intensity of a specific peak is proportional to the number of photoelectrons per second from that peak, given by the following equation:

$$I = nf\sigma\theta y\lambda AT \qquad (2.19)$$

where n is the number density of atoms of that element in the sample, f is the x-ray flux, σ is the photoelectric cross-section for the atomic orbital of interest, θ is the angular efficiency factor for

the instrumental arrangement, y is the efficiency of the photoelectric process for formation of photoelectrons with the normal photoelectron energy, λ is the mean free path of the photoelectrons in the sample, A is the area of the sample from which photoelectrons are detected, and T is the detection efficiency. If rearranged in terms of the density:

$$n = \frac{I}{f\sigma\theta y\lambda T} = \frac{I}{S} \tag{2.20}$$

where the denominator is defined as the atomic sensitivity factor S and used only in calculations involving a ratio of sensitivity factors. This is because quantities in S can vary depending upon the standards used but the ratio is unaffected. The atomic fraction of an element in the film can then be determined from the fraction of corrected integrated intensity of one peak from the element of interest over the summed corrected integrated intensities of each peak from all of the elements in the film as shown in the following equation:

$$C_x = \frac{n_x}{\sum_i n_i} = \frac{I_x / S_x}{\sum_i I_i / S_i} \tag{2.21}$$

The atomic sensitivity factors used in this work are from the Casa XPS Database and are tabulated along with the spin orbital splitting values and peak binding energy in Table 2-2.

Table 2-2 :XPS Atomic Sensitivity Factors (ASFs) for elements of interests.

Element	Line	B.E. (eV)	S.O.S	ASF	Element	Line	B.E. (eV)	S.O.S	ASF
B	1s	190.3	-	0.159	La	3d	834.8	16.8	9.12
C	1s	284.6	-	0.278	Hf	4f	14.15	1.68	2.64
O	1s	531.6	-	0.780	Si	2p	99.4	0.60	0.328
Cl	2p	199.9	1.60	0.891					

The XPS system used to take the measurements in this study was a Kratos XPS Axis Ultra DLD unit. The Al Kα anode (1486.6 eV emission) was used with a monochromator at a 90° takeoff angle. Survey scans were performed at 160 eV pass energy, 1 eV step size and 100 ms dwell time, while detailed scans were performed at 20 eV, 0.1 eV step size and 400 ms dwell time.

2.5.2 Quartz Crystal Microbalance for In-Situ Etch Rate Measurement

The quartz crystal microbalance (QCM) is a sorption detector that is commonly used in vacuum systems to detect deposition or removal of material with a very high degree of accuracy. A simple schematic of a QCM system along with its equivalent circuit diagram and a sample frequency response for the sputtering of $Hf_{0.25}La_{0.12}O_{0.63}$ in a 400 W, 15 mT Ar plasma at -150 V bias voltage are shown in Figure 2.12.

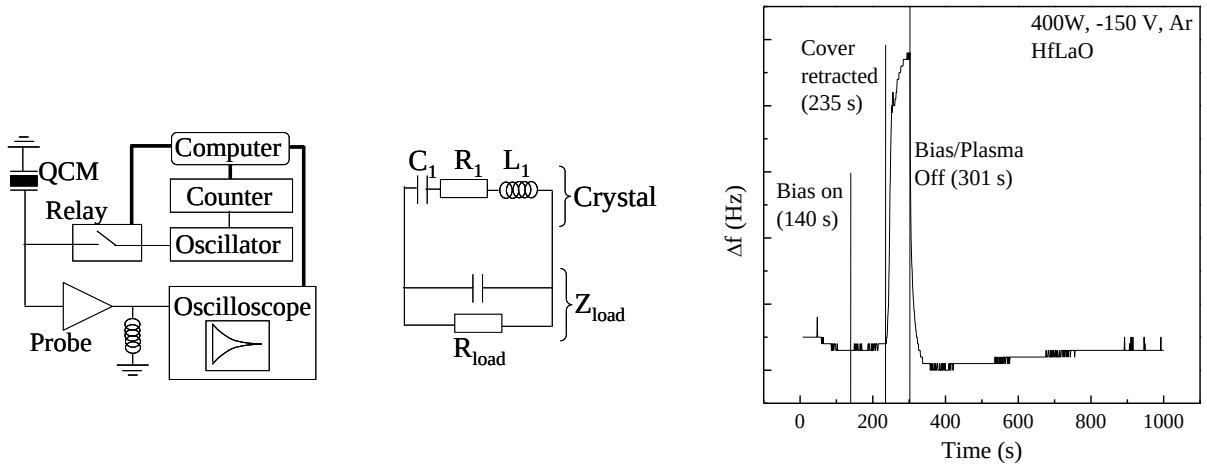

Figure 2.12 Schematic of the QCM system with equivalent circuit diagram and a figure of sample frequency response.

The operating principle of a QCM is the extremely high sensitivity of a piezoelectric quartz crystal to the presence of any foreign material. A relationship between the weight of deposited/etched films and the change in oscillation frequency of the crystal was first established by Sauerbrey, allowing for precise measurements to be made as to the deposition/etching rates being studied. The relation is given by the following equation:

$$\Delta f = -\frac{f_0^2}{N.\rho_q}.\varphi \qquad (2.22)$$

where Δf is the frequency change, f_0 is the resonant frequency, N is half of the tranverse wave velocity in quartz ($v_{tr}/2$), ρ_q is the density of quartz and $\varphi = \Delta m/A$ where Δm is the mass change and A is the surface area of the quartz/electrode.(Sauerbrey 1959) Since v_{tr} is defined as the square root of the quartz shear modulus divided by the density of quartz ($v_{tr} = \sqrt{\mu_q/\rho_q}$), the equation can be expressed as:

$$\Delta f = \frac{-2 f_0^2}{A\sqrt{\rho_q \mu_q}} \Delta m \qquad (2.23)$$

For an AT-cut quartz crystal with resonance frequency of 14 MHz, N = 0.167 MHz cm, ρ_q = 2.648 g/cm^3, and A = 1 cm^2, the mass change corresponds to the frequency change divided by a factor of 443.22 Mhz/g. The measured mass change by the QCM can be divided by the area of the electrode to yield a mass change per unit area (g cm^{-2}).

The QCM is usually applied to measure deposition or growth rates (O'Sullivan and Guilbault 1999; Lucklum and Hauptmann 2001), however it can also be used to provide an *in situ* etch rate measurement. Such use was demonstrated for the sputtering of gold in Ar^+ from as

early as 1961 (McKeown 1961) using a custom-built apparatus. The subsequent production of commercial QCM systems allowed the technique to be extended to a variety of systems, including the plasma assisted etching of polyimide and tungsten films in $CF_4/O_2/H_2$ (Fracassi and Coburn 1986) and SiO_2 in C_xF_y/ $C_xH_yF_z$ chemistries. (Chae, Vitale et al. 2003) More recently, the technique has been utilized for investigating the interactions of polymers such as polystyrene, poly(methyl methacrylate) and poly(ethylene terephthalate) with environments ranging from weakly ionized plasmas (120 W, 0.56 Torr) to ion beams of 1 keV energy. (Zekonyte, Zaporojtchenko et al. 2005; Doliska, Vesel et al. 2012) Outside of vacuum systems, QCM has also been applied to study wet chemical etching of oxides in solutions of ammonia peroxide and HF. (Lee and Raghavan 1999; Zamani, Keswani et al. 2012) As the accuracy of data from *ex situ* film thickness measurement techniques such as ellipsometry can be compromised by unwanted surface reactions, e.g. oxidation, occurring rapidly on post-etched surfaces during ambient exposure, the ability to monitor the etch rate *in situ* is a distinct advantage. In situations where the disparity between the base frequencies of the loaded crystal and a bare one are less than 5%, the small load approximation can be used to convert the measured frequency change data to an etch rate. The equation for the conversion is given below:

$$\frac{\Delta f^*}{f_f} = -\frac{2f}{Z_q} m_F \tag{2.24}$$

Where Z_q is the acoustic impedance of AT-cut quartz (8.8 x 10^2 kg cm^{-2} s^{-1}) and m_F is the mass change per unit area. The etch rate can then be calculated from m_F if the mass density of the film is known. The densities of several materials that was etched in this study are listed in Table

2-3, along with the expected frequency change for the removal of one monolayer (~5Å) of each material.

Table 2-3 Expected frequency changes for monolayer removal of the various oxide materials considered in this study.

Material	Density (g/cm^3)	m_f for ~1 ML removal (x 10^{-7} g/cm^2)	Corresponding Δf (Hz)
HfO_2	9.68	-4.8	39.26
La_2O_3	6.51	-3.3	26.40
Si	2.33	-1.2	9.46

For composite films such as $Hf_{0.25}La_{0.12}O_{0.63}$, a weighted average of the densities for the constituent oxides was used. Based on the HfO_2 and La_2O_3 stoichiometries, the aforementioned film would have a density given by the following equation:

$$\rho_{film} = \frac{x_{Hf}\rho_{HfO_2} + \frac{1}{2}\left(x_{La}\rho_{La_2O_3}\right)}{x_{Hf} + \frac{1}{2}x_{La}} \tag{2.25}$$

Which gives 9.1 g/cm^3.

Conversion to the etch yield of a process is also possible. The m_F can be converted to an atomic quantity by calculating the number of atoms present in the mass removed. This is done by dividing the mass removed by the molecular weight of the material being etched, which is equivalent to the molar weight divided by Avogadro's number, which produces units of atoms cm^{-2}. This quantity can then be normalized to the incident flux (atoms cm^{-2}) to the sample to obtain the etch yield of the process, which is unitless.

Complications of using the QCM for measuring etch rates include high sensitivity to temperature gradients (Oiseth, Krozer et al. 2004) and electrical interference. Given that the

resolution of the technique is between pico- and nanograms/cm^2, even minor disruptions to the signal path could result in erroneous readings and thus a high level of caution should be exercised when analyzing the data. To reduce the influence of these factors, the sensing head array housing was situated outside of the plasma environment, with a plasma beam extracted through a grounded grid prior to impingement on the quartz crystal surface. This is similar to the setup employed by Chae et. al, but is in contrast to the study by Fracassi and Coburn where the QCM head was directly exposed to the plasma. Additionally, in both of the aforementioned works, the QCM assembly was electrically isolated from the main reactor body using ceramic spacers and biased directly to attract ionic species. In the ICP system used in this study, the QCM probe was grounded to the chamber body and the bias ring electrode was electrically isolated by its placement on the reactor's quartz bell jar. The probe assembly was covered by a retractable stainless steel plate attached to a separate manipulator during plasma ignition and bias setting. After the conditions for the experiment were established this cover was withdrawn to expose the crystal to the extracted plasma beam from the upper chamber. This was done to ensure that any measured frequency change was not simply a result of electrical interference between the electronics (e.g. RF generator, DC bias controller) and the QCM rate monitor. In this work, a Sycon 501-009 QCM sensor head assembly was used to house Maxtek SC-101 AT-cut 6 MHz quartz sensor crystals with gold electrodes. HfLaO and La_2O_3 films of thickness ~1000 - 2000 Å were deposited on these crystals. The sensor head was connected to a Sycon STM-100/MF rate monitor with a resolution of 0.1 Å/s to measure the frequency change induced in the loaded crystals upon exposure to the extracted plasma beam.

2.5.3 Scanning Electron Microscopy

The scanning electron microscope (SEM) allows observation of a surface at significantly higher resolutions than that of an optical microscope, with a depth of field that is orders of magnitude larger. Figure 2.13 displays a schematic of the essential components of an SEM adopted from Nixon. (Nixon 1971), as well as an image of etched poly-Si with a Si_3N_4 hard mask taken using the technique.

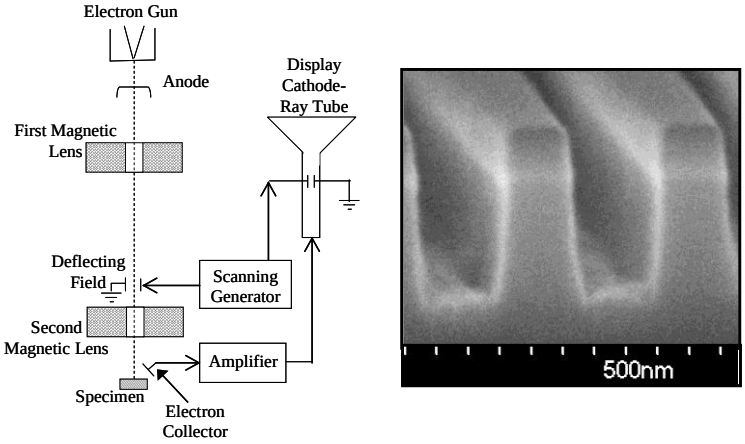

Figure 2.13 Components of a scanning electron microscope and cross-sectional image taken of a patterned silicon wafer after etching in a Cl_2 plasma with 2% O_2 for 80s.

A simple explanation of the operational concept follows. Electrons are accelerated towards the anode with energies ranging from volts to tens of kilovolts, and subsequently pass through one or more lenses which serve to reduce the image of the electron source to a nanometer scale as it impinges on the plane of the surface. A scanning generator is used to deflect the path of the electron beam, which allows the beam to be moved over the sample surface in a pattern. The interaction between the electron beam and the surface generates secondary electrons which are collected and passed through an amplifier before being

transmitted to a display cathode ray tube (CRT). Other types of emission such as light, x-rays, IR and UV radiation may also be produced, which can also be collected. From the obtained images, information about the physical dimensions of the pre- and post-etched samples can be derived, which can be used to calculate effect of the plasma parameters and chemistry on the etch rate and sidewall angles of the features. SEM images in this work were taken using two systems, the JEOL JSM-6700F and the Nova 600. Each system possessed resolutions of 1 nm, and typical scan settings were 5 - 10 kV with magnification ranging from with magnification ranging from 1,500 to 250,000x.

2.6 Theoretical Methods

2.6.1 Thermodynamic Calculations

Fundamental thermodynamic data (e.g. Gibbs Free Energy) concerning the reactants and products of potential etching pathways can be used to construct maps of equilibrium phases. One such construct, the volatility diagram, relates the partial pressure of gaseous phase etch products to the pressure of reactive gas supplied, which makes it particularly useful in the context of selecting plasma chemistries for a given target material. This section starts with a primer on plotting volatility diagrams, followed by application of the method to the etching of metal oxides (in this case HfO_2 and La_2O_3) in chlorine and fluorine chemistries. While fluorine is known to react with most materials owing to its innate electronegativity, potential environmental consequences regarding its usage (as a constituent of noted greenhouse gases such as SF_6 and CF_4) have led industry to begin seeking alternatives. Both the molecular and atomic forms of

each halogen etchant are considered and a comparison is made between the two gases. The addition of boron to chlorine chemistry and its effect on oxygen removal is then considered.

A general summary of volatility diagram construction follows. Reactions can be of four types: (i) reaction between a solid (condensed) specie and a gaseous specie to form condensed and gaseous products (i.e. aA(s) + bB(g) → cC(g) + dD(s)), (ii) reaction between a condensed specie and a gaseous specie to form a gaseous product (i.e. aA(s) + bB(g) → cC(g)), (iii) reaction between a condensed specie and a gaseous specie to form a condensed product (i.e. aA(s) + bB(g) → cC(s)), and (iv) transition between a condensed specie and its gaseous phase without reaction with any other gaseous species (i.e. A(s) → A(g)). [A fifth reaction type involves the production of multiple gaseous species from a single condensed phase one (i.e. aA(s) → bB(g) + cC(g)) and is responsible for the existence of so-called metastable equilibrium states. However these reactions are not considered at the moment but are examined in more detail later as relating their presence in the context of the general reaction mechanism for metal oxide etching is somewhat difficult.] For any particular reaction, the equilibrium constant K is related to the partial pressures of gaseous phase species through the general reaction equation:

$$\log(K) = \log\left(\frac{\prod P_{PRODUCT}^{x}}{\prod P_{REACTANT}^{y}}\right) \tag{2.26}$$

Where $P_{PRODUCT/REACTANT}$ is the partial pressure of the product and reactant species involved in the particular reaction being considered, and x and y are the coefficients representing the molar quantity of the products and reactants respectively in the same reaction. For species in the condensed phase, the activity coefficient a is used in place of the partial pressure, and under the

assumption that the condensed species are in their natural states, this value is set to unity. Applying this formulation to the four reaction types listed above yields the following equations for log(*K*):

$$\text{(i)}\ \log(K_i) = \log\left(\frac{P_C^c a_D}{P_B^b a_A}\right) = \log\left(\frac{P_C^c}{P_B^b}\right),\ \log K_i = c\log(P_C) - b\log(P_B)$$

$$\text{(ii)}\ \log(K_{ii}) = \log\left(\frac{P_C^c}{P_B^b a_A}\right) = \log\left(\frac{P_C^c}{P_B^b}\right),\ \log K_{ii} = c\log(P_C) - b\log(P_B)$$

$$\text{(iii)}\ \log(K_{iii}) = \log\left(\frac{a_C}{P_B^b a_A}\right) = \log\left(\frac{1}{P_B^b}\right),\ \log K_{iii} = -b\log(P_B)$$

$$\text{(v)}\ \log(K_{iv}) = \log\left(\frac{P_A}{a_A}\right) = \log(P_A),\ \log K_{iv} = \log(P_A)$$

Converting these equations into the generalized form for that of a straight line gives:

$$\text{(i), (ii)}\ \log(P_C) = \frac{b}{c}\log(P_B) + \frac{1}{c}\log(K)$$

$$\text{(iii)}\ \log(P_B) = -\frac{1}{b}\log(K)$$

$$\text{(iv)}\ \log(P_a) = \log(K)$$

Thus, for reaction types (i) and (ii) the partial pressure of product C can be plotted as a function of the partial pressure of reactant B, yielding a straight line with gradient *b/c* and y-intercept log(*K)/c.* Reaction type (iii) plots the value of partial pressure of reactant B at which equilibrium exists between two solid species (A(s) and B(s)) as a vertical line with x-intercept -log(*K*)/*b*, and reaction type (iv) plots the partial pressure at which a particular species' solid and gas phases are in equilibrium as a horizontal line independent of reactant particular pressure, with y-intercept

log(*K*). In turn, log(*K*) for a particular reaction can be calculated from the Gibbs Free Energy using the following equation:

$$\Delta G(T) = -RT\ln K(T) = -2.303RT\log K(T),\ \log K(T) = \frac{-\Delta G(T)}{RT} \qquad (2.27)$$

For the test cases being considered, i.e. metal oxide etching in halogen chemistry, the four major reaction groups outlined above can be related to specific processes. In the first group, the impinging reactant species react to form condensed phase halogenated products, as well as gaseous O_xX_y-type compounds (where capital X denotes either Cl or F). This is consistent with past formulations of the process where the breaking of the metal-oxygen bond is postulated to be the rate-limiting step. In the second group of reactions, the condensed phase metal halide products are converted to the gas phase upon further addition of chlorine species. The third group comprises equilibrium between condensed phases with varying degrees of halogenation (e.g. $MX_n(c) \rightarrow MX_{n+1}(c)$), and the four group contains reactions which define the equilibrium between condensed and gaseous phases without any halogen addition (e.g. $MX_n(c) \rightarrow MX_n(g)$). The reaction set for the etching of HfO_2 in Cl_2/F_2 chemistry is given in Table 2-4, with reactions of type (i) numbered 1-13, reactions of type (ii) numbered 14-19, reactions of type (iii) numbered 20-22, and reactions of type (iv) numbered 23-29. The different reaction groupings are separated by a double-lined horizontal border. Data for the change in Gibbs Free Energy taken from the Philips Journal Of Research (Dittmer and Niemann 1987) and log(*K*) values for reactions involving the molecular (X_2) and atomic (X) etchants are also provided.

Table 2-4 Reaction set for HfO_2 etching in halogen based-based chemistry, where *X* refers to either Cl or F.

		Cl_2		**Cl**		**F_2**		**F**	
	Reaction	ΔG (kJ/ mol)	Log (*K*)	ΔG	Log (*K*)	ΔG	Log (*K*)	ΔG	Log (*K*)
1	$HfO_2(c)+3X_2(g)/6X(g)\rightarrow HfX_4(c)+2XO(g)$	305	-53	-327	57	-446	78	-820	144
2	$HfO_2(c)+\frac{5}{2}X_2(g)/5X(g)\rightarrow HfX_3(c)+2XO(g)$	653	-114	126	-22	125	-22	-187	33
3	$HfO_2(c)+2X_2(g)/4X(g)\rightarrow HfX_2(c)+2XO(g)$	1035	-181	614	-108	697	-122	448	-78
4	$HfO_2(c)+X_2(g)/2X(g)\rightarrow HfOX(c)+XO(g)$	463	-81	253	-44	274	-48	149	-26
5	$HfO_2(c)+\frac{3}{2}X_2(g)/3X(g)\rightarrow HfOX_2(c)+XO(g)$	201	-35	-115	20	-179	31	-366	64
6	$HfO_2(c)+\frac{5}{2}X_2(g)/5X(g)\rightarrow HfX_4(c)+XO_2(g)$	229	-40	-297	52	-618	108	-929	163
7	$HfO_2(c)+2X_2(g)/4X(g)\rightarrow HfX_3(c)+XO_2(g)$	577	-101	156	-27	-46	8	-295	52
8	$HfO_2(c)+\frac{3}{2}X_2(g)/X(g)\rightarrow HfX_2(c)+XO_2(g)$	959	-168	643	-113	526	-92	339	-59
9	$HfO_2(c)+4X_2(g)/8X(g)\rightarrow HfX_4(c)+2X_2O(g)$	305	-53	-538	94	-573	101	-1072	188
10	$HfO_2(c)+\frac{7}{2}X_2(g)/7X(g)\rightarrow HfX_3(c)+2X_2O(g)$	652	-114	-85	15	-2	0	-438	77
11	$HfO_2(c)+3X_2(g)/6X(g)\rightarrow HfX_2(c)+2X_2O(g)$	1035	-181	403	-71	570	-100	196	-34
12	$HfO_2(c)+\frac{3}{2}X_2(g)/3X(g)\rightarrow HfOX(c)+X_2O(g)$	463	-81	147	-26	210	-37	23	-4
13	$HfO_2(c)+2X_2(g)/4X(g)\rightarrow HfOX_2(c)+X_2O(g)$	201	-35	-221	39	-242	43	-492	86
14	$HfX_3(c)+\frac{1}{2}X_2(g)/X(g)\rightarrow HfX_4(g)$	-297	52	-402	71	-369	65	-431	76
15	$HfX_2(c)+\frac{1}{2}X_2(g)/X(g)\rightarrow HfX_3(g)$	-158	28	-263	46	-261	46	-323	57
16	$HfX_2(c)+X_2(g)/2X(g)\rightarrow HfX_4(g)$	-679	119	-890	156	-941	165	-1066	187
17	$HfX(c)+\frac{1}{2}X_2(g)/X(g)\rightarrow HfX_2(g)$	-56	10	-161	28	-239	42	-301	53
18	$HfX(c)+X_2(g)/2X(g)\rightarrow HfX_3(g)$	-552	97	-763	134	-857	150	-982	172
19	$HfX(c)+\frac{3}{2}X_2(g)/3X(g)\rightarrow HfX_4(g)$	-1074	188	-1389	244	-1538	270	-1725	302
20	$HfX(c)+\frac{1}{2}X_2(g)/X(g)\rightarrow HfX_2(c)$	-395	69	-500	88	-596	105	-659	116
21	$HfX_2(c)+\frac{1}{2}X_2(g)/X(g)\rightarrow HfX_3(c)$	-383	67	-488	85	-572	100	-634	111
22	$HfX_3(c)+\frac{1}{2}X_2(g)/X(g)\rightarrow HfX_4(c)$	-348	61	-453	79	-571	100	-634	111
23	$HfO_2(c)\rightarrow HfO_2(g)$	759	-133	759	-133	759	-133	759	-133
24	$HfX_4(c)\rightarrow HfX_4(g)$	51	-9	51	-9	202	-35	202	-35
25	$HfX_3(c)\rightarrow HfX_3(g)$	225	-39	225	-39	311	-55	311	-55
26	$HfX_2(c)\rightarrow HfX_2(g)$	339	-59	339	-59	357	-63	357	-63
27	$HfX(c)\rightarrow HfX(g)$	433	-76	433	-76	450	-79	450	-79
28	$HfOX(c)\rightarrow HfOX(g)$	480	-84	480	-84	530	-93	530	-93
29	$HfOX_2(c)\rightarrow HfOX_2(g)$	242	-43	242	-43	344	-60	344	-60

In the case of reactions involving lanthanum, thermodynamic data was limited. Gibbs Free Energy for La_2O_3(c) and $LaCl_3$(c) was available in the compilation by Barin and Knacke (Barin and Knacke 1973). Data for LaF_3 was calculated using values provided in a text from

Argonne National Laboratory, however these were noted to be merely estimates (Glassner, Argonne National et al. 1957) Neither text provided information on $LaOX_n$-type compounds or on halogenated states of La besides LaX_3, a fact which should be considered during the subsequent analysis. The reaction set for La_2O_3 is provided in Table 2-5.

Table 2-5 Reaction set for La_2O_3 etching in halogen based-based chemistry, where *X* refers to either Cl or F. Asterisks denote calculated data from estimated values.

		Cl_2		**Cl**		**F_2**		**F**	
	Reaction	ΔG (kJ/ mol)	Log (*K*)	ΔG	Log (*K*)	ΔG*	Log (*K*)*	ΔG*	Log (*K*)*
30	$La_2O_3(c)+\frac{9}{2}X_2(g)/9X(g)\rightarrow 2LaX_3(c)+3XO(g)$	-102	18	-1049	184	2134	-374	1573	-276
31	$La_2O_3(c)+\frac{15}{4}X_2(g)/\frac{15}{2}X(g)\rightarrow 2LaX_3(c)+3/2\,XO_2(g)$	-215	38	-1005	176	1877	-329	1410	-247
32	$La_2O_3(c)+6X_2(g)/12X(g)\rightarrow 2LaX_3(c)+3X_2O(g)$	-102	18	-1366	239	1943	-341	1196	-210

Figure 2.14 shows the volatility diagram for Cl_2 chemistry. It is observed for HfO_2 that even at extremely low partial pressures the predicted dominant condensed state is $HfCl_4$. As mentioned earlier, these lines could not be plotted for $La_2O_3/LaCl_x$ due to a lack of thermodynamic data. As expected for reaction types (i) and (ii), higher values of log(*K*) resulted in larger values for the y-intercept (the partial pressure of the gaseous product when the pressure of Cl_2 = 1 atm). However, an evaluation of feasible etching pathways cannot be carried out by simply determining the reactions with the highest values of log(*K*). From a practical standpoint, the region of particular interest in this diagram is the intersection between a typical operating regime for plasma reactors (5-50 mTorr = 6.56 x 10^{-6} - 5.63 x 10^{-5} atm), and the vapor pressure range in which material removal can be measured (for a therogravimetric analyzer > ~10^{-8} atm). A shaded box representing this region has been overlaid on the graph. This region is examined in more detail later in this section, however at the moment it can be readily observed that the only lines intersecting this area belong to Reactions (30) and (32), representing the formation of

$LaCl_3$(c) and gaseous O_xCl_y-type compounds from the reaction between La_2O_3(c) and Cl_2(g), i.e. Reaction Type 1. Conversely, the analogous Type 1 reactions for HfO_2 do not possess a high enough slope or y-intercept to pass through this region. Type 2 reactions involving the conversion of condensed phase metal halides to the gas phase (Reactions (14)-(19)) are seen to generate products with significantly higher partial pressures than those of Type 1. Due to the lack of information on $LaCl_3$(g), equilibrium lines for Type 2 reactions involving La_2O_3 could not be expressed. This is a potential concern given the noted low volatility of $LaCl_3$(c), however, $HfCl_4$ is also not considered a particularly volatile species but has been experimentally observed in a plasma environment. It should be noted that the construction of volatility diagrams is based on principles of thermodynamic equilibrium, while a plasma is by nature a non-equilibrium environment. This contradiction makes it difficult to definitively draw conclusions from the data. However, the relative magnitude of the pressures generated does suggest that the first phase of the reaction process - the breakage of the metal-oxygen bond - is indeed the rate limiting step.

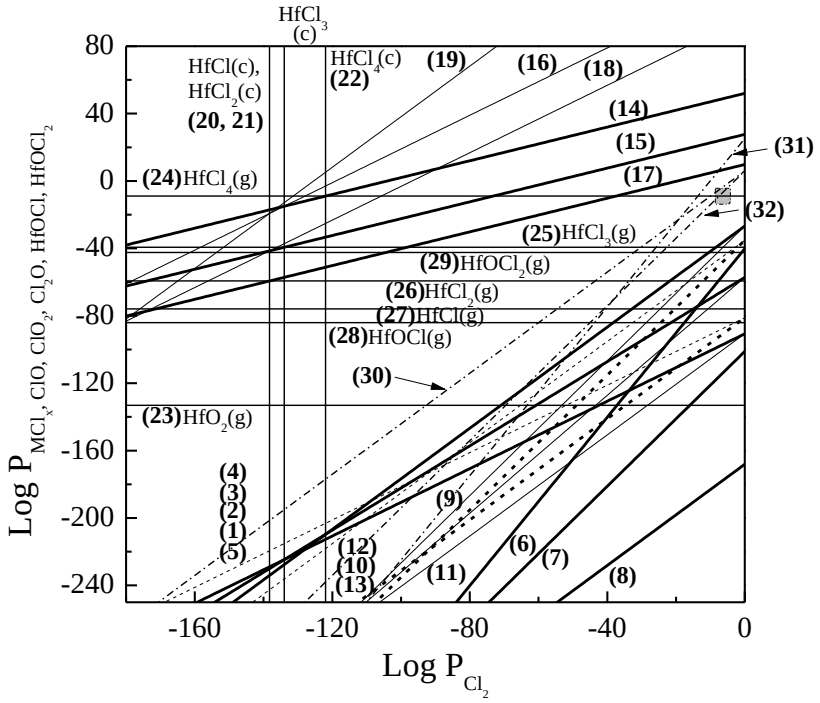

Figure 2.14 Volatility diagrams for HfO_2 etching in Cl_2 chemistry. Numbers in parentheses correspond to the reactions in Tables 2-4 and 2-5. The shaded box represents the intersection of the typical operating pressure range of the ICP reactor with the pressure required for appreciable mass removal.

The case of F_2 chemistry is plotted in Figure 2.15. It should be noted that the HfF_4 condensed state spans the entire x-axis of the plot, indicating that the formation of HfX_y-type compounds occurs more readily in F_2 chemistry than Cl_2. The overall slopes of the equilibrium lines for reactions involving the breaking of the Hf-O bond are higher in the case of F_2 chemistry compared to Cl_2, corresponding to a general trend of lower or negative Gibbs Free Energy values. Both of these observations can be attributed to the higher electronegativity of F over Cl, as well as the higher strength of the Hf-F bond compared to the Hf-Cl bond. Consequently, it can been seen that Reactions (7) and (10), both of which lead to the formation of HfF_3(c), intersect the region of interest - unlike the case of Cl_2 chemistry. However, the opposite is true for reactions with La - it can be seen that Reactions (30) - (32) generate significantly lower partial pressures than those for Cl_2. This was due to the calculated Gibbs Free Energy for LaF_3(c) being -6.8

kJ/mol, approximately two orders of magnitude lower than the value for $LaCl_3$(c) obtained in literature. As the data sets for different chemistries were obtained from separate sources, this observation should be regarded cautiously.

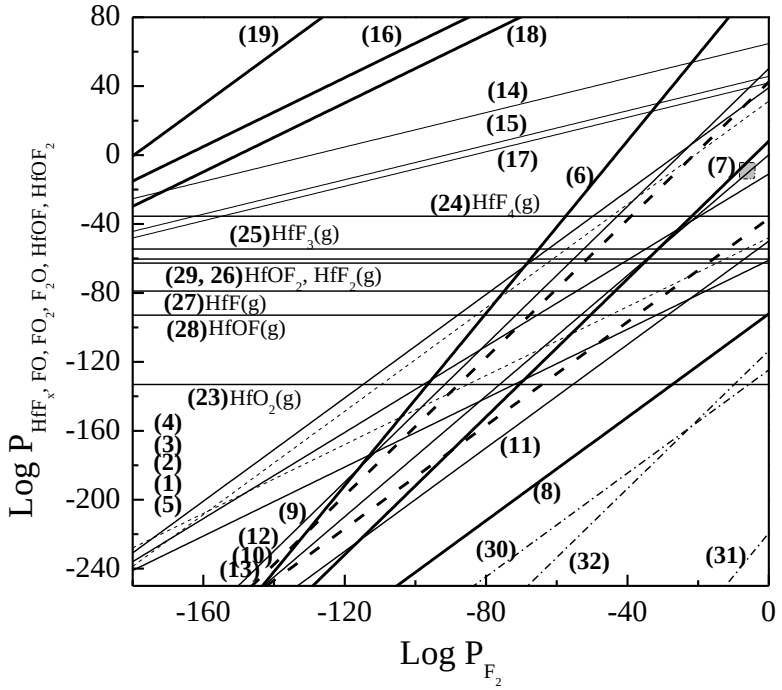

Figure 2.15 Volatility diagrams for HfO_2 etching in F_2 chemistry. Numbers in parentheses correspond to the reactions in Tables 2-4 and 2-5. The shaded box represents the intersection of the typical operating pressure range of the ICP reactor with the pressure required for appreciable mass removal.

A magnified view of the region of interest where appreciable mass removal occurs at typical operating pressures is shown below in the left plot of Figure 2.16. Reaction (24) is provided as a reference for the location, indicating the transition between gas and condensed phase $HfCl_4$. As previously noted, it is evident in this region that the partial pressures of Cl_xO_y gaseous products generated in reactions involving HfO_2 do not meet the threshold for measurable material removal, as only Reactions (7) and (10) using F_2 as the etchant gas are visible, which is in accordance with the higher reactivity of fluorine over chlorine. However, two such reactions

for La_2O_3 involving Cl_2 gas, (30) and (32), intersect this region. It should be noted that conceptually, the breaking of metal-oxygen bonds is required primarily to facilitate the halogenation of metal (as a preface to desorption of metal halides, the primary etch products), and does not necessarily lead to the simultaneous formation of gaseous oxyhalide products. However, as such products provide an avenue for oxygen removal, evaluating the partial pressures generated is of utility in examining the feasibility of an etch process.

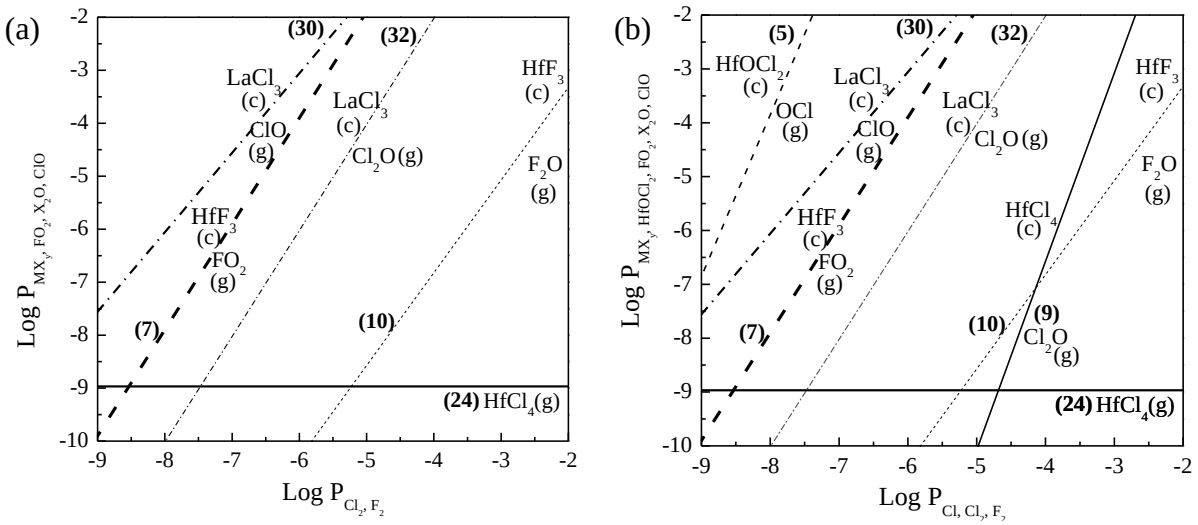

Figure 2.16 (a) Magnification of the region where appreciable mass removal and standard operating pressure intersect for Cl_2/F_2 chemistry and (b) Cl radical addition. Numbers in parentheses correspond to the reactions in Table 2-6.

If the atomic form of each halogen is used in lieu of the molecular one, the corresponding shift in ΔG values and molar quantity of reactant results in changes to log(*K*) and the gradient of the reaction lines for reaction types (i) and (ii). The vertical equilibrium lines between the condensed phase hafnium mono-, di-, tri- and tetrahalides are also shifted due to the change in ΔG - in comparison to the molecular forms the required partial pressures are higher. However, the horizontal condensed/gas phase equilibrium lines do not change as they are by definition independent of the reactant species partial pressure. The right hand plot of Figure 2.17 reflects

this shift in the operating region as it can now be seen that Reactions (5) and (9) using Cl radicals are now closer to the measurable partial pressure range for mass removal. However, it should be noted that the amount of radicals generated in an ICP is typically estimated at 5-10 orders of magnitude smaller than the molecular gas concentration. (Kulkarni and DeHoff 2002).

Thus far, the analysis suggests that Cl_2 can potentially serve as an etchant for La_2O_3 but is a less suitable candidate than F_2 for the etching of HfO_2. This difficulty can be potentially circumvented by Cl radical addition, however, the mass balance criterion must be simultaneously met. Figure 2.17 shows the isomolar line in the region of interest, which is the graphical representation of the mass balance equation for the governing reaction: (a line with a gradient of 1 and a y-intercept of log(x)).

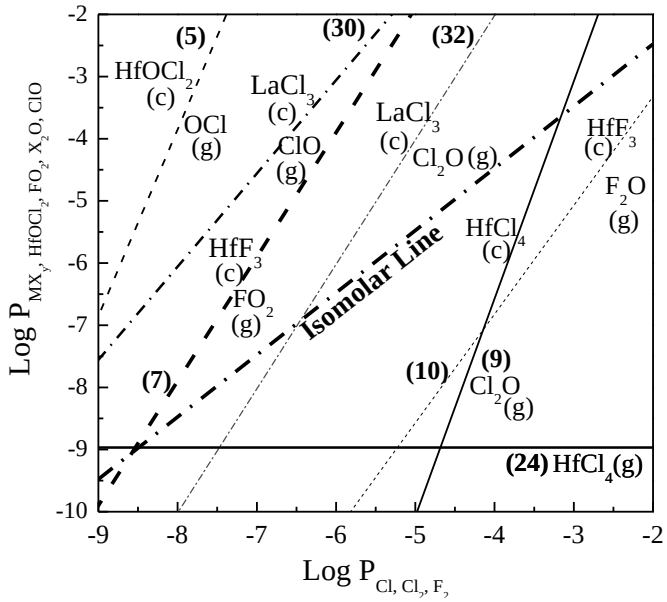

Figure 2.17 Illustration of the isomolar line signifying the mass balance criterion

Equilibria states above the isomolar line are technically considered metastable but cannot exist due to their violation of the mass balance. It can be seen that this eliminates Reactions (5),

(7) and (30) as potential pathways for etching. While Reactions (9) and (10) fulfill the mass balance criterion, the etchant pressure required for appreciable mass removal is ~80 mTorr, which is towards the high end of operating pressures used in most high-density plasma reactors. This leaves Reaction (32) as the most viable reaction, with a segment passing beneath the isomolar line while simultaneously generating etch product pressures of ~10^{-8} atm. However, since this reaction only applies to La_2O_3, if a non-fluorine chemistry is to be considered for the etching of HfLaO, pathways for the removal of HfO_2 also need to be present.

Next, the effect of BCl_3 chemistry is considered. It is known that its use results in the formation of $B_xO_yCl_z$ compounds which provide additional reaction pathways for the removal of oxygen. One such compound whose thermodynamic data has been profiled in literature is $(BOCl)_3$ (Blauer and Farber 1963). Recently, BCl_3 chemistry was illustrated as a potential replacement for perfluorocarbon gases such as CF_4 and SF_6 owing to their high global warming potentials and long lifetimes in the atmosphere (Frankwicz, Gardner et al. 2012). Some potential reactions leading to the formation of $(BOCl)_3$ from BCl_3 chemistry are detailed in Table 2-6.

Table 2-6 List of potential reactions of HfO_2 in BCl_3 chemistry

		ΔG (kJ/mol)	Log (*K*)
(33)	$HfO_2(c) + 2BCl_3(g) \rightarrow HfCl_4(c) + \frac{2}{3}(BOCl)_3(g)$	-298.8	52.8
(34)	$HfOCl_2(c) + BCl_3(g) \rightarrow HfCl_4(c) + \frac{1}{3}(BOCl)_3(g)$	-197.9	34.7
(35)	$HfOCl(c) + BCl_3(g) \rightarrow HfCl_3(c) + \frac{1}{3}(BOCl)_3(g)$	-112.2	19.7
(36)	$HfO_2(c) + 2BCl_2(g) \rightarrow HfCl_2(c) + \frac{2}{3}(BOCl)_3(g)$	-159.6	28.0
(37)	$HfOCl_2(c) + BCl_2(g) \rightarrow HfCl_3(c) + \frac{1}{3}(BOCl)_3(g)$	-145.4	25.5
(38)	$HfOCl(c) + BCl_2(g) \rightarrow HfCl_2(c) + \frac{1}{3}(BOCl)_3(g)$	-25.4	4.4
(39)	$HfOCl_2(c) + BCl(g) \rightarrow HfCl_2(c) + \frac{1}{3}(BOCl)_3(g)$	23.3	-4.1
(40)	$HfOCl(c) + BCl(g) \rightarrow HfCl(c) + \frac{1}{3}(BOCl)_3(g)$	155.7	-27.3

Figure 2.19 shows that Reaction (39) potentially allows BCl_x to etch HfO_2, as it satisfies both the mass balance criteria and the pressure requirement for mass removal. When combined with Reaction (32), a pathway is provided for material removal at typical plasma reactor operating pressures, an area highlighted by the gray box in Figure 2.18.

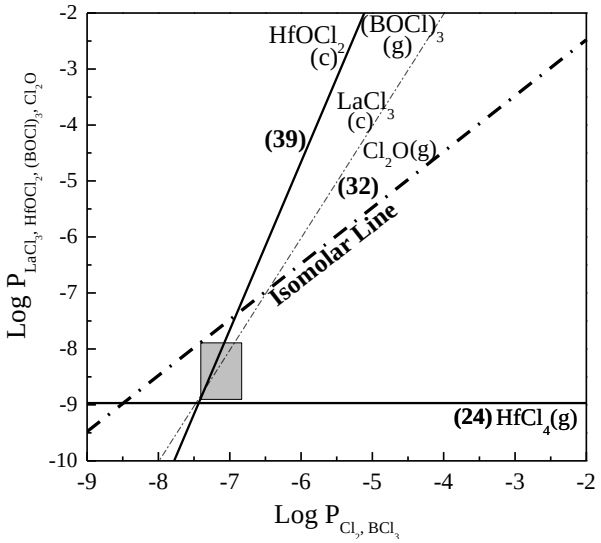

Figure 2.18. The effect of the addition of BCl_3 chemistry is shown in the region of interest - Reaction 39 is shown as a solid line. Reactions that required substantial etchant gas pressure or were above the isomolar line were removed from the plot for clarity. The shaded gray box represents the area where appreciable mass removal and reactor operating pressures intersect.

In conclusion, the use of volatility diagram analysis as applied to the etching of HfO_2 and La_2O_3 showed that a combination of Cl_2 and BCl_3 chemistry can indeed serve as an adequate alternative to fluorine-based chemistry at typical operating conditions. In this way, environmental ramifications can be minimized without sacrificing process efficacy.

2.6.2 Surface Site-Based Phenomenological Model

The details of the phenomenological model have been discussed in greater detail in literature (Martin and Chang 2009) and as such only a brief summary is provided here. The reaction process for etching of a metal oxide was summarized in four major pathways: (i) etch rate of the substrate (ER_s), (ii) etch rate of the polymer (ER_p), (iii) deposition rate on the substrate (DR_s) and (iv) deposition rate on the polymer (DR_p). The equations for these rates are shown below:

(i) $$ER_s = J_i \theta_{es} \left[A_s \left(E_{ion}^{1/2} - E_{th,s}^{1/2} \right) + B_s \left(E_{ion}^{1/2} - E_{tr,s}^{1/2} \right) \right] = J_e \nu_{es} S_{es} \theta_1$$

(ii) $$ER_p = J_i \theta_{ep} C_p \left(E_{ion}^{1/2} - E_{th,p}^{1/2} \right) = J_e \nu_{ep} S_{ep} \theta_2$$

(iii) $$DR_s = D_s \theta_{ds} = J_d \nu_{ds} S_{ds} \theta_1$$

(iv) $$DR_p = D_p \theta_{dp} = J_p \nu_{dp} S_{dp} \theta_2$$

In the etching reactions, $J_{i,e}$ are ion and neutral fluxes, $E_{th,s}$ and $E_{tr,s}$ are the threshold energy for etching and the transition energy between the physical and chemical etching regimes, A_s, B_s and C_p are terms describing the volume of material (oxide = s, polymer = p) removed as a function of ion energy, $\nu_{es,ep}$ describes the volume of oxide or polymer removed as a function of incoming etchant flux and $S_{es,ep}$ are the sticking coefficients for etching species on the oxide and polymer, respectively. The deposition reactions lead to the following additional terms: J_d (depositing species flux), (volume of polymer removed as a function of ion energy), $D_{s,p}$ (deposition rates on oxide and polymer), $\nu_{ds,dp}$ (volume deposited on oxide and polymer as a function of incoming flux), and $S_{ds,dp}$ (sticking coefficients of depositing species on the oxide and polymer). $\theta_{es,ds,ep,dp}$ refers to the surface sites available for etching and deposition on the substrate and polymer. For

simplifying purposes, the product of the ν and S terms is referred to as Z for the remainder of the work (i.e. $Z_{xy} = \nu_{xy} S_{xy}$).

At steady state, it is assumed that reactions (ii) and (iii) are equal (the deposition rate on substrate is equivalent to the etch rate of the polymer film). Using a site balance to eliminate the surface coverage terms and solving for the net etch/deposition rate yields the following equation:

$$R_t = ER_s - DR_s + ER_p - DR_p = \frac{J_e^2 Z_{es} Z_{ep} - J_d^2 Z_{ds} Z_{dp}}{\left(\begin{array}{c} J_d Z_{ds} + J_e Z_{ep} + \dfrac{J_d^2 Z_{ds} Z_{dp}}{D_p} + \dfrac{J_d J_e Z_{ds} Z_{dp}}{D_s} \\ + \dfrac{J_d J_e Z_{ds} Z_{dp}}{J_i C_p \left(E_{ion}^{1/2} - E_{th,p}^{1/2} \right)} + \dfrac{J_e^2 Z_{es} Z_{ep}}{\left[A_s \left(E_{ion}^{1/2} - E_{th,s}^{1/2} \right) + B_s \left(E_{ion}^{1/2} - E_{tr,s}^{1/2} \right) \right]} \end{array} \right)} \quad (2.28)$$

In the absence of a deposition and etching fluxes, this master equation reduces to forms proposed in literature by Stafford and Pearton (Stafford, Pearton et al. 2006) and Ding and Hershkowitz (Ding and Hershkowitz 1996), respectively:

$$R_t = \frac{J_i \left[A_s \left(E_{ion}^{1/2} - E_{th,s}^{1/2} \right) + B_s \left(E_{ion}^{1/2} - E_{tr,s}^{1/2} \right) \right]}{1 + J_i \left[A_s \left(E_{ion}^{1/2} - E_{th,s}^{1/2} \right) + B_s \left(E_{ion}^{1/2} - E_{tr,s}^{1/2} \right) \right] / J_e Z_{es}} \quad \text{(no deposition flux, } J_d = 0) \quad (2.29)$$

$$R_t = \frac{J_d Z_{dp}}{1 + J_d Z_{dp} / D_p} \quad \text{(no etching flux, } J_e = 0) \quad (2.30)$$

A residual sum of squares (RSS) minimizing algorithm was used to fit plots of the etch rate as a function of ion energy and in the process obtain multiple parameter combinations resulting in an RSS error below a certain threshold. Disparity between the obtained parameters thus provided a range over which the fits were deemed valid, as opposed to a single value for each parameter. In order to reduce computational burden, parameter fitting ranges were

constrained when possible based on experimental observations, e.g. threshold and transition energies were estimated based on the etch rate plots, and the ratio of neutral to ion fluxes determined via Langmuir Probe measurements.

2.6.3 Translating Mixed Layer Model

A general summary of the TML model was provided earlier in Chapter 1. The key advantage of this model lies in its ability to couple bulk scale and feature scale modeling. This is accomplished using the kinetic parameters for the discrete reactions in the TML system as input for a feature profile simulator. A diagram depicting this process, along with a highly simplified reaction set for metal oxide etching in Cl_2 chemistry, is shown in Figure 2.19.

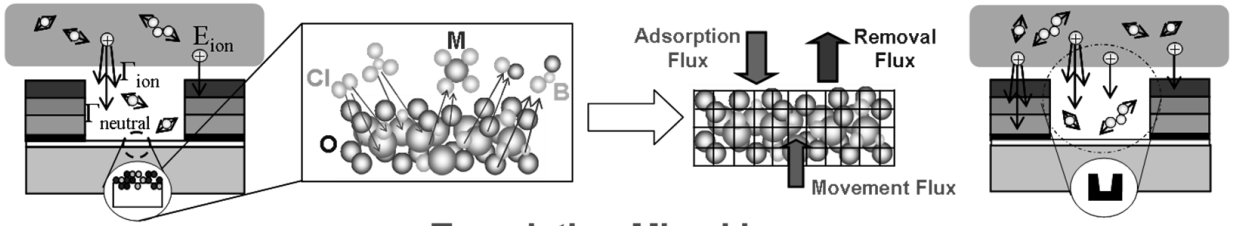

Translating Mixed Layer

$Cl_{(g)} \rightarrow Cl_{(s)}$	$r_{A1} = s_{Cl\_on\_M} R_{Cl} x_{M\_for\_Cl}$
$Cl^{+}_{(g)} \rightarrow Cl_{(s)}$	$r_{A2} = s_{Cl^{+}} R_{Cl^{+}}$
$Cl_{(s)} + O_{(s)} \rightarrow ClO_{(g)}$	$r_{E1} = \beta_{ClO}(J_{Cl-O})$
$BCl_{(s)} + O_{(s)} \rightarrow BOCl_{(g)}$	$r_{E2} = \beta_{BOCl}(J_{B-Cl})(J_{B-O})$
$M_{(s)} + 4Cl_{(s)} \rightarrow MCl_{4(g)}$	$r_{E3} = \beta_{MCl_4}(J_{M-Cl})^4$

$$r_M = r_{A1} + r_{A2} - 2r_{E1} - 3r_{E2} - 5r_{E3}$$

Figure 2.19 Schematic of the TML model illustrating the potential of coupling to feature scale profile simulation through the discretization of fluxes and cellular arrangement. Sample equations for the etching of a metal oxide (MO_x) in Cl_2/BCl_3 chemistry are shown.

The following sections examine further details about the constituent equations of the three major fluxes (arrival, removal and movement) in the TML model and their relation to measured experimental parameters.

Arrival Flux: The TML model accounts for addition of species in three ways: (i) the implantation of individual ionic species, (ii) the absorption of individual neutral species, and (iii) the addition of vacancies into the mixing layer. These processes are detailed below, using representative equations specific to metal oxide etching in chlorine-based chemistry.

(i) Ion implantation - In this reaction an ionic specie from the gas phase becomes implanted in the mixing layer, resulting in the destruction of a vacancy and the addition of the number of atoms in that specie, e.g. Cl_2^+ implantation results in two chlorine atoms being added to the mixing layer. The representative equation for the ion implantation yield (using Cl^+ ions as an example) is given below:

$$R_{A\_Cl\_i} = S_{Cl\_i} G_{Cl\_i} f \tag{2.31}$$

Where $R_{A\_Cl\_i}$ is the Cl^+ ion implantation yield, S_{Cl_i} is the "sticking coefficient" of Cl^+ ions (set to unity), G_{Cl_i} is the Cl^+ ion flux normalized to the total ion flux, and f is the threshold adjustment factor. The threshold adjustment factor follows a step function distribution: for ion energies above the threshold for physical sputtering its value is 1, and for ion energies below the threshold its value is 0. This prevents the simulated deposition of a blanket layer of chlorine

atoms over the surface at low ion energies, which is not observed experimentally and is thus considered nonphysical.

(ii) Neutral absorption - In this reaction a neutral specie from the gas phase adsorbs onto a specific atom in the mixing layer. Unlike ion implantation this reaction rate is dependent on the concentration of the mixing layer. It results in the destruction of a vacancy and the addition of the number of atoms in the specie, e.g. Cl adsorption results in a single chlorine atom being added to the mixing layer. The representative equation for neutral absorption rate from the gas phase (using Cl neutrals and Hf surface atoms) is given below:

$$R_{A\_Cl\_on\_Hf} = S_{Cl\_on\_Hf} G_{Cl} J_{Hf\_V} \tag{2.32}$$

Where $R_{A\_Cl\_on\_Hf}$ is the neutral absorption yield due to Cl atom chemisorption, $S_{Cl\_on\_Hf}$ is the sticking coefficient of Cl atoms on active sites associated with Hf, G_{Cl} is the Cl neutral flux normalized to the total ion flux, and J_{Hf_V} is the active site concentration on Hf atoms. Chemisorption is proposed to take place on metal and oxygen atoms, resulting in $x(n+1)$ equations for neutral absorption (where x is the number of distinct neutral species impinging on the surface and n is the number of distinct metal elements in the film).

(iii) Vacancy generation – Vacancies are generated by energetic ion species impacting and breaking interatomic bonds in the mixing layer. The rate equation is represented as follows (using Ar^+ ions as an example):

$$R_{A\_V\_by\_Ar} = \beta_{V\_by\_Ar} G_{Ar\_i} \tag{2.33}$$

Where $R_{A\_V\_by\_Ar}$ is the vacancy generation yield due to Ar^+ bombardment, $\beta_{V\_by\_Ar}$ is the linear coefficient and G_{Ar_i} is the Ar^+ flux normalized to the total ion flux. As the initial stoichiometry of the mixing layer does not include any vacancies, without the vacancy generation reaction it would be impossible for neutrals to adsorb (recall that vacancies are the "active sites" of the mixing layer). The linear coefficient is dependent on the square root of the ion energy. Vacancy generation is modeled as a first order process and is dependent on the flux of the ionic specie in question. A compilation of the arrival flux equations for Cl_2/BCl_3 etching of HfO_2, Al_2O_3, La_2O_3,HfAlO and HfLaO in the TML model are available in Appendix B.

Removal Flux: The TML model has multiple avenues for the removal of material from the mixed layer: (i) physical sputtering, (ii) ion-enhanced chemical etching, (iii) densification (vacancy destruction), (iv) dangling bond annihilation and (v) surface recombination. These processes are detailed below.

(i) Physical sputtering – In a sputter process a single atom is transferred from the mixing layer to the gas phase, i.e. M(s) → M(g). The representative equation for this process(using the case of Ar^+ impacting Hf mixing layer atoms) takes the following form:

$$R_{S\_Hf\_by\_Ar} = Y_{Hf\_by\_Ar} x_{Hf} G_{Ar\_i} \tag{2.34}$$

Where $R_{S\_Hf\_by\_Ar}$ is the sputtering yield of Hf by Ar^+, $Y_{Hf\_by\_Ar}$ is the sputtering yield coefficient, x_{Hf} is the fraction of Hf atoms in the mixed layer and G_{Ar_i} is the flux of Ar^+ normalized to the

total ion flux. The sputtering yield coefficient is itself a function of the ion bombardment energy, sputtering threshold energy, linear proportional coefficient and angular dependence function. The particulars of these terms are discussed in literature (Guo, Bai et al. 2009) and are not discussed here. In the case of Cl_2 etching, metal, chlorine and oxygen atoms are considered susceptible to sputtering (vacancies are connected to dangling bonds and are thus subject to a separate set of reactions), and so the total number of sputtering equations is $x(n + 2)$ where x is the number of distinct impacting ionic species and n is the number of separate metal elements in the film. For BCl_3 etching, boron atoms are also considered susceptible to sputtering and thus the number of equations is $x(n + 3)$.

(ii) Ion-enhanced chemical etching – Etch products experimentally observed through QMS are used to formulate the equations for the rate of ion-enhanced chemical etching. The yield is dependent on the nearest-neighbor bond concentrations of the pertinent species. In order to illustrate, the yield equation for $HfCl_3$ is shown below:

$$R_{E\_HfCl_3} = \beta_{HfCl_3} \left(J_{Hf-Cl} \right)^3 \tag{2.35}$$

Where β_{HfCl_3} is the coefficient for $HfCl_3$ formation and $J_{Hf\text{-}Cl}$ is the nearest neighbor probability between hafnium and chlorine atoms. The β coefficients are a function of the square root of ion energy and have a cosine-based angular dependence. It can be seen that as the number of atoms in an etch product goes up, its odds of formation become smaller as the nearest neighbor probabilities (≤ 1) are multiplied together.

(iii) Densification – The impact of energetic ions can remove vacancies as well as create them. For the example of vacancy destruction by Ar^+ impact, the yield equation takes the form:

$$R_{d\_V\_by\_Ar} = B_{d\_V\_by\_Ar} x_V G_{Ar\_i} \tag{2.36}$$

Where $B_{d\_V\_by\_Ar}$ is the densification yield coefficient and x_V is the fraction of vacancies in the mixed layer. The densification yield coefficient is a function of the square root of the ion energy. Similar to their generation, destruction of vacancies is modeled as a first order process. As the creation of a vacancy is technically considered an "addition" to the mixing layer, the possibility exists of eventually having a mixing layer which consists of over 50% "vacancies". The densification process serves as a control over that scenario. This situation becomes even more important if the extracted kinetic parameters are fed into a feature scale model, where cell addition or subtraction can take place based on the calculated yield (addition or subtraction of particles from the cell). If a sufficient amount of vacancies are added then a new cell is created, resulting in the unphysical deposition of material.

(iv) Dangling bond annihilation – This process refers to the spontaneous removal of two vacancy species from the mixed layer. Its contribution to the removal flux is a summation of dangling bond annihilation on metal, oxygen and chlorine atoms in the case of Cl_2 etching, as well as boron atoms in the case of BCl_3 etching. The yield equation is shown below:

$$R_{an\_V} = \sum \beta_{M-V} \left(J_{M-V} \right)^2 \tag{2.37}$$

Where *M* are elements present in the mixed layer.

(v) Surface recombination – Recombination refers to the spontaneous reaction of a single surface specie (attached to a dangling bond) with an impinging specie from the gas phase to form a product. The result is the removal of an atom from the surface and the destruction of a vacancy without any implantation or adsorption. The surface recombination yield equation (using Cl_2 formation as an example) is:

$$R_{R\_Cl\_Cl} = A_{Cl\_Cl} J_{Cl-V} G_{Cl} \tag{2.38}$$

Where $A_{Cl\text{-}Cl}$ is the recombination coefficient. In general for Cl_2 chemistry the value of this coefficient tends to be small (on the order of a few percent). However for oxide materials with low etch yields, even reactions such as these with small rates can influence the outcome of the simulation. . The removal flux reactions for Cl_2/BCl_3 etching of HfO_2, Al_2O_3, La_2O_3,HfAlO and HfLaO are also available in Appendix B.

Movement Flux: The final step of the modeling process is to solve the equation sets for the etching process and obtain a value for etch rate or yield as a function of the input parameters discussed in the previous sections, as well as the ion energy and neutral to ion (n/I) ratio. In the phenomenological model this is achieved by performing a surface site balance to eliminate coverage terms which cannot be measured directly. Solving this equation together with the four etching and deposition equations gives the etch (or deposition) rate. In the TML model, time

dependent differential equations for each species in the mixing layer are expressed by summing up all the terms associated with arrival or removal of that species according to stoichiometry. Integrating these differential equations with respect to time (using the initial substrate composition as the initial condition) achieves a steady state solution. The difference between the total arrival and removal fluxes leads to an overall *movement flux* which determines whether net etching or deposition is observed. Thus, the overall etch yield and composition of the mixing layer can be determined through this model.

2.6.4 Monte Carlo-Based Feature Profile Simulator

The feature scale model used in this work is a cellular-based direct simulation Monte Carlo (DSMC) model. The concepts and theory have been discussed in more detail in the literature (Hoang, Hsu et al. 2008) so this section only provides a brief description. The feature scale model is a pseudo-3D model, whereby plasma species are individually sampled at the source plane and given a 3D trajectory but are advanced by grid length steps in 2D space with the assumption that the trenches extend indefinitely. In this method, the simulation domain is translated into a discrete cellular space resulting in potential misrepresentations in particle fluxes and surface normals. These problems were addressed by adapting a polynomial fit in order to determine the surface topography and normals in three dimensions, as described in literature. (Guo and Sawin 2009) The resulting species fluxes and surface normals were shown to be more accurate than previous methods such as the cell center surface representation and least squares method. (Mahorowala and Sawin 2002)

The source code for the profile simulator was written in Visual C++ and compiled and executed through Microsoft Visual Studio. The details of running the simulation are examined in Appendix C. The code comprises several sub-modules which possess different functionalities related to various facets of the profile simulation, e.g. the outcome of chemical reaction processes are determined in a separate module from geometric calculations. These modules are then run in conjunction with an input file that specifies global parameters such as the maximum dimensions of the simulation domain, the number of particles sampled per iteration, the total number of iterations, energy of ionic species, and flux composition of the gas phase environment. In the following section, brief descriptions of the various sub-modules of the profile simulator code are provided.

Header: In the header file the various functions, data arrays, and variable classes are declared for use by the other modules in the source code. This includes prebuilt function libraries included in Visual Studio. The total numbers of chemical species, reactions, and particles in a cell are also defined in this module.

NrUtil2: This is a second header file which declares the variables and functions used by a random number generator within the source code.

Main: This module reads the aforementioned input file for all of the Visual C++ code modules and is the first module to be executed. It also allocates memory, calls initial functions, e.g. feature definition, handles the display of the simulation progress, reports error messages and

creates output files. When the code has finished running this module is also responsible for closing the files used by the model.

Mcarlo: After the feature geometry has been defined and all pertinent functions and variables have been loaded, the next step of the simulation is to initialize individual particles based on the specified total (number of particles per iteration multiplied by the number of iterations). This module uses random number generation to assign species identities and trajectories, and is also responsible for calling the functions that write data to the output files.

Track: Once a particle has been generated, this module adds a unit length to its initial location based on the specified trajectory. It then advances the particle until it either leaves the simulation domain through the gas phase or reaches a surface. In the case of the former, the simulation then returns to the *Mcarlo* module to generate another particle. In the case of the latter, the module performs polynomial fitting to determine the surface normal and point of intersection of the particle. It then calls the *Chemistry* module to begin the process of determining whether the particle sticks or scatters.

Chemistry: This module contains all of the parameters for the chemical reactions in the process being considered. It is called when a particle is determined to have made contact with a a solid cell. Depending on the identity of the particle (ion or neutral) routines are performed to establish whether the particle is adsorbed or scatters. If scattering occurs the *Track* module is recalled to follow the particle until it reaches a surface again (in which case *Chemistry* is utilizedd), or until it leaves the simulation domain. In the case of adsorption, the reaction set containing kinetic

parameters from the translating mixed layer model is applied to determine whether etching or deposition occurs.

Distribution: This module contains statistical distribution functions used within the MC code, such as Gaussian or isotropic distributions for particle scattering.

File: This module is responsible for writing data to the simulation output files. It also specifies the exact dimensions of features as options which can be selected in the input file. In this way multiple scenarios can be stored and easily accessed simply by changing the a variable in the input file, rather than manually adjusting the geometry each time a different initial profile is desired.

Geometry: This module contains basic mathematical functions used to calculate quantities such as intersection locations and edge positions in the feature.

Math: This module performs mathematical operations such as boundary condition calculation and handling arrays or matrices.

Nr Util: This module contains a random number generator that is used throughout the module for determining probabilities.

Specific: This module contains simple mathematical functions which are required by the program, such as the calculation of cosine values.

A flow chart showing a typical process flow involving the modules in the MC simulator is shown below in Figure 2.20.

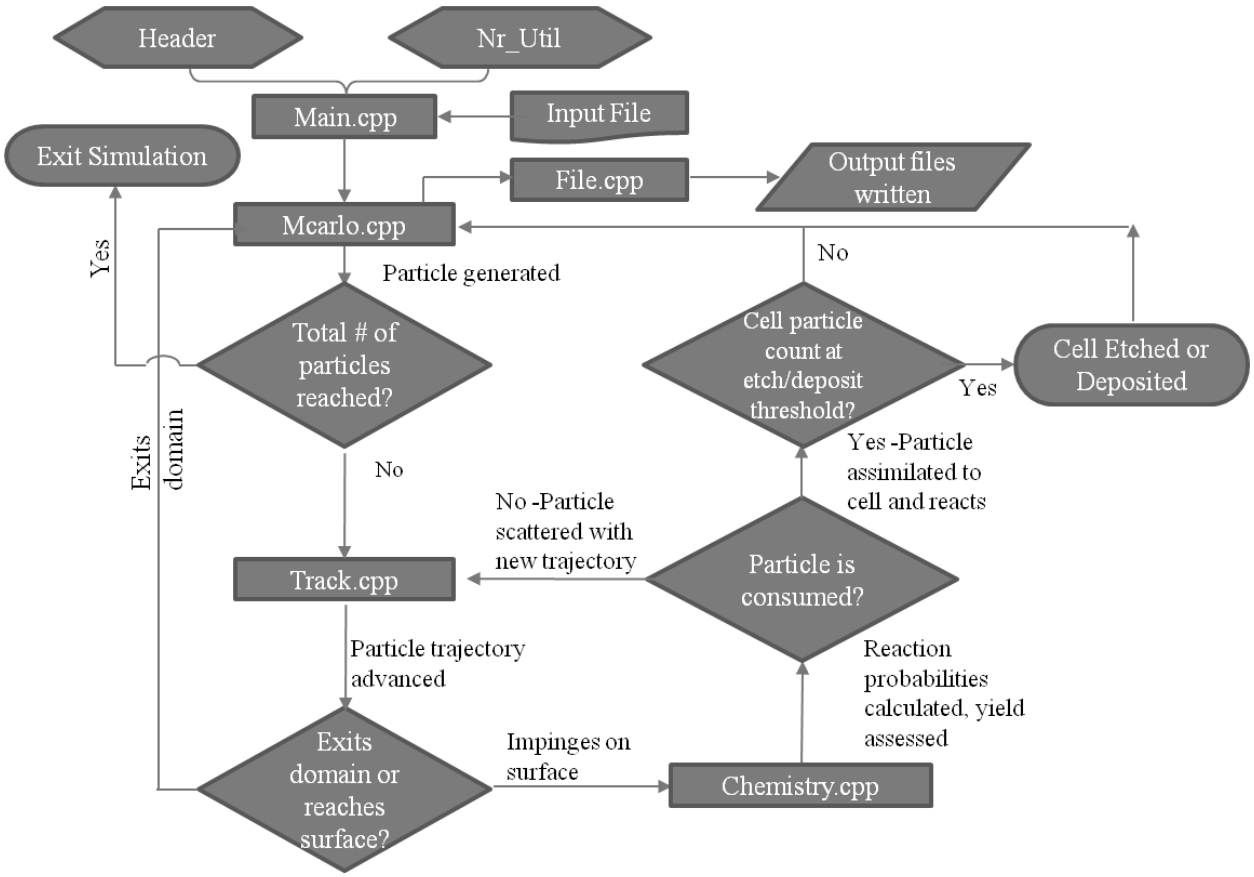

Figure 2.20 Flow chart showing the process of co-ordination between the previously discussed source code modules in the feature profile simulator.

CHAPTER 3: IN-SITU ETCH STUDY OF $Hf_xLa_yO_z$ IN Cl_2/BCl_3 PLASMA

For the baseline conditions of 400W, 5 mT, Cl_2 and 400 W , 15 mT BCl_3, the in-situ etch rates of $Hf_{0.25}La_{0.12}O_{0.63}$ and La_2O_3 films were measured *in situ* using a quartz crystal microbalance (QCM) as a function of ion energy, La-containing etch products were identified via quadrupole mass spectrometry (QMS) and the surface composition of the films after plasma exposure was investigated using x-ray photoelectron spectroscopy (XPS). The calculated etch rates of the $Hf_{0.25}La_{0.12}O_{0.63}$ films at the Cl_2 baseline condition varied from 4 to 35 Å/min (for -25 to -175 V bias voltage, respectively), while the maximum etch rate observed at the BCl_3 baseline was 22 Å/min (at -175V bias voltage). The results were verified by comparing to cross-sectional SEM measurements. LaCl and LaOCl (3.9 : 1.0) and LaB, LaB_2O, LaBOCl and LaO_2Cl (1.2 : 1.1 : 1.3 : 1.0) were observed as the dominant La-containing species for La_2O_3 films exposed to the Cl_2 and BCl_3 baseline conditions, respectively at -100 V bias voltage. The surface compositions of the $Hf_{0.25}La_{0.12}O_{0.63}$ films after etching at the aforementioned conditions showed an increase in the Hf/La ratio for both chemistries, with a greater change in BCl_3 compared to Cl_2 chemistry. XPS analysis of pure La_2O_3 films after 5 minutes etching revealed a significantly larger percentage of O-La-Cl present in the surface layer for the BCl_3 exposed films, suggesting the development of a stable $LaCl_x$ layer which could potentially serve as an etch stop barrier for this material. These observations were consistent with quantitatively lower etch rate of $Hf_{0.25}La_{0.12}O_{0.63}$ in BCl_3 compared to Cl_2, as well as the differing characteristics of the QCM frequency response curves.

3.1 Etch Rate Quantification

The methods of measuring the etch rate of a material can be divided into two main categories: *ex situ* and *in situ* measurements. As the name implies, *ex situ* measurements are performed outside of the experimental environment. With regards to the etch rate, this entails measuring the film thickness before and after the etch process, then dividing the thickness change by the total exposure time. Two available *ex situ* means of measuring the film thickness for this study were spectroscopic ellipsometry and cross-sectional scanning electron microscopy (SEM). The relative advantages and disadvantages of each method are briefly listed in Table 3-1.

Table 3-1 Comparison of SEM and Ellipsometry for Assessing Film Thickness

	SEM	Ellipsometry
Time Required	Moderate (requires vacuum environment, special sample mounts)	Low (can be performed in ambient conditions, single data scan obtained almost instantly)
Maximum Resolution	High (~1 nm, dependent on charging effects)	High (< 1 nm theoretically, dependent on accuracy of model used to fit optical data)
Range of Material Applicability	High (insulators require conductive coating, usually Au or Au/Pd)	Moderate (limited use for optically opaque materials, accuracy dependent on ability of light to reach lower interfaces)
Ability to Examine Patterned Features	Yes	No (possible if used with a CCD detector, however this capability was not available on the available system)
Other Limitations	High voltage of electron beam can potentially damage features in softer materials (e.g. photoresist).	Accuracy compromised if: (a) roughness of surface or film interface exceeds 10% of the probe beam wavelength, or (b) film thickness variation greater than 10% across beam spot size (typically 10 μm - 3 mm)

For the purpose of this study, SEM was chosen as the primary means of ex-situ measurement, as the roughness of the HfLaO and La_2O_3 film samples after plasma etching contributed to difficulty with consistently fitting the optical models to the ellipsometric measurements. Additionally, the ability of SEM to examine patterned features was critical to a later part of this study (discussed in Chapter 5).

However, a major disadvantage of *ex situ* etch rate measurements is the fact that after exposure to a plasma environment, the film surface is often highly reactive and exposure to ambient conditions results in additional reactions. Such reactions, e.g. oxidation, can affect the film characteristics and thus influence the thickness measurement. As such, an *in situ* method of characterization is desirable to provide further insight into the etching process as it happens. For this study, the method chosen was the quartz crystal microbalance (QCM), which measures the frequency change of a quartz crystal as material is either deposited or in this case, removed. In order to establish the frequency response behavior of the QCM, unloaded crystals and ones coated with the material of interest, HfLaO, were exposed to the extracted Cl_2 plasma for different time periods at a constant bias voltage of -100V, as illustrated in Figure 3.1.

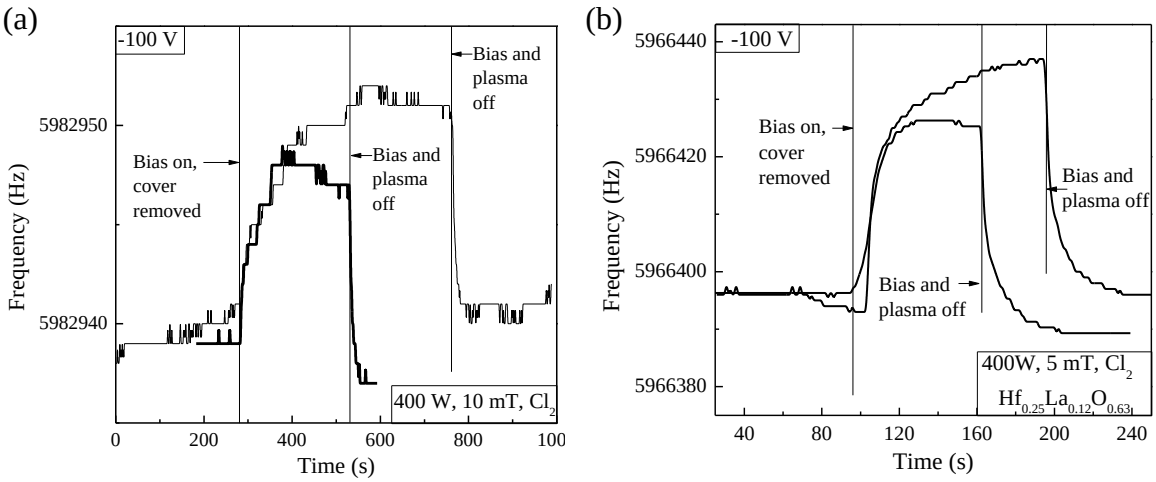

Figure 3.1 Illustration of frequency change on (a) an unloaded QCM crystal in a 400W, 10 mT, Cl_2 plasma at -100 V and (b) a crystal loaded with 1000 Å $Hf_{0.25}La_{0.12}O_{0.63}$ at 400W, 5 mT, Cl_2, -100 V). Vertical lines are labeled to indicate the time when the bias was applied and the cover retracted from over the QCM assembly, as well as the time at which the bias and plasma were switched off.

In the frequency response for both crystals, three distinct regions are observed: an initial region of sharp increase (upon exposing the crystal to the plasma beam by removing the cover as described in Section II), a region of slower frequency increase leading to saturation, and a region of sharp decrease in frequency (coinciding with the switching off of DC bias and RF power). For a constant bias voltage the curves were found to follow the same progression into the gradually increasing region. An increase in frequency correlates to the load (i.e. the film) on the quartz crystal being removed. In the case of the unloaded crystal, the top gold electrode surface was directly exposed to the plasma chemistry. The formation of the volatile compound $AuCl_3$ could be responsible for the frequency increase of the uncoated crystal. It was observed that the transition into the region of gradual increase occurred sooner in the case of the uncoated crystal, possibly a result of the lower reactivity of gold with Cl_2 compared to HfLaO with Cl_2. The higher density of gold compared to HfLaO (19.3 vs. ~8.1 g/cm^3) also corresponds to a lower etch rate

for a given frequency change (further explanation in Section 3.2), providing further evidence for the comparatively higher reactivity between HfLaO and Cl_2. However, it should be noted that the magnitude of the frequency shift for the uncoated crystal was significantly less than that of the coated one, resulting in a lower signal to noise ratio. Additionally, in both frequency responses, the trend towards saturation of the frequency value after a certain time period would indicate a process that results in the termination of the etch process, e.g. the formation of an etch resistant layer, or a shift in the equilibrium between competing deposition and etch processes towards deposition. The former phenomenon can be investigated through surface analysis methods such as XPS, which is discussed in Section 3.5.

The region of pronounced frequency decrease after the disengagement of the bias and plasma was divided into two areas, an area of sharp decrease followed by a gradual tapering of the frequency to a steady value, a fact more apparent in t Figure 3.1 (b) due to the higher signal to noise ratio. It was observed that the frequency decrease occurred primarily in the first (steep) region, with minimal change happening in the second (gradual) period before a constant frequency was reestablished. This could be interpreted as an effect of the plasma afterglow interacting with the surface, which would possess a heightened reactivity caused by the prior exposure to energetic ions. Low energy species could then rapidly react at the available sites until a certain level of coverage was achieved, after which point the rate of adsorption would decrease rapidly. Another possible cause for the frequency increase could be the physisorption of higher mass etch products on the exposed surface via redeposition, a phenomenon which has been documented in the literature. (Kimura, Coburn et al. 2004; Vasenkov, Li et al. 2004) It is known that plasma-surface interactions often involve competing etch and deposition processes. As the bias is applied and energetic ion and radical species continue to impinge upon the surface,

the removal of material competes with ion implantation and neutral adsorption. Once the bias voltage is no longer present, the deposition reactions dominate, resulting in a decrease in frequency.

Calibration of the QCM was performed using Si-coated crystals to establish the value of the impinging ion flux in the lower section of the reactor. This was important due to the specific geometry of this plasma reactor, in which the bulk plasma is extracted from the upper chamber to the lower area housing the QCM through a grounded grid. As such, it was desirable to quantify any disparity between the ion flux estimated from Langmuir Probe measurements in the upper chamber and the actual flux reaching the QCM. The frequency response of an Si-coated QCM crystal compared to a HfLaO-coated one at the Cl_2 baseline condition and -100 V bias voltage is shown in Figure 3.2(a). It should be noted that the curves were superimposed to illustrate the differences more clearly and thus only the change in frequency (Δf) is provided.

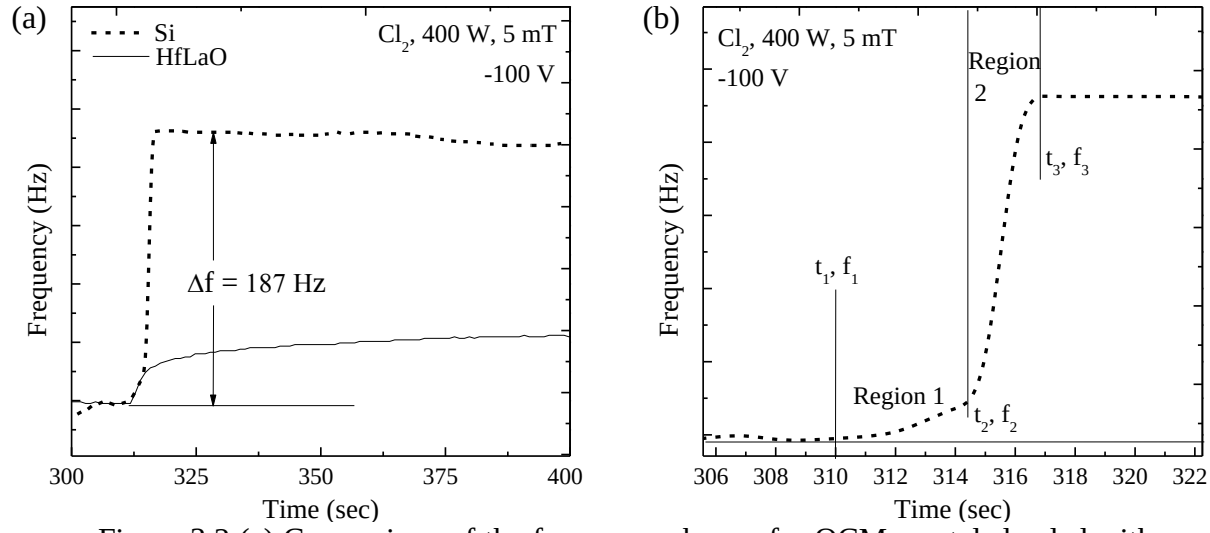

Figure 3.2 (a) Comparison of the frequency change for QCM crystals loaded with 1000 Å $Hf_{0.25}La_{0.12}O_{0.63}$ and 5000 Å Si in a 400W, 5 mT, Cl_2 plasma at -100 V. (b) Magnification of the frequency curve for the Si-coated crystal.

At the start of the etching process the two curves follow roughly the same gradient. For the Si-coated crystal this could indicate the presence of a thin SiO_2 layer on the film surface. When the HfLaO curve begins to saturate, the gradient of the Si-coated crystal increases sharply. It was noted that the frequency of the Si-coated crystal eventually saturates despite the bias voltage being applied, rather than continually increasing. The reason for this phenomenon is currently unclear, but could possibly be attributed to tolerances of the monitoring equipment.

Figure 3.2 (b) shows a magnified view of the frequency response for the Si-coated crystal. In order to calculate the etch rate, a weighted average of the frequency changes in Regions (1) and (2) is taken, representing the change in frequency before the onset of saturation. Rearranging the small load approximation equation provided in Section 2.5.2 yields an expression for the mass removed per unit area m_F:

$$m_F = \frac{-Z_q(f - f_f)}{2f \cdot f_f} \quad [\text{g/cm}^2] \tag{3.1}$$

The etch rate can then be calculated from m_F using the following expression:

$$ER = \frac{m_F}{\rho_{film}(t_{end} - t_{start})} \quad [\text{cm/s}] \tag{3.2}$$

Where ρ_{film} is the mass density of the film (2.33 g/cm^3 for Si, 8.65 g/cm^3 for $Hf_{0.25}La_{0.12}O_{0.63}$, 7.54 g/cm^3 for $Hf_{0.11}La_{0.23}O_{0.66}$, 6.51 g/cm^3 for La_2O_3). The weighted average of the etch in Regions 1 and 2 as shown in Figure 3.2 (b) is given by the expression:

$$ER_{NET} = \frac{ER_1 \cdot (t_2 - t_1) + ER_2 \cdot (t_3 - t_2)}{(t_3 - t_2) + (t_2 - t_1)} = \frac{ER_1 \cdot (t_2 - t_1) + ER_2 \cdot (t_3 - t_2)}{(t_3 - t_1)} \tag{3.3}$$

It should be noted that for the QCM frequency response spectra displayed in Figures 3.1 and 3.2, the magnitude of error (random fluctuations) was on the order of ~1-2 Hz. From Table 2-3, this corresponds to approximately one tenth of a monolayer of Si (lower for denser materials). As such, it is likely that the largest source of uncertainty in calculating the etch rate comes from defining the different regions in the frequency response spectra (human error). Using this method, the calculated etch rate of poly-Si in a 400 W, 5 mT Cl_2 plasma at -100 V bias voltage was 875 - 941 Å/min. Assuming the etch yield of Si atoms in Cl_2 plasma at ~110 eV to be between 1.6 and 2.3, a range taken from experiments (Hsu, Marchack et al., submitted) and literature (Balooch, Moalem et al. 1996), the ion flux required to satisfy this yield criterion was calculated as (3.5 - 5.0) × 10^{15} cm^{-2} s^{-1}. In order for this calculation to be valid, it must also be

assumed that at the operating conditions of the ICP reactor, the etch yield is independent of the neutral to ion (n/I) ratio.

By comparison, the ion flux in the upper section of the ICP reactor was estimated using the following equation:

$$J_{ion} = n_i \left(\frac{T_e}{M} \right)^{1/2} \quad [\#.\ cm^{-2}\ s^{-1}] \tag{3.4}$$

where n_i is the ion density, T_e is the electron temperature and M is the mass of the ion. From Langmuir Probe measurements taken at the Cl_2 operating condition (400W, 5 mT), T_e and n_i were calculated as 4.17 eV and 2.9 x 10^{11} cm^{-3} respectively, translating to an ion flux of 6.9 x 10^{16} cm^{-2} s^{-1}. This suggests a reduction in ion flux of approximately one order of magnitude between the upper and lower sections of the reactor, presumably caused by losses to the grid through which the extracted plasma beam passes. While this is a higher value than expected, it should be noted that noise in the Langmuir Probe measurements could affect the estimate of the ion flux.

3.2 Etch Rate of HfLaO/La_2O_3 as a Function of Ion Energy in Cl_2 Plasma

The effect of increasing ion energy on the etch rate of the HfLaO films was characterized by varying the negative bias applied to the ring electrode in the upper chamber, and measuring the corresponding frequency change of the HfLaO-coated QCM crystals in the lower chamber. A plot of frequency change (Δf) with respect to time for bias values of -50, -100, -150V and -200V at the aforementioned Cl_2 plasma baseline condition is shown in Figure 3.3 (a), with the curves

superimposed on each other in (b) to better illustrate the variation of frequency from a common alignment point. Frequency curves for the -25, -75, -125, and -175V bias conditions were also obtained but were not plotted here. The dashed line in (a) is provided to guide the eye and illustrate that the baseline of the frequency response curve gradually increases. This indicates a net removal of material as the etch process continues. The gray rectangle in (b) represents the area which was selected to calculate the etch rate at each bias voltage value. The boundaries on the x-axis for this area were defined from the onset of etching (i.e. the initial rise in frequency) to the onset of saturation (i.e. the point at which the value of frequency stops changing). If the saturation region was included in the etch rate calculation, the selection of the end point would be completely arbitrary given the constant value of the frequency.

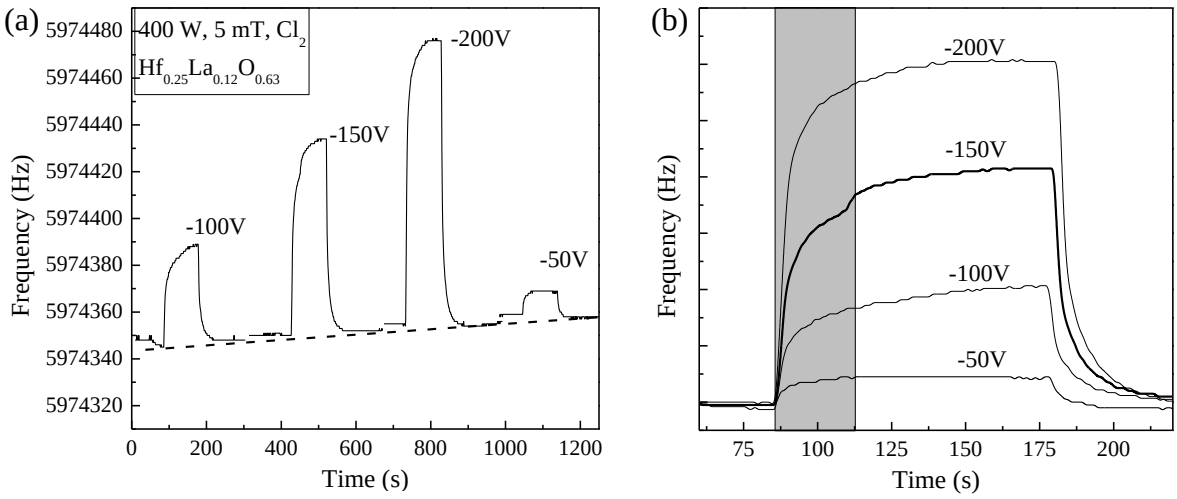

Figure 3.3 (a) Raw data for the frequency change of QCM crystals coated with $Hf_{0.25}La_{0.12}O_{0.63}$ as a function of bias voltage and time in a Cl_2, 400 W, 5 mT plasma. The dashed line is provided to guide the eye and illustrate the increase in baseline frequency over time. (b) Curves superimposed on each other to better illustrate the difference in frequency. The gray rectangle indicates the region in which the etch rate calculations were made.

Using the method described in Section 3.1, the etch rate for $Hf_{0.25}La_{0.12}O_{0.63}$ as a function of ion energy for the ICP baseline Cl_2 condition was derived from the QCM frequency response

data. The results are shown in Figure 3.4. The dashed line was provided to guide the eye. Error bars were plotted from the standard deviation between QCM measurements from two separate crystals at this plasma condition.

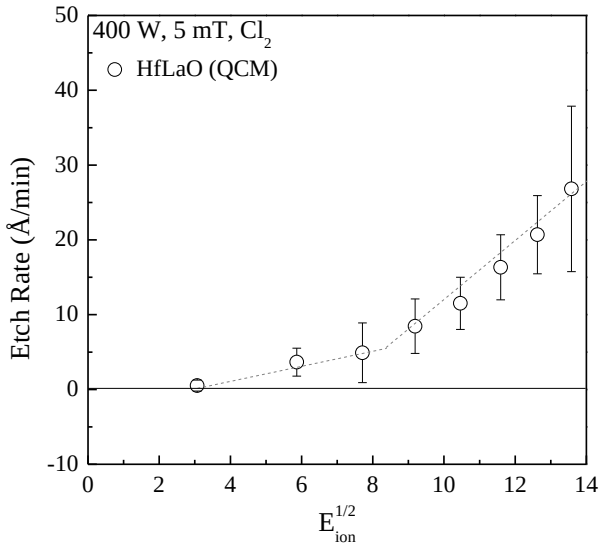

Figure 3.4 Etch rates of $Hf_{0.25}La_{0.12}O_{0.63}$(○) from in situ QCM data in a Cl_2, 400W, 5 mT plasma at various ion energies. The dashed line is provided to guide the eye and illustrate the dual ion energy dependence.

The calculated etch rates of the $Hf_{0.25}La_{0.12}O_{0.63}$ film varied from 3.7 to 26.9 Å/min for -25V to -175V bias voltage, respectively. Beyond the upper limit of that bias voltage range, instability in the plasma contributed to the larger fluctuation of the calculated etch rates. The etch rate of HfLaO exhibited the dual ion energy dependence found in experiments conducted on HfO_2, Al_2O_3 and HfAlO, which was discussed by Martin and Chang. (Martin, Blom et al. 2009) It was postulated that at low ion energies, etching is primarily due to ion-enhanced formation of volatile reaction products (ion mixing effects), while at higher ion energies etching is dominated by the ion-assisted desorption of non-volatile etch products, leading to a marked increase in etch rate. The threshold energy (E_{th}) at which etching begins is related to the strength of the metal-

oxygen bonds in the material, while the transition energy (E_{tr}) at which the change in etching regimes occurs describes the energy requirement for chemical reactions.

For comparison, QCM measurements on pure La_2O_3 were performed at the same plasma baseline. The frequency response data is shown in Figure 3.5.

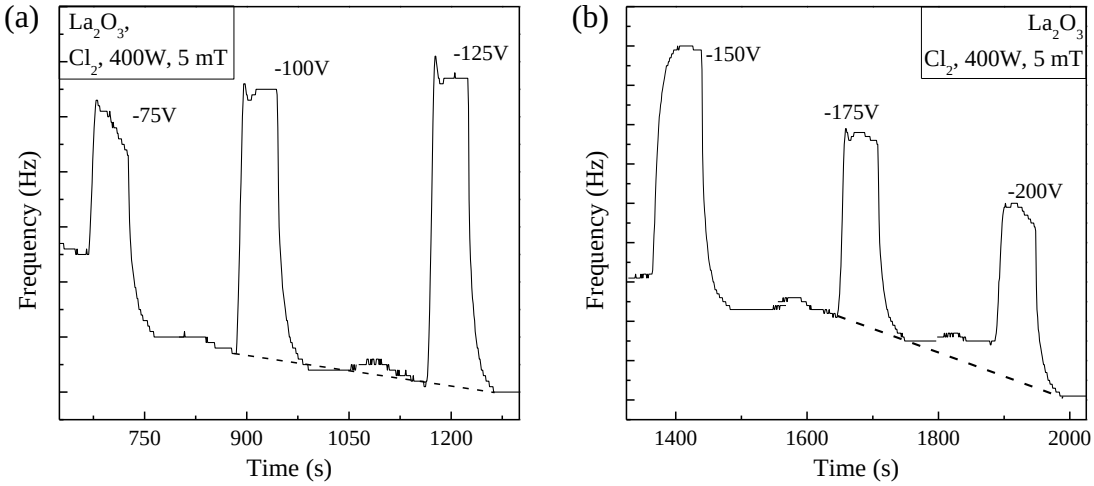

Figure 3.5 Frequency response curves for La_2O_3 in a 400W, 5 mT Cl_2 plasma at (a) -75, -100 V and -125 V and (b) -150, -175, and -200 V. Dashed lines are provided to guide the eye and illustrate the decrease in baseline frequency.

It is evident that there are several differences between the QCM frequency response data during the etching ofLa_2O_3 versus HfLaO. At -75 V bias the initial sharp frequency increase is followed almost immediately by a gradual *decrease* in frequency rather than a gradual increase or plateau. As the applied bias is made more negative through -100 V the curve shape changes, with the frequency saturating after the initial increase rather than slowly decreasing. A similar curve shape is observed at -125 V. At -150 V the curve takes on the form seen in the case of HfLaO, however as the bias voltage is made more negative past this point the shape reverts to the form observed earlier at -75 V. These observations could reflect transitions in the equilibrium of the interaction between La_2O_3 and the impinging species from the Cl_2 plasma, with deposition

dominating at lower ion energies and a shift towards etching occurring between 100 and 150 eV. As a result, calculating the etch rate from the QCM frequency response for pure La_2O_3 was made increasingly complicated, owing to the difficulty in defining the regions of the curve in a manner similar to that for HfLaO. A magnified view of the -100 V response curve for La_2O_3 etching at the Cl_2 baseline condition (400 W, 5 mT) is illustrated in Figure 3.6 so that the methodology can be discussed.

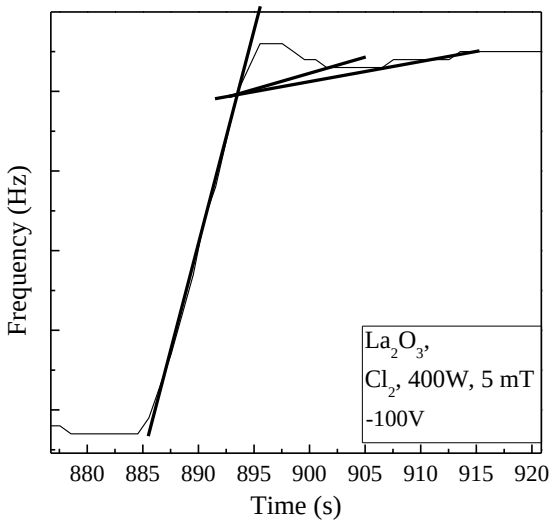

Figure 3.6 Magnified view of the etching region of the -100 V bias response curve for the La_2O_3 coated QCM crystal exposed to Cl_2 plasma at 400 W, 5 mT.

When calculating the weighted average of the frequency increases observed upon application of the bias, the irregular region near the top of the curve is avoided. Instead, when a linear fit of the initial steep increase begins to deviate from the curve, another line is fitted to the point of saturation. However, as shown in Figure 3.6, determining the onset of saturation is subjective, especially when the frequency change is close to the margin of error of the QCM monitor (~1-2 Hz). As an example, for the two lines plotted in Figure 3.6, the calculated etch rate varied from 15.4 to 19.3 Å/min, a ~25% change. When attempting to repeat this process care was taken to be

as consistent as possible, but due to the unique nature of each response curve some form of calculation error should be expected.

Another notable feature is that the baseline frequency of the response curves for La_2O_3 was observed to decrease, which did not occur in the case of HfLaO. are significantly shown in Figure 3.9 with the entire frequency response curve for the La_2O_3-coated QCM crystal exposed to the Cl_2 baseline condition at -100 V bias. It can be seen that the final frequency of this curve lies below the initial value, a phenomenon not seen for the case of HfLaO etching.

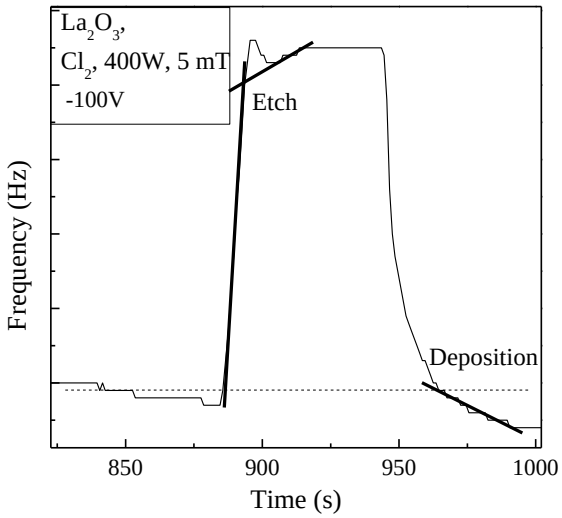

Figure 3.7 The -100 V bias response curve for the La_2O_3 coated QCM crystal exposed to Cl_2 plasma at 400 W, 5 mT, showing the etching and deposition regions.

The frequency decrease in general can be divided into two regions (somewhat analogous to the frequency increase of the curve). As the sharp decrease upon switching off the bias and plasma is seen for all material systems, and given that this was not taken into account when calculating the etch rate of HfLaO (which was supported by agreement with ex situ measurements), that portion of the curve was not examined. Instead, focus was placed on the lower section of the curve (marked by a solid line in Figure 3.8) that was found to typically begin

around the initial frequency value. Assuming that the sharp decrease is due to afterglow effects, this region could be considered as an area where either deposition reactions dominate or a non-volatile layer is formed due to reaction with low energy species. For the case of pure La_2O_3, non-volatile $LaCl_3$ or $La_xO_yCl_z$ could be a potential candidate for such a reaction product. Using the same equation for mass change and the mass density of $LaCl_3$ (3.84 g/cm^3), a deposition rate for this region can be obtained. The etch rates of the La_2O_3 film before and after subtraction of the calculated deposition rates are shown in Figure 3.8. Dashed lines are provided to guide the eye. It should be noted that only one La_2O_3 coated QCM crystal was available and thus error bars could not be calculated for the etch rate of this material.

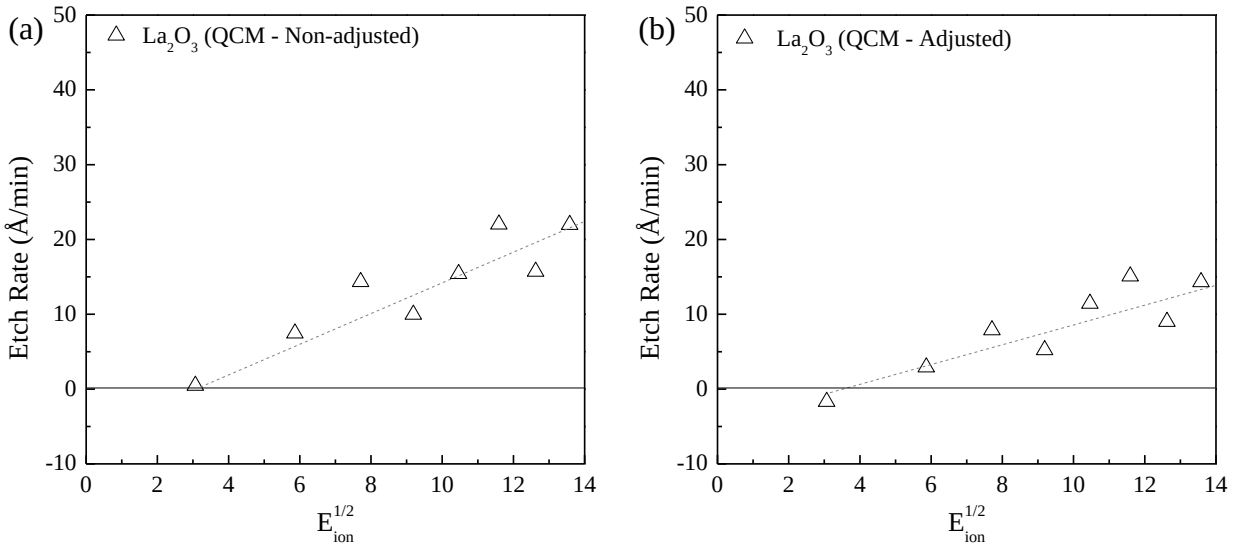

Figure 3.8 (a) Unadjusted and (b) adjusted etch rate of La_2O_3 by QCM (Δ) in a Cl_2, 400W, 5 mT plasma. Dashed lines are provided to guide the eye.

It can be seen that there is a noticeable difference when the etch rates are adjusted, with the maximum etch rate (at -175 V bias voltage) dropping from 22 to 14 Å/min. The main difference between the results for La_2O_3 and HfLaO is that the La_2O_3 curve does not appear to

exhibit the dual ion energy dependence, i.e. the etch rate does not substantially increase at higher ion energy values (E_{ion} > 100 eV). In the case of the $Hf_{0.25}La_{0.12}O_{0.63}$ film, it is probable that the film behavior would follow the characteristics of the dominant material (i.e. the film would behave in a manner more similar to HfO_2 than La_2O_3). The pure La_2O_3 film shows a linear dependence, possibly indicating that the etching of this material primarily follows a physical sputtering process.

3.3 Comparison with Etch Rate of HfLaO/La_2O_3 in BCl_3 Chemistry

The QCM frequency response data for HfLaO and La_2O_3 at the BCl_3 baseline condition exhibited similar characteristics to the case of La_2O_3 etching in Cl_2. Thus, the method of adjustment was used for these frequency response spectra. It was noted that the calculated rates of the deposition region for the QCM response curves of La_2O_3 in BCl_3 were significantly higher than those for La_2O_3 in Cl_2. The rate of deposition for HfLaO in BCl_3 was comparable to that of La_2O_3 in Cl_2. These rates are plotted in Figure 3.9.

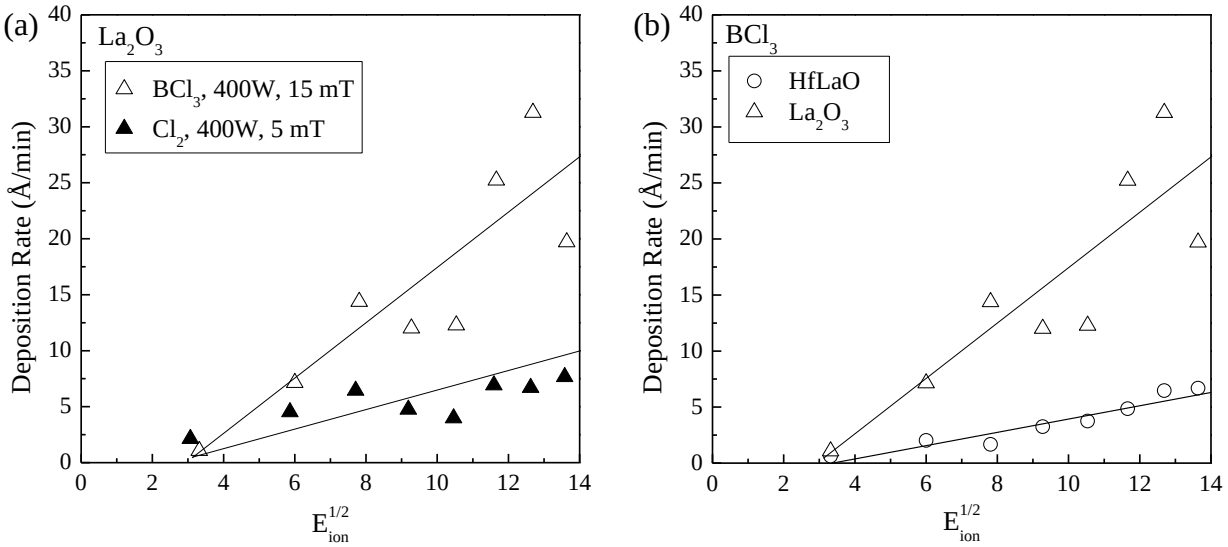

Figure 3.9 (a) The calculated rates from the deposition regions of the La_2O_3 QCM frequency response curves in Cl_2 and BCl_3 chemistry. (b) The corresponding rates for La_2O_3

From Figure 3.9 (a) it can be seen that for pure La_2O_3 the deposition rate in the case of both chemistries was observed to scale with ion energy. In the case of Cl_2 the dependence was not particularly strong, with the deposition rate staying relatively constant above 36 eV. However in the case of BCl_3 chemistry the rate showed a significant rise above 110 eV. Similar scaling of the deposition rate with ion energy was seen in the HfLaO composite film exposed to BCl_3, albeit at a much lower deposition rate. The relatively small fraction of La in the film compared to Hf could account for the lower rate. Thus, for BCl_3 chemistry where the energetic probability of forming $LaCl_3$ is much higher than in Cl_2 chemistry, the corresponding reduction in etch rate could be expected to be significantly greater.

The calculated etch rates are shown in Figure 3.10 (b), with the Cl_2 etch rates shown in (a) for comparison. Error bars could not be calculated for La_2O_3 etching in BCl_3 for the reason mentioned in the preceding paragraph. For the case of HfLaO in BCl_3, only four data points were

obtained for one of the crystals tested, thus only allowing four error bars to be plotted - in Figure 3.10 (b) the error bar for E_{ion} = 111 eV is very small, and the E_{ion} = 211 eV measurement suffered from plasma instability (this also occurred in Cl_2 chemistry) and was thus not plotted.

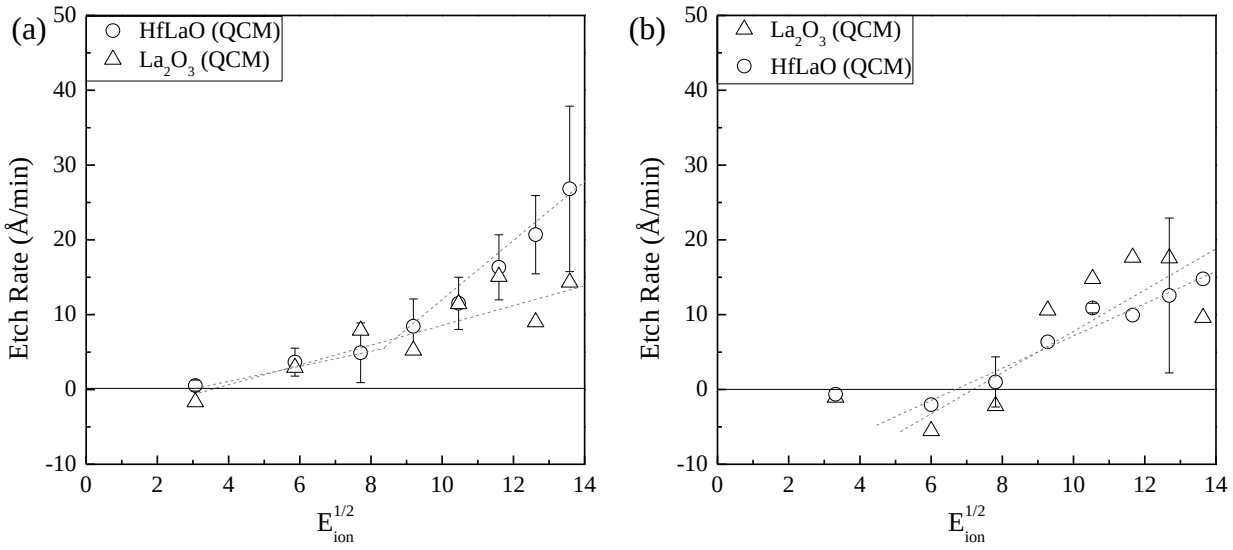

Figure 3.10 The etch rate of La_2O_3 (Δ) and $Hf_{0.25}La_{0.12}O_{0.63}$ (○) measured by QCM in (a) 400W, 5 mT, Cl_2 plasma and (b) 400W, 15 mT BCl_3 plasma. Dashed lines are provided to guide the eye.

BCl_3 chemistry is known to facilitate oxide etching through the shift to a heavier dominant ionic specie (BCl_2^+), as well as the removal of oxygen through the formation of $BOCl_x$ type compounds. However, no enhancement of the etch rate is seen for either HfLaO or La_2O_3 - the etch rate of HfLaO in BCl_3 is actually lower than the case of Cl_2 and the etch rate of La_2O_3 is comparable between the two chemistries. This indicates that the reactions of HfO_2 and La_2O_3 in BCl_3 chemistry must be considered.

Table 3-2 shows thermodynamic parameters related to the etching of the constituent oxides HfO_2 and La_2O_3, e.g. the metal-oxygen bond strength, volatility of the metal halide products, and heat of formation of potential reactions, taken from the CRC Handbook of

Chemistry and Physics, 92nd Edition. (Haynes 2011) From the heat of formation calculations, the condensed (solid) states of the metal chlorides were used owing to the fact that information was not available for the gas phase form of $LaCl_3$ in any reference source. While information for $HfCl_4$(g) was available from other references (e.g. the NIST-JANAF thermodynamic database), an effort was made to keep the calculations as consistent as possible by limiting the data to a single source.

Table 3-2 Comparison of thermodynamic properties for oxides and chlorides of Hf and La

Oxide	Bond	Bond Strength (kJ/mol)	Etch Product	Sublimation Point (°C)
HfO_2	Hf-O Hf-Cl	801.7 497.2	$HfCl_4$	318
La_2O_3	La-O La-Cl	798.0 521.6	$LaCl_3$	1150

Reaction Equation	ΔH_f (kJ/mol)
$HfO_2(c)+3Cl_2(g)\rightarrow HfCl_4(c)+2ClO(g)$	357.9
$HfO_2(c)+6Cl(g)\rightarrow HfCl_4(c)+2ClO(g)$	-369.9
$HfO_2(c)+2BCl_3(g)\rightarrow HfCl_4(c)+\frac{2}{3}(BOCl)_3(g)$	-144.7
$La_2O_3(c)+\frac{9}{2}Cl_2(g)\rightarrow 2LaCl_3(c)+3ClO(g)$	-45.3
$La_2O_3(c)+9Cl(g)\rightarrow 2LaCl_3(c)+3ClO(g)$	-1137.0
$La_2O_3(c)+3BCl_3(g)\rightarrow 2LaCl_3(c)+(BOCl)_3(g)$	-799.1

From the table, it is evident that the energy required to break the La-O bond is almost identical to that of Hf-O, while the energies of formation for La-Cl and Hf-Cl vary by ~25 kJ/mol. Considering the stoichiometry of both oxides and their chlorinated etch products, it could be predicted that forming $HfCl_4$ from HfO_2 would require less energy than forming $LaCl_3$ from La_2O_3. However, the heat of formation for the reaction of La_2O_3 with Cl_2(g) to form $LaCl_3$(c) suggests an exothermic process whereas the analogous reaction to form $HfCl_4$(c) is endothermic. Similarly, the reaction of La_2O_3 with molecular Cl is significantly more exothermic than that of HfO_2. The exothermic nature of the reactions indicate a higher probability of formation of $LaCl_3$

compared to $HfCl_4$. Given that the relative sublimation points for each chlorinated product indicate that $LaCl_3$ is a highly stable product compared to $HfCl_4$, the increased formation of $LaCl_3$ could potentially result in a lower etch rate due to the lower rate of removal of this material to the gas phase.

3.4 Comparison with Ex-Situ Measurements

As a means of verifying the *in situ* QCM measurements, the etch rate data was compared to *ex situ* measurements performed using SEM. Additionally, data for the etch rate of HfO_2 from a previously conducted etch study in an ECR reactor was considered. However, owing to the difference in the experimental setups, it was important to consider any differences between the reactor baseline conditions. A summary of the Cl_2 baseline conditions for the ECR and ICP systems is shown in Table 3-3, while the BCl_3 baseline conditions are shown in Table 3-4.

Table 3-3 Comparison of Cl_2 baseline conditions for the ECR reactor used by Martin and the ICP reactor used in this study.

Cl_2	ECR	ICP	
		Upper	Lower
Power (W)	500	400	--
Pressure (mT)	3	5	0.05 - 0.1
Ion Flux (cm^{-2} s^{-1})	1.1×10^{16}	6.9×10^{16}	$(3.5 - 5.0) \times 10^{15}$
Neutral Flux(cm^{-2} s^{-1})	5.4×10^{17}	1.6×10^{18}	$(1.6 - 3.2) \times 10^{16}$
T_e (eV)	2.63	4.17	--

Table 3-4 Comparison of BCl_3 baseline conditions for the ECR reactor used by Martin and the ICP reactor used in this study.

Cl_2	ECR	ICP	
		Upper	Lower
Power (W)	500	400	--
Pressure (mT)	3	15	0.15 - 0.30
Ion Flux (cm^{-2} s^{-1})	6.9×10^{15}	4.32×10^{16}	4.32×10^{15}
Neutral Flux(cm^{-2} s^{-1})	5.2×10^{17}	1.6×10^{18}	$(1.6 - 3.2) \times 10^{16}$
T_e (eV)	2.63	3.85	--

Figure 3.11 shows the *in situ* QCM measurements for the etching of HfLaO and La_2O_3 in plotted alongside *ex situ* measurements from the ICP and ECR Cl_2 and BCl_3 baselines described in Tables 3-3 and 3-4.

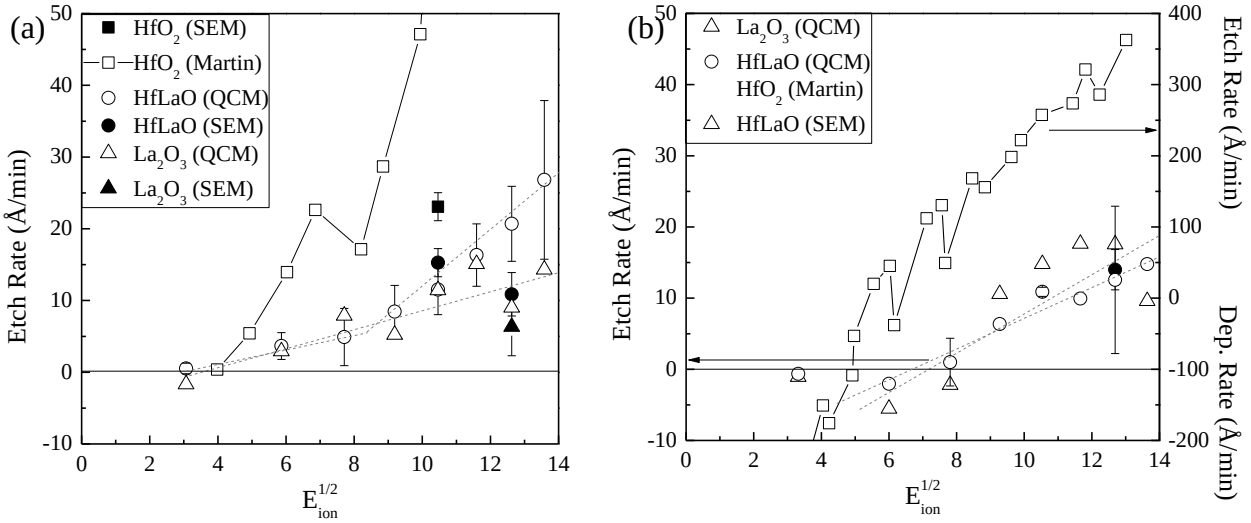

Figure 3.11 The etch rate of $Hf_{0.25}La_{0.12}O_{0.63}$ (○) and La_2O_3 (Δ) measured by QCM in 400W, 5 mT, Cl_2 plasma and (b) 400W, 15 mT BCl_3 plasma. The rates are compared to ex-situ measurements for La_2O_3 (▲ = ICP), $Hf_{0.25}La_{0.12}O_{0.63}$ (● = ICP) and HfO_2 (■ = ICP, □ = ECR). Dashed lines are provided to guide the eye.

It was observed that the etch rate of the $Hf_{0.25}La_{0.12}O_{0.63}$ film as measured by the QCM fell within the range established by the ex-situ measurements, thus supporting the method of calculation. The etch rate of HfO_2 in this reactor at -100 V bias voltage via ex-situ measurement was found to be ~23 Å/min. This value was found to be approximately half of the rate reported

by Martin and Chang (Martin, Blom et al. 2009). It was established in Table 3-2 that the lower boundary of the ion flux estimate for the ICP reactor was approximately half that of the ECR system, which could account for the difference in the etch rates.

For BCl_3 chemistry, the difference is much more pronounced, leading to the ECR data (□) being plotted on a separate axis. First, the differences in reactor baseline conditions are considered. Evidence has been provided in literature to show that in BCl_3-containing ICP plasmas the electron temperature and ion density can decrease by up to 28.6% and 50% respectively as the pressure varies from 3 to 15 mTorr. (Malyshev, Donnelly et al. 2000) According to the equation provided earlier, the aforementioned reductions can lead to the ion flux being diminished by a factor of 4. For a BCl_3 plasma at 300 W, 30 mT, Langmuir Probe measurements in the upper portion of the ICP chamber gave values for T_e and n_i of 3.85 eV and 2.02 x 10^{11} cm^{-3} respectively, which correlates to an ion flux of 4.32 x 10^{16} cm^{-2} s^{-1} (assuming BCl_2^+ is the dominant ionic specie). However, given the general trend of T_e and n_i increasing as the pressure decreases, the values at the actual ICP operating condition of 400W, 15 mT could be larger than the value calculated here. As such, this calculated value is a low end estimate. Assuming the same loss of ion flux through the grid for BCl_2^+ compared to Cl_2^+, the estimated value of 3.1 x 10^{15} cm^{-2} s^{-1} is approximately half that of the BCl_3 baseline condition for the ECR reactor (6.9 x 10^{15} cm^{-2} s^{-1}). However, as the relative rate reduction of HfLaO and La_2O_3 is significantly greater than a factor of two, this reinforces the hypothesis that the chemical reactions of La_2O_3 in Cl-based chemistries play the largest role. In the following sections the chemical reaction products and surface composition of the films are examined through QMS and XPS results, in order to elucidate the observed etch behavior and confirm this hypothesis.

3.5 Etch Products of La_2O_3 in Cl_2 and BCl_3Plasmas

As the reaction products of HfO_2 in Cl_2/BCl_3 plasmas were previously documented by Martin (Martin and Chang 2009), the etch products formed from the reaction of lanthanum with these chemistries were of particular interest. To collect the data, larger wafer pieces (area ~ 20 cm^2) consisting of ~1000-2000 Å La_2O_3 on Si(100) were placed in the upper section of the ICP chamber where the QMS chamber was mounted. In attempting to draw comparisons between the QMS data and the QCM etch rate measurements, it should be noted that the QCM etch rate measurements were performed in the lower section of the chamber, which experienced a significant (approximately one order of magnitude) reduction in ion flux through losses to the grounded extraction grid. Sample spectra for the etching of La_2O_3 at the Cl_2 and BCl_3 baseline conditions using a bias voltage of -100V are shown in Figure 3.12.

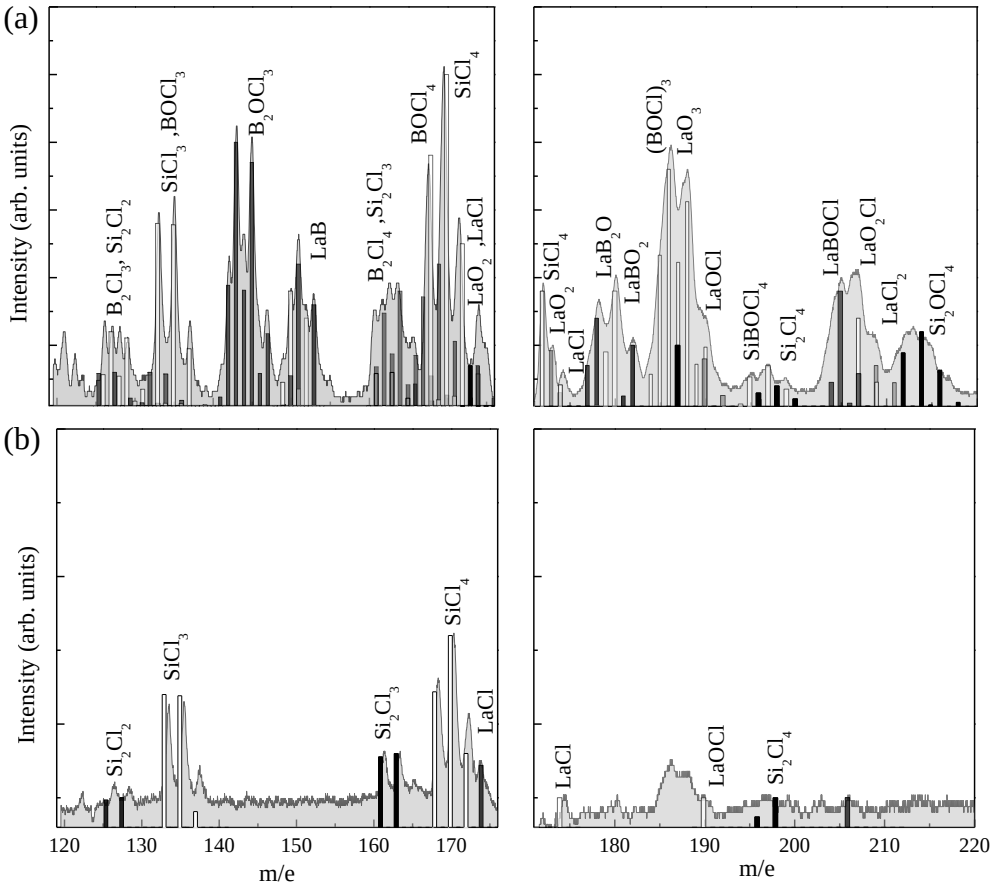

Figure 3.12 QMS spectra from etching of La_2O_3 films deposited on Si(100) wafer pieces in (a) BCl_3, 400W, 15mT, -100V bias and (b) Cl_2, 400W, 5mT, -100V bias. Isotope cracking patterns are overlaid as bar graphs to show identification of etch products.

Spectra obtained at the BCl_3 baseline condition possessed a higher signal to noise ratio and were first used to identify etch products containing lanthanum and boron, listed by ascending mass to charge ratio in Table 3-5. B_2OCl_3 and $(BOCl)_3$ were also confirmed as the most prominent sources of oxygen removal via reaction with BCl_x species. Si-containing etch products were observed in distributions consistent with those observed by Sha and Chang from the reaction of the BCl_3 plasma with the SiO_2 (quartz) chamber liners. (Sha and Chang 2003) The

most abundant La-containing species in BCl_3 plasma were determined to be LaB, LaB_2O, LaBOCl and LaO_2Cl (70.0, 64.2, 72.6 and 57.8% of the $SiCl_4$ quantity, respectively).

Table 3-5 Boron and lanthanum containing etch products observed during the etching of La_2O_3 in Cl_2 (5 mT) and BCl_3 (15 mT) plasma at 400W and -100V bias. The % value represents the species concentration normalized to that of $SiCl_4$ present in each plasma.

		Cl_2	BCl_3			Cl_2	BCl_3
Product	m/e	%	%	Product	m/e	%	%
B_2Cl_3	129	-	30.5	LaB	150	-	70.0
$BOCl_3$	134	-	12.1	LaO_2	171	-	15.4
B_2OCl_3	145	-	123.4	LaCl	174	24.6	15.6
B_2Cl_4	164	-	65.1	LaB_2O	177	-	64.2
$BOCl_4$	169	-	43.7	$LaBO_2$	182	-	20.6
$(BOCl)_3$	188	-	135.3	LaO_3	187	-	37.4
$SiBOCl_4$	197	-	42.7	LaOCl	191	6.2	30.6
				LaBOCl	202	-	72.6
				LaO_2Cl	207	-	57.8
				$LaCl_2$	210	-	29.3

At the Cl_2 baseline conditions, the La-containing etch products were LaCl, and LaOCl (24.6 and 6.2% of the $SiCl_4$ quantity, respectively). As in the BCl_3 condition, Si-containing species such as $SiCl_3$ and $SiCl_4$ were observed via QMS. Broadness in the peaks was attributed to residual BCl_3 species in the plasma. Figure 3.13 shows the distribution of etch products for each plasma.

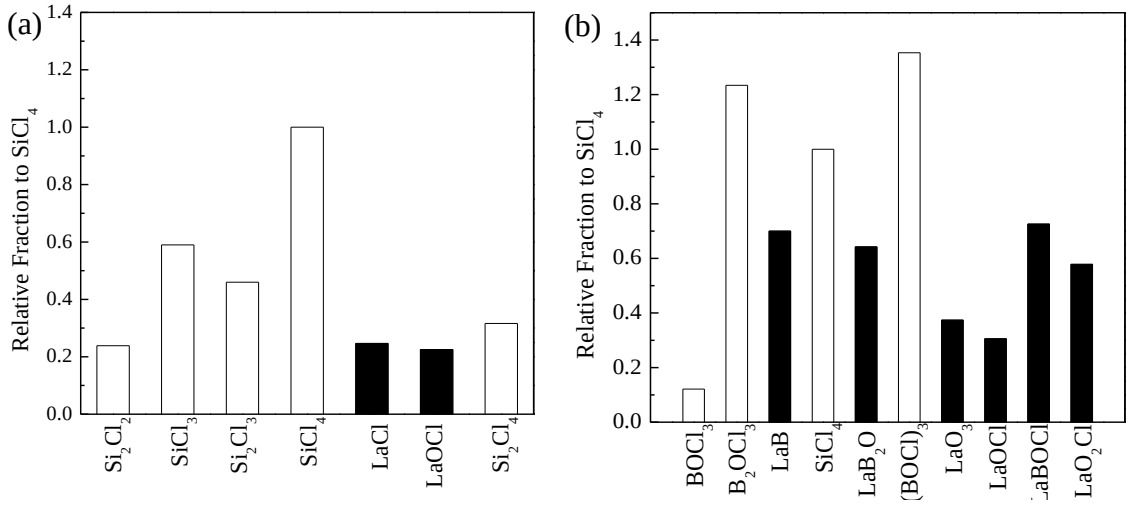

Figure 3.13 Bar graphs showing the distribution of La-containing etch products for etching of La_2O_3 in Cl_2 (left) and BCl_3 (right) plasmas at 400 W, 5 mT and 400 W, 15 mT respectively, with -100 V bias.

It was observed that La-containing etch products were more abundant in the case of BCl_3 chemistry compared to Cl_2. However as the etch rate of La_2O_3 was comparable between the two chemistries, one possibility that could be considered is whether the observed La containing species were removed from the surface through ion bombardment rather than spontaneously desorbed through a chemical reaction. In Section 3.2 it was observed that the rate of the deposition region in the QCM response curve for La_2O_3 exposed to BCl_3 was approximately twice as high at the considered ion energy as that of Cl_2. The substantial presence of B_2OCl_3 and $(BOCl)_3$ in the QMS spectra suggests that the mechanism of oxygen removal is not completely stifled in BCl_3 plasma, but is offset within the context of the QCM measurement (which only measures the frequency change) by the formation of non-volatile species such as $LaCl_3$.

QMS measurements on HfLaO composite films of two compositions ($Hf_{0.25}La_{0.12}O_{0.63}$ and $Hf_{0.11}La_{0.23}O_{0.66}$) were also performed to look for the presence of Hf-containing etch products. The results are shown in Figure 3.14. The peak at ~265 m/e in (a) was considered to be

a non-physical artifact caused by one of the electronics units, based on the dip in the baseline of that region which was also observed in (b). The range was selected based on the locations of $HfCl_2$ and $HfCl_3$, and the maximum m/e value (300) of this particular QMS system.

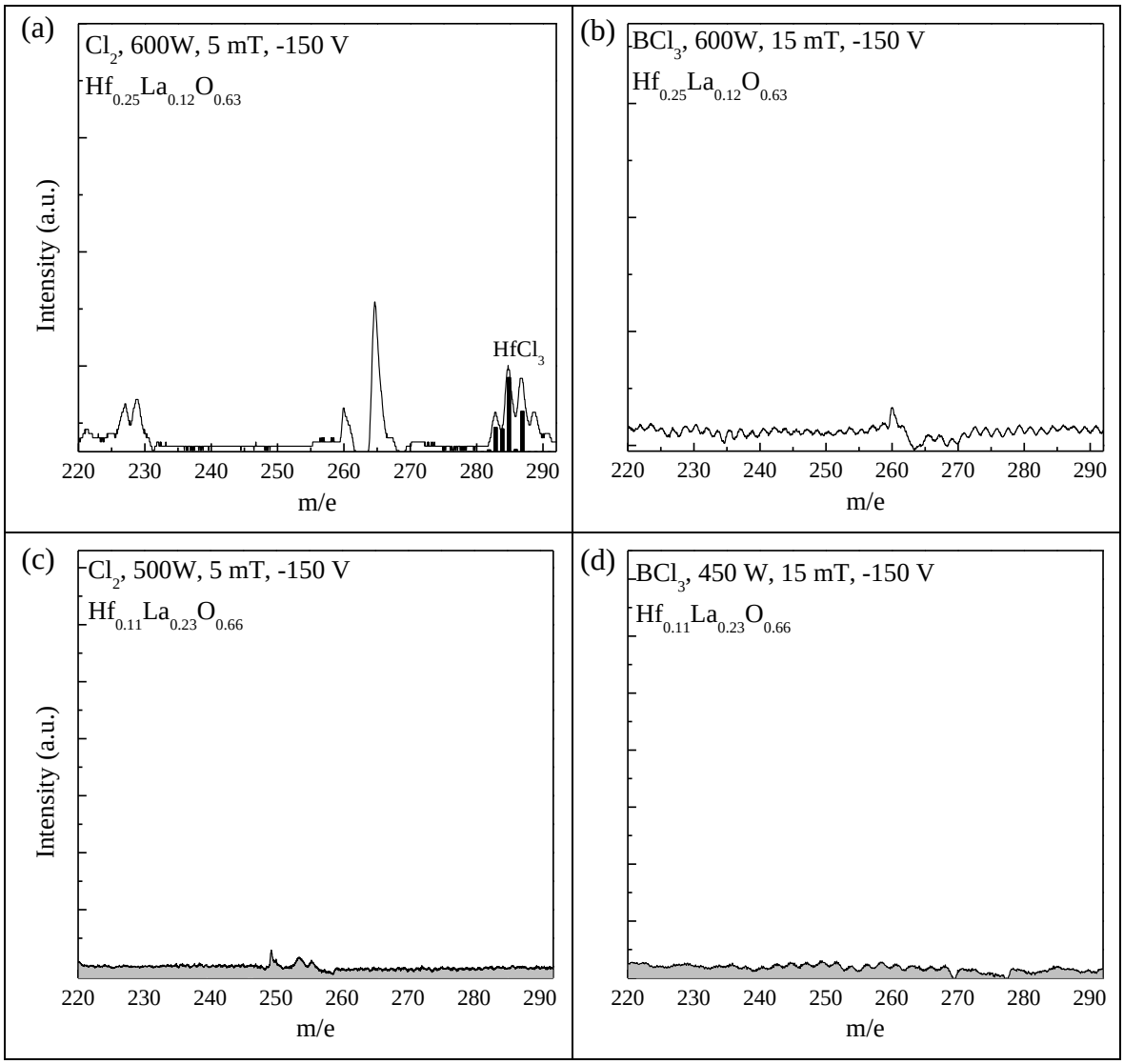

Figure 3.14 Top row shows QMS spectra of $Hf_{0.25}La_{0.12}O_{0.63}$ in (a) Cl_2, 600 W, 5 mT plasma and (b) BCl_3, 600 W, 15 mT plasma. Bottom row shows QMS spectra for $Hf_{0.11}La_{0.23}O_{0.66}$ in (a) Cl_2, 500 W, 5 mT plasma and (b) BCl_3, 450 W, 15 mT plasma. All spectra were taken at a bias voltage of -150 V.

It can be seen that for $Hf_{0.25}La_{0.12}O_{0.63}$, the presence of $HfCl_3$ was detected in the Cl_2 plasma, but not in BCl_3. This agrees with the higher etch rate observed for $Hf_{0.25}La_{0.12}O_{0.63}$ in Cl_2 chemistry compared to etching in BCl_3. It also possibly suggests that the reactions of BCl_3 with the La component of the film can affect the overall etch process. This observation is supported by the fact that neither the Cl_2 or BCl_3 QMS spectra for $Hf_{0.11}La_{0.23}O_{0.66}$ (La-rich composite) exhibited $HfCl_x$ etch products. For this reason it was important to investigate the surface composition of the La_2O_3 and HfLaO films after exposure to Cl_2 and BCl_3 plasmas by a technique such as x-ray photoelectron spectroscopy (XPS). The results of these measurements are detailed in the following section.

3.6 Surface Composition of $Hf_xLa_yO_z$ and La_2O_3 Post- Cl_2 /BCl_3 Exposure

Wafer pieces of the $Hf_{0.25}La_{0.12}O_{0.63}$ and La_2O_3 films (~1000 Å thick on Si(100) substrates) approximately 2 cm^2 in area were loaded into the lower section of the ICP chamber and exposed to the extracted plasma beam in a manner similar to the QCM array. The etch experiments were conducted at 400 W, 5 mT, and -100 V bias voltage for durations of 1 and 5 minutes in both Cl_2 and BCl_3 plasmas. Samples were then analyzed via ex-situ XPS at a takeoff angle of 90° to investigate the effects of plasma exposure. The XPS spectra for the Hf 4f, La 3d, O 1s and Cl 2p peaks of the unetched (○), 1 minute (●) and 5 minute (Δ) plasma exposed $Hf_{0.25}La_{0.12}O_{0.63}$ films are presented below in Figure 3.15 for Cl_2 (a) and BCl_3 (b) plasmas. The peak at 196 eV in the region scanned for Cl 2p spectra corresponds to La 4p. The FWHM of this peak was assessed for the unetched film and used to fit the etched spectra as well to provide an accurate measurement of the Cl 2p area.

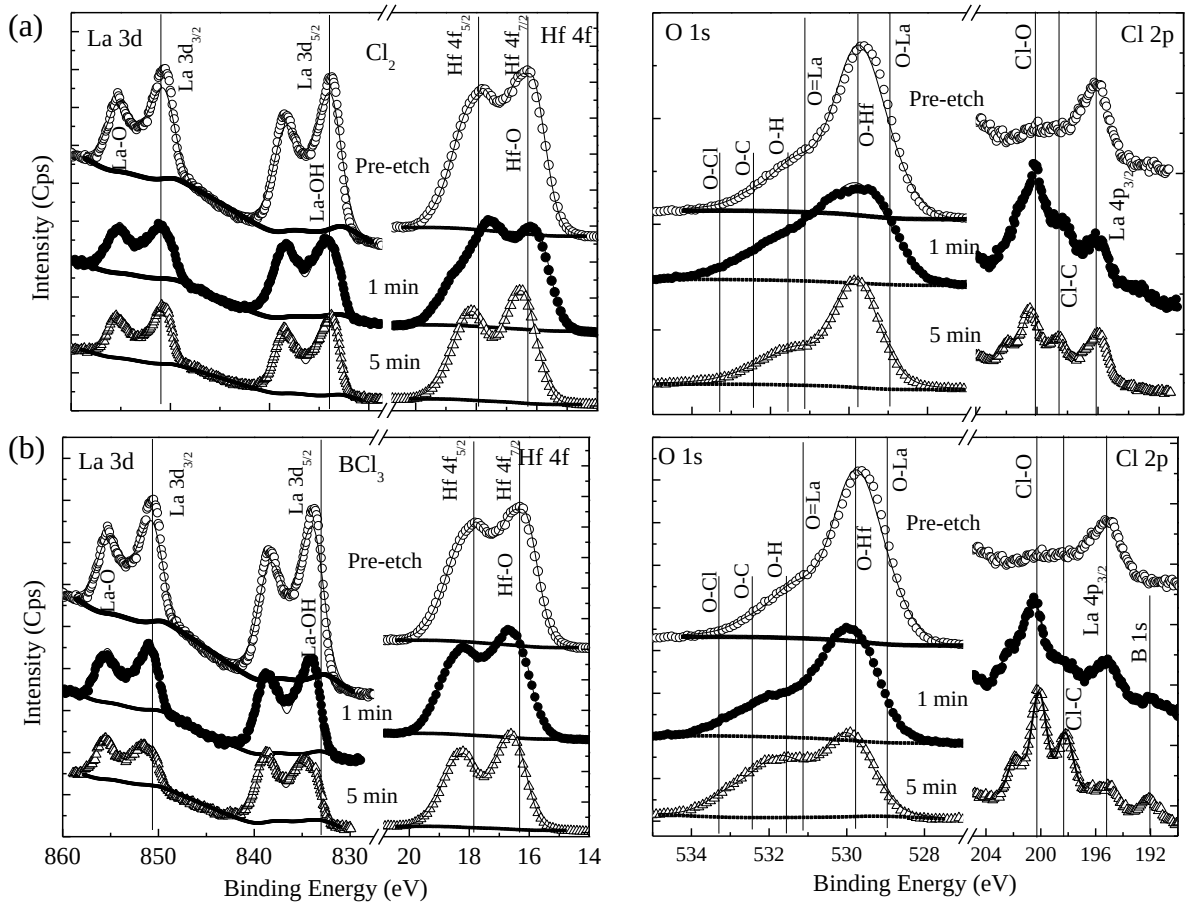

Figure 3.15 XPS spectra of the Hf 4f, La 3d, O 1s and Cl 2p peaks for unetched (○), 1 minute (●) and 5 minute (Δ) plasma exposed $Hf_{0.25}La_{0.12}O_{0.63}$ films at 400 W, 5 mT, and -100 V bias, for Cl_2 (a) and BCl_3 (b).

In order to better illustrate the specific chemical bonding changes as a result of plasma exposure, XPSPeak software was used to deconvolute the spectra. This process thus allowed more detailed information to be extracted beyond overall composition fractions. Due to the many peaks that had to be assigned in the case of oxygen, Figure 3.16 shows the specific deconvolution of the O 1s region to better illustrate the bonding changes. The same peak location values that were assigned in Figure 2.4 of Chapter 2 were used to align the bonding states in these spectra.

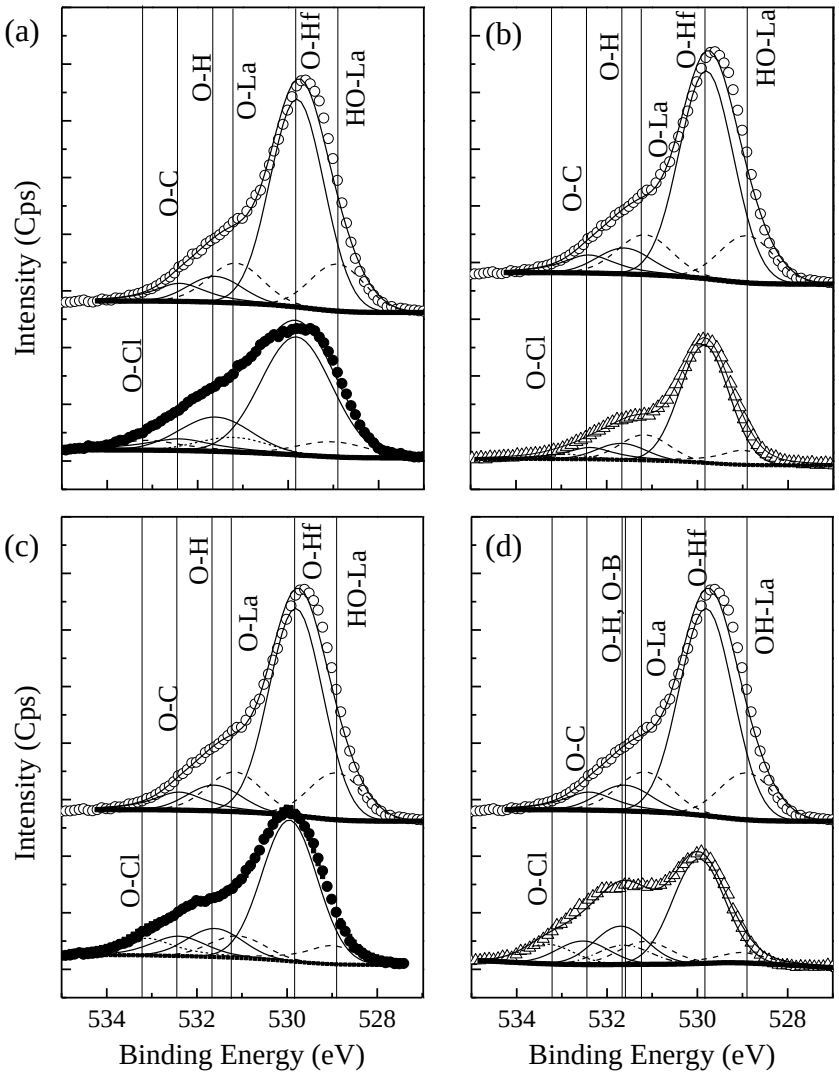

Figure 3.16 Deconvoluted O 1s XPS spectra for Cl_2 etching of $Hf_{0.25}La_{0.12}O_{0.63}$ at 400 W, 5 mT, and -100V bias for (a) 1 min and (b) 5 min. The corresponding spectra for samples exposed to BCl_3 are shown in (c) and (d).

As noted previously in Chapter 2, while hydrogen is not directly observable via XPS, its bonding to other elements (such as O) can be assigned due to differences in electronegativity betwen H and other elements (such as Hf, La and C). In this case the O-H peak as labeled represents a hydroxylated surface or dangling bonds caused by the rupturing of M-O. Dividing the raw area of each bond peak by the ASF values presented in Chapter 2 and then dividing by the sum of all regions yielded the normalized atomic compositions as presented in Figure 3.17.

For the different components of the O 1s spectra, the values were normalized by dividing by the total fraction of oxygen present in the film.

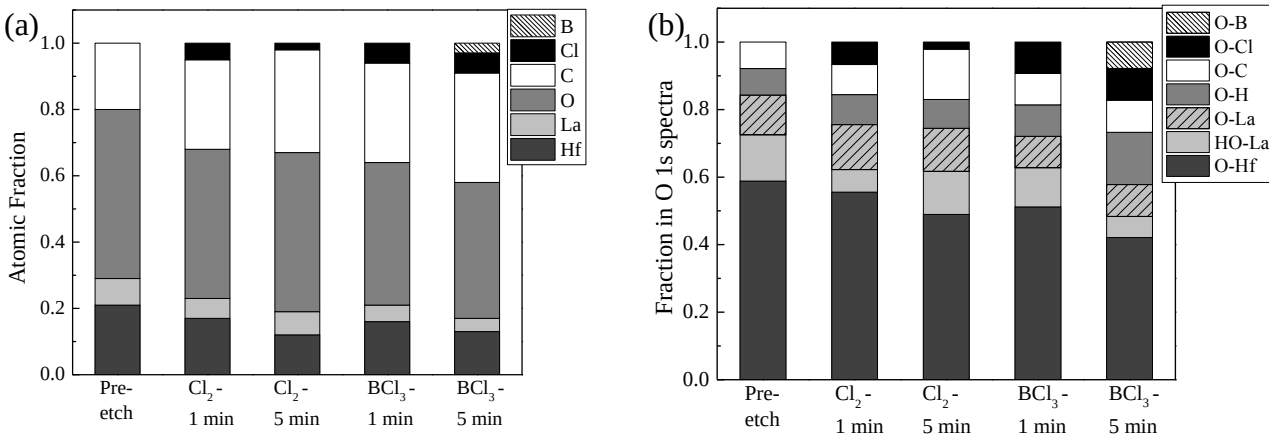

Figure 3.17 (a) Change in overall surface composition of $Hf_{0.25}La_{0.12}O_{0.63}$ films etched in Cl_2 and BCl_3 plasmas at 400 W, 5mT, -100 V bias for 1 and 5 minutes. (b) Change in bonding fractions of the O 1s spectra.

After 1 minute plasma exposure in Cl_2 and BCl_3 the fraction of La in the analyzed surface layer was reduced from 0.08 to 0.06 and 0.05, while the fractionof Hf decreased from 0.21 to 0.17 and 0.16. Consequently, the ratio of La/Hf decreased in both chemistries from an initial value of 0.38, however the decrease was observed to be more significant in BCl_3 chemistry (0.31) compared to Cl_2 (0.35). A higher proportion of Hf in the film indicates more La_2O_3 is removed compared to HfO_2. Given the reduced rate of etching of La_2O_3 vs. HfO_2 in both chemistries, this could account for the etch rate reduction of HfLaO compared to HfO_2. The percentage of oxygen after etching was reduced in both cases, with the total remnant metal to oxygen ratio being similar for BCl_3 and Cl_2 after 1 minute of exposure. This observation is somewhat inconsistent with evidence in the literature that the addition of boron from BCl_3 plasmas facilitates reactions producing $BOCl_x$ species (namely $(BOCl)_3$), which in turn results in heightened removal of oxygen compared to Cl_2 plasmas. However, the discrepancy can possibly

be explained by the lower calculated ion flux for the BCl_3 baseline condition in the ICP compared to that of the Cl_2 baseline. In both chemistries the reduction in oxygen was mainly attributed to a decrease in the proportion of M-O bonding, particularly that of La-O, which supports the theory that rupturing the metal-oxygen bond is the first step of the reaction process. The residual surface chlorination in both chemistries after one minute of plasma exposure was roughly equivalent (5~6%). An increase in carbon content on the surface of the post-etched films was deemed to be the result of enhanced surface reactivity promoting the absorption of ambient carbon. This effect was more pronounced after treatment in BCl_3 chemistry versus Cl_2.

Upon increasing the etch time to 5 minutes in both chemistries, the fraction of Hf present in the analyzed surface layer continued to decrease (to 0.12 and 0.13 for Cl_2 and BCl_3 respectively). By contrast, the La fraction of the film remained relatively constant (0.07 in the case of Cl_2, 0.04 in the case of BCl_3), resulting in a La/Hf ratio of 0.58 for Cl_2 chemistry and 0.31 for BCl_3 The higher value of this ratio for Cl_2 indicates more Hf is removed than La in Cl_2 chemistry and is consistent with the QMS spectra that indicate $HfCl_3$ is present in the Cl_2 etching of $Hf_{0.25}La_{0.12}O_{0.63}$ but not in BCl_3. While the decrease in the oxygen fraction for the BCl_3-exposed film was small (0.43 to 0.41), closer analysis of the O 1s spectra revealed decreases in M-O bonding offset by increases in O-C and O-H, as well as the presence of B-O bonding related to the appearance of the B 1s peak at 192 eV. In the case of the 5 minute Cl_2 exposure, the oxygen content was slightly higher than the sample exposed for 1 minute (0.48 to 0.45). However, the higher percentage of oxygen was largely a result of increased C-O bonding and did not correspond to an increase in Hf-O or La-O bonding. This could possibly be attributed to carbon contamination in the chamber. Also noted was a difference the trend of surface chlorination - a decrease was seen for Cl_2 chemistry, compared to an increase in the case of BCl_3.

Heightened surface reactivity could result in the loss of chlorine through reactions with water vapor and oxygen in ambient conditions. However as this was not observed for the sample treated in BCl_3, it is possible that the Cl present on the surface is bonded in non-volatile species, as postulated earlier when discussing the lower etch rate of HfLaO in BCl_3.

In Section 3.2 it was observed that La_2O_3 does not exhibit the dual ion energy dependence. It was thus postulated that the etching of La_2O_3 is largely based on a physical sputtering dependence. To investigate this phenomenon, etching of $Hf_{0.25}La_{0.12}O_{0.63}$ was performed in a 400 W, 15 mT Ar plasma at -100 V bias for 10 minutes (an environment where only sputtering reactions occur due to the inert nature of argon) and the results were compared to etching of $Hf_{0.25}La_{0.12}O_{0.63}$ at the ICP Cl_2 baseline condition for 5 minutes. The XPS spectra are shown in Figure 3.18.

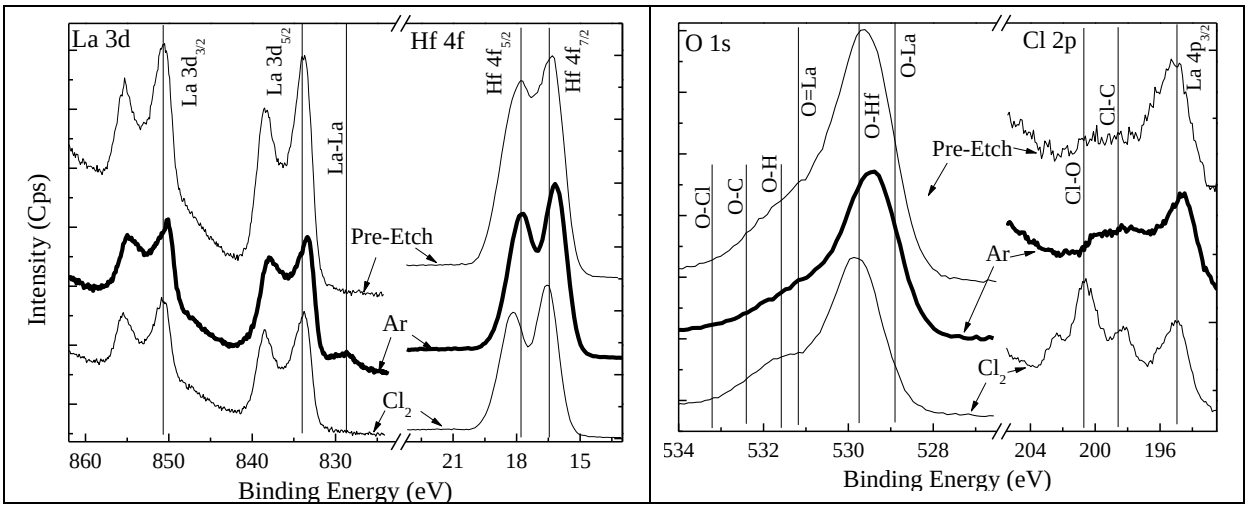

Figure 3.18 XPS spectra of (a) La 3d, Hf 4f, and (b) O 1s and Cl 2p for $Hf_{0.25}La_{0.12}O_{0.63}$ etched in a 400 W, 15 mT, Ar plasma at -100 V for 10 minutes, and a 400 W, 5 mT, Cl_2 plasma for -100 V for 5 minutes.

It was observed that in the La 3d region, a peak appeared at 828.8 eV after Ar sputtering that was not seen in the case of Cl_2 exposure. This peak was assigned to La-La, indicating that in

the Ar plasma the oxygen component of the film is preferentially removed. This phenomenon was not observed in the Hf 4f spectra. The compositional analysis is shown in Figure 3.19.

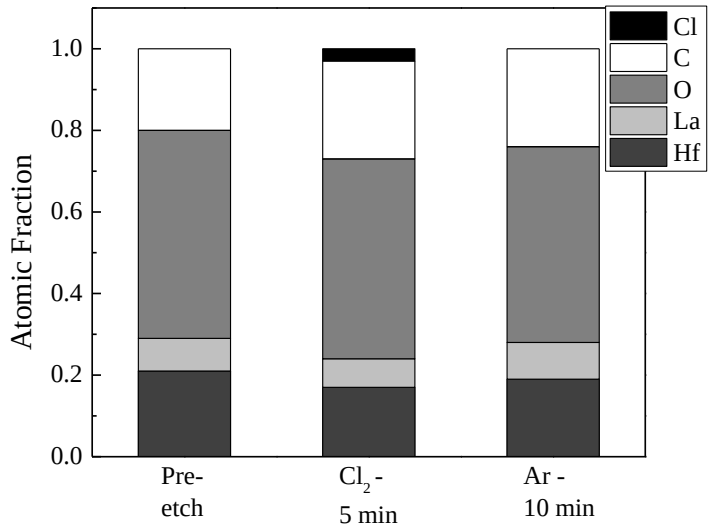

Figure 3.19 Atomic composition of $Hf_{0.25}La_{0.12}O_{0.63}$ before and after exposure to 400 W, 15 mT, Ar plasma at -100 V for 10 minutes, and a 400 W, 5 mT, Cl_2 plasma for -100 V for 5 minutes.

The La/Hf ratios of the films etched in Ar and Cl_2 were 0.47 and 0.41 respectively, while the ratios of metal to oxygen present after etching in Ar and Cl_2 were 0.60 and 0.48 respectively. The latter observation supports the theory for the preferential removal of oxygen (due to ease of sputtering) in the Ar plasma. In the Cl_2 plasma, the lower ratio indicates greater removal of the metal components of the film, suggesting that there is chemical etching involvement (compared to purely physical sputtering).

While XPS analysis of the HfLaO films provided evidence that supported the etch rate data, there was no major evidence for the formation of a $LaCl_x$-type layer on the surface. However the relatively low La content of the films could complicate such observations, as identifying peaks the overall change to the surface would not be as pronounced in the context of the larger Hf content. Thus, XPS analysis of pure La_2O_3 films exposed to 400W, 5 mT, Cl_2 and

BCl_3 plasmas for 5 minutes at -100 V bias was performed. The La 3d, O 1s and Cl 2p spectra are shown in Figure 3.20.

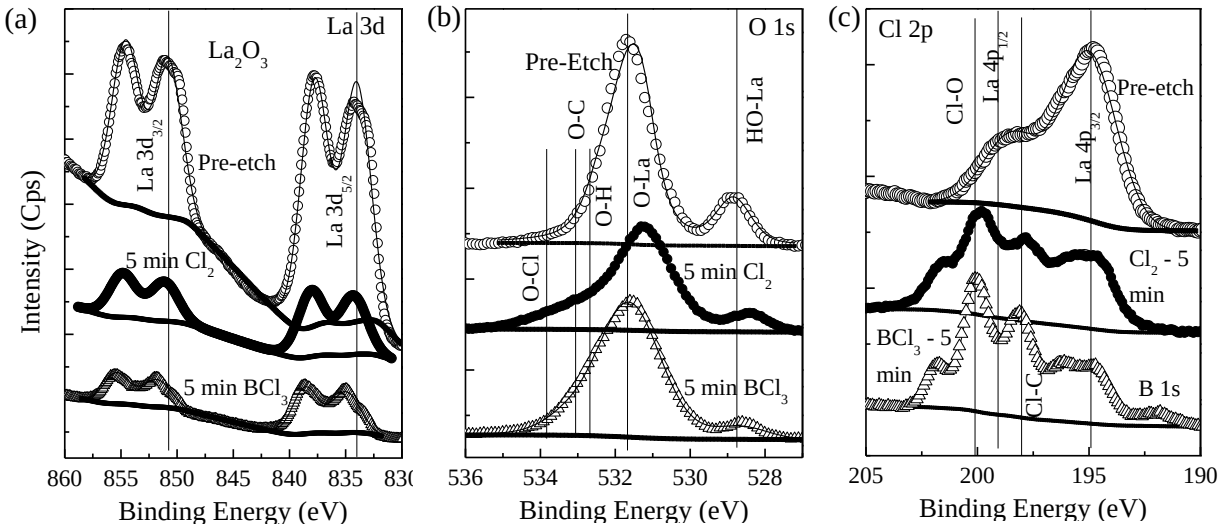

Figure 3.20 XPS spectra of the (a) La 3d, (b) O 1s and (c) Cl 2p peaks for unetched (○), Cl_2 (●) and BCl_3 (Δ) plasma exposed La_2O_3 films at 400 W, 5 mT, -100 V bias for 5 minutes.

From the spectra it can be seen that the most noticeable change is in the intensity of the La 3d peaks, which decreased noticeably for both etched samples. The La 4p peaks present in the Cl 2p binding energy region were also noted to decrease in intensity. It was observed that while the intensity of the O 1s peak decreased in both chemistries, the loss was higher in Cl_2 than BCl_3. In order to better illustrate the specific changes in the O 1s spectra, this region was plotted separately and magnified as shown in Figure 3.21.

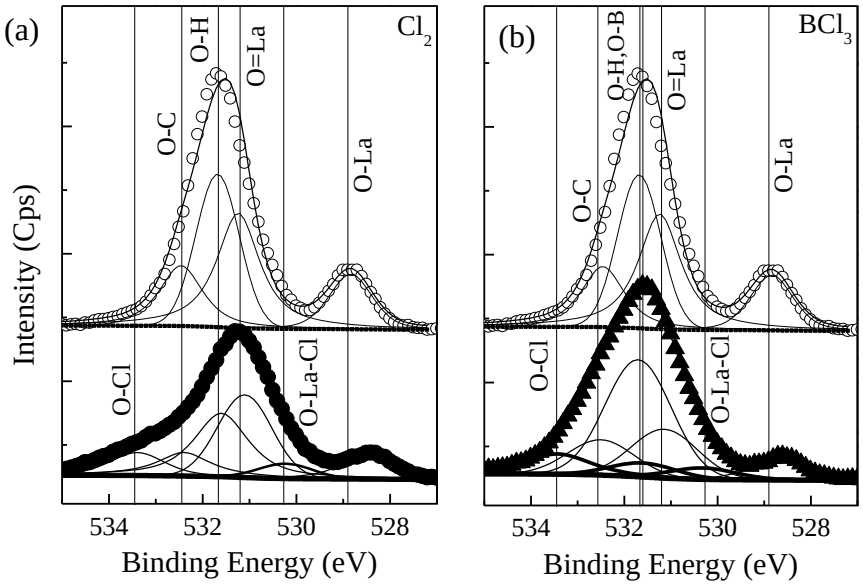

Figure 3.21 The magnified O 1s spectra for La_2O_3 films etched in (a) Cl_2 (●) and (b) BCl_3 chemistry (▲) at 400 W, 5 mT, -100 V for 5 minutes.

From Figure 3.16 it can be seen that there is significant broadening of the O 1s spectra between 533 and 534 eV, which was a result of the formation of O-Cl bonding. While the La-O and La=O peaks decreased in intensity, the relatively constant level of the signal between the two peaks was attributed to the formation of Cl-La-O bonding. This bonding assignment was present in several of the observed QMS products (e.g. LaOCl, LaO_2Cl, LaBOCl). Additionally, slight shifts towards lower binding energies were observed for both La-O peaks, indicating formation of bonds with a less electronegative element (Cl vs. O). A similar trend was observed in La 4p peaks present in the Cl 2p spectra, as shown in Figure 3.22.

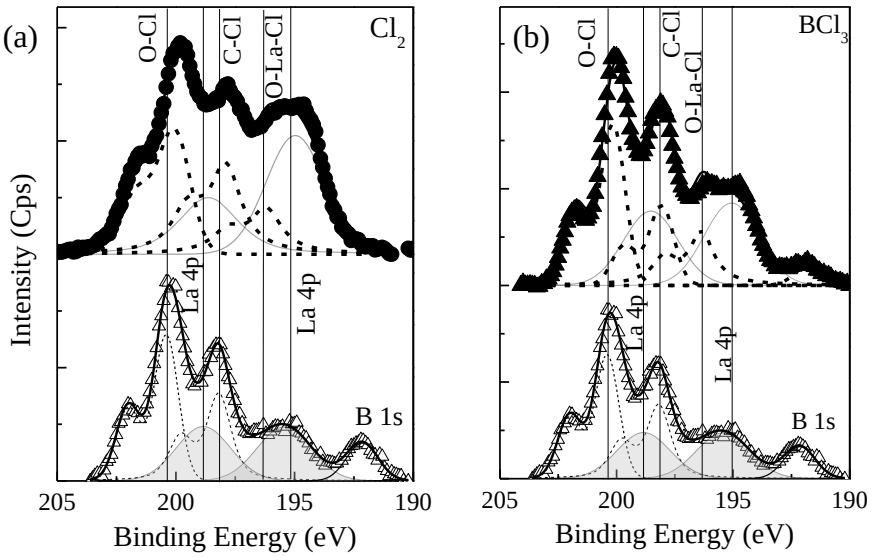

Figure 3.22 The magnified Cl 2pspectra for La_2O_3 films etched in (a) Cl_2 (●) and (b) BCl_3 chemistry (▲) at 400 W, 5 mT, -100 V for 5 minutes. The signal from BCl_3 etching of $Hf_{0.25}La_{0.12}O_{0.63}$ (Δ) is shown in comparison.

In these spectra the background was subtracted in order to make the comparison clearer. It can be seen that the presence of an intermediate state between the La 4p peaks is necessary to achieve a proper fit of the spectra. This peak was attributed to Cl-La-O at 196.3 eV. In the spectra of $Hf_{0.25}La_{0.12}O_{0.63}$ **(**Δ**)** etched in BCl_3 this peak was not observed, however it is possible that it exists but was not as apparent due to the comparatively low fraction of La present. This is consistent with the calculated lower rate of deposition in HfLaO films compared to La_2O_3 as shown in Section 3.3. The presence of Cl-O bonding at ~200.5 eV is also noted. The overall atomic composition and O bonding fractions of the pre- and post-etched films calculated from these spectra are shown in Figure 3.23.

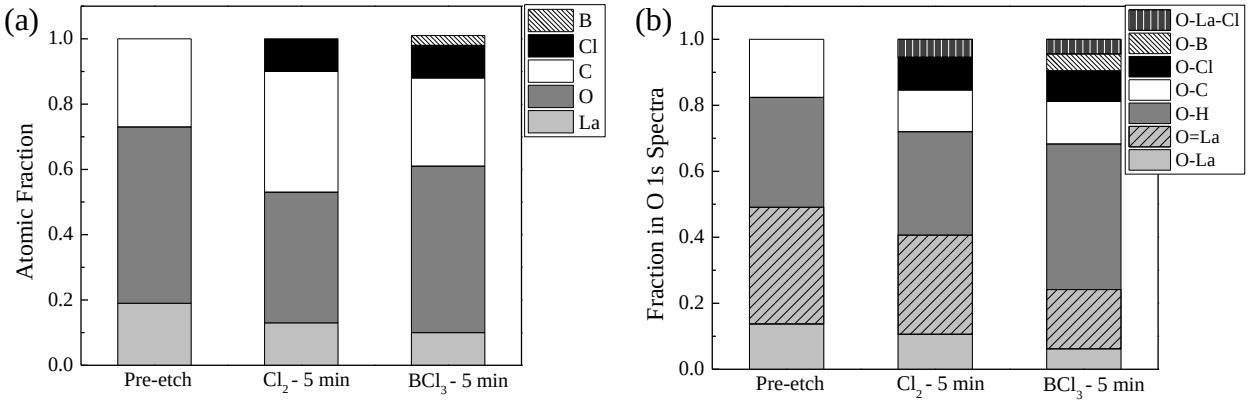

Figure 3.23 (a) Change in overall surface composition of La_2O_3 films etched in Cl_2 and BCl_3 plasmas at 400 W, 5mT, -100 V bias for 5 minutes. (b) Change in bonding fractions of the O 1s spectra.

For both chemistries it was observed that the overall surface chlorination present in the pure La_2O_3 films was substantially higher than that of the HfLaO composite films. It was reported in the literature that exposure of Cl_2-treated Si films to ambient conditions resulted in significant reduction of the percentage of Cl present (~3% compared to ~27% as measured *in situ*) (Layadi, Donnelly et al. 1997) Thus the high percentage of Cl present here could indicate its bonding in a non-volatile state. The decrease in the La fraction of the analyzed surface layer was about 32% for Cl_2 and 47% for BCl_3. In contrast, the percentage of oxygen was much lower in the Cl_2 etched film - 40% vs. 51%. As with the HfLaO films, investigation of the deconvoluted O 1s spectra for the BCl_3 exposed sample showed that this decrease was largely due to an increase in the peak assigned to O-H, while the La-O and La=O fractions decreased. This indicates that the rupturing of the La-O bond continues to occur in BCl_3 chemistry, but the reactive film surface after etching may experience increased uptake of O from ambient conditions, thus affecting the compositional analysis. For Cl_2 chemistry the level of carbon present was noticeably higher than that of BCl_3, which was not observed for the HfLaO composite films. However, the C-O fraction of both films were roughly the same in relation to the total oxygen content. The relative fraction

of the peak assigned to Cl-La-O was the same for both chemistries. While the calculated deposition rate at this bias voltage was significantly higher in BCl_3 chemistry than in Cl_2 (12.6 vs. 3.9 Å/min), the relatively similarity of the etch rates of La_2O_3 in Cl_2 and BCl_3 chemistry would suggest that the enhanced deposition is balanced by increased removal of material (as indicated by the more significant reduction of the La-O fractions in BCl_3 compared to Cl_2.

3.7 Summary and Analysis of $Hf_xLa_yO_z$ Etch Rate and Mechanisms

The addition of La_2O_3 to HfO_2 has the effect of significantly reducing the etch rate by approximately half at comparable ion flux levels in Cl_2 chemistry. This observation was attributed to the thermodynamic favorability of the formation of non-volatile $LaCl_3$ compared to $HfCl_4$, causing La_2O_3 to undergo preferential reaction over HfO_2 when the composite $Hf_xLa_yO_z$ film was exposed to Cl_2. The lower volatility of $LaCl_x$ products thus results in a lower etch rate in Cl_2 chemistry than that of pure HfO_2. In BCl_3 chemistry, the reaction to form $LaCl_3$ was substantially more exothermic than that in Cl_2, which was reinforced by the calculated deposition rates on pure La_2O_3 for both chemistries. In BCl_3 the deposition rate was found to scale with ion energy on both La_2O_3 and HfLaO films, however the rate was much lower on the composite films, probably due to the low fraction of La present. In Cl_2 chemistry the rate was found to scale with ion energy on pure La_2O_3 and was negligible on HfLaO, suggesting that while the mechanisms for enhanced etch rate associated with BCl_3 chemistry (namely the removal of oxygen through the formation of $(BOCl)_3$) were still present, this was offset by the increased rate of non-volatile product formation.

QMS measurements of pure La_2O_3 in BCl_3 chemistry confirmed the presence of $B_xO_yCl_z$ compounds for oxygen removal, while also showing larger quantities of La-containing products in the case of BCl_3 compared to Cl_2. However, as the QMS measurements were done in the upper section of the reactor, the effect of ion to neutral flux ratios should be considered as this condition would be different in the lower chamber where the QCM was situated. Another possibility considered was the sputtering of the La-containing species from the surface as opposed to their spontaneous desorption. XPS analysis of pure La_2O_3 films supported this hypothesis, showing significant Cl retention (~10%) compared to HfLaO and also revealing the presence of Cl-O-La bonding for both chemistries.

CHAPTER 4: KINETICS-BASED MODELING OF COMPLEX OXIDE FILMS

A kinetics-based, translating mixed layer (TML) model is developed from the foundation of a phenomenological surface site-based approach. First, the etch rate data of HfLaO and La_2O_3 films in Cl_2 plasma was fitted using the phenomenological model and the extracted parameters were compared to that of hafnium aluminate composite films etched in Cl_2 plasma from a previous study conducted using an ECR reactor. Successful fitting was demonstrated, establishing the efficacy of the model for fitting different material systems. Subsequently, the etch rate data was fit using the translated mixed layer model approach, where the equation set was based upon QMS measurements providing the ratio of etch products present. As an additional means of verification, the surface composition as measured by XPS was also fitted. Similarities and discrepancies with the phenomenological approach are discussed in order to provide context for the adaption to the kinetics-based form. Good agreement was shown between the TML model's simulated results and etch rate data. The goal of potentially extending this methodology beyond the bulk scale via integration with feature profile simulation tools, e.g. Monte Carlo-based methods, is also discussed.

4.1 Phenomenological Modeling of HfLaO Etch Behavior

This section documents the application of a previously developed, surface site-based phenomenological model to the $Hf_xLa_yO_z$ etch rate data. This model was proven to successfully capture the etch rates of HfO_2, Al_2O_3 and $Hf_xAl_yO_z$ films based on experiments performed in an ECR plasma etcher with Cl_2/BCl_3 chemistries. Fitted parameters for the different data sets are

analyzed in the context of the variation in plasma conditions between the ECR and ICP chambers, as well as the thermodynamic properties of HfO_2, Al_2O_3 and La_2O_3. The model demonstrated good fits for the experimental etch rates of $Hf_xLa_yO_z$ and La_2O_3, providing evidence of its robust nature.

4.1.1 Fitting of $Hf_xLa_yO_z$ and La_2O_3 Etching In Cl_2 Chemistry

Based on the experimental results presented in Chapter 3, Cl_2 chemistry appeared to be the more effective chemistry in etching the HfLaO composite films. Based on previous experimental observations, deposition reactions do not occur in Cl_2 plasmas to a significant extent, even at low values of ion energy. However, the reactions of La to form largely non-volatile chlorinated products may effectively create a competing "deposition" term as the changing composition of the surface layer hinders material removal, as seen in the different regions of the QCM data for pure Cl_2 etching of pure La_2O_3. The phenomenological model simplifies deposition into an incoming species flux which deposits on the surface layer below a certain ion energy threshold but does not affect the etch rate beyond that threshold. However the detailed QCM analysis suggests that the formation of the non-volatile products competes with material removal throughout the entire process at a relatively constant rate independent of ion energy. As such, the fitted parameters for the etching terms of the Cl_2 reaction with La_2O_3 can be modeled with the knowledge that the values are offset by a constant amount. For HfLaO films the amount of deposition observed was negligible, as a result of the low fraction of La present. For this reason, fitting of the phenomenological model for $Hf_xLa_yO_z$ and La_2O_3 in Cl_2 chemistry was performed while maintaining the assumption that $J_d = 0$. The model fitting of etch rate data for $Hf_xLa_yO_z$ (○) and La_2O_3 (▲) is shown below in Figure 4.2.

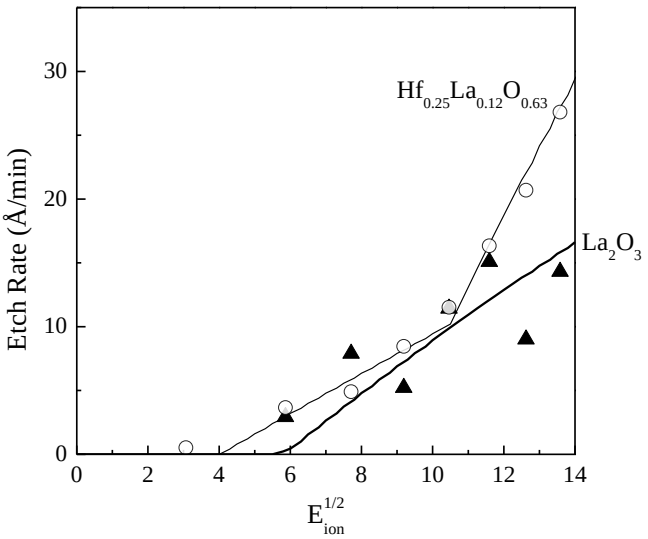

Figure 4.1 Phenomenological model fitting of the etch rates of HfLaO (○) and La_2O_3 (▲) in a 400 W, 5 mT Cl_2 plasma.

The relevant parameters to compare for the different material systems are A_s, B_s and Z_{es}, as the impinging species fluxes J_i and J_e are properties of the plasma itself and $E_{th,s}$ and $E_{tr,s}$ are constrained based on extrapolation from the data. This group of parameters has been highlighted in Table 4-1 by a double lined border. In order to use the model to compare the properties of different material systems, the fitted parameters for the etching of HfAlO in a previous study conducted are included. The fact that the etch rate experiments were conducted in different plasma reactors is accounted for by adjusting the J_i and J_e according to the estimated differences in ion and neutral flux values calculated in Chapter 3. The lower limit used for the ICP etch rate data was the ECR value reduced by a factor of 3, while the upper limit was the ECR value multiplied by 1.4, in accordance with the flux values measured by QCM and Langmuir Probe .

Table 4-1 Comparison of phenomenological model parameters for HfAlO films etched in a Cl_2, 500W, 3 mT plasma (ECR) and HfLaO and La_2O_3 films etched in a Cl_2, 400W, 5 mT plasma (ICP). Extracted parameters are surrounded by a double lined border.

	HfAlO	HfLaO	La_2O_3	
Parameter	Range	Range	Range	Unit
J_i	0.6 - 0.8	0.2 – 0.95	0.2 – 0.95	#/Å^2.s
J_e	45 - 60	70 - 100	70 - 100	#/Å^2.s
$E_{th,s}$	6 - 20	16 - 22	22 - 30	eV
$E_{tr,s}$	8.2 - 9	8.8 - 10.5	8.8 - 12	eV$^{1/2}$
A_s	0.1 - 0.9	0.03 - 0.06	0.01 - 0.09	Å^3/eV$^{1/2}$
B_s	0.9 - 3.9	0.08 - 0.17	0.01 - 0.12	Å^3/eV$^{1/2}$
Z_{es}	0.05 - 1.0	0.05 - 0.14	0.01 - 0.07	Å^3/#

The terms A_s and B_s describe the volume of material removed as a function of ion energy in the ion bombardment (physical sputtering) and ion-enhanced thermal desorption (chemical etching) regimes, respectively. Lower values for these terms imply that more energy is required to both break the metal-oxygen bond of the material in question (leading to sputtering or formation of chlorinated metal species) and volatilize these species so they can enter the gas phase. It can be observed that for the HfLaO films the upper limits for the fitting range of A_s and B_s are lower than those of HfAlO by factors of 15 and 23 respectively. The larger discrepancy in B_s compared to A_s could indicate that the reduced volatility of $LaCl_x$ compounds contributes more to the lower etch rate of HfLaO than the relative strengths of the La-O and Al-O bonds (798 vs. 502 kJ/mol). The difference of the B_s parameter was even more pronounced in the case of the pure La_2O_3 films, which accounts for the lack of a transition from the physical sputtering to chemical etching regime. The range of fitting for A_s was similar to the HfLaO film, which follows the similarity in etch rates of the two materials at lower ion energies.

Next, the Z_{es} term was considered, which describes the volume of material removed as a function of impinging etchant flux. For this term, the upper limits of the fit values for HfLaO and La_2O_3 were lower than HfAlO by factors of 7 and 14 respectively. The range of fitting for this

parameter fell inside the range established for HfAlO, unlike the energy dependent terms. If one uses the high estimate of the ion flux in the ICP reactor (comparable to that the ECR), the difference in the fitted values is consistent with the comparative etch rates of HfAlO vs. HfLaO and La_2O_3, which differed by factors of 6 and 11 respectively at the maximum etch rate value. The higher energy required to break the La-O bond, as well as the lower volatility of $LaCl_3$ compared to $AlCl_3$, (b.p. 1150 vs. 178°C) could be viewed as contributing factors to the lower etch rate.

4.1.2 Fitting of $Hf_xLa_yO_z$ and La_2O_3 Etching In BCl_3 Chemistry

In BCl_3 chemistry, the shifting of the dominant ion to BCl_2^+ results in additional reaction mechanisms that complicate the etch process. At low ion energies, incoming BCl_x species react with the oxygen present in the film to form a non-volatile polymer layer, which results in a net deposition on the surface. Increasing the ion energy results in the formation of volatile compounds such as $(BOCl)_3$ which promote oxygen removal. For La-containing systems, the formation of a non-volatile surface layer also took place as a result of the chemical reactions related to oxygen removal. This rate was found to scale with ion energy as documented in Chapter 3. As such, fitting of the BCl_3 etch rate data requires additional parameters beyond those listed for Cl_2 chemistry, specifically C_p (volume of polymer removed a function of ion energy), D_s and D_p (deposition rates on substrate and polymer, respectively), and $Z_{ds,}$ Z_{dp} and Z_{ep} (volume of polymer deposited on the substrate and existing polymer layer and volume of polymer etched as a function of species flux). Additionally, a depositing species flux J_d must be considered, and the A_s term is not fitted owing to the non-observance of the dual ion energy dependence in BCl_3

chemistry. The fitting of the phenomenological model to the etch rate data of HfLaO and La_2O_3 films in a 400 W, 15 mT, BCl_3 plasma as a function of ion energy is shown in Figure 4.2.

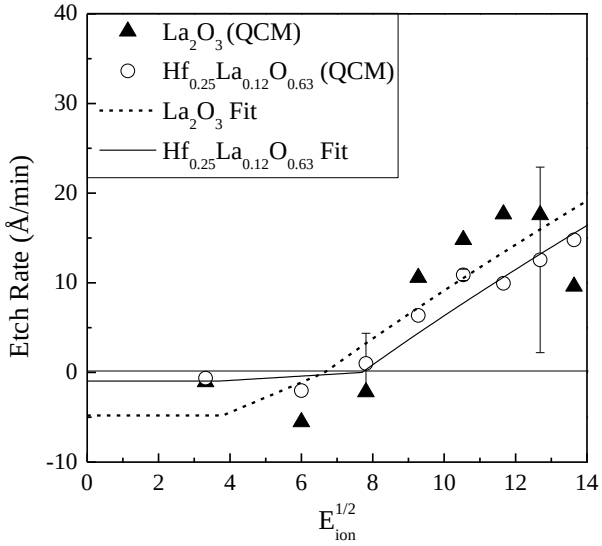

Figure 4.2 Phenomenological model fitting of the etch rates of HfLaO (○) and La_2O_3 (▲) in a 400 W, 15 mT BCl_3 plasma.

It can be seen that the slopes of the fits are very similar, with the main difference lying in the fitted threshold energy at which the fit crosses from net deposition into net etching. The lower value for the La_2O_3 curve could be a result of the RSS minimization method of fitting employed by the model, as this would disagree with the thermodynamic data for the relative strengths of the Hf-O and La-O bonds. However, the highly exothermic nature of the reaction of La_2O_3 with BCl_3 chemistry could partially account for this discrepancy, as it was observed for the case of Cl_2 chemistry that the fitted thresholds of both HfLaO and La_2O_3 were very similar as well. The maximum net deposition rate of the fit for the pure La_2O_3 film was approximately five times as large as that for HfLaO, which coincided with the maximum difference in deposition rates as measured by the QCM for these two material systems in BCl_3. However, the maximum

deposition rate in the phenomenological fitting is assumed to take place at the lowest value of ion energy, whereas from the QCM measurements it was postulated to scale up with increasing ion energy. Thus, the fact that the magnitude of these parameters match should not be regarded as particularly significant. The extracted parameters from the fits are presented in Table 4-2, with the parameters for HfAlO provided for comparison.

Table 4-2 Comparison of phenomenological model parameters for HfAlO films etched in a BCl_3, 500W, 3 mT plasma (ECR) and HfLaO and La_2O_3 films etched in a BCl_3, 400W, 15 mT plasma (ICP). Extracted parameters are surrounded by a double lined border.

	HfAlO	HfLaO	La_2O_3	
Parameter	Range	Range	Range	Unit
J_i	0.6 - 0.9	0.4 – 1.0	0.4 – 1.0	#/Å^2.s
J_e	40 - 60	100 - 200	100 - 200	#/Å^2.s
J_d	5 - 25	4 - 34	4 - 34	#/Å^2.s
$E_{th,s}$	1.5 - 2.5	3.0 - 4.4	2.4 - 3.8	eV$^{1/2}$
$E_{tr,s}$	5 - 6	6-8	6-8	eV$^{1/2}$
B_s	1 - 4	0.02 - 0.12	0.02 - 0.12	Å^3/eV$^{1/2}$
C_p	0.5 - 2.0	0.01 - 0.05	0.05 - 0.09	Å^3/eV$^{1/2}$
D_s	0.1-1.5	0.05 - 0.15	0.15 - 0.25	Å^3/s
D_p	0.1-1.5	0.1 - 0.7	1.1 - 1.7	Å^3/s
Z_{es}	0.1-2.0	0.08 - 0.23	0.08 - 0.23	Å^3/#
Z_{ds}	0.01-1.00	0.004 - 0.01	0.01 - 0.03	Å^3/#
Z_{ep}	0.1-1.5	0.01 - 0.06	0.01 - 0.07	Å^3/#
Z_{dp}	0.01-1.00	0.004 - 0.01	0.01 - 0.03	Å^3/#

The flux terms J_i, J_e, and J_d were constrained based on the calculated differences between the fluxes in the ECR and ICP reactors for the BCl_3 baseline condition. In the case of BCl_3 chemistry, the term labeled transition energy, $E_{tr,s}$, refers to the transition between net etching and net deposition and as such was constrained based on the ion energy value range where this transition was observed to take place. The threshold energy term ($E_{tr,s}$) in this chemistry refers to the value of ion energy where the etch rate begins to change (even if this change is occurring in the deposition regime). As the deposition rate of both HfLaO and La_2O_3 was observed to change

at the lowest applied value of bias voltage (-25 V), the value for $E_{tr,s}$ was constrained accordingly between 0 and 25 eV. The fitted parameters of interest are encircled by a double-lined border.

For the HfLaO films, the fitting ranges of the terms for etch rate of the material and polymer layer as a function of ion energy (B_s, C_p) were lower than those of HfAlO by 1 - 2 orders of magnitude. The larger discrepancy was seen in the case of the substrate etch term, which can be attributed to the difference in strength of the La-O vs. Al-O bonds. Quantifying the energy dependence of the etch rate between the deposited layers on HfAlO and HfLaO is somewhat more difficult. However, as the polymer layer on HfAlO is typically thought to be mostly organic ($B_xO_yCl_z$), whereas the HfLaO layer contains O and Cl bonded to La, it could be reasonably assumed that the etch rate of the deposited layer in the HfLaO films would be lower, which agrees with the fitted parameter range. The fitting range of these terms for the pure La_2O_3 films was nearly identical to that of the HfLaO composite films, with the range of C_p being slightly higher. Based on the similarity of the etch rate data for these terms, it could be expected that the fitted ranges for these values would not differ significantly.

The terms related to rate of deposition on the substrate and polymer layer (D_s, D_p) were also observed to be smaller for HfLaO compared to HfAlO. However it was noted that range of fitting for D_p was very similar to that of HfAlO (the upper limit differed by a factor of 2), and in the case of pure La_2O_3 the range of fitting for this term was actually higher (1.1 - 1.7 for La_2O_3 compared to 0.1 - 1.5 for HfAlO). The lower value of D_s could be associated with the nature of the deposition on La_2O_3 - as the breaking of La-O bonds is actually a requisite for the formation of La-Cl, the rate of this process could be expected to be lower than the rate of formation of $B_xO_yCl_z$, especially at lower values of ion energy. The D_p parameter is more complicated to explain as the change in kinetics with the evolution of the deposited layer composition is beyond

the scope of this model. Additionally, as minimal information is available on the reactions of $LaCl_3$(c) or LaOCl intermediates, it is difficult to compare analogous reactions with HfO_2 or Al_2O_3. Perhaps the simplest comparison is to note that the range of fitting for deposition rates on the substrate and polymer for HfAlO was identical, whereas for the La-containing films this value was significantly lower in the case of the substrate. This denotes that the rate limiting step for deposition on La-containing films involves the breaking of La-O bonding, which supports the earlier hypothesis of the nature of the deposited layer as containing lanthanum (compared to being purely organic). The fact that the rate of deposition on the polymer layer is comparable in both films also suggests that a lower etch rate as a result of lanthanum addition is indeed connected to the formation of an inherently etch-resistant surface layer and not due to excessive amounts of material deposition on the surface. However it also suggests that the deposited layer is not entirely impervious to reactions.

Finally, the terms related to rate of etch or deposition as a function of incoming species flux are analyzed. The etch terms Z_{es} and Z_{ep} (for substrate and polymer respectively) were lower than that of the HfAlO films which agrees with the thermodynamic properties discussed earlier in this section. The upper limit of the fitting was an order of magnitude lower for both HfLaO and La_2O_3 compared to HfAlO. Given that the maximum difference between fluxes in the ICP reactor compared to the ECR is a factor of two, this suggests that the chemical kinetics of La weigh more heavily in the etch behavior of these films rather than large discrepancies in the physical environment, which supports the earlier discussion. The deposition terms Z_{ds} and Z_{dp} were also lower for the La-containing films compared to HfAlO, with the upper limits differing by two orders of magnitude. Once again, as these terms are much lower than any potential flux

disparity between the two systems, this observation would suggest that the chemical kinetics of La compared to Al or Hf are primarily response for the changes in etch behavior.

4.1.3 Summary Of Phenomenological Model Fitting

The phenomenological model was applied to the etching of HfLaO and La_2O_3 in Cl_2 chemistry. After accounting for discrepancies in the plasma properties of the ICP system compared to the previously utilized ECR reactor, good agreement was shown between the experimental data and the model fits. For both Cl_2 plasmas, terms related to volume of material removed as a function of ion energy and species flux were consistently lower for both HfLaO and La_2O_3 than HfAlO. This was consistent with thermodynamic data relating to the material properties, e.g. metal-oxygen bond strengths of La-O and Al-O and the volatilities of the metal halide products. The disparity between the range of fitting for ion energy dependent terms in the chemical etching (higher E_{ion}) regime was greater than that for the physically sputtering regime (lower E_{ion}) between HfLaO and La_2O_3, suggesting that the chemical reactions of La with Cl_2 to form stable products are the primary reason for the reduced etch rate between the films. The comparative magnitudes of the flux-dependent terms in Cl_2 chemistry was consistent with the etch rate disparities between the HfAlO, HfLaO and La_2O_3 films.

For BCl_3 chemistry, good agreement was also shown between the experimental data and the model fits. The fitting of the deposition rate parameters suggested that the initial reaction of the La-containing substrates with the plasma environment is the rate liming step for the deposition process. Additionally, the relative values of the parameters support the theory that the etch rate is hindered by the layer's characteristics, rather than a much a greater deposition rate. However, it should be noted that as postulated, the formation of the LaOCl surface layer is

inextricably connected to the removal of oxygen via chemical reactions, and as such the generalized nature of the parameters in this model makes it unfeasible to attempt to decouple such mechanisms.

4.2 Translating Mixed Layer Model Adaptation

The phenomenological model discussed in the previous section provided a robust, effective means of analyzing the etch behavior of multi-component oxide films in chlorine containing plasmas. However, the simplifying assumptions of the model, e.g. the grouping of multiple etching/deposition reactions into a single expression, make it unsuitable for detailed modeling at scales below that of the bulk film, where detailed information about the kinetics of individual reactions is of paramount importance. In order to take steps towards developing predictive capabilities at the level of individual features, it is thus necessary for this model to be adapted into a kinetics-based form. The details of the TML model have been discussed in Chapter 2 and the following sections thus focus on the direct application of the model to the aforementioned plasma and material combination. This testing serve as a base system, with potential applicability to other complex oxides. The results are compared to experimental data related to the etch yield, etch products, and surface composition after plasma exposure with good results. For the substantially more complex TML formulation, Cl_2 plasma chemistry was focused on exclusively, in large part due to the higher etch rates compared to BCl_3 for the HfLaO composite films.

4.2.1 TML Fitting of Cl_2 Etch Rate Data

The TML model fits for the etch rate data of HfO_2, Al_2O_3, La_2O_3, HfAlO and HfLaO films in Cl_2 plasmas are shown in Figure 4.3. Good agreement is demonstrated between the model results and the experimental data. It should be noted that the TML model outputs a predicted etch yield (as compared to an etch rate), which is a dimensionless quantity dependent on the ion flux impinging on the film surface. The etch rate data was converted to a yield value using the following equation:

$$Yield = \frac{ER \cdot MW \cdot J_{ion}}{\rho_{film} \cdot N_A}$$

Where ER is the etch rate in $cm.s^{-1}$, ρ_{film} is the film mass density in $g.cm^{-3}$, N_A is Avogadro's constant, MW is the molar weight of the film, and J_{ion} is the incoming ion flux. For the purpose of these calculations an ion flux of 5.5×10^{15} ions cm^{-2} s^{-1} was used for data from the ICP reactor, which represents an intermediate value between the low and high end estimates of the flux reaching the QCM in the lower chamber, as calculated in Chapter 3. For the ECR chamber, a reduction factor of 2.5 was applied to the ICP value (from the ratio of Langmuir Probe measurements), giving an ion flux of 2.2×10^{15} ions cm^{-2} s^{-1}. A neutral to ion ratio of 50 was used in the calculations.

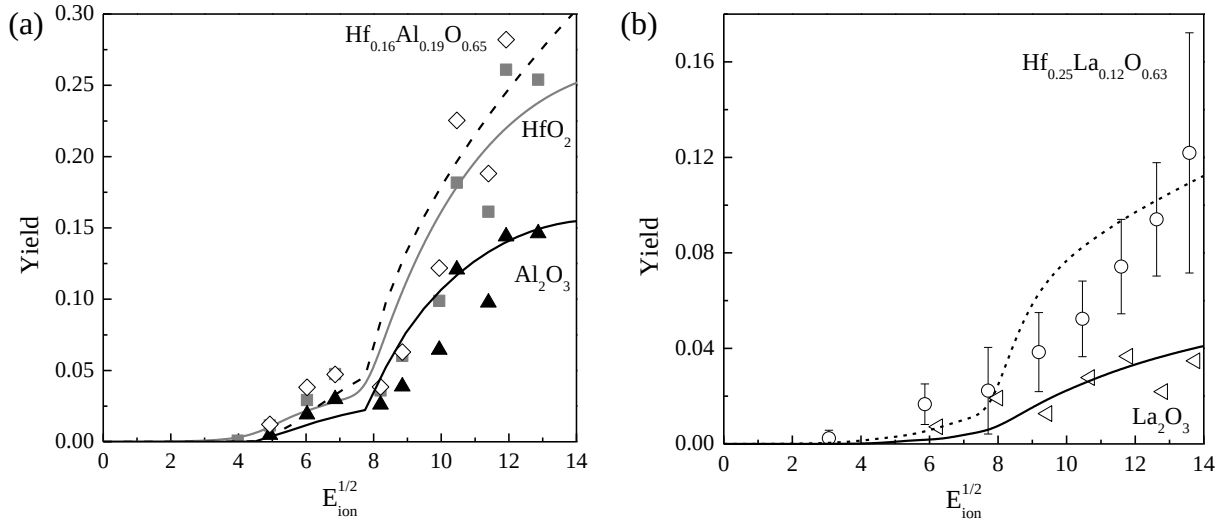

Figure 4.3 TML model fits for the etch yields of (a) HfO_2, Al_2O_3, and HfAlO and (b) La_2O_3 and HfLaO films etched in a 400 W, 5 mT, Cl_2 plasma as a function of ion energy.

As discussed in Chapter 2, the TML model divides reactions into three major fluxes: (i) arrival from the gas phase to the mixing layer, (ii) removal from the mixing layer to the gas phase and (iii) movement from the substrate to the mixing layer. The reactions and parameters comprising the arrival flux are considered first and are examined in Table 4-3.

Table 4-3 Arrival flux parameters for Cl_2 etching of HfO_2, Al_2O_3, HfAlO, La_2O_3 and HfLaO

Material System	Reaction Listing	Coefficient Value	Threshold Energy$^{0.5}$
HfO_2	$R_{A\_X\_i}$, X = Cl, Cl_2	1, 1	3.87, 3.87
	$R_{A\_Cl\_on\_Y}$, Y = Hf, O	0.04, 0.6	
	$R_{A\_V\_by\_X\_i}$, X = Cl, Cl_2	2.25, 2.12	3.16, 4.35
Al_2O_3	$R_{A\_X\_i}$, X = Cl, Cl_2	1, 1	4.47, 4.47
	$R_{A\_Cl\_on\_Y}$, Y = Al, O	0.32, 0.6	
	$R_{A\_V\_by\_X\_i}$, X = Cl, Cl_2	2.5, 2.4	3.74, 4.80
HfAlO	$R_{A\_X\_i}$, X = Cl, Cl_2	1, 1	4.47, 4.47
	$R_{A\_Cl\_on\_Y}$, Y = Hf, Al, O	0.04, 0.32, 0.6	
	$R_{A\_V\_by\_X\_i}$, X = Cl, Cl_2	1.25, 1.12	3.46, 4.69
La_2O_3	$R_{A\_X\_i}$, X = Cl, Cl_2	1, 1	5.00, 5.00
	$R_{A\_Cl\_on\_Y}$, Y = La, O	0.002, 0.3	
	$R_{A\_V\_by\_X\_i}$, X = Cl, Cl_2	1.64, 1.44	4.24, 5.19
HfLaO	$R_{A\_X\_i}$, X = Cl, Cl_2	1, 1	3.87, 3.87
	$R_{A\_Cl\_on\_Y}$, Y = Hf, La, O	0.04, 0.02, 0.3	
	$R_{A\_V\_by\_X\_i}$, X = Cl, Cl_2	1.95, 1.22	3.16, 4.35

The reactions are grouped into three categories: ion implantation, neutral adsorption and vacancy creation (from top to bottom). The dominant ionic species as measured by QMS for the case of Cl_2 chemistry in the ECR reactor (500 W source power, 3 mT pressure) were Cl^+ and Cl_2^+, comprising 0.42 and 0.53 of the total ion concentration respectively. For the ICP reactor at 400W and 5 mT the ratio was found to be similar. The remaining ionic fraction is accounted for by the presence of Ar for actinometry purposes. Ar^+ ions were assumed to be inert and not incorporated into the surface layer, resulting in a total of two equations for ion implantation in the case of Cl_2 chemistry. In all the ion implantation reactions the sticking coefficients are set to unity, regardless of the material. However, the threshold energy for implantation to occur varied with material, with the highest value for La_2O_3, followed by Al_2O_3 and then HfO_2. This

corresponded to the higher energy required to break La-O and Al-O bonding in stoichiometric La_2O_3 and Al_2O_3 compared to that of Hf-O in HfO_2. The values for the threshold energy of ion implantation were constrained within a range of 5 eV around the observed experimental values for the threshold of etching. For the composite films, the values were based on the dominant oxide in the film, i.e. for $Hf_{0.16}Al_{0.19}O_{0.65}$ the threshold energy was set to that of Al_2O_3, and for $Hf_{0.25}La_{0.10}O_{0.65}$ the value was set to that of HfO_2.

Cl neutrals make up nearly the entire population of neutral species measured at the specified plasma conditions. The sticking coefficients of this specie on the various metal elements were first fitted for the pure films. It was found that in the case of HfAlO, the sticking coefficients for Hf and Al could be kept constant. However, for HfLaO, the sticking coefficient for La had to be increased significantly to fit the requisite surface composition as determined by XPS. This observation could be linked to the low sticking coefficient of La compared to that of the other metals (one to two orders of magnitude lower on average). The reason for the lower sticking coefficient on La could be attributed to the limitations of the model formulation. In Chapter 3 it was postulated that the lower etch rate of La_2O_3 was the result of two factors: the strength of the La-O bond and the formation of non-volatile $LaCl_x$ products. While the former factor can be addressed in the model by increasing the threshold for chemical etch reactions involving La, the latter is difficult to model effectively in the TML format, as all ion-enhanced chemical etch reactions are assumed to create species which immediately leave the mixing layer. While changes to the mixing layer composition as a result of ion implantation and neutral adsorption affect the probability of these reactions occurring (the model approximates bond concentrations from the elemental fractions in the mixing layer), the end result would probably be a higher rate of removal, as presence of M-Cl bonds in the mixing layer is a requisite for the

reaction to form MCl_x gaseous species. As a result, the lower sticking coefficient on La was likely a means of approximating the lower etch rate through a controllable parameter. A lower probability of Cl adsorption would correspond to a lower calculated probability of M-Cl and O-Cl bonding in the mixing layer, which would consequently result in the lower rate of formation of chemical etch products. A similar trend was observed for the sticking coefficient of oxygen, which was set to 0.6 for all non-La containing films but was fitted to a value of 0.3 for La-containing ones. In all cases the sticking coefficient of Cl on O was found to be higher than the values for the metal elements of the oxides.

The final category of arrival flux reactions, vacancy generation comprised three equations, corresponding to impacts by Cl^+, Cl_2^+ and Ar^+ ions. However, owing to the relatively low concentration of Ar^+ in the system, any equations involving this specie had insignificant effects on the overall results, thus only the equations referring to Cl^+ and Cl_2^+ are reported. The threshold energy required to create vacancies in each pure oxide film increased with M-O bond strength but did not vary significantly. For the HfAlO film, a better fit was achieved using an intermediate value for the threshold energy (between that of HfO_2 and Al_2O_3), whereas for the hafnium rich HfLaO film, the value of HfO_2 was used. The reaction rate coefficients for these reactions were generally lower for the composite films than the pure oxides, except for La_2O_3. Both the threshold energies and reaction coefficients for the vacancy generation were constrained within narrow ranges (10 - 23 eV and 1.12 - 2.25) as a result of solution convergence problems if the values were too large or small, and also to maintain the percentage of vacancies in the mixing layer below 50%.

Etching reactions are known to dominate in Cl_2 chemistry, and as such there are accordingly many more reactions in the removal flux that need to be considered. A reaction list

is provided in Table 4-4. For the pure films, the threshold energy and reaction rate coefficient for the ion assisted reaction leading to the formation of OCl were maintained within a relatively small range. However in the case of the composite films, the fitted value of the coefficient was smaller. Recombination (reaction of surface O or Cl species with impinging Cl radicals to produce gaseous OCl or Cl_2 without any adsorption) was modeled with low probabilities (1.2 - 4%) in all the films.

Table 4-4 Removal flux parameters for Cl_2 etching of HfO_2, Al_2O_3, HfAlO, La_2O_3 and HfLaO

Material System	Reaction Listing	Coefficient Value	Threshold Energy$^{0.5}$
HfO_2	$R_{S\_Y\_by\_X\_i}$, Y = Hf, O, Cl X = Cl, Cl_2	0.153, 0.015, 0.045, 0.206, 0.018, 0.055	3.77, 6.41, 5.11, 4.10, 7.86, 6.22
	R_{E_B}, B = $HfCl_2$, $HfCl_3$, $HfCl_4$, Cl_2, OCl	0.4, 13.7, 22.8, 6.2, 1.32	8.18, 8.42, 8.66, 0.0, 7.87
	$R_{d\_V\_by\_X}$, X = Cl, Cl_2	2.17, 2.06	4.47, 4.35
	$\beta_{Y-V}\left(J_{Y-V}\right)^2$, Y = Hf, Cl, O	0, 550, 0	
	$R_{R\_Cl\_Cl}$, $R_{R\_O\_Cl}$	0.02, 0.013	
Al_2O_3	$R_{S\_Al\_by\_X\_i}$, X = Cl, Cl_2	0.033, 0.040	5.52, 6.74
	R_{E_B}, B = AlCl, $AlCl_2$, Cl_2, OCl	0.41, 0.51, 7.2, 1.32	5.00, 8.31, 0.0, 7.87
	$R_{d\_V\_by\_X}$, X = Cl, Cl_2	1.87, 1.96	4.69, 4.35
	$\beta_{Y-V}\left(J_{Y-V}\right)^2$, Y = Al, Cl, O	0, 450, 0	
	$R_{R\_Cl\_Cl}$, $R_{R\_O\_Cl}$	0.03, 0.012	
HfAlO	Same as tabulated above		
	R_{E_B}, B = $HfCl_3$, $HfCl_4$, AlCl, $AlCl_2$, Cl_2, OCl	10.7, 22.8, 0.41, 0.41, 7.2, 0.95	8.42, 8.66, 5.00, 8.31, 0.0, 7.87
	$R_{d\_V\_by\_X}$, X = Cl, Cl_2	2.17, 2.06	4.58, 4.80
	$\beta_{Y-V}\left(J_{Y-V}\right)^2$, Y = Hf, Al, Cl, O	0, 0, 900, 0	
	$R_{R\_Cl\_Cl}$, $R_{R\_O\_Cl}$	0.04, 0.012	
La_2O_3	$R_{S\_La\_by\_X\_i}$, X = Cl, Cl_2	0.013, 0.017	3.84, 4.32
	R_{E_B}, B = LaCl, LaOCl, Cl_2,OCl	0.13, 0.16, 6.8, 0.11	9.06, 8.42, 0.0, 7.87
	$R_{d\_V\_by\_X}$, X = Cl, Cl_2	1.97, 1.79	4.69, 4.35
	$\beta_{Y-V}\left(J_{Y-V}\right)^2$, Y = La, Cl, O	0, 0, 35, 0	
	$R_{R\_Cl\_Cl}$, $R_{R\_O\_Cl}$	0.02, 0.002	
HfLaO	Same as tabulated above		
	R_{E_B}, B = $HfCl_3$, $HfCl_4$, LaCl, LaOCl Cl_2,OCl	2.7, 4.8, 1.57, 3.46 2.7, 0.15	8.43, 8.66, 9.22, 8.54 0.0, 7.87
	$R_{d\_V\_by\_X}$, X = Cl, Cl_2	2.17, 2.06	4.47, 5.38
	$\beta_{Y-V}\left(J_{Y-V}\right)^2$, Y = Hf, La, Cl, O	0, 0, 60, 0	
	$R_{R\_Cl\_Cl}$, $R_{R\_O\_Cl}$	0.012, 0.007	

From Table 4-2 it is observed that the threshold energies for the majority of the physical sputtering reactions were lower than those for chemical etching, in accordance with the dual energy dependence observed experimentally. According for the equation for calculating sputer rate coefficients and threshold energies, the ease of sputtering is proportional to the mass of the target atom in the mixing layer, assuming the identity of the impinging ion is constant. At lower values of ion energy, desorption of non-volatile products (sputtering due to ion bombardment) is the primary mechanism for removal of material from the surface. As the ion energy increases, enhanced chemical reactions begin to take place, leading to a higher rate of etching with the formation of species such as chlorinated metal products. The one exception is the spontaneous reaction to form Cl_2, which has appeared in previous iterations of the TML model and largely serves as a mechanism to control the chlorine percentage in the mixing layer. The coefficients for the ion-enhanced chemical etching reactions are sized based on the quantified ratios of observed etch products via QMS measurements. In the TML model, the probability of forming such etch products is proportional to the concentration of the requisite bonding raised to a power of the number of bonds. For example, MCl_2 formation is proportional to $(J_{M\text{-}Cl})^2$, whereas MCl_3 formation is proportional to $(J_{M\text{-}Cl})^3$. This effectively means the probability of forming a more chlorinated/higher mass etch product is lower (as the bond concentration between any two species in the mixing layer cannot be larger than one), and thus larger values for the rate coefficient do not necessarily translate to larger quantities of the etch product in question. Finally, it was found that the relative values of the threshold energy for densification and vacancy creation had to be maintained at a certain ratio (E_{th} for densification approximately one order of magnitude lower than that for vacancy creation) in order to prevent excessive vacancy content of the films at the steady state condition.

The obtained surface composition values via XPS provide an additional means of validation as the TML model can predict these values for a given ion energy (corresponding to the bias voltage used in the etch experiment). Figure 4.4 shows the comparison of experimentally obtained values and the TML model values for HfAlO (a) and La_2O_3 (b), demonstrating the ability of the model to match data for pure and multicomponent films.

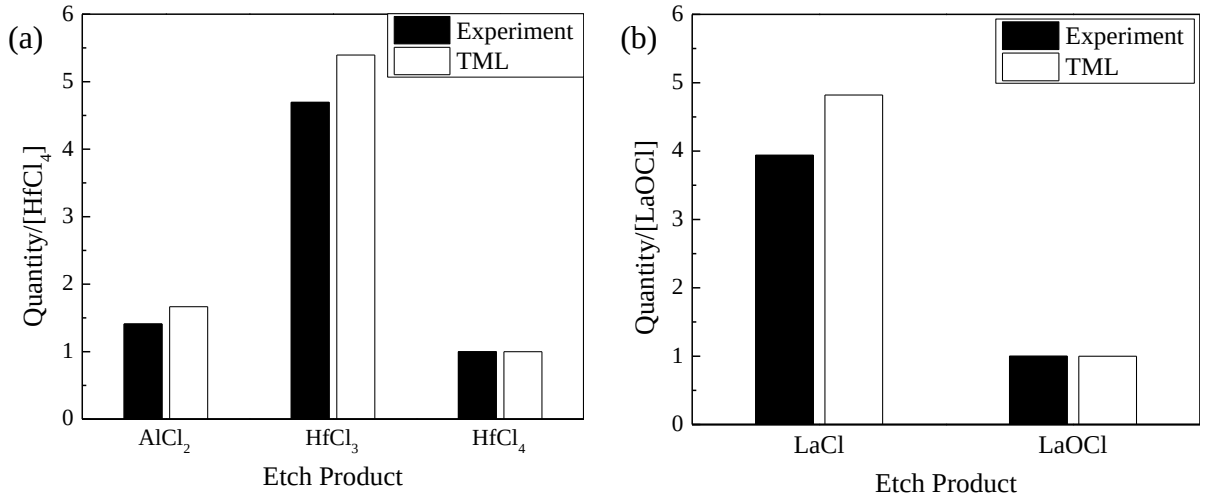

Figure 4.4 Comparison of the ratio of etch products between experimental QMS measurements and the TML model for (a) HfAlO and (b) La_2O_3.

In addition to the etch product ratios and etch rate data, the TML model can be applied to the surface composition of the films measured via XPS as an additional verification step. Figure 4.5 shows the predicted surface compositions for HfAlO (a) and HfLaO (b) films compared to XPS measurements after Cl_2 exposure at E_{ion} ~100 eV. Good agreement is demonstrated between the model prediction and the experimental measurement with respect to the relative ratios of the metal elements (Hf, Al and La). However, large discrepancies are observed in the Cl and O compositions. The discrepancy can be possibly explained when one considers that the XPS measurements were taken ex-situ, leading to reactions of the film surface upon exposure to

ambient conditions. It was observed by Layadi and Donnelly that Si samples etched in a Cl_2 plasma environment underwent significant changes in surface composition after coming into contact with air - the detected Cl concentration decreased from 27% to 3%, while the measured O content simultaneously increased from negligible levels to 35%. (Layadi, Donnelly et al. 1997) A similar re-oxidative effect was observed by Hsu and Marchack with Si samples treated with pure Cl found to contain ~20% O on the surface. Additionally, absorption of carbon from atmospheric exposure owing to the enhanced surface reactivity could affect the XPS signal via attenuation, leading to variations in the measured composition.

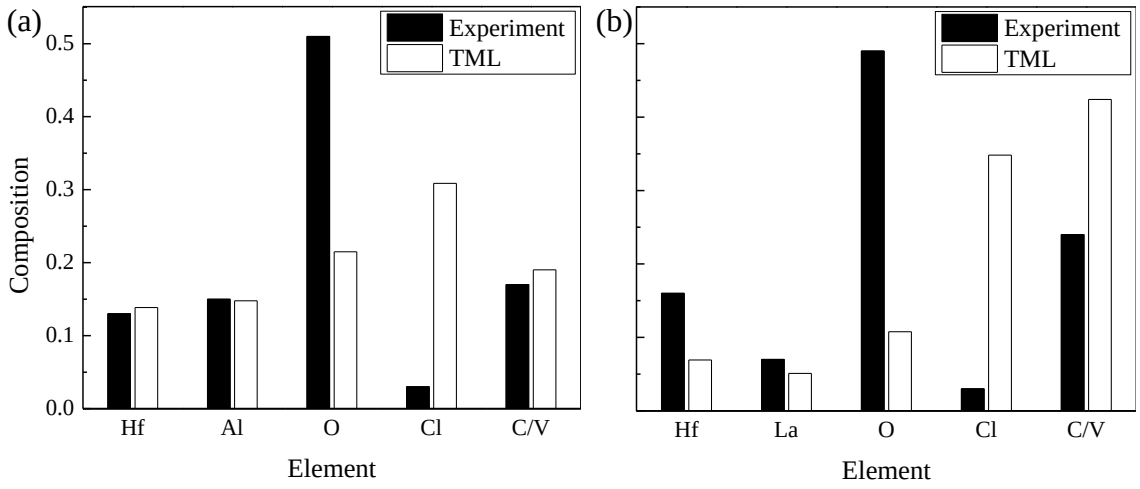

Figure 4.5 Prediction of mixing layer composition for Cl_2 etching of HfLaO (left) and HfLaO (right) at E_{ion} = 100 eV, compared to ex-situ XPS measurements.

In the case of the La-containing films, larger discrepancies between the TML predictions and experimental data were recorded, specifically in the case of the absolute values of the metal fractions where the simulation values were notably less than those of the experimental measurements. The higher mass of La-containing etch products (compared to Al) would make them more prone to redeposition. (Kimura, Coburn et al. 2004; Vasenkov, Li et al. 2004) Given

the estimated attenuation length (~17-26 Å) of an HfO_x film via simulation, it is possible that such a process could affect the measured surface composition. Additionally, when fitting the La_2O_3 etch rate data, only the net etch rate was used, which was the sum of the competing etch and deposition regions as identified in the QCM frequency response data. However, accurately depicting the deposition regime was beyond the scope of this model and was thus not included, which could have a significant effect on the dynamic evolution of the mixing layer. Qualities such as the vacancy generation rate as a function of ion energy or the comparative rate of spontaneous dangling bond annihilation can only provide very general comparisons between two films but it is evident that other factors must be considered when studying the etch behavior of novel multicomponent materials.

4.3 Summary of TML Modeling of Cl_2 Etching

The TML format allowed for the detailed modeling of the etch processes for HfO_2, Al_2O_3, La_2O_3, HfAlO and HfLaO films in Cl_2 chemistry. By fitting the model to three sets of experimental data (etch yield, etch product ratios and surface composition), kinetic parameters related to specific chemical reactions were extracted. The values of the threshold energies for the formation of chemical etch products correlated to thermodynamic data concerning metal-oxygen bond strengths. La_2O_3 addition was found to introduce more uncertainty to the fitting of the TML model, which could be attributed to the difficulty in modeling the separate etch and deposition regions of this material system in Cl_2 as observed by QCM measurements. However, the ultimate validation of the model's accuracy involves coupling the extracted kinetic parameters to a feature

profile simulator, thus bridging the divide between bulk scale kinetics and the geometrical effects of individual features. Initial attempts to extend the TML results to patterned features are discussed in the following chapter.

CHAPTER 5: EXTENSION TO FEATURE SCALE MODELING

The approach to capturing the kinetics of complex oxide etching in Cl-based chemistry discussed in Chapters 3 and 4 utilized a combination of experimental and theoretical methods to verify its efficacy. Although bulk-scale experimentation and modeling on blanket films is necessary to gain sufficiently detailed insight into the etch characteristics of a material, patterning well defined geometries at nanometer length scales is required to realize functional devices. Using the kinetic parameters from the TML modeling, feature profiles for HfO_2/HfLaO films were obtained using a Monte Carlo based feature profile simulator and compared to experimentally obtained feature profiles results. This approach was also extended to the shallow trench isolation process (Si etching in Cl_2/O_2 chemistry), demonstrating the ability of the TML model to handle variations in gas chemistry with a material system besides that of high-k dielectrics.

5.1 Patterning Features on $Hf_xLa_yO_z/La_2O_3$ Films

Trenches with critical dimensions of 100 nm and 200 nm at a fixed pitch width of 500 nm were created on HfLaO and La_2O_3 films using a Vistec EBPG 5000+ES electron-beam writer. A mask layer consisting of ZEP520A photoresist (PR) was deposited on ~4 cm^2 wafer pieces via spin coating at 3000 RPM for 60 seconds. Prior to the spincoating procedure, the samples were exposed to hexamethyldisilazane (HMDS) vapor for 10 - 15 minutes in order to promote adhesion of the PR to the substrate. In order to control the thickness of the PR layer, the dilution

ratio of the ZEP520A with anisole (methoxybenzene) was adjusted, as the resist did not exhibit a strong dependence on the spin coater RPM setting for these materials. The spin coating process was followed by a 180°C post-bake for 3 minutes.

The PR-coated wafer pieces were then patterned using the e-beam writer. The feature specifications were edited using KLayout Software, which allowed for the creation of line patterns down to 100 nm resolution. Files were saved in GDS format, which could then be read directly by the software which controlled the e-beam writer. Figure 5.1 shows an example of a pattern created using the software, zoomed in at two different scale lengths to illustrate the definition capabilities.

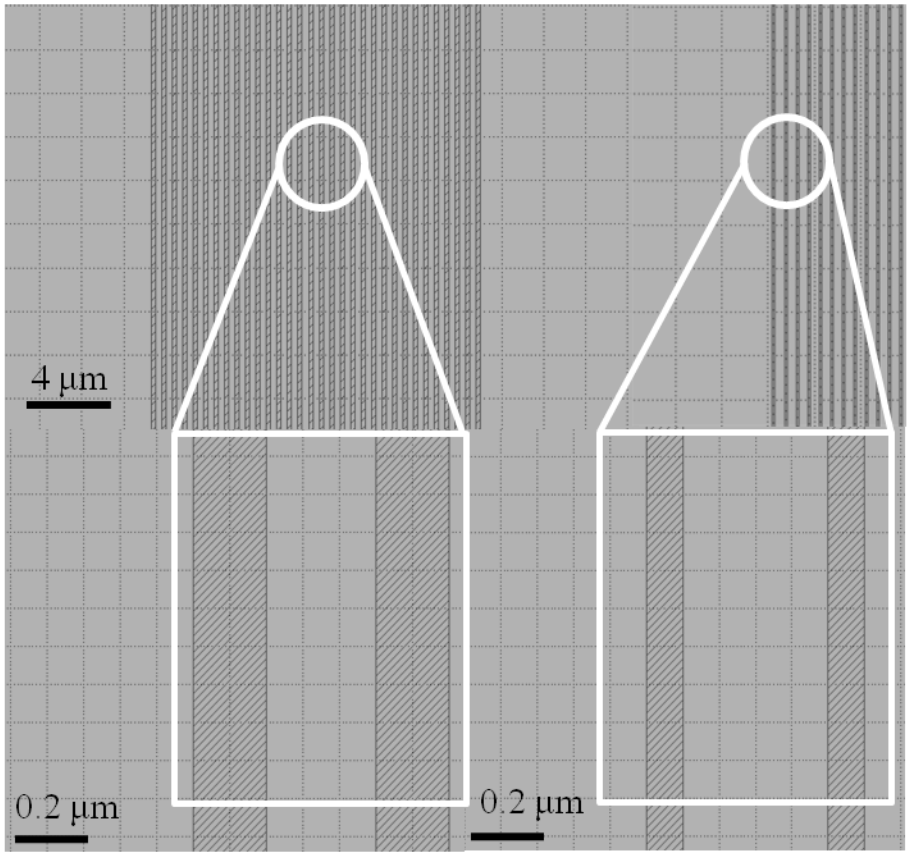

Figure 5.1 Schematic of trenches with critical dimension 100 and 200 nm at two different scale lengths created by the KLayout Software.

The dose value used in the writing of the photoresist was ~300 - 400 μC/cm^2 (dependent on PR thickness) at a beam current of 15 nA. After exposure of the PR, the samples were developed using n-Amyl-acetate (ZED-N50) for 60 - 70 seconds, followed by a rinse in iso-propyl alcohol and N_2 blow drying. Using this method, features with aspect ratios of up to 5 : 1 were successfully defined. Figure 5.2 shows a variation in aspect ratio achieved for patterned samples (AR = 2, 3 and 5) before exposure to plasma, with the PR mask, HfLaO film and Si substrate labeled. The granular appearance of the material in the feature with an aspect ratio of 5 (Figure 5.2(c)) is due to an Au/Pd coating deposited via sputtering to prevent charging artifacts. For the images in Figures 5.2(a) and (b), the samples were cleaved after this coating and thus coating did not extend to the cross section pictured.

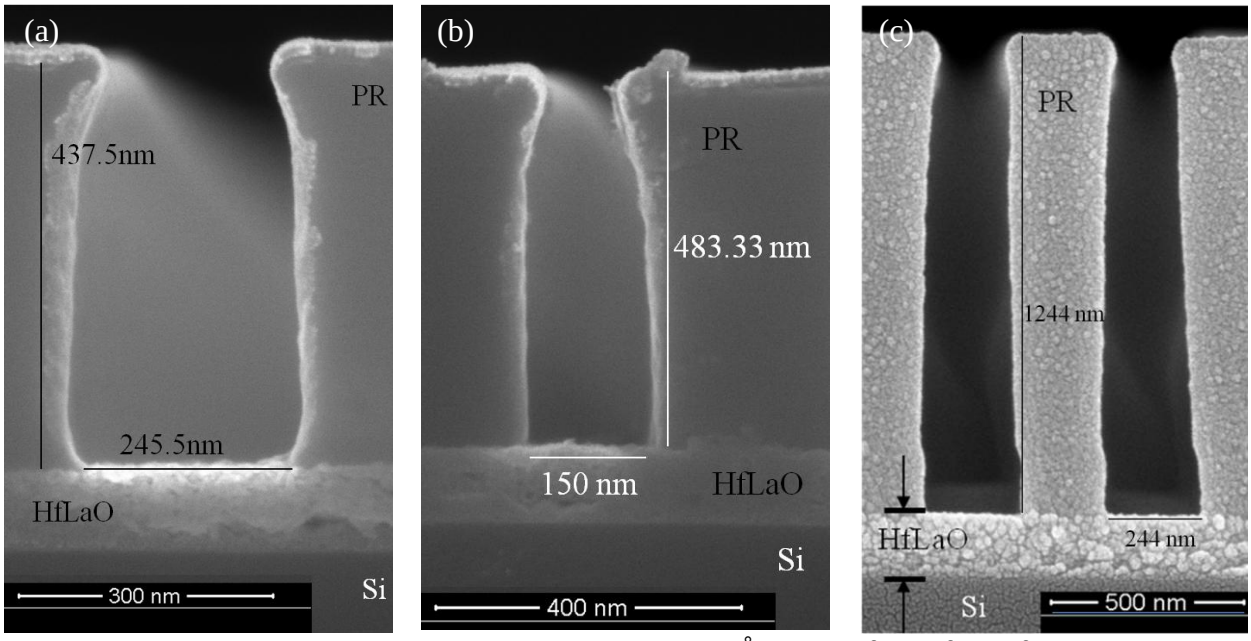

Figure 5.2 ZEP520A patterned trenches on 1000 Å thick HfLaO films for (a) AR ~ 2, (b) AR ~ 3 and (c) AR ~ 5 on 2000Å thick HfLaO film.

5.2 MC Predictions of $Hf_xLa_yO_z$ Aspect Ratio and Ion Energy Dependence

The MC model was used to predict the variation in the etched profiles with changing aspect ratio and ion energy. The former parameter was manipulated by changing the mask (photoresist) dimensions within the file.cpp module of the MC code that defined the feature geometry, while the latter was adjusted by varying the ion energy value in the input file. It should be noted that in these simulations the PR mask was set to be non-reactive. While this was not strictly accurate (the etch rate of ZEP520A in Cl_2 plasma has been documented as varying between 300 and 2000 Å/min), this assumption was deemed necessary to simplify the simulation, as modeling the etch chemistry of the mask was outside of the focus of this work. However, as the composition of the mask and its reaction with the selected etchant chemistry can undoubtedly play a role in the development of the feature, this is a factor that should be considered in future work. Aspect ratios of 1.5, 3 and 6were modeled over a simulation domain of height 500 nm and width 250 nm. Ion energies of 75, 100 and 175 eV were used in the simulations. In order to facilitate direct comparisons between the different aspect ratios, profiles were captured at the same point of progress in the simulation, in this case after 6 and 13 iterations of 4.0 x 10^7 particles. A neutral to ion ratio of 50 was used for the initial flux composition, which was pure Cl_2 (0.9804 Cl neutrals, 0.0092 Cl^+, 0.0094 Cl_2^+). The results of varying the aspect ratio from 1.5 to 6 at E_{ion} = 100 eV are shown in Figure 5.3. In this case the mask height was maintained at a constant value of 300 nm in the domain while the width of the feature was varied from 150 nm to 50 nm. The PR mask and the initial surface of HfLaO are labeled.

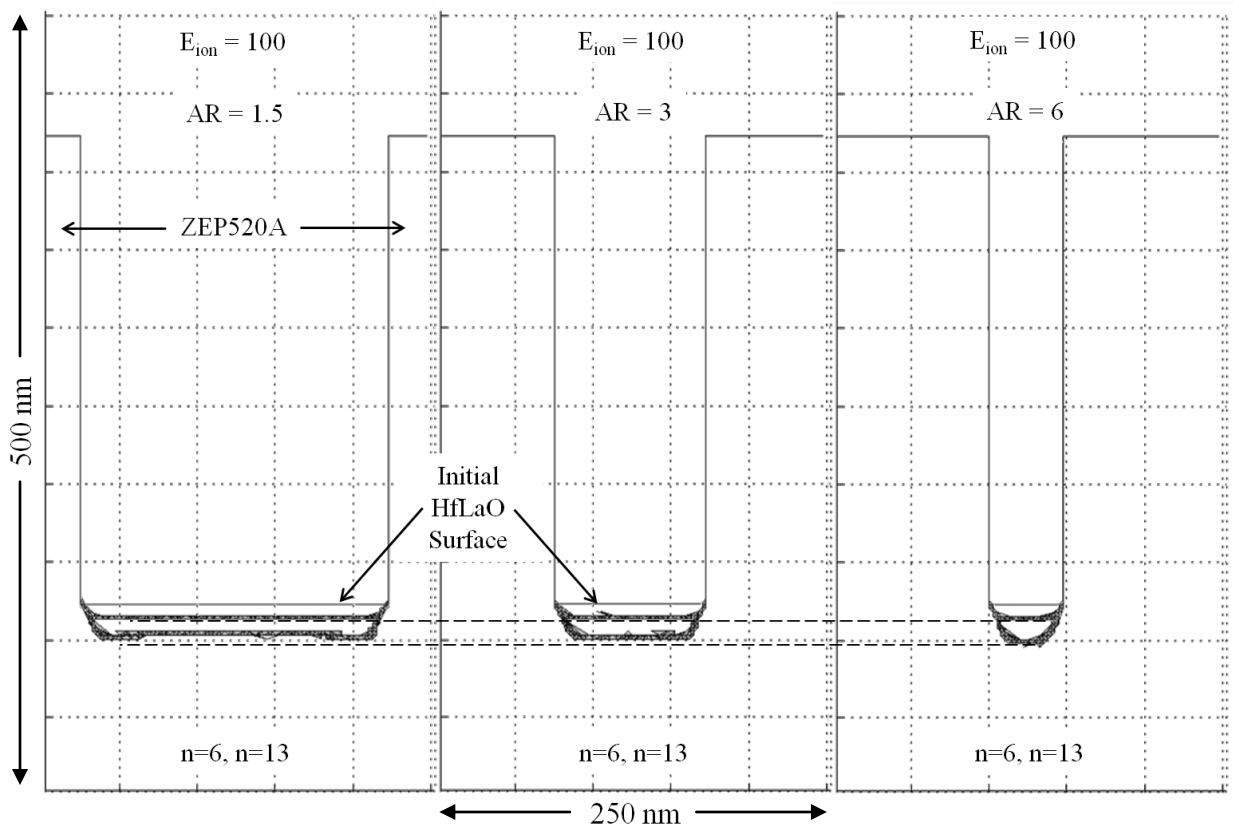

Figure 5.3 MC simulations showing the effect of increasing aspect ratio at E_{ion} = 100 eV for the etching of $Hf_{0.25}La_{0.12}O_{0.63}$ in Cl_2 chemistry.

It was observed that the depth of the etched profile exhibited a weak dependence on aspect ratio (shown by the horizontal dashed lines), with the difference becoming more pronounced with successive iterations. At an aspect ratio of 1.5, slight trenching was observed in the corners of the etched profile, leading to the center of the profile being slightly elevated above the edges. This effect was not observed for the two higher AR values. As the aspect ratio increased, the lower portion of the profile sidewalls became less vertical, while the angle of the upper portion remained relatively constant. The probability of scattered particles impinging on a surface near the bottom of the feature would be presumably higher at lower feature widths, possibly explaining this development.

A lower ion energy case was considered next (E_{ion} = 75 eV), using the same aspect ratio progression. The results of these simulations are shown in Figure 5.4.

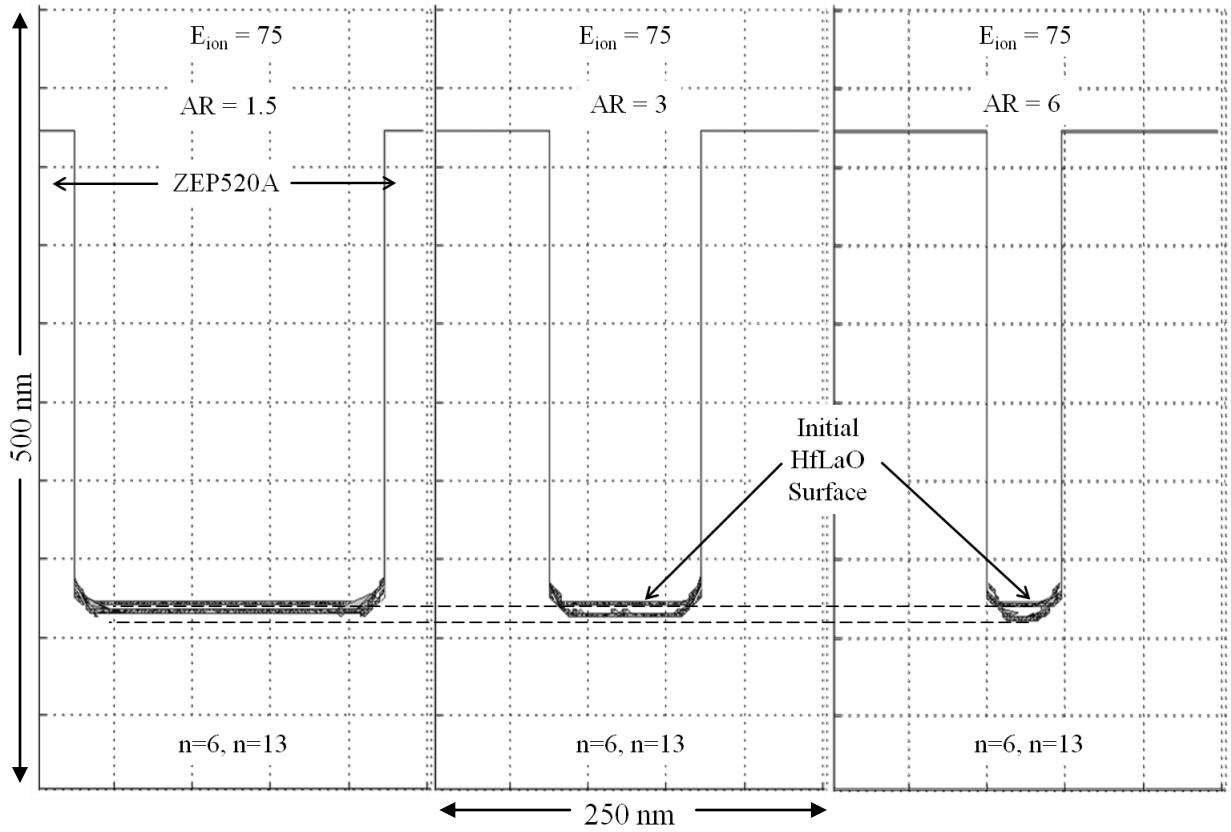

Figure 5.4 MC simulations showing the effect of increasing aspect ratio at E_{ion} = 75 eV for the etching of $Hf_{0.25}La_{0.12}O_{0.63}$ in Cl_2 chemistry.

The maximum etch depth at this ion energy was observed to be about half that of the 100 eV case, which was consistent with the observed etch rate curve via QCM measurement (~10Å/min at 100 eV vs. ~6Å/min at 75 eV, extrapolated from the curve). It was noted that after six iterations, there was minimal material removal past the initial surface. Continued evolution at thirteen iterations showed propagation of the feature sidewalls above the plane of the initial surface, as well as a deeper etched profile near the center of the feature. The profile development at the corners could be the result of two factors: differing flux ratios owing to the anisotropic

distribution of ions compared to neutral species, or deposition of scattered species on the sidewalls after impacting in other areas of the simulation domain. Firstly, cells which consume different fluxes of ions and neutrals would undergo reactions in different ratios according to the kinetics described in the translating mixed model, i.e. the calculation of the etch yield is dependent on the flux ratios. Variation in the ion energy would subsequently affect these calculations, e.g. higher energies lead to the promotion of ion-enhanced chemical reactions over physical sputtering. Regarding the second issue, the scattering distributions for neutrals and ions themselves differ in this model - ions follow a Gaussian scattering profile while neutrals scatter isotropically. Therefore, the scattered particle trajectories from cells would also vary if subjected to different fluxes of ions and neutrals. Additionally, the scattering probability of ionic species was dependent on the angle of incidence as well as the weighted average of the yields for the etching reactions that could occur at a given ion energy. For example, at lower ion energies, the curve representing the scattering probability function would tend to favor the angular dependence of physical sputtering, whereas at higher ion energies, a shift towards the angular dependence for chemical etching should be observed. This would lead to different scattering or consumption probabilities at different ion energies, particular at values below the threshold for certain reactions to occur. For example, in the TML modeled case of HfLaO etching in Cl_2 plasma, the threshold energies for the formation of MCl_x type products (where M = Hf, La) were all in the range of 71 - 85 eV. For ion energies below or just past this value (e.g. 75 eV), the reduced contribution of these etch products could result in a shift in the nature of the scattering probability curves. The results of the variation in scattering curves for the three ion energy values considered in the MC simulations are plotted in Figure 5.5.

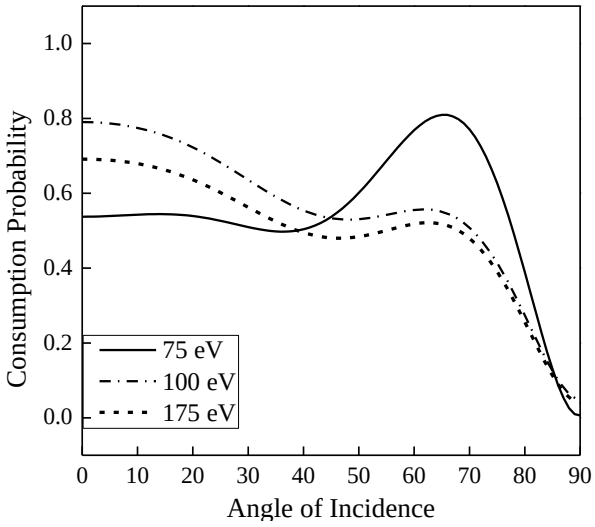

Figure 5.5 The angular dependence of consumption/scattering probability for E_{ion} = 75, 100 and 175 eV in the etching of $Hf_{0.25}La_{0.12}O_{0.63}$.

It should also be noted that if a cell was determined to have been deposited, its composition was based on that of the cells adjacent to it. This signifies that the material deposited above the initial surface is not entirely composed of chlorine, which would be unphysical, but would also consist of hafnium, lanthanum, oxygen and chlorine. This aspect of the MC model is related to the "movement flux" from the substrate to create a well mixed layer.

Finally, the case of E_{ion} = 175 eV was considered. The results are shown in Figure 5.6. The maximum predicted etch depth of the HfLaO film at this value of ion energy was about twice that of the 100 eV simulated value. This was also in good agreement with the relative etch rates measured via QCM (~23 Å/min for 175 eV compared to ~10 Å/min). It can be seen that that the trenching effect at the feature corners became visible for the feature of aspect ratio 3, as well as the 1.5 case, however this development was not observed in the 6 feature. The feature profiles for all three aspect ratio values displayed the development of a nearly vertical upper sidewall with a tapered lower region. Only slight variations in the angle of the lower sidewall

were present, however the exaggeration of the trenching phenomenon makes defining the exact region somewhat difficult.

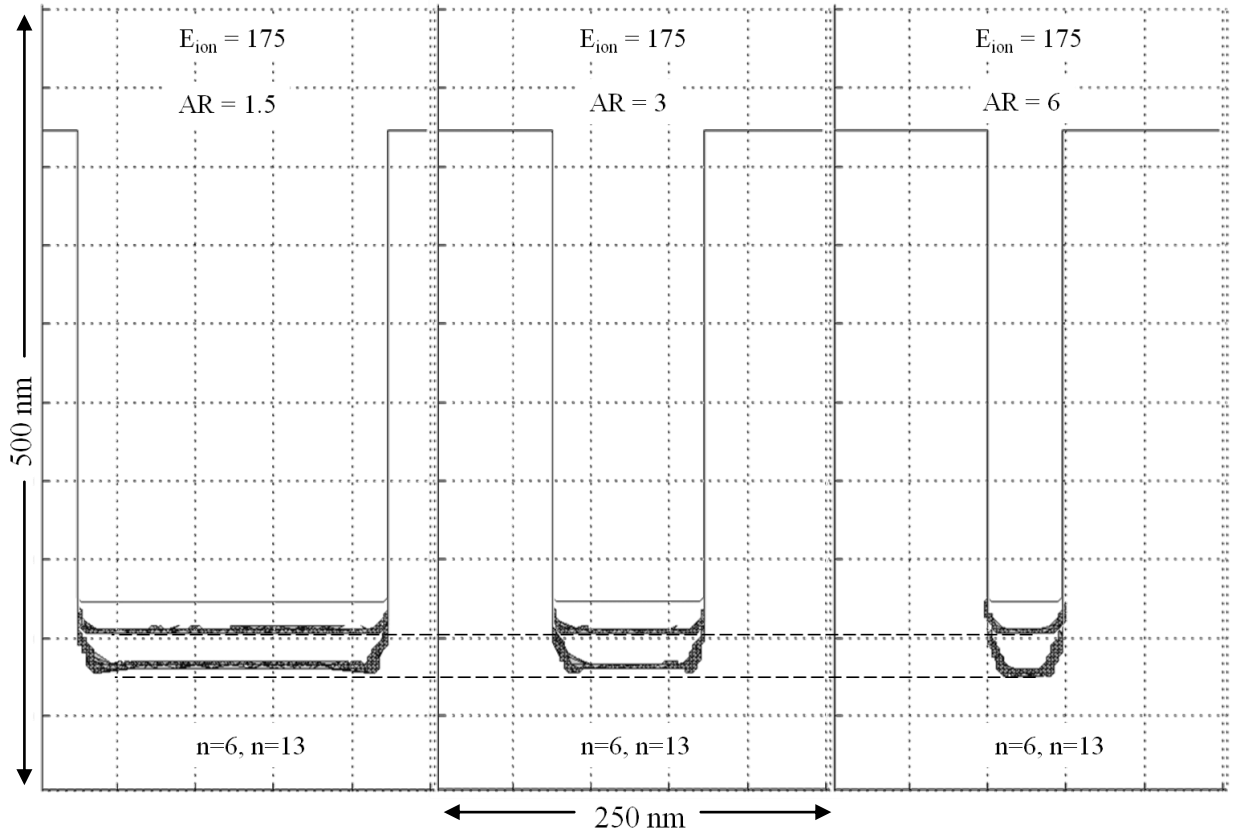

Figure 5.6 MC simulations showing the effect of increasing aspect ratio at E_{ion} = 175 eV for the etching of $Hf_{0.25}La_{0.12}O_{0.63}$ in Cl_2 chemistry.

Figure 5.7 shows the effect of ion energy variation at a fixed aspect ratio more clearly, illustrating the trend that may not have been apparent from the previous plots. The formation of notches in the corners starts to develop during the E_{ion} = 175 eV simulation, even as the upper portion of the sidewall becomes more vertical.

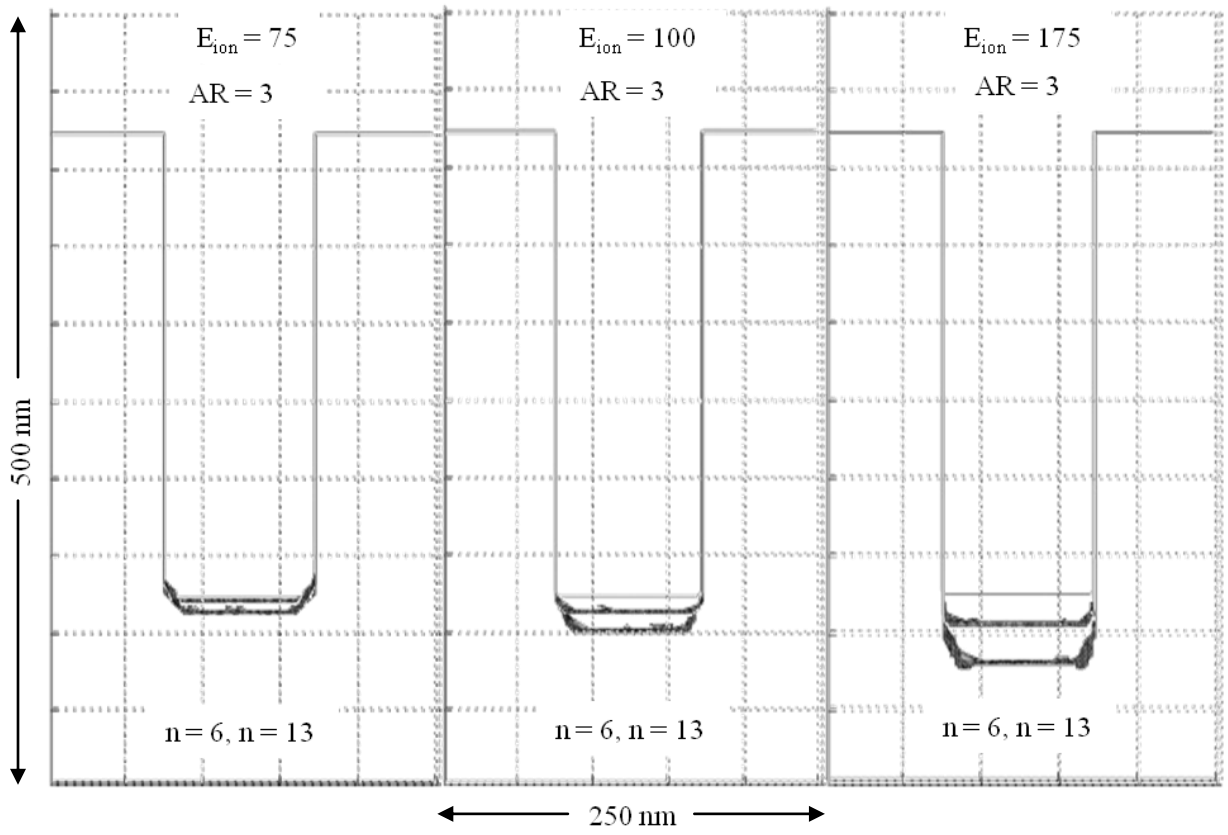

Figure 5.7 MC simulations showing the effect of increasing E_{ion} at AR =3 for the etching of $Hf_{0.25}La_{0.12}O_{0.63}$ in Cl_2 chemistry.

5.3 Comparison of Different Material Systems - HfO_2 vs. HfLaO

As La addition to HfO_2 was demonstrated to lower the macroscopic etch rate in Chapter 3, the effect on the profile geometry was subsequently of interest. Simulations were carried out using the fitted parameters for HfO_2 films that were etched in the ECR reactor in a prior study. To compensate for the difference in fluxes between the system, the neutral to ion ratio used in the MC simulations for HfO_2 was half that of the value used for the HfLaO simulations. The comparison between the simulation results for AR = 3, E_{ion} = 100 eV are shown in Figure 5.8.

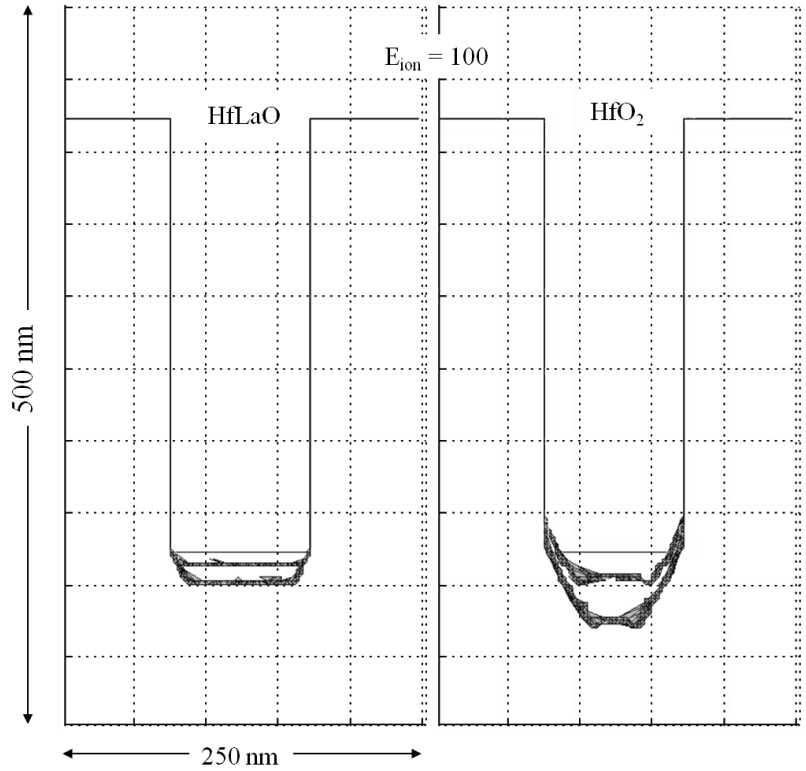

Figure 5.8 MC simulations comparing the etched profiles in $Hf_{0.25}La_{0.12}O_{0.63}$ (left) and HfO_2 (right) in Cl_2 chemistry for E_{ion} = 100 eV, AR = 3.

The maximum etch depth observed for HfO_2 was reproduced in the feature profile simulator in accordance with the etch rate measurements. Overall, the HfO_2 profile showed a profile with more sloped sidewalls, as well as more pronounced trenching effects. For this material, the deposition above the initial feature plane was observed at E_{ion} = 100 eV, whereas this effect was only seen at the low ion energy condition (E_{ion} = 75 eV) for HfLaO. The most likely cause for variations in profile would be the different sticking coefficients for neutrals used in the La-containing film compared to pure HfO_2.

5.4 Comparison of MC Modeling with Experimental Profiles

In order to compare the predictions from the MC simulations to experimental work, the patterned $Hf_{0.25}La_{0.12}O_{0.63}$ samples were exposed to a 400 W, 5 mT, Cl_2 plasma at varying bias energy and process times. This baseline condition was selected in order to match the TML model fitting conditions as closely as possible. Images of the samples were taken before and after the etch process in order to select the appropriate aspect ratio. First, the results of etching the ~2000 Å thick $Hf_{0.25}La_{0.12}O_{0.63}$ film at the aforementioned baseline condition for 15 minutes at -100 V were tested. It was found that in this case the aspect ratio of the features was roughly 6. It should be noted that owing to constraints on the dimensions of the simulation domain in the vertical dimension that the MC simulation results had to be scaled up to match the height of the PR mask. Care was taken to maintain the aspect ratio when scaling. The leftmost panel of Figure 5.7 shows the pre-etch SEM image with the MC prediction after 9 iterations of 4 x 10^7 particles superimposed. The middle image shows the feature after plasma exposure. It should be noted that the PR mask appeared to have been entirely etched away. Based on the previous thickness of the mask (~1300 nm) and the total etch time employed, the calculated rate of etching was ~866 Å/min, which falls within the range found in literature for this resist.

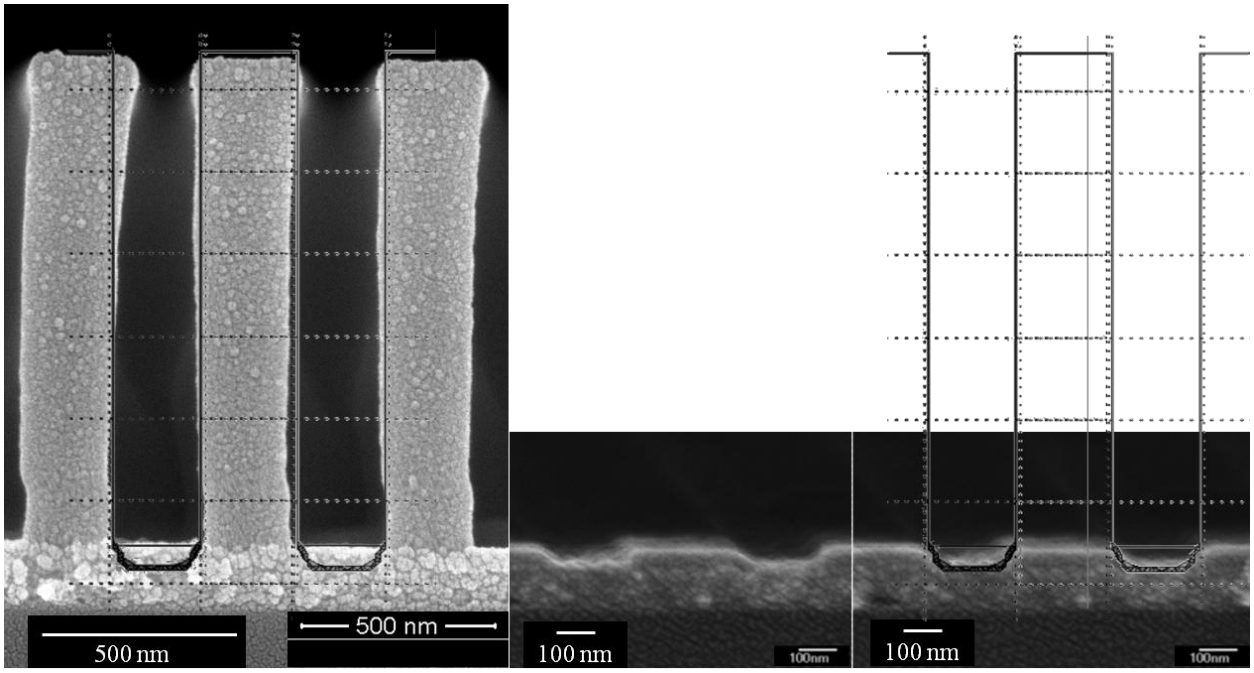

Figure 5.9 Comparison of simulated feature profiles with experimental results for the etching of $Hf_{0.25}La_{0.12}O_{0.63}$ in a 400 W, 5 mT, Cl_2 plasma at -100 V bias for 15 minutes.

Good agreement was observed between the simulated and experimental profiles. While the removal of the resist did not appear to have a noticeable effect on the development of the profile, i.e. no deposition of resist was observed, it should be noted that in the case of a non-reactive mask, scattering effects could become more significant. Additionally, if the selectivity calculation for the resist vs. the underlying film is not properly considered, this could have substantial effects on the desired profile due to the aspect ratio of the features changing rapidly.

5.5 Application to Shallow Trench Isolation (STI)

In order to test the TML model's robustness, the methodology that has been utilized thus far for Hf-based oxides was applied to a different material and chemistry system - Si patterning

in Cl_2 with O_2 addition (the STI process). Although Si is a simple material compared to HfLaO, the variation in feed gas chemistry for the STI process provides a separate and distinct degree of complexity that serves as a good test of the model's adaptability. The TML module was calibrated based on experimental etch rate and QMS measurements taken in the ECR chamber for 0% and 6% O_2 addition. Predictions for other values of O_2 addition were then obtained by simply varying the initial flux ratios of the simulation input file. Comparison of modeling to the three major data sources is provided in a condensed summary here as the details are available in literature [Hsu and Marchack, submitted]. The list of resulting kinetic parameter from fitting the TML model for this case is provided in Appendix B. These parameters were then used as inputs into the feature scale Monte Carlo (MC) method discussed in the following section, ensuring consistency and robustness for this hybrid approach.

5.5.1 Effect of Feed Gas Chemistry on Etch Rate

The etch rate of Si in a 500 W, 3 mT, Cl_2 plasma was measured using laser interferometry in the previously mentioned ECR reactor as a function of ion energy for 0% and 6% O_2 addition, and as a function of O_2 addition for E_{ion} = 80 eV. The results are shown in Figure 5.10 below.

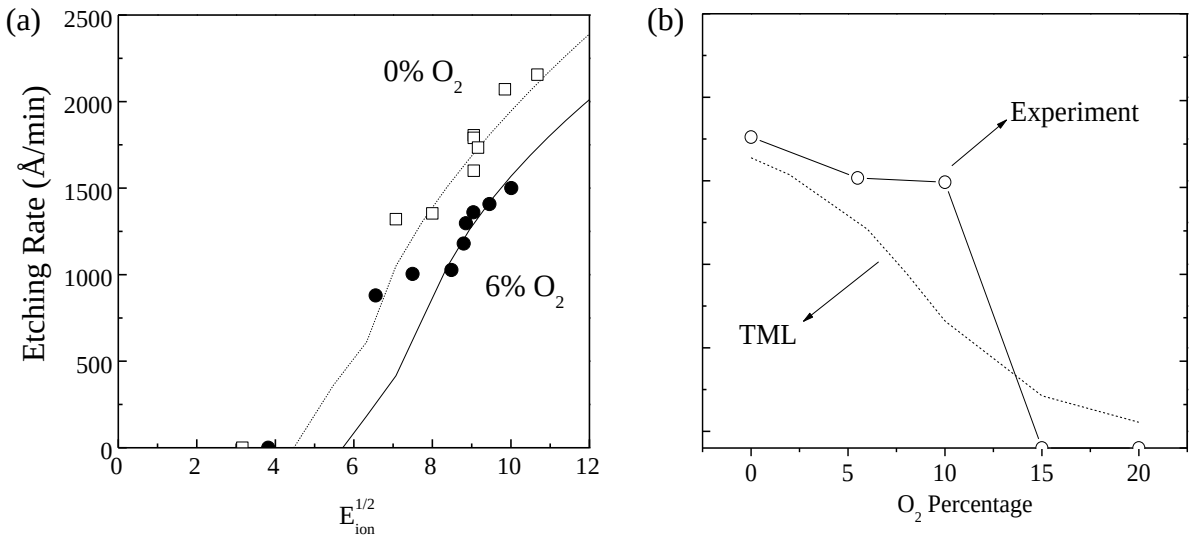

Figure 5.10 (a) Plot of Si etch rate as a function of E_{ion} for 0% and 6% O_2 addition and (b) as a function of O_2 concentration for E_{ion} = 80 eV. In both plots the experimental data is presented as scattered points and the corresponding TML fits are dashed or solid lines.

In the absence of O_2, the threshold energy was approximately 9 eV, which is consistent with the reported values, 4 eV ~ 10 eV, for ion assisted etching of Si in chlorine plasmas. (Vitale, Chae et al. 2001; Sha and Chang 2004) For 6% O_2 addition, the square-root-dependency of the ion energy remains, however the threshold energy increased to ~12 eV. It can be seen that the TML model matches the reduction in etch rate well.

For the case of O_2 addition at constant ion energy, the etching rate does not change significantly with up to ~10 % O_2 addition. As the O_2 addition increases from 10% to 15%, the etching rate decreases abruptly. At O_2 concentrations over 15%, the etching rate was below the measurement sensitivity using laser interferometry. Since the etch rate measurements using this technique rely on a dynamic change of the film thickness, accurate measurements are only possible above a 200 Å/min etch rate. Overall the TML model agrees well with the trend displayed but does not exhibit the sharp decrease from 10 to 15% O_2 addition as seen in the

experimental results. The general decrease in the etch rate as O_2 is added can be explained by the extent of surface passivation. It is generally accepted that addition of O_2 promotes the oxidation of Si to SiO_2, and additionally leads to the formation of SiO_xCl_y type products which ultimately adsorb on the surface. The following section deals with experimental support for this theory through surface analysis.

5.5.2 Surface Composition

Figure 5.11 compares ex-situ XPS measurements (left) of the Si surface as a function of O_2 concentration in the inlet gas to the predicted mixing layer composition (right) as obtained by the TML model. The percentage of oxygen in the mixing layer is shown to increase to about 40% for the case of 15% addition, which corresponds to a comparable decrease in the percentage of Si present from 60% to 10%. The amount of chlorine increases slightly with increasing oxygen addition by about 10%, which indicates that O predominantly bonds to Si. The degree of surface chlorination for the pure Cl_2 plasma (~32%) agrees well with previously published results.(Cheng, Guinn et al. 1994)

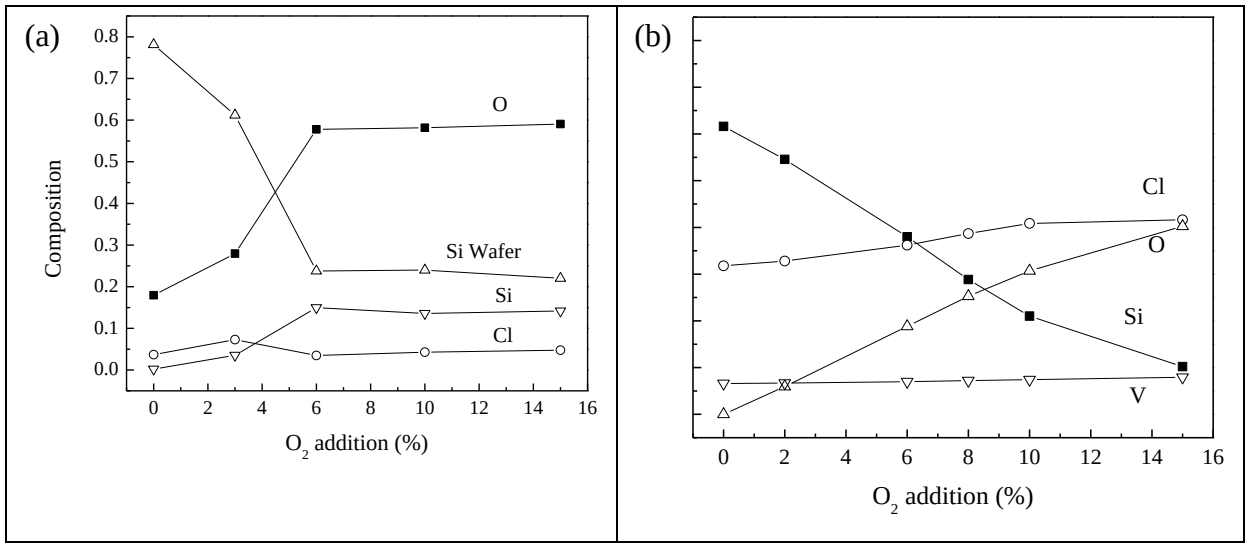

Figure 5.11 (a) Elemental composition of Si, O, and Cl of the surface etched using Cl_2 plasmas with increasing O_2 addition for two minutes under 5 mT, 500 W ECR power, and 80 eV ion energy measured by XPS. (b) TML model prediction of mixing layer composition.

Discrepancies between the experimental and simulated compositions can partially be attributed to the fact that XPS measurements were done ex-situ and thus samples were exposed to ambient oxygen levels prior to their analysis, leading to additional surface reactions(e.g. the 0% O_2 case contains ~20% O). Additionally the mixing layer refers to the top 25Å of the surface whereas XPS can potentially detect electrons from an escape depth of 100Å.

5.5.3 Etch Products Distribution

The effect of O_2 addition to Cl_2 plasmas on Si etching was also investigated through the study of the ionic etch products distribution. Figure 5.12 (a) shows the dominant ionic species measured using QMS. It is shown that the dominant ionic species are $SiCl^+$ and $SiCl_3^+$ in the absence of O_2. With 6 % O_2 addition, the dominant ionic species remain the same and approximately 4% of $SiOCl_2^+$ and 0.5% of $Si_2OCl_5^+$ are observed. The detection of silicon

oxychloride species suggests oxygen is involved in the surface reaction kinetics. Figure 5.12 (b) shows the simulated proportions of etch products from the TML model, which capture the qualitative trends observed experimentally.

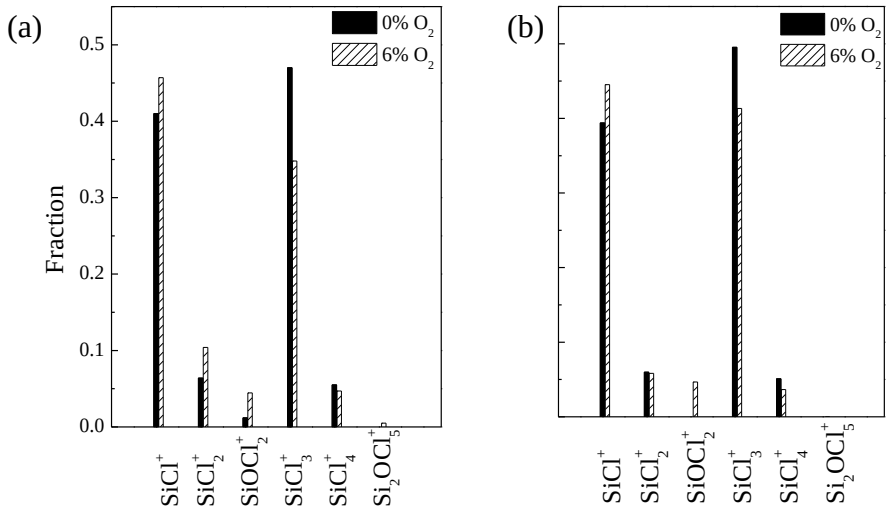

Figure 5.12 (a) The dominant ionic species measured by the mass spectrometer while etching silicon using Cl_2 plasmas with 0 % and 6 % of O_2 addition under 5 mT, 500 W ECR power and 80 eV ion energy. (b) TML simulation of the ionic etch products.

5.5.4 Feature Profile Simulation

To study the effect of O_2 addition to the etched feature profile of STI, patterned samples were etched using the baseline conditions without and with up to 8% O_2 addition for 40 and 80 second durations. The initial stack for trench definition in these experiments consisted of silicon nitride, followed by pad silicon oxide over a silicon substrate. The thicknesses of the silicon nitride and the pad silicon oxide layers were 100 nm and 10 nm respectively. Silicon nitride serves as the hard mask and was patterned prior to STI definition. The etched trench profiles were examined using SEM. The trench sidewall angle as a function of the amount of O_2 addition

and representative SEM images are shown in Figure 5.13. It is shown that the top sidewall angle is approximately 90° regardless of the amount of O_2 addition. This attribute can be explained by very low sticking probabilities of the nitride hard mask or rather the lack of available surface sites. As a result, the initial profile sidewalls receive a relatively constant flux of neutrals until the aspect ratio increases and shadowing becomes significant. The averaged bottom sidewall angle decreases from 77.6° to 73.6° from 0% to 8% O_2 addition. We note that the error bars were determined by the standard deviation of numbers of measurements over several trench profiles shown in the SEM images.

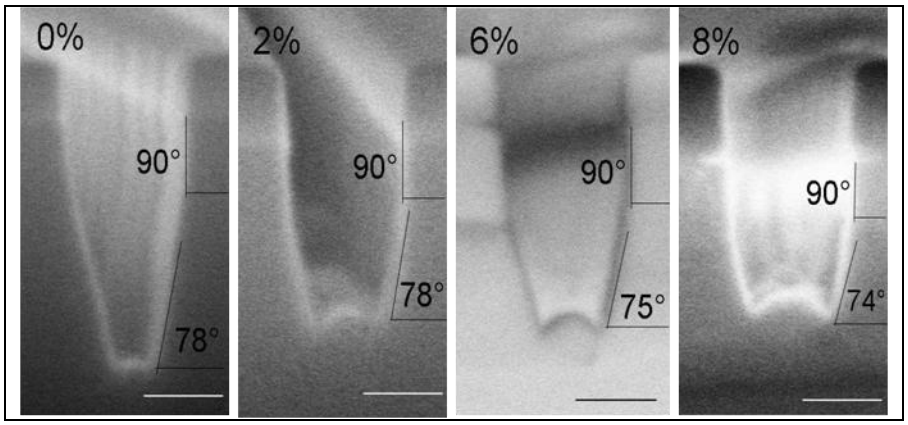

Figure 5.13 Representative cross sectional SEM images of the samples etched for 80 seconds under 500 W, 5 mT, and 80 eV ion energy using Cl_2 plasmas under various degrees of O_2 addition. The scale bars shown are 100 nm.

It is known that the deposition of etch products, surface passivation (by surface oxidation), ion scattering and the ion angular distribution are the major factors that affect the etched trench profile. (Hoang, Hsu et al. 2008) In patterned samples, the fraction of the area with Si (as opposed to silicon nitride hard mask) exposed to the plasma is small and is estimated to be well below 15%. The amount of etch products formed during etching is not large and the etch products play a less significant role in affecting the etched feature profile in the present study.

The ion angular distribution is a function of the sheath voltage, sheath thickness and ion temperature.(Lieberman and Lichtenberg 2005) These are not expected to change significantly with a relatively small amount of O_2 addition (no more than 8%) in the Cl_2 plasma under the baseline condition. The most important factor that alters the etched profile with various amounts of O_2 addition in this study is therefore believed to be the incorporation of oxygen in the surface kinetics. Surface oxidation increases the scattering of ions from sloped trench side walls. (Dalton, Arnold et al. 1993) MD simulations by Abrams also showed disparity between the scattering angle of ions off of Si and O atoms, although it should be noted that this was for the case of Ar ions. (Abrams and Graves 1998) This could be responsible for the formation of microtrenches observed in the samples etched with O_2-containing conditions, shown in Figure 9(b). In addition, the etched surface changes to a more SiO_2-like surface with surface oxidation. Chang et al. reported that the ion angular dependence in etching SiO_2 shows a maximum etching yield at about 60° off normal incidence. (Chang and Sawin 2001) As a result, the etched trench conforms to a smaller sidewall angle (closer to 60°) as the surface changes to SiO_2-like. This qualitatively explains the decrease of the bottom sidewall angle with the addition of O_2.

The feature scale profile simulator was then used to obtain simulated etch profiles for comparison to the experimental work. The ion energy value and neutral to ion ratio used were 80 eV and 50 respectively as calculated from the aforementioned experimental measurements in the ECR reactor. The reaction coefficients and other kinetic parameters from the TML model in Appendix B were used in this MC module. Simulations were compared to both 40s and 80s etch time profiles in order to evaluate the model's accuracy in capturing the feature evolution throughout the etching process. Only the plasma composition values were changed from simulation to simulation to reflect the addition of oxygen in the inlet gas feed. The 40s and 80s

simulation profiles were captured after 7 and 15 iterations of 1.0 x 10^7 particles respectively. Good agreement was demonstrated between the experimental and simulated profiles for both time values as shown in Figure 5.14.

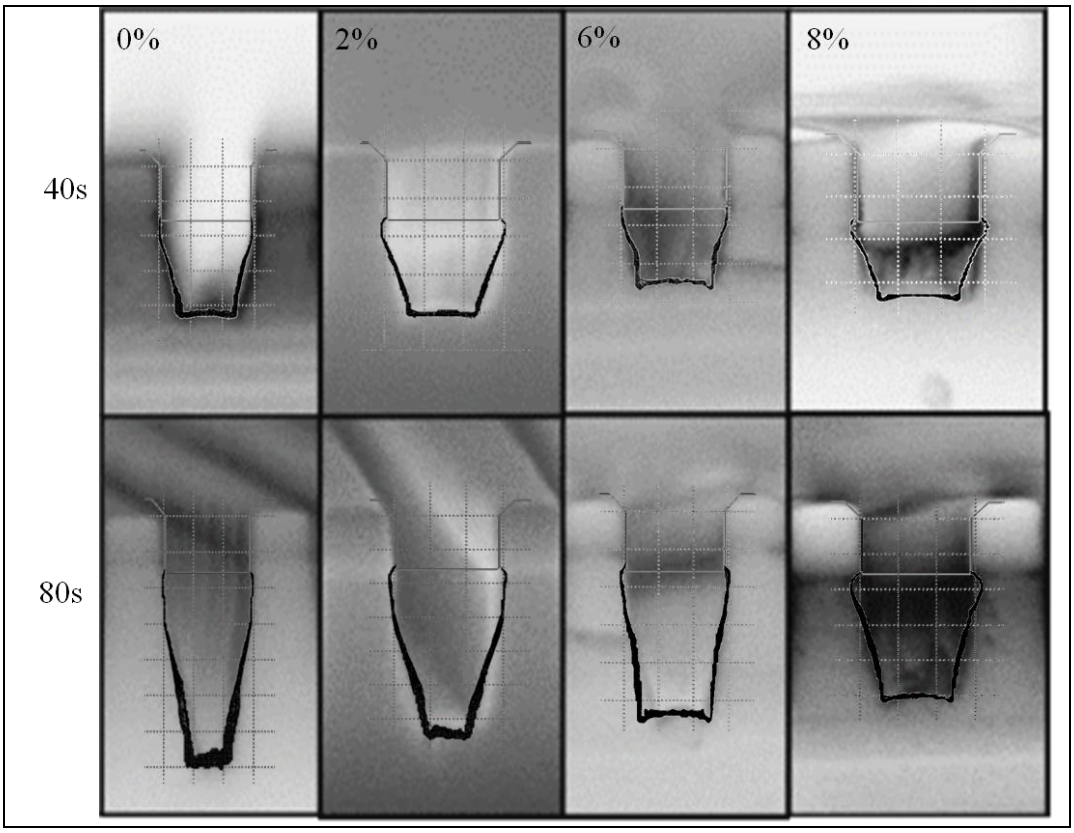

Figure 5.14 Comparison of the simulated and experimental etch profiles for samples etched for 40 s (top row) and 80 s (bottom row) at 500W, 5mT and 80 eV ion energy using Cl_2 plasmas under various degrees of O_2 addition.

The MC module captured the microtrenching effect with increasing oxygen addition, as well as the variation in trench depth. This result provided strong support for the depiction of the etching process used in the TML module.

5.6 Summary of Feature Profile Modeling

Input of fitted kinetic parameters from TML modeling of two distinct material systems into a Monte Carlo based feature profile simulator yielded good results in predicting the evolution of these materials at nanometer length scales. The model demonstrated a capacity to handle both complex substrates (HfLaO composites) and gas chemistries (Cl_2 + O_2). Future potential application of the model to a system where both components are complex, e.g. a multi-component, multi-functional oxide treated in a F-based gas chemistry would serve as an even more strenuous test of the validity of this approach.

CHAPTER 6: SUMMARY

Thermodynamic assessment using volatility diagrams for the etching of HfO_2 and La_2O_3 in Cl_2/BCl_3 and F_2 chemistries was carried out to demonstrate the importance of fundamental thermodynamic information in assessing etch feasibility. It was predicted that Cl_2-based chemistries could serve as a viable candidate for etching these constituent oxides, thus providing a more environmentally sensitive approach. An in-situ etch study of $Hf_{0.22}La_{0.16}O_{0.62}$ films in Cl_2/BCl_3 plasmas was then carried out in a modified inductively coupled plasma (ICP) reactor using a quartz crystal microbalance, quadrupole mass spectrometer and x-ray photoelectron spectroscopy to provide quantitative information about the *in situ* etch rate, etch products and surface composition post-plasma exposure.

From QCM measurements of the *in situ* etch rate, the maximum calculated etch rate of $Hf_{0.25}La_{0.12}O_{0.63}$ films exposed to a 400W, 5 mT, Cl_2 plasma was 27 Å/min , while the maximum etch rate observed at the 400W, 15 mT, BCl_3 baseline was 17 Å/min. The results were verified by comparing to cross-sectional SEM measurements. The QCM frequency response spectra provided a greater level of insight into progression of the etch progress than was available from ex situ measurements alone, with a "deposition" region observed shortly after disengaging the bias and plasma for the case of pure La_2O_3 etching in Cl_2 and BCl_3. This region was found to scale with ion energy in the case of BCl_3 chemistry but was relatively constant for Cl_2. LaCl and LaOCl (3.9 : 1.0) and LaB, LaB_2O, LaBOCl and LaO_2Cl (1.2 : 1.1 : 1.3 : 1.0) were observed as the dominant La-containing species for La_2O_3 films exposed to the Cl_2 and BCl_3 baseline conditions, respectively at -100 V bias voltage. The surface compositions of the $Hf_{0.25}La_{0.12}O_{0.63}$ films after etching at the aforementioned conditions revealed a preferential reaction of La over

Hf in BCl_3 compared to Cl_2 chemistry. XPS analysis of pure La_2O_3 films after 5 minutes etching also revealed O-La-Cl bonding in the surface layers for both chemistries as well as a significant amount of Cl retained (~10%), suggesting the development of a stable $LaCl_x$ layer which could potentially serve as an etch stop barrier for this material. These observations were consistent with quantitatively lower etch rate of $Hf_{0.25}La_{0.12}O_{0.63}$ in BCl_3 compared to Cl_2, as well as the differing characteristics of the QCM frequency response curves. Overall, Cl_2 chemistry provided a higher overall etch rate for the HfLaO composite films, but in future considerations over etch chemistry the desired stoichiometry of the final film, as well as the difficulties in removing potentially non-volatile $La_xO_yCl_z$ layers should be taken into account.

A previously developed, surface site-based phenomenological model was used to fit the $Hf_xLa_yO_z$ and La_2O_3 etch rate data. The model demonstrated good fits for the experimental etch rates of $Hf_xLa_yO_z$ and La_2O_3, providing evidence of its robust nature. Fitted parameters for this data were compared to that of HfAlO. The results were analyzed in the context of the variation in plasma conditions between the ECR and ICP chambers, and were found to agree with the thermodynamic properties of HfO_2, Al_2O_3 and La_2O_3. Building upon this foundation, a kinetics-based, translating mixed layer (TML) model was constructed using the experimental measurements that were detailed for the high-k oxides in Chapter 3. Good agreement was shown between the TML model's simulated results and etch rate data. An additional degree of validation was provided through a comparison of the model's predicted composition of the surface mixing layer and the XPS-measured film compositions after plasma exposure. In the case of the La-containing films, larger discrepancies between the TML predictions and experimental data were recorded, specifically in the case of the absolute values of the metal fractions where the simulation values were notably less than those of the experimental measurements. This was

largely attributed to the complexity of modeling the La_2O_3 etch behavior where the QCM frequency response data revealed competition between material removal and the formation of non-volatile surface species found through XPS.

The final validation of this approach was to assess the fitted kinetic parameters for complex oxide etching in Cl-based chemistry (such as reaction rate coefficients, threshold energies and sticking probabilities) at feature scale levels. The results from the TML model were coupled to a Monte Carlo based feature profile simulator and used to predict the variation of the etched feature profiles of $Hf_{0.25}La_{0.12}O_{0.63}$ films for varying aspect ratios (1.5, 3 and 6) and ion energies (75, 100 and 175 eV). In order to compare to experimental results, patterned features of varying aspect ratio were written using an e-beam tool on the HfLaO films using a ZEP520A photoresist mask. Good agreement was achieved with the etched profile at 100 eV and AR = 5. As a test of the model's ability to handle variations in gas chemistry with a material system besides that of high-k dielectrics, this methodology was also applied to the shallow trench isolation process (Si etching in Cl_2/O_2 chemistry). The model showed good fitting of the major process parameters (etch rate, etch product ratios and surface composition) and showed an ability to predict the profile variation with 0, 2, 6 and 8% oxygen addition to a pure Cl_2 plasma for the etching of Si.

APPENDICES

APPENDIX A

APPENDIX A.1 Inductively Coupled Plasma Chamber Guidelines

A.1.1. Emergency Shut Down Procedures

I. In case of Cl_2 is smelled

1. Close tank valve.
2. Close others valve if possible. The diaphragm valve D4, located directly behind chamber, and the regulator R1 on Cl_2 cylinder located in gas cabinet to the right of the MFC cabinet.

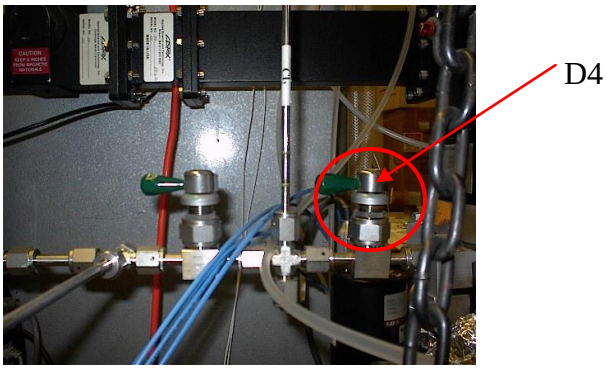

Figure 1. D4 valve directly behind chamber

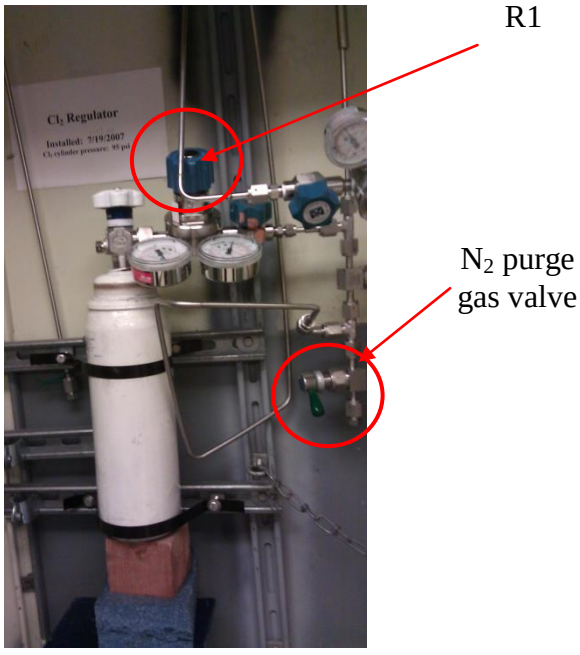

Figure 2. R1 regulator located in chlorine gas cabinet

3. Evacuate.
4. Contact EH&S as needed.

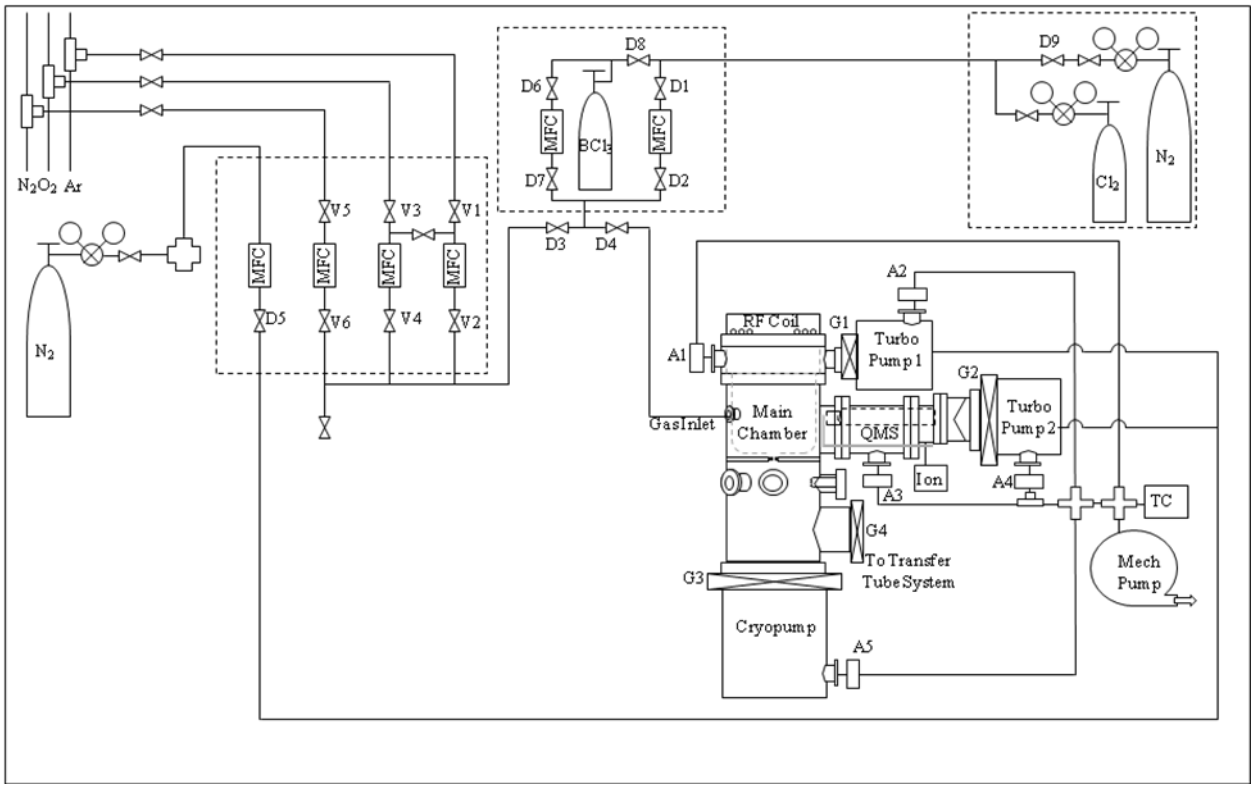

Figure 3. Gas line system for ICP system including corrosive gases Cl_2 and BCl_3, inert gases Ar and N_2, and O_2.

The ICP system includes corrosive and inert gas lines, turbomolecular pump, cryopump and mechanical pump. V1 and V2 are the valves for Ar, V3 and V4 are the valves for O_2. Since the flow rate of the Ar MFC is small (10 sccm), a connection was installed between the Ar and O_2 gas lines to enable a higher flow rate through the O_2 MFC (50 sccm). V5 and V6 are the valves for high purity N_2 and D5 is a valve for industrial N_2 which flows through the back of the TMP to dilute the corrosive gas into mechanical pump. Two corrosive gases are used: Cl_2 and BCl_3, which share a double wall corrosive gas line leading to the reactor. A N_2 cylinder is connected which allows cycle purging of the system. D1 and D2 are the valves for Cl_2 and the purge N_2 gas, and D6 and D7 are the valves for BCl_3. D3 and D4 control the inert and corrosive gas flow into the chamber. A1 and A3 are the roughing valves which connect the chamber to its

mechanical pump, and A2 and A4 are the roughing valves between the TMPs and the mechanical pump.

II. In case a noise is heard from turbo molecular pump on Main Chamber

1. Close manual gate valve between turbo pump and chamber.

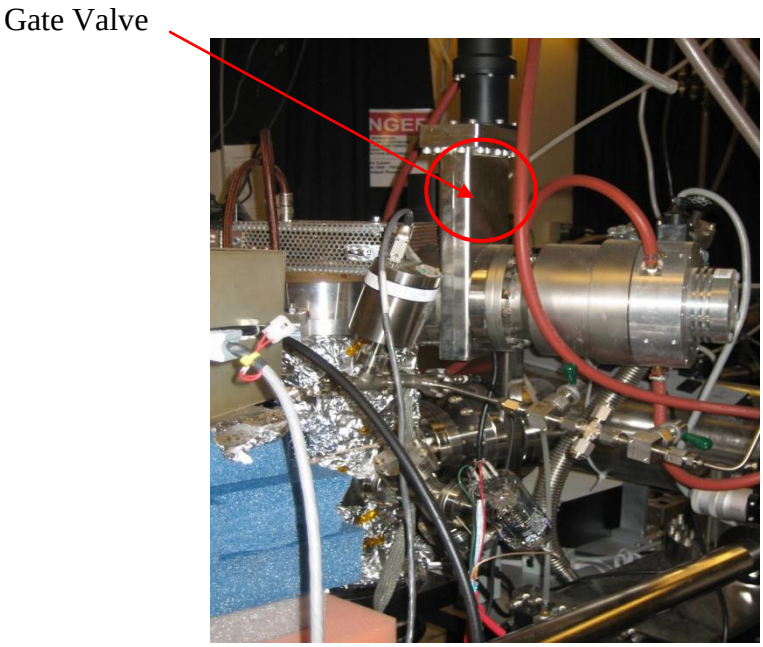

Figure 4. Gate Valve for Main Chamber Turbo Pump

2. Turn off the turbo molecular pump by pushing the "stop" button on the controller.

Stop button (read label to confirm)

Figure 5. Turbo Pump Controller for Chamber

3. Isolate mechanical pump by closing manual valve between turbo and MP.

III. In case a noise is heard from mechanical pump on Chamber

1. Close manual gate valve between turbo pump and chamber. (See Figure 3)
2. Turn off the turbo molecular pump by pushing the "stop" button on the controller. (See Figure 4) And close the roughing from turbo pump to mechanical pump.
3. Switch off the mechanical pump by turning off the breaker.

IV. In case a ratcheting is heard from Cryopump on Chamber

1. Close the pneumatic gate valve between ICP and Cryopump by pressing the corresponding switch on the control box (trace the cable if unsure). (See Figure 5)

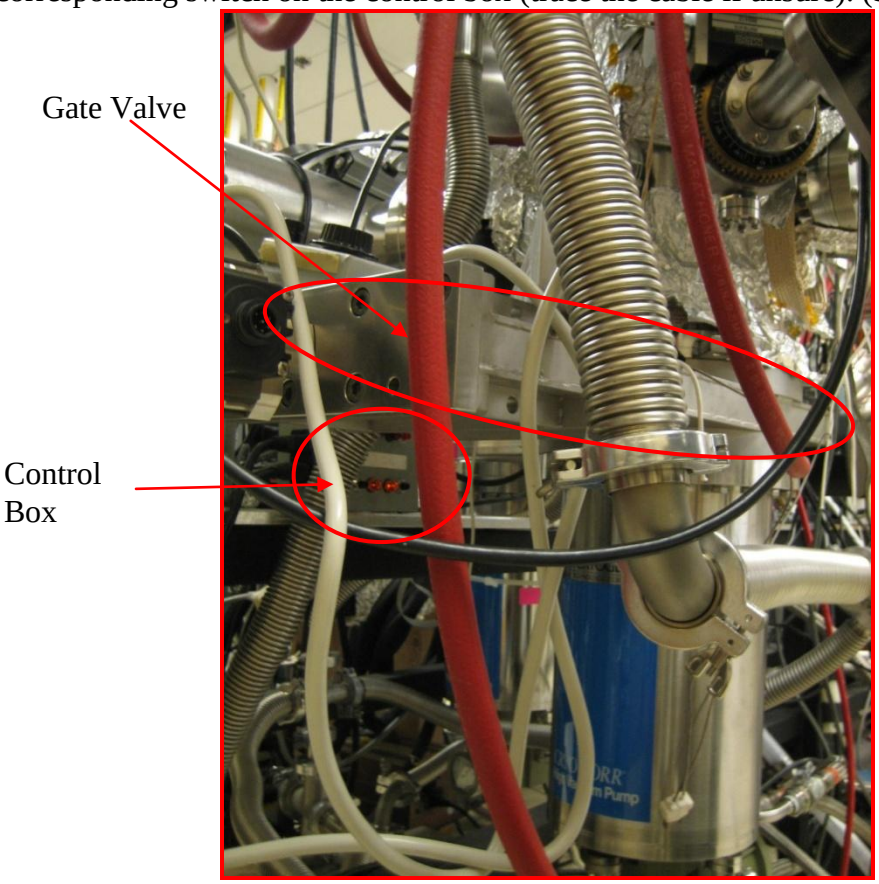

Figure 6. Gate Valve between Cryopump and ICP

2. Ensure that the roughing valve between the cryopump and the chamber mechanical pump is closed.

3. Turn off the cryopump by flipping the white circuit breaker on the compressor (See Figure 6 - in the event of pump failure this may turn off automatically – check to see if the unit is operating).

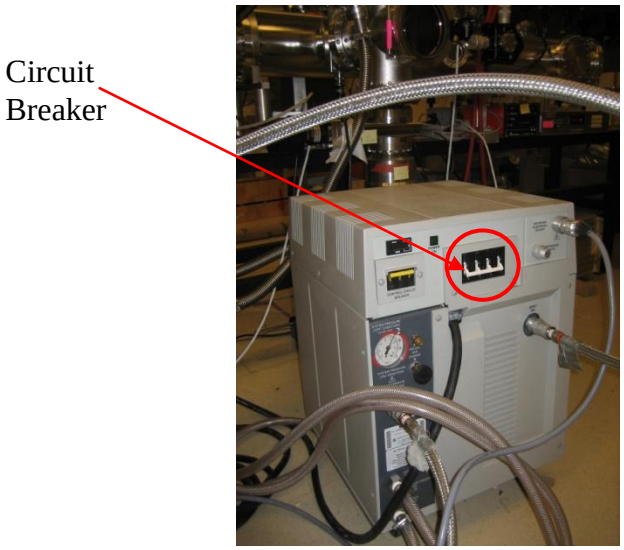

Figure 7. Compressor and Circuit Breaker Switch

V. In case noises are heard from any of the electronics

1. If units have power switches, turn them off and unplug all units (see pictures below).

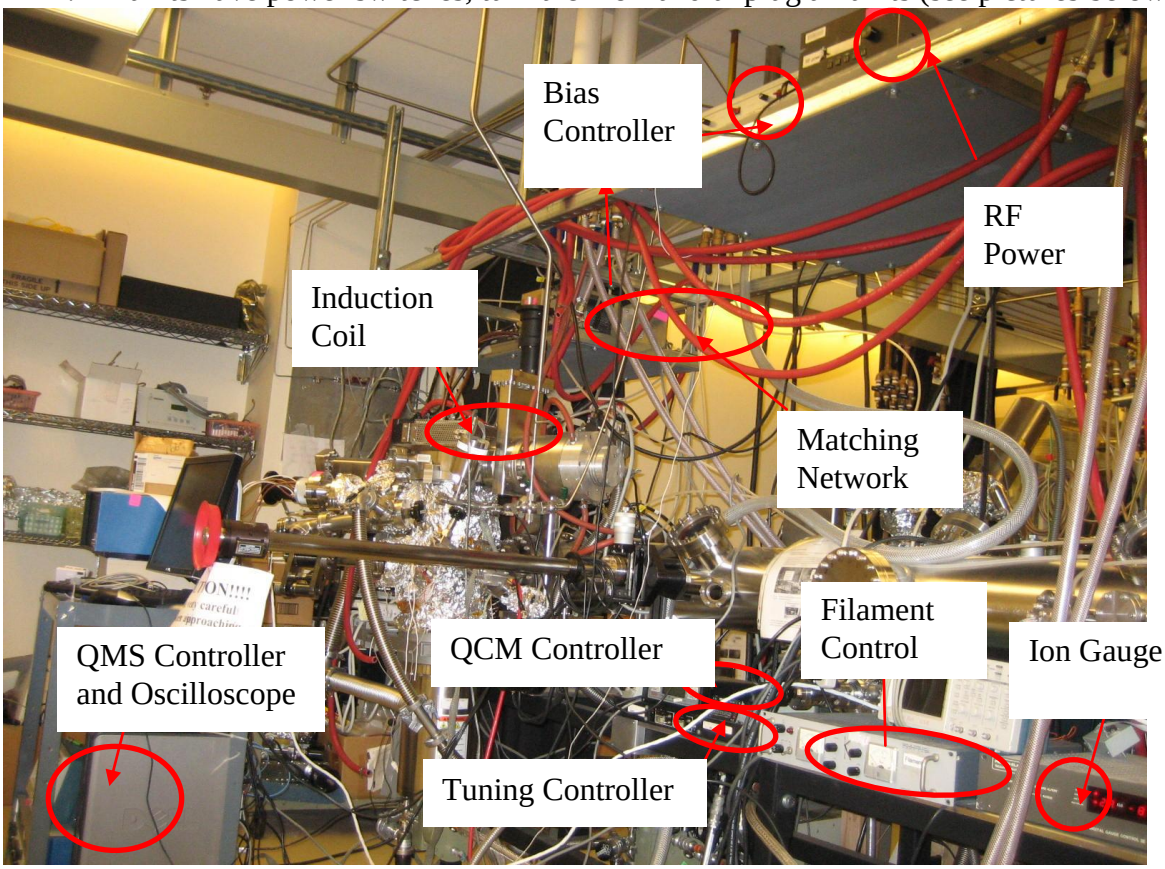

Figure 8. The components of ICP system

A.1.2. Schematics

ICP reactor

Main chamber – Side view

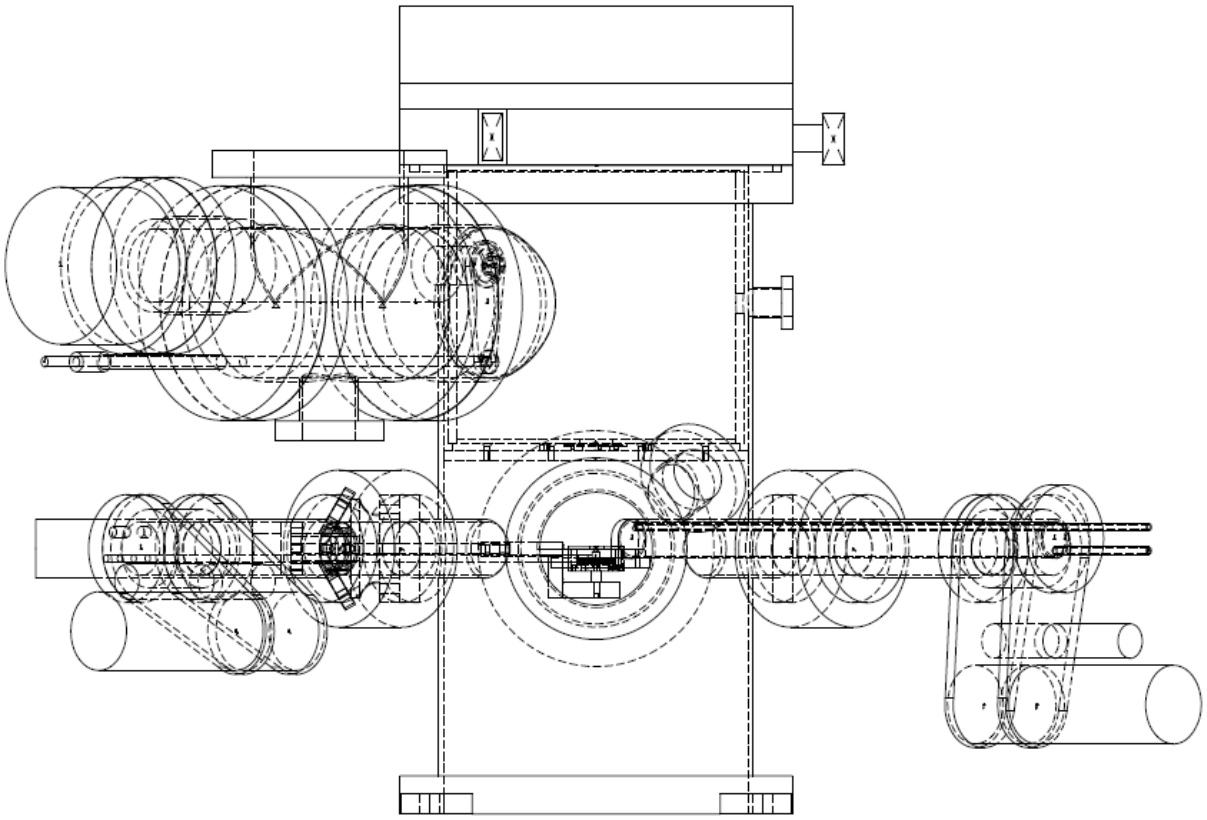

University of California, Los Angeles, Department of Chemical and Biomolecular Engineering

Part		Material	Stainless steel				
Filename		Scale	Yes	Units	inch	Quantity	1
Designer	Yunpeng Yin(MIT)	Date	6/11/2003				
Revised by		Date					
Contractor	Applied Vacuum Technologies	Date	6/11/2003				
Comments			Tolerance			+/- .0001	

ICP reactor

Main chamber – Isometric view

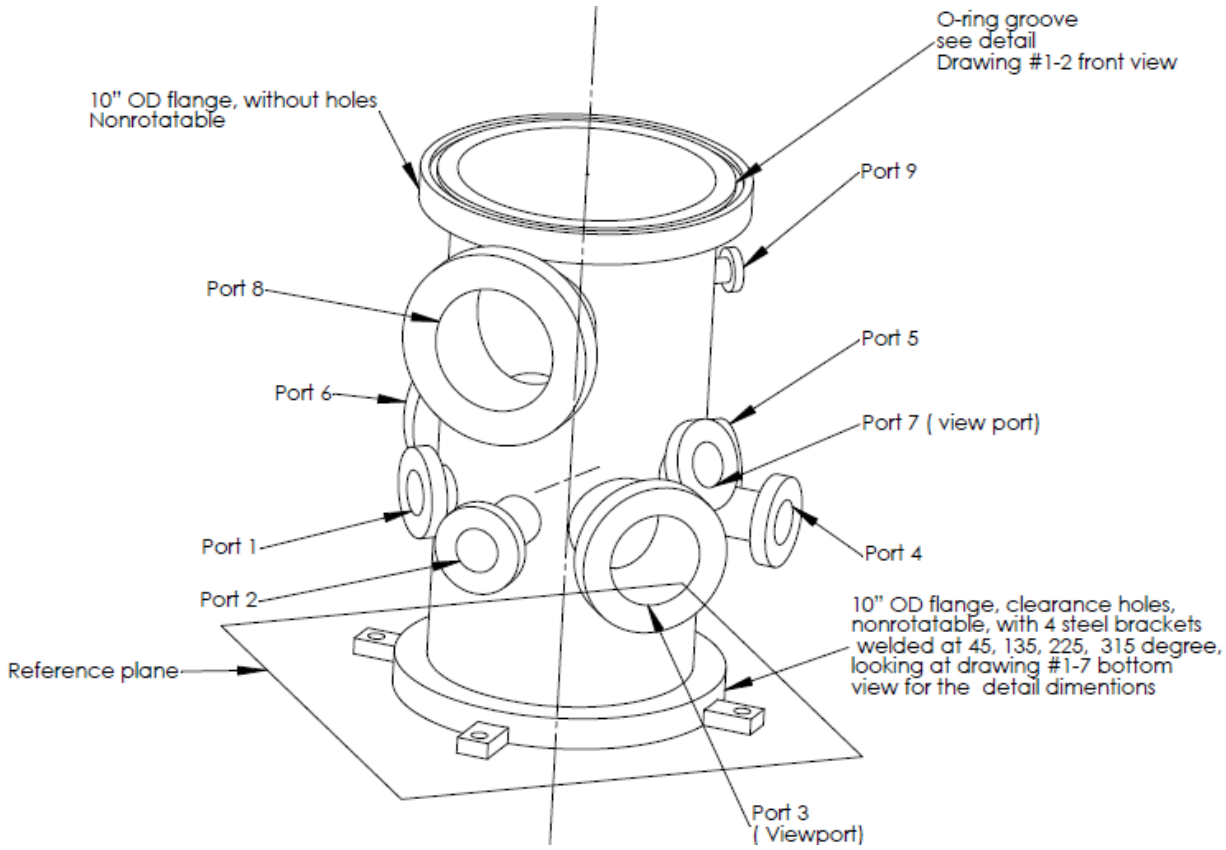

University of California, Los Angeles, Department of Chemical and Biomolecular Engineering

Part		Material	Stainless steel					
Filename		Scale	Yes	Filename		Scale	Yes	
Designer	Yunpeng Yin(MIT)	Date	6/11/2003					
Revised by		Date						
Contractor	Applied Vacuum Technologies	Date	6/11/2003					
Comments			Tolerance			+/- .0001		

ICP reactor

Main chamber – Front view

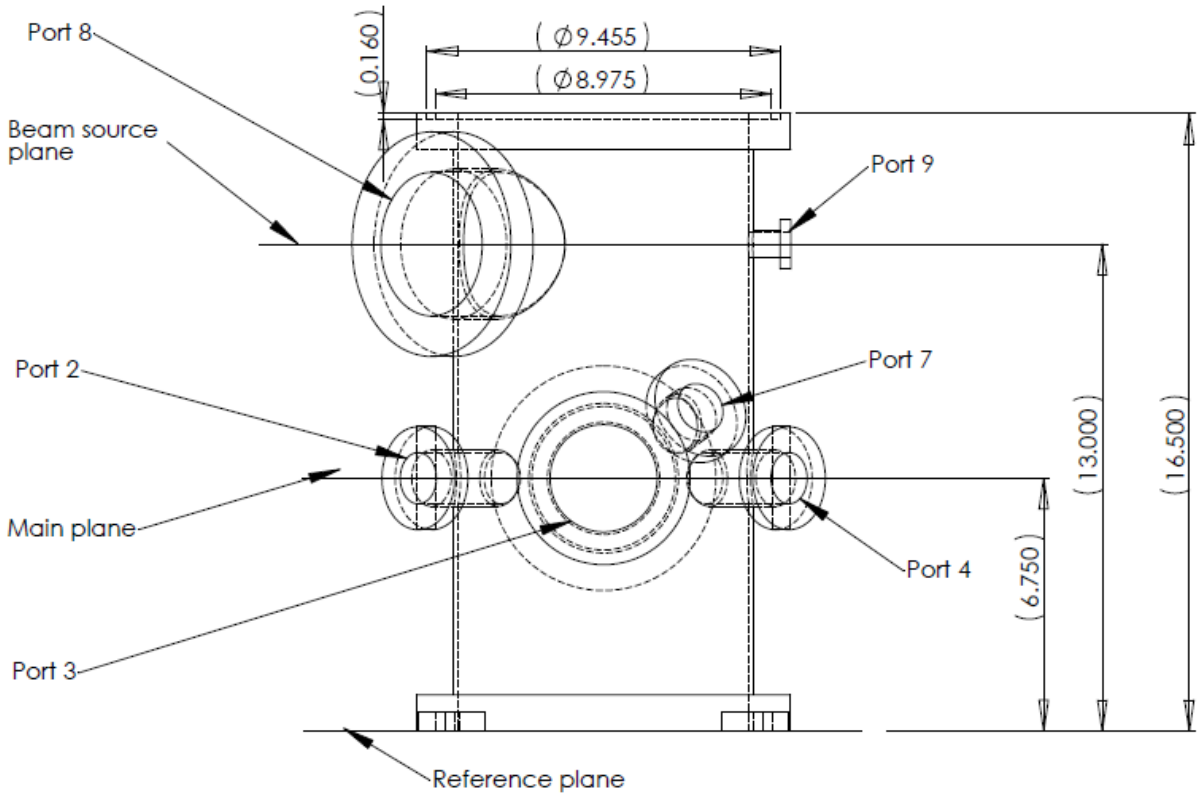

University of California, Los Angeles, Department of Chemical and Biomolecular Engineering

Part		Material	Stainless steel					
Filename		Scale	Yes	Filename		Scale	Yes	
Designer	Yunpeng Yin(MIT)	Date	6/11/2003					
Revised by		Date						
Contractor	Applied Vacuum Technologies	Date	6/11/2003					
Comments			Tolerance			+/- .0001		

ICP reactor

Main chamber – Top view

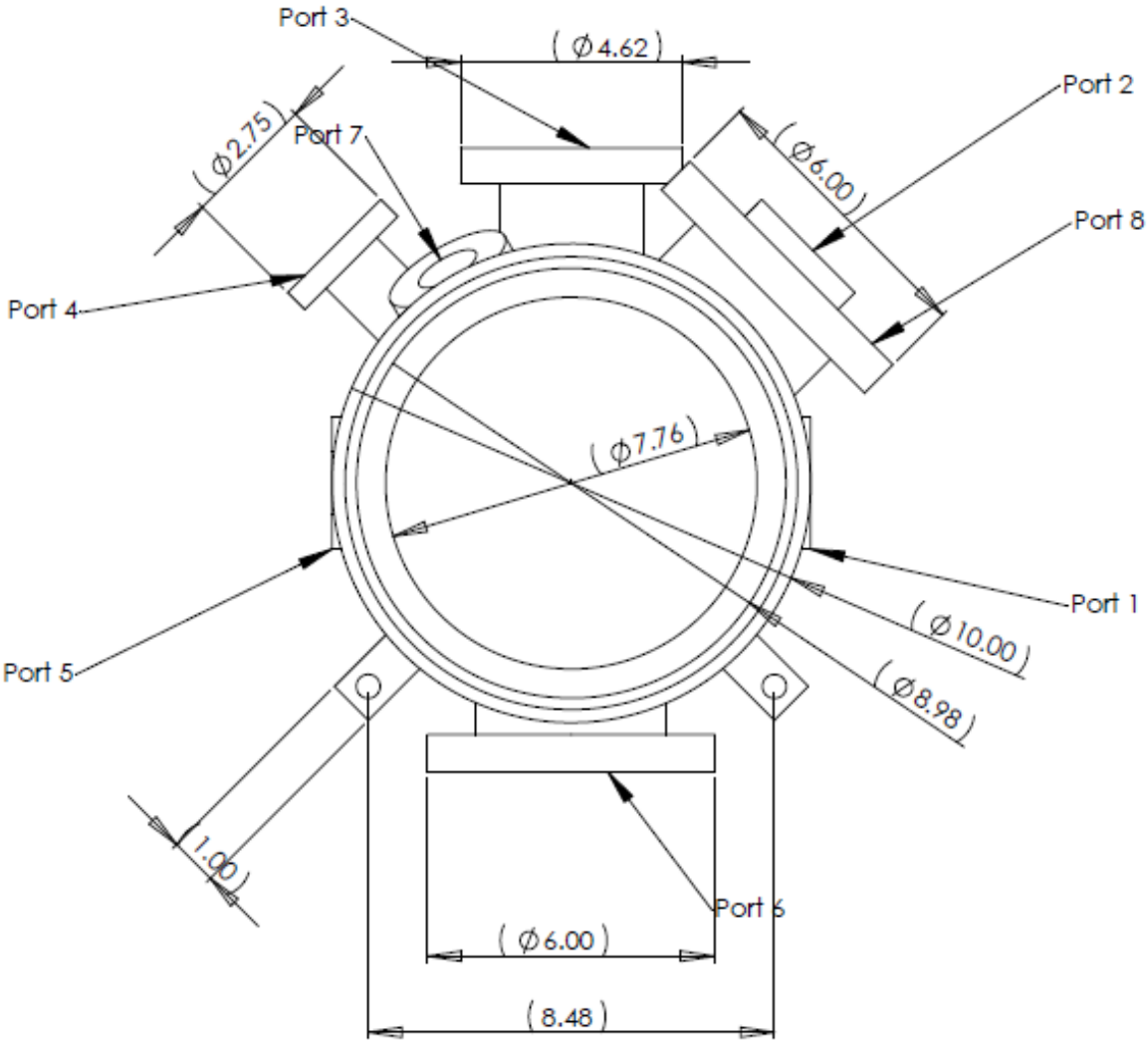

University of California, Los Angeles, Department of Chemical and Biomolecular Engineering

Part		Material	Stainless steel				
Filename		Scale	Yes	Filename		Scale	Yes
Designer	Yunpeng Yin(MIT)	Date	6/11/2003				
Revised by		Date					
Contractor	Applied Vacuum Technologies	Date	6/11/2003				
Comments			Tolerance			+/- .0001	

ICP reactor

Main chamber – Button view

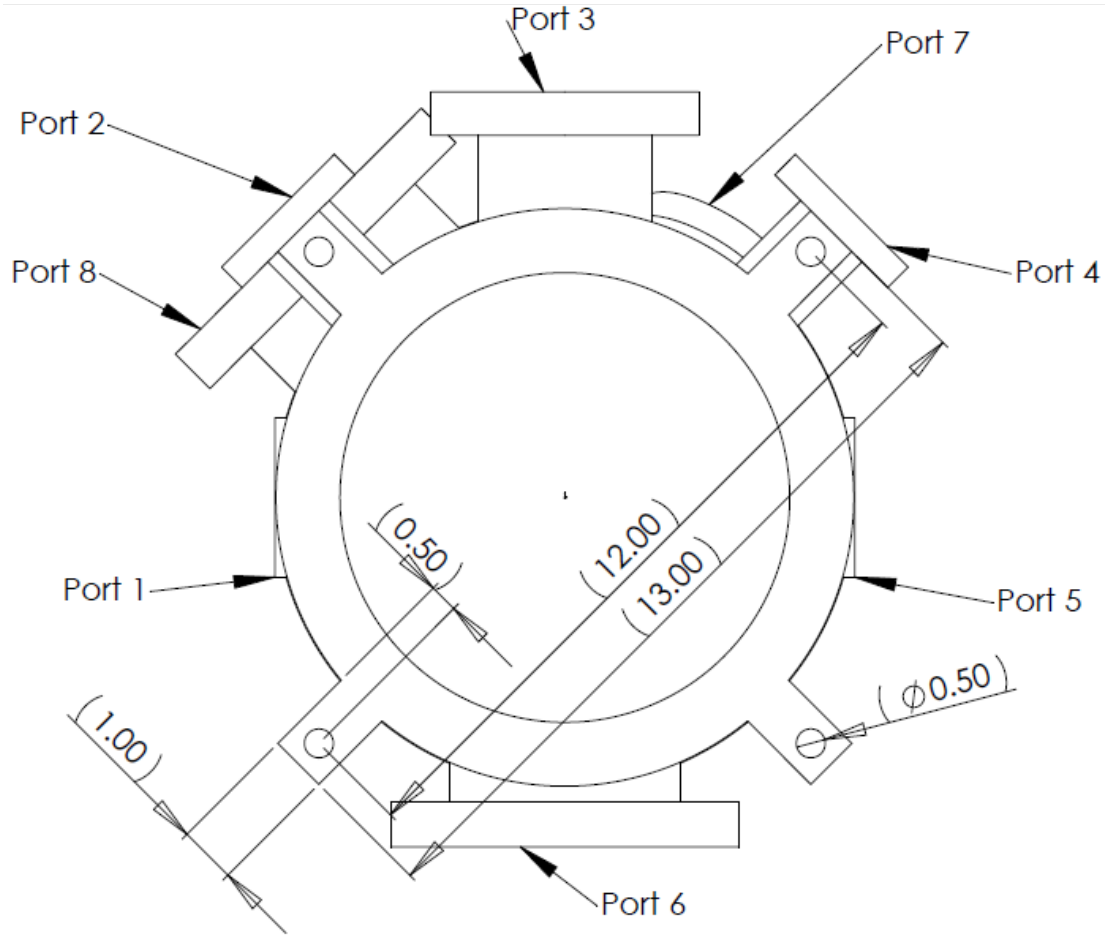

University of California, Los Angeles, Department of Chemical and Biomolecular Engineering

Part		Material	Stainless steel				
Filename		Scale	Yes	Filename		Scale	Yes
Designer	Yunpeng Yin(MIT)	Date	6/11/2003				
Revised by		Date					
Contractor	Applied Vacuum Technologies	Date	6/11/2003				
Comments			Tolerance		+/- .0001		

ICP reactor

Main chamber – QMS chamber

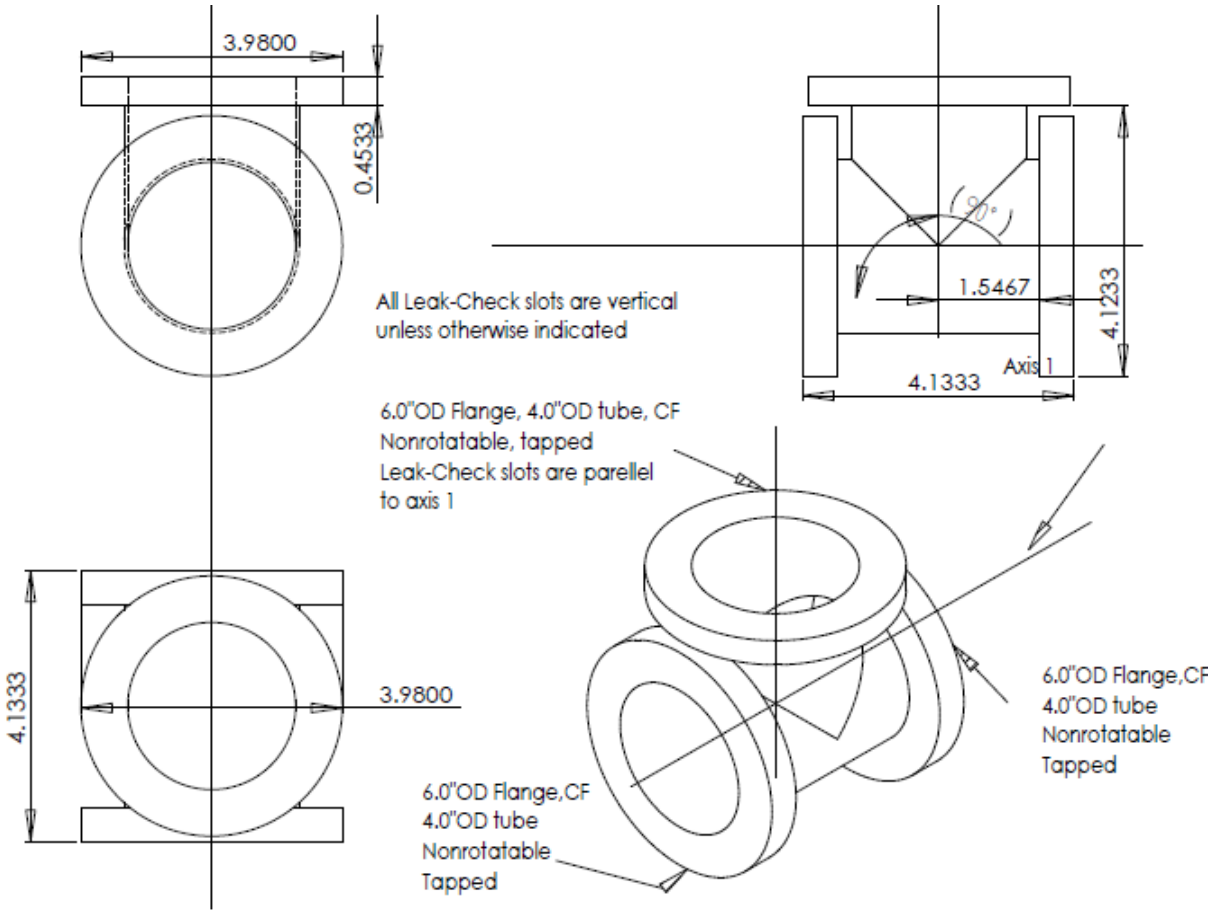

University of California, Los Angeles, Department of Chemical and Biomolecular Engineering

Part		Material	Stainless steel					
Filename		Scale	Yes	Filename		Scale	Yes	
Designer	Yunpeng Yin(MIT)	Date	6/11/2003					
Revised by		Date						
Contractor	Applied Vacuum Technologies	Date	6/11/2003					
Comments			Tolerance			+/- .0001		

ICP reactor

Sample stage

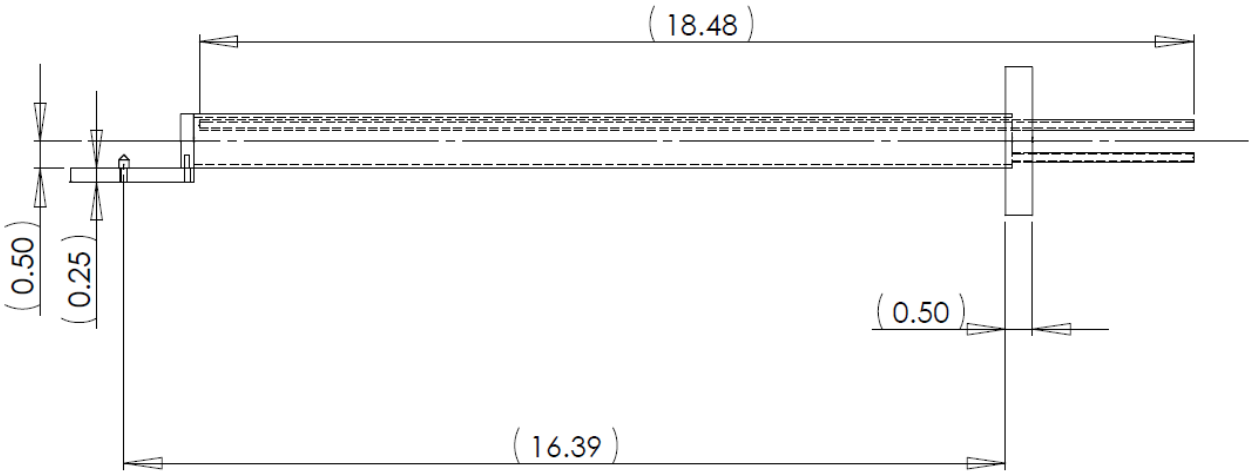

University of California, Los Angeles, Department of Chemical and Biomolecular Engineering

Part		Material	Stainless steel				
Filename		Scale	Yes	Filename		Scale	Yes
Designer	Yunpeng Yin(MIT)	Date	6/11/2003				
Revised by		Date					
Contractor	Applied Vacuum Technologies	Date	6/11/2003				
Comments			Tolerance		+/- .0001		

ICP reactor

Quartz in the ICP chamber

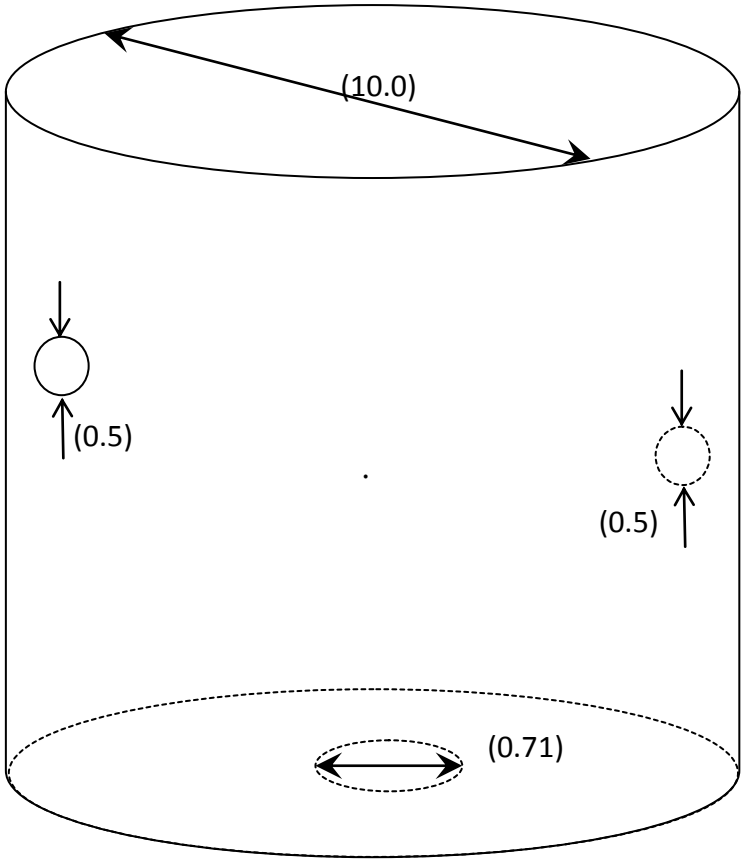

University of California, Los Angeles, Department of Chemical and Biomolecular Engineering

Part		Material	Stainless steel				
Filename		Scale	Yes	Filename		Scale	Yes
Designer	Yunpeng Yin(MIT)	Date	6/11/2003				
Revised by		Date					
Contractor	Applied Vacuum Technologies	Date	6/11/2003				
Comments			Tolerance		+/- .0001		

Transfer Tube

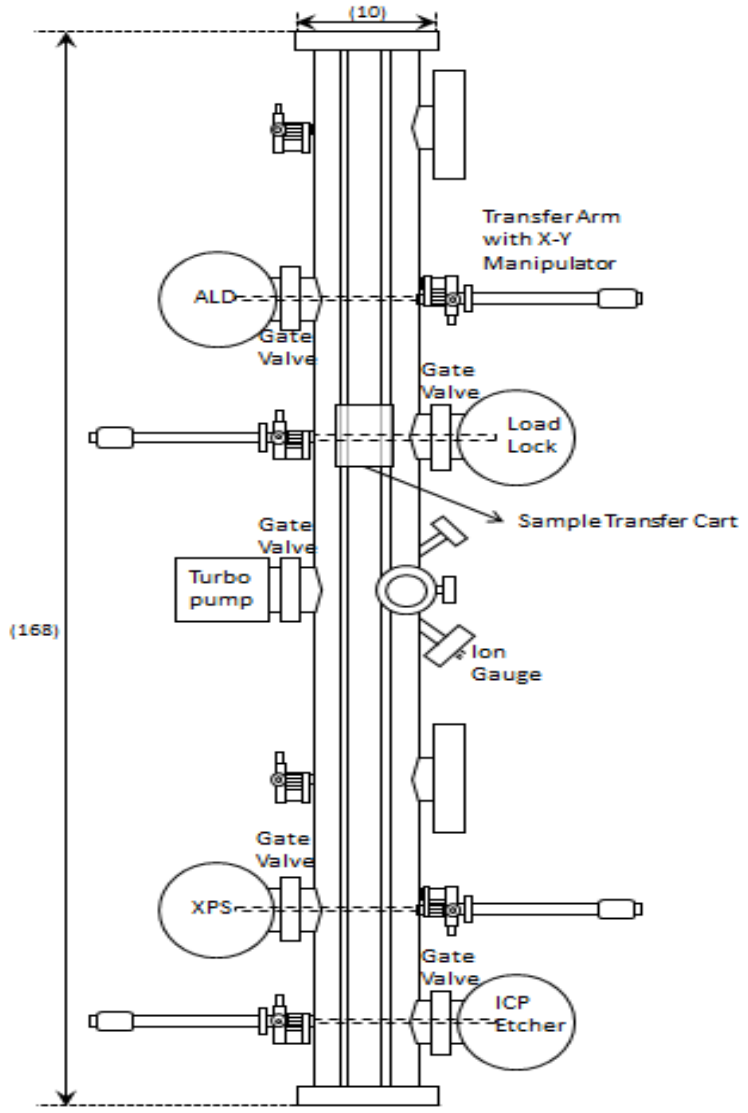

University of California, Los Angeles, Department of Chemical and Biomolecular Engineering

Part		Material	Stainless steel				
Filename		Scale	Yes	Filename		Scale	Yes
Designer	Jane Chang (MIT)	Date	1994				
Revised by		Date					
Contractor	Applied Vacuum Technologies	Date	1994				
Comments			Tolerance		+/- .0001		

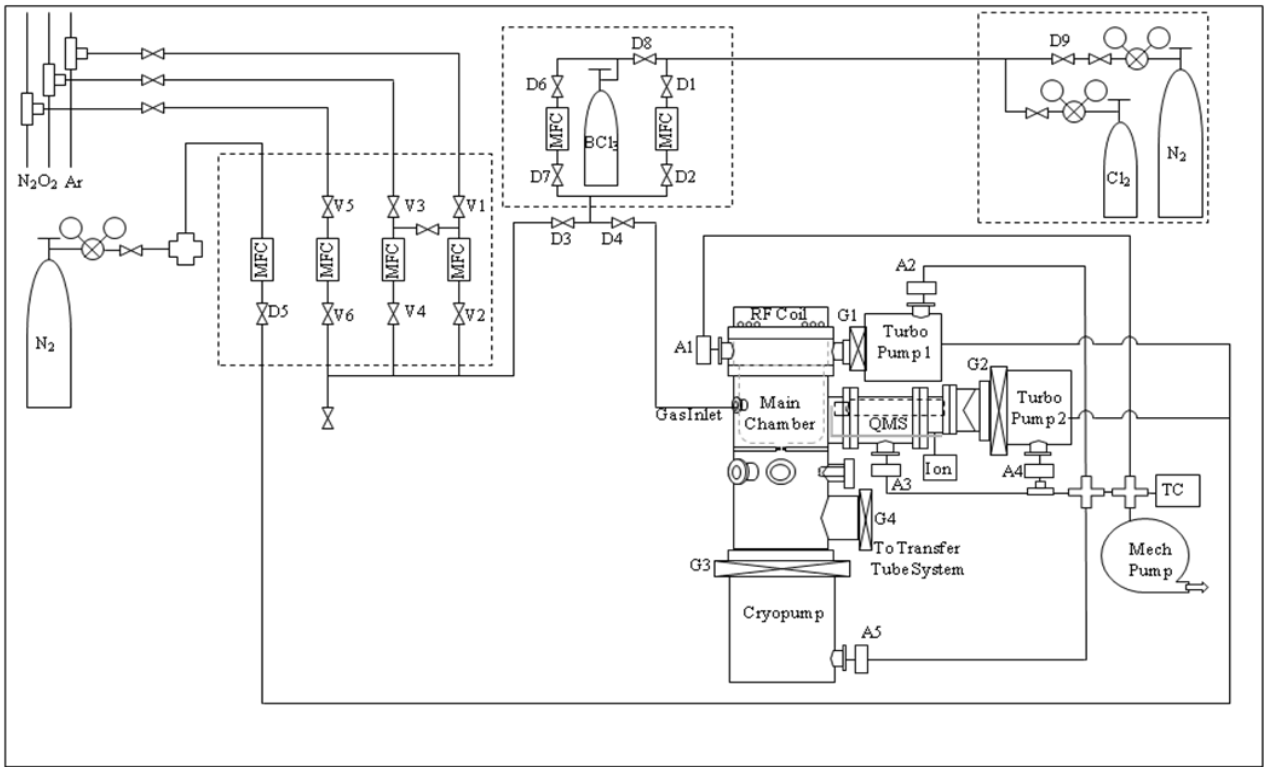

Figure 9. Gas line system for ICP system including corrosive gases Cl2 and BCl3, inert gases Ar and N2, and O2.

The ICP system includes corrosive and inert gas lines, turbomolecular pump, cryopump and mechanical pump. V1 and V2 are the valves for Ar, V3 and V4 are the valves for O_2. Since the flow rate of the Ar MFC is small (10 sccm), a connection was installed between the Ar and O_2 gas lines to enable a higher flow rate through the O_2 MFC (50 sccm). V5 and V6 are the valves for high purity N_2 and D5 is a valve for industrial N_2 which flows through the back of the TMP to dilute the corrosive gas into mechanical pump. Two corrosive gases are used: Cl_2 and BCl_3, which share a double wall corrosive gas line leading to the reactor. A N_2 cylinder is connected which allows cycle purging of the system. D1 and D2 are the valves for Cl_2 and the purge N_2 gas, and D6 and D7 are the valves for BCl_3. D3 and D4 control the inert and corrosive gas flow into the chamber. A1 and A3 are the roughing valves which connect the chamber to its mechanical pump, and A2 and A4 are the roughing valves between the TMPs and the mechanical pump.

A.1.3. Operating Procedures

1. Pump down the main chamber (Note: The chamber's default state should be pumped down, check the pressure reading on the ion gauge to verify. The following steps should only be taken if you aware that the chamber has been vented and not pumped back down).

a. The following interlocks for the pump down procedure must be met to begin pumping:
   I. cooling water for main chamber turbo molecular pump(TMP) must be on
   II. cooling water flow to compressor should be between 2.3 and 3.5 gpm.
b. Check that all the flanges are tightened and all the valves are in the closed position.
c. Check all the cables are correctly connected.
d. Check the oil level in the mechanical pump(MP), which should be 2/3 full in view window.
e. Check MP and its exhaust for liquid leaks. (oil, condensation, exhaust fluid)
f. Turn on MP by turning on the breaker. The thermocouple(TC) gauge reading should start going down within 20 seconds. If not, turn off the pump and check connections to chamber, turbopump and cryopump for vacuum leaks.
g. Wait until MP reaches the base pressure ~60 mTorr. This process may take several minutes if system was shut down for some time.
h. If the gas lines have been exposed to ambient conditions, diaphragm valve D3 and D4 should be open so that the gas lines could be pumped down as well. Rough pump the chamber using MP until a base pressure of ~75-85 mTorr is achieved.
i. After the TC gauge reaches the base pressure, close roughing valve between chamber and MP and gradually open roughing valve between TMP and MP.

2. Before TMP is turned on, check:

a. The cooling water is running
b. The roughing valve between the chamber and TMP should be always CLOSED while the TMP is on.
c. If TMP is running, the base pressure should be achieved right away. (This would occur only if MP was turned off for less than approximately 10 minutes and TMP was isolated prior to shut off of MP)

d. If pumping down after TMP has been off for a few hours it may be safer to purge TMP with N_2 using the N_2 MFC for 30 seconds. Then gradually open the roughing valve and wait until base pressure is reached in MP.
e. Open the gate valve between TMP and chamber. At this stage, the TC gauge readout should NOT vary at all.
f. Turn on TMP by pushing the start button on the Leybold controller, unless already on. The green acceleration indicator should be on.
g. Within 5 minutes, the turbo molecular pump should reach full speed and the yellow indicator should be on normal.

   • If any strange noise is heard from TMP, turn it off right away by pushing the off button on the controller.

   • If corrosive gas is anticipated to be used, 36 sccm industrial level nitrogen (corresponding to ~50 mTorr rise in TC pressure) should be provided through the purging port on the bottom of the pump by opening valve D5 and switching on the MFC "N_2 ind." on the control panel once the pump has reached full rotation, which is indicated by the normal light being lit on the TMP controller. (Refer to Leybold 361C Turbo Molecular Pump manual.)
h. Wait until the chamber reaches the base pressure 6.0 $x10^{-7}$. This process may take up to couple of days depending on how long the chamber has been under atmosphere.

   • If the chamber has been exposed to ambient or pumping system has been off for more than a day, baking the chamber is necessary to achieve base pressure and remove any build up on the sidewalls of the chamber. Two heating tapes are used to bake the chamber. Do NOT turn on the power over 20% of the full range on the variable transformer to prevent over heating. At this point the chamber pump down procedure is complete. If no processing is to be performed system should be left in this idle state.

After base pressure in the chamber is achieved, plasma processing can begin using the following procedure. If a sample is to be processed the following procedure must be followed to load the sample in to the chamber. However, it is better to warm up the plasma before processing a sample, in which case skip to steps 3-6, and then return to step 2 and repeat the following steps.

3. Transfer the sample from transfer tube to the chamber:
   a. See instructions for loading a sample from the loadlock in the Transfer Tube SOP.
   b. Move the cart into position for transfer to the ICP.
   c. Before opening the gate valve between the ICP and the TT check that their pressures are roughly equivalent. If the ICP pressure is over 10^{-7} torr which is 2 order higher than TT pressure, 10^{-9} torr, then the gate valve between the TT and its cryopump/turbo pump should be closed. Ensure that no gas is flowing into the ICP.
   d. Open the gate valve (G4) using the controller box (trace the cable to ensure). Check the ion gauge controllers on both the ICP and TT to ensure that the pressure has not changed significantly.
   e. Secure the sample by sliding the holding fork attached to the end of the transfer arm around the upper groove of the sample holder.
   f. Using the manipulator, lift the sample off the cart. Verify that the arm has cleared the cart (a setting of about 4-5 on the Y-axis manipulator is sufficient).
   g. Slowly slide the transfer arm forward to move the sample into the ICP chamber.
   h. Visually confirm the location of the sample in relation to the sample stage pin by checking through the viewport on the lower section of the ICP chamber.
   i. Lower the sample holder onto the protruding pin. Visually confirm.
   j. Slowly begin sliding the transfer arm out. The holder should stay on the stage.
   k. When re-entering the transfer tube ensure the height of the transfer arm is readjusted so as not to hit the cart or holding pin in front of the ICP chamber.
   l. Fully withdraw the transfer arm into the tube so that it has cleared the gate valve.
   m. Close the gate valve (G4) between the ICP and TT.

With the sample loaded, if necessary, plasma processing can begin. Processing gases must be introduced into the reactor prior to striking plasma by performing the following procedure. Proceed to step 3, 4, or 5 depending on plasma chemistry.

4. Feed in process gas for plasma for inert gas only:
   a. Check that the chamber is at the base pressure of 1.0×10^{-7} torr.
   b. Check regulators for all the desired gases (N_2, Ar, O_2) by opening the gas tank.

c. Check the cylinders are filled with enough gas to obtain required flow rate.
d. Open the pneumatic valves for gases to be used before the Mass Flow Controller (MFC), which are V1, V3, and V5.
e. Gradually open the corresponding valve after the MFC, which are V2, V4, and V6, to prevent a large pressure difference to the MFCs.
f. Adjust the set point on the MFC control unit to desired flow rate for each gas.
g. Open Diaphragm valve D3 and then gradually open D4. The chamber pressure should go slightly higher; wait until it goes back to the base pressure. This will pump down the gases which have been sitting in the line.
h. Turn off the ion gauge, which cannot go above $1x10^{-3}$ torr.
i. Turn on the MFCs for the gases to be used. Wait until a steady flow is achieved. Do fine adjustments if needed.
j. Record pressure achieved in chamber after steady flow is reached

5. Feed in corrosive process gas (Cl_2 and/or BCl_3) only:

The following interlock for corrosive gas use must be met to begin: n_2 purge to main chamber and QMS turbo pumps must be on.

a. Check that the chamber is at the base pressure of 1.0×10^{-7} torr.
b. Check there is enough Cl_2 gas in the cylinder and the tank and regulator should be CLOSED. (This regulator should always be closed while Cl_2 gas is not in use.)
c. Check that 36 SCCM nitrogen is supplied to the purging ports of TMP1 and 2 by MFC.
d. Gradually open Diaphragm valve D4. The chamber pressure should go slightly higher; wait until it goes back to the base pressure.
e. Adjust the set point on MFC control unit, which is channel 1, to desired flow rate for Cl_2 gas.
f. Turn off the ion gauge.
g. Open the valve on Cl_2 cylinder and the isolation valve after the regulator. Adjust the regulator to get 12 Torr outlet pressure. Then close gas cabinet door.
h. Gradually open the Diaphragm valve D1 and then D2 for Cl_2 and/or D6 and D7 for BCl_3. Close the gas cabinet door.
i. Turn on the MFC. Wait until the steady flow is achieved.

j. Record pressure in chamber once steady flow is achieved.

6. For corrosive gas and inert gas mixture (Cl_2, BCl_3, Ar, O_2, N_2):

The following interlock for corrosive gas use must be met to begin: n_2 purge to main chamber and qms turbo pumps must be on.

a. Check that the chamber is at the base pressure of 1.0×10^{-7} torr.
b. Check there is enough Cl_2 and or BCl_3 gas in the cylinder.
c. The regulators should be CLOSED. (This regulator should always be closed while Cl_2 gas is not in use.)
d. Check 36 SCCM nitrogen is supplied to the purging ports of Turbopumps 1 and 2.
e. Gradually open Diaphragm valve D3 and D4. The chamber pressure should go slightly higher; wait until it goes back to the base pressure.
f. Adjust the set points on MFC control unit to desired flow rates for gases.
g. Turn off the ion gauge.
h. Open the regulator on Cl_2 cylinder/ and or BCl_3 at their respective gas tanks.
i. Open the pneumatic valves, for the inert gas, before the MFC (V1, V3, and V5) first, and then open the corresponding valve after the MFC (V2, V4, and V6).
j. Turn on the MFCs for the inert gases.
k. Gradually open the Diaphragm valve D1 and then D2 for Cl_2 and/or D6 and D7 BCl_3.
l. Close the gas cabinet doors.
m. Turn on the Cl_2 and/or the BCl_3 MFC. Wait until the steady flow is achieved.
n. Record chamber pressure once flows have stabilized.

7. Turning on the plasma

The following interlock for plasma generation must be met to begin: 1. Induction coil fan on.

a. Ensure the fan on the induction coil is plugged in and operating.
b. Turn on the main power of the RF generator (Seren R1000) by flipping the main power switch.
c. Turn on the main power of the matching network tuning controller (RFPP 761 Unit) and ensure its operation mode is set to "Auto".

d. If bias is desired, turn on the main power and bipolar voltage control of the DC bias controller (Kepco BOP 500M).
e. If etching in the lower chamber is desired, turn on the filament power supply (Harrison Labs 6263A). Let all the electronics units warm up for 30 - 45 minutes.
f. Flow the process gases (pressures should be adjusted in steps 2-4).
g. Set the RF generator to the desired source power and press the "RF on" button. A red light should indicate RF power is being supplied.
h. If plasma does not strike, check that the reflected power as indicated on the generator display is not higher than 70 W, or that no warnings are displayed. If the reflected power is low, consider increasing the gas flow using the appropriate MFC. If the power is high or if warnings are displayed, turn off the RF supply by pressing the "RF on" button again and check the connections between the generator, matching network and source coil.
i. If bias is desired, set the DC bias to the appropriate voltage.
j. If etching in the lower chamber is desired, set the filament power supply to ~2 Amps. Usually this should be done a minute or two before the experiment to ensure the filament is receiving current (indicated by a reddish glow).
k. After the process is finished, turn off the RF power by pushing the "RF on" button on the front panel of the Seren R1000. Processes should not exceed 15 minutes so as to not over heat system.
l. Turn off the corrosive process gases first on the MFC.
m. Leave the inert gases running for about 5 minutes.
n. Turn off the MFCs, close the corresponding pneumatic valves and the Diaphragm valve D4 and D3 for Cl_2 and/or D6 and D7. BCl_3.
o. Turn off TMP1 purging nitrogen.

8. Troubleshooting

This section details major problems occurring on ICP chamber and the steps taken to fix them. 3/2012:

Problem: Unable to strike the plasma such as O2(g) and N2(g).

Solution:

1. Check the connection of cable on the top of chamber.
2. Shine the light into chamber while turning on the RF generator.
3. Flowe the Ar gas with O2 or N2 to strike the plasma, once the plasma been ignited then Ar could be slowly decreased to 0.

7/2012:

Problem: The wire connected from voltage supplier to bias ring was burn out.

Solution:

1. Order stainless steel wire from Mcmaster carr.
2. Clean up the stainless steel wire by IPA and alcohol, cut into a suitable length and then replace old one.
3. Check by the multimeter for connection between voltage supplier and bias ring.

8/2012:

Problem: The turbo pump started making a high pitch noise.

Solution:

1. Check the turbo pump controller is in normal condition.
2. Isolated the turbo pump. First, close gate valve to chamber, and then switch off the turbo pump by controller. Wait 20 mins to pump out the turbo pump by mechanical pump, and close the roughing valve to mechanical pump.

8/2012:

Problem: The bias beam couldn't be observed during the plasma etching process.

Solution:

1. Check the mesh at the center of upper chamber is clean and grounded.
2. If mesh is covered by green species or other contamination, the mesh need to be cleaned.
    a. Flip up the plate in the upper chamber, undo the filament connection carefully.
    b. Take out the plate and undo the screws at the center mesh. Be careful that there are three small of stainless steel piece between the plate and mesh which can make the mesh grounded.
    c. Sonicate the mesh with IPA for 10 mins two times.
    d. Reinstall the mesh and plate into the chamber, and connect the filament wire.
    e. Use multimeter to check the mesh is grounded.

APPENDIX A.2. Quadrupole Mass Spectrometer Operational Guidelines

A.2.1. Emergency Shut Down Procedures

1. Turn off the UTI100C Electronics Controller by following the sequence labeled below in the order indicated.

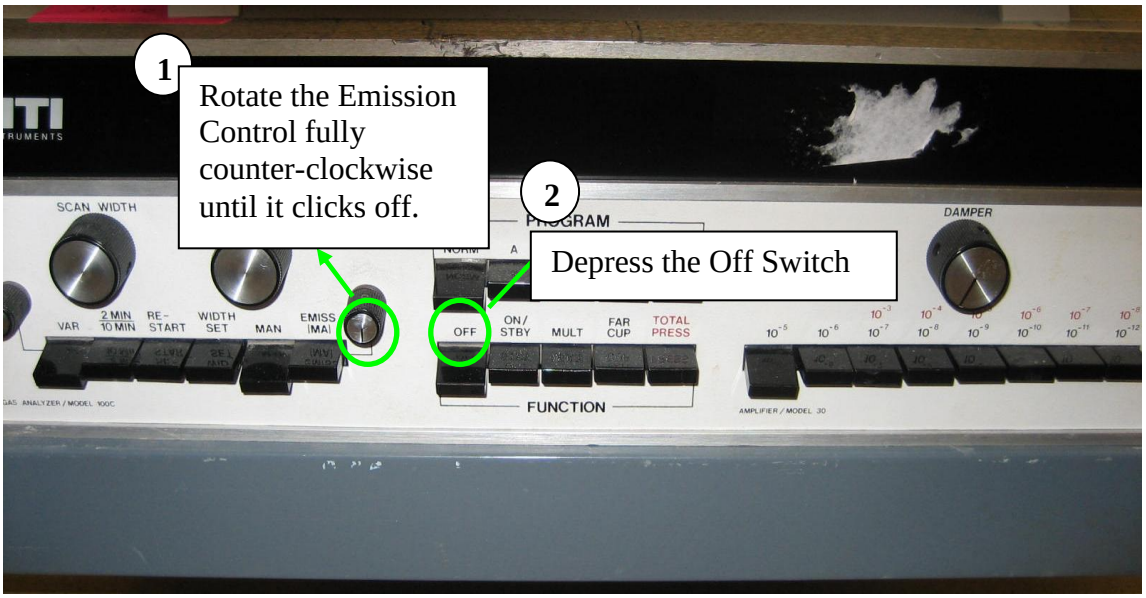

Figure 10. QCM panel

2. Turn off the oscilloscope by pressing the power button:

Figure 11. Oscilloscope panel

A.2.2. Schematics

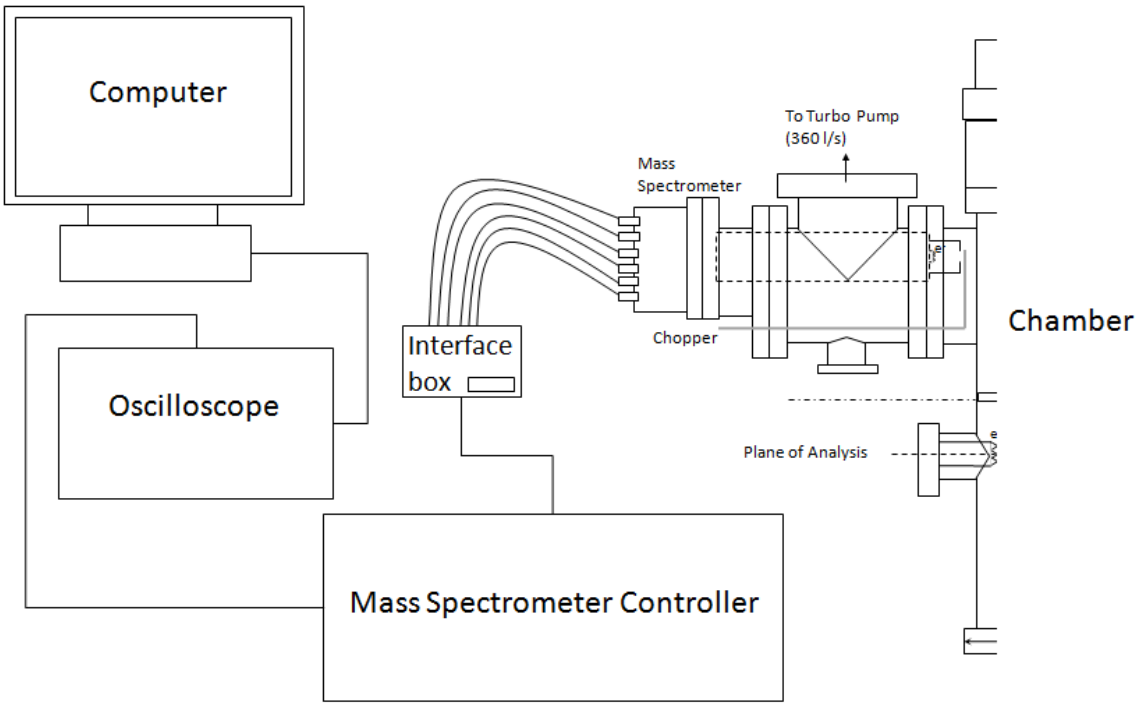

Figure 12. QMS schematics

A.2.3. Operation Procedures

1. Check the base pressure of the system, which should be about $2.8*10^{-8}$ Torr. Write the base pressure in the logbook.

2. Check the connections between the Spectrometer and the Interface Box, the Interface Box and the Spectrometer Control Unit (SCU), the SCU and the Oscilloscope, and the Oscilloscope and the Computer (Illustrated below). Turn on the computer.

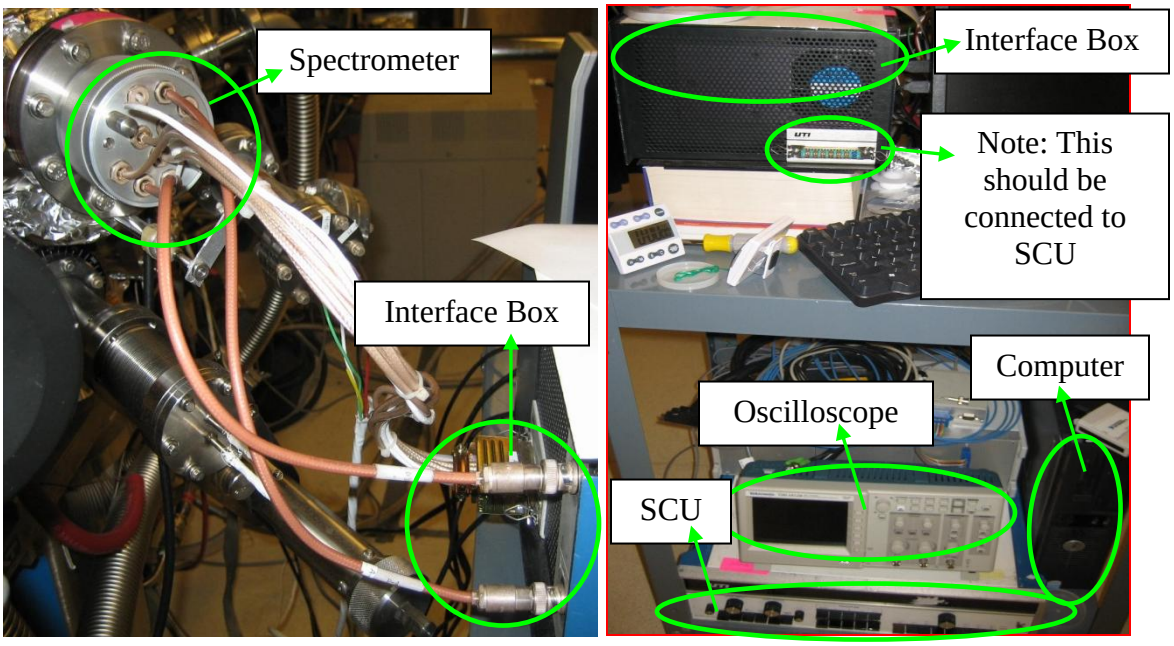

Figure 13. The connection of interface box and spectrometer

3. Ensure that the power cable into the SCU is plugged in. Check that the follow switches are depressed (labeled below): "Var" and "Man" in the Scan section, "Norm" in the Program Section, "Off" in the Function Section and "10^{-5}" in the Damper Section. Also make sure the emission control is off (rotated fully counter-clockwise).

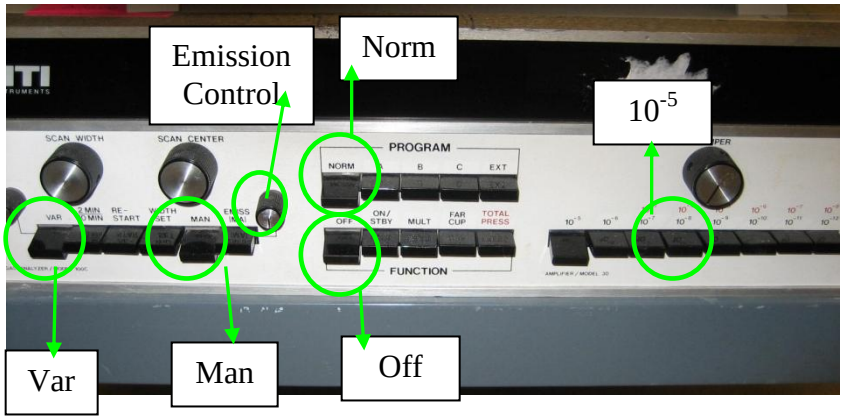

Figure 14. QCM panel

4. Depress the "On/Stby" switch on the SCU directly to the right of the "Off" switch. Let the electronics warm up for 30 minutes. Power on the oscilloscope by pressing its power button. Windows should indicate that new USB device has been plugged in and you need to select the software option to view the device.
5. Select TekDesktopAcquisition (the TDS 1012B should be selected as device by default).
6. After the electronics have warmed up set the scan center and width using the Scan Control section of the SCU. To set the center "Man" has to be depressed. To set the width, "Width Set" has to be depressed and "Man" should be released. Both of these values are set by using the corresponding rotary controls above the switches (can be seen in the preceding image).
7. Flow gas and strike plasma as required by your experiment.
8. Monitor the QMS pressure. The maximum operating pressure for QMS is $5*10^{-6}$ Torr.
9. Start the QMS scan by releasing the "Man" switch, and depressing "Emiss (mA) and "Mult" switches at the same time. Adjust the emission current using the rotary control (max = 0.5 mA). If no signal is seen adjust the Damper (max = 10^{-9}).
10. Monitor the scan on the oscilloscope and adjust the visual as necessary using the controls for the y- and x-axis. A visual can be captured using the Tektronic software "Data Capture" button.
11. After finishing all the experiments, close the software and transfer all the data files to the server.
12. Turn off the power to the SCU by using the steps outlined below:

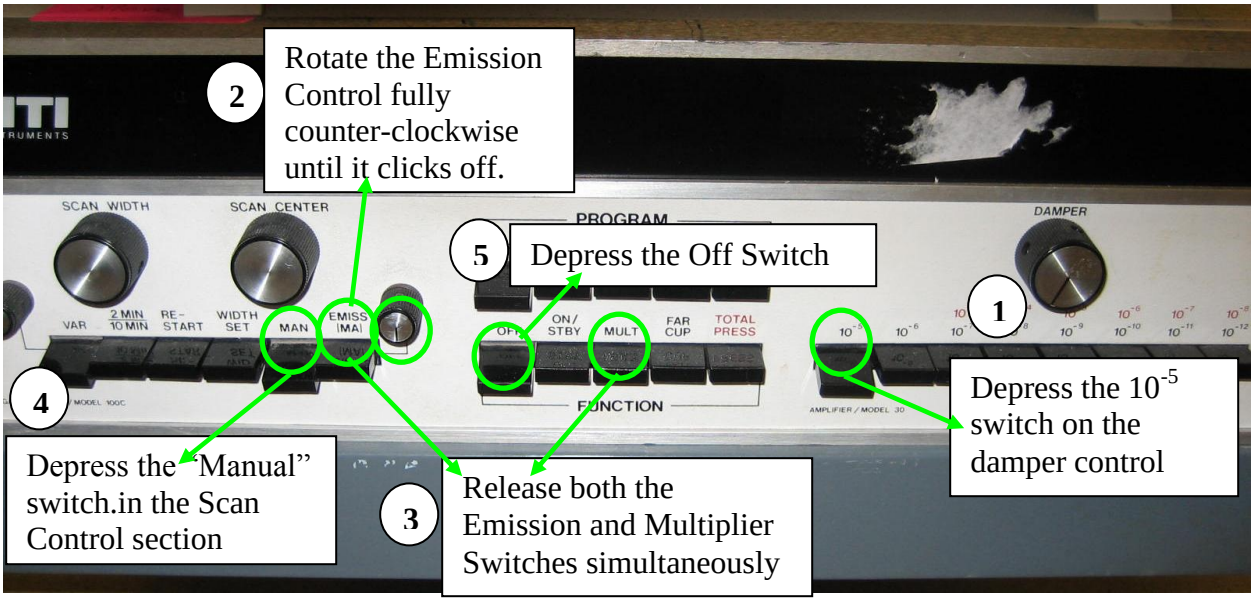

Figure 15. QCM panel

13. Turn off the oscilloscope by pressing its power switch.
14. Finish the logbook.

APPENDIX A.3. Langmuir Probe Operation Procedure

A.3.1. Emergency Shut Down Procedures

I. In case of an emergency overpressure situation in the plasma etcher

1. Stop any current scans using the Hiden ESPsoft software: STOP SCAN
2. If necessary, pull the probe tip out of the etcher main chamber and back it's housing unit by homing the z-stage: Probe → Home ZStage.
3. Exit the Hiden ESPsoft program: File → Exit.
4. Turn off the Langmuir probe electronics by pressing the "OFF" switches on the front panels of both electronics units.

II. In case probe has been driven into the closed gate valve

1. Immediately stop the motor of the z-stage by pressing "Cancel" on the "Probe Positioning" window of the ESPsoft software.
2. Home the z-stage.
3. At this point, the Langmuir probe housing will need to be disassembled off the etcher system in order to assess damage to the probe.

A.3.2. Schematics

The Hiden Analytical Langmuir Probe system consists of the following components:

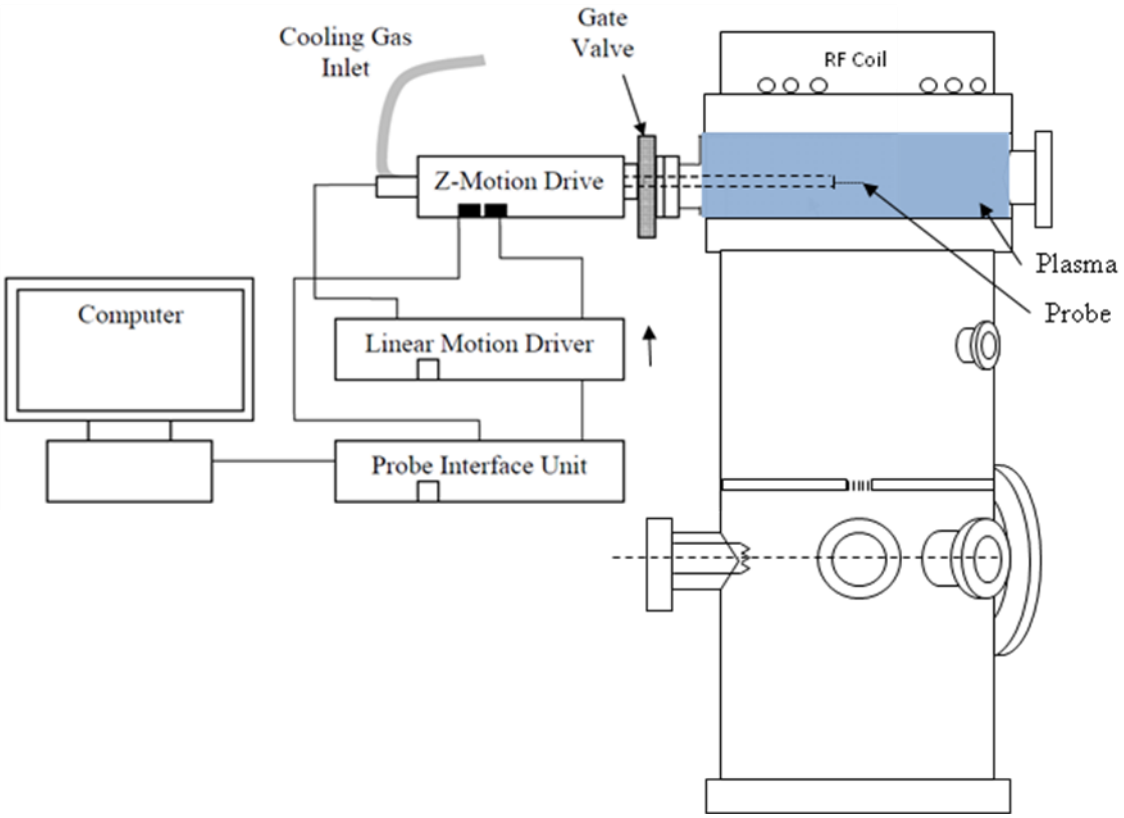

Figure 16: Schematic of Langmuir Probe System and ICP chamber connection.

A.3.3. Operating Procedures

I. Install Langmuir probe into upper ICP chamber

This section details how to install probe into chamber.

1. Replace the window in upper chamber with Langmuir Probe:

   Prepare the adaptor, gate valve, Cu gasket, nuts, bolts and screws beforehand, calculate the length of the bolt for each adaptor and valve. The following is the necessary component for the connection:

Component	Quantity	Component	Quantity	Component	Quantity
Adaptor 4 5/8”	1	Nuts 2 3/4”	6	Cu gasket 2 3/4”	3
Extension 2 3/4”	1	Nuts 1 5/8”	10	Cu gasket 4 5/8”	1
Gate Valve	1	Nuts 2”	6		

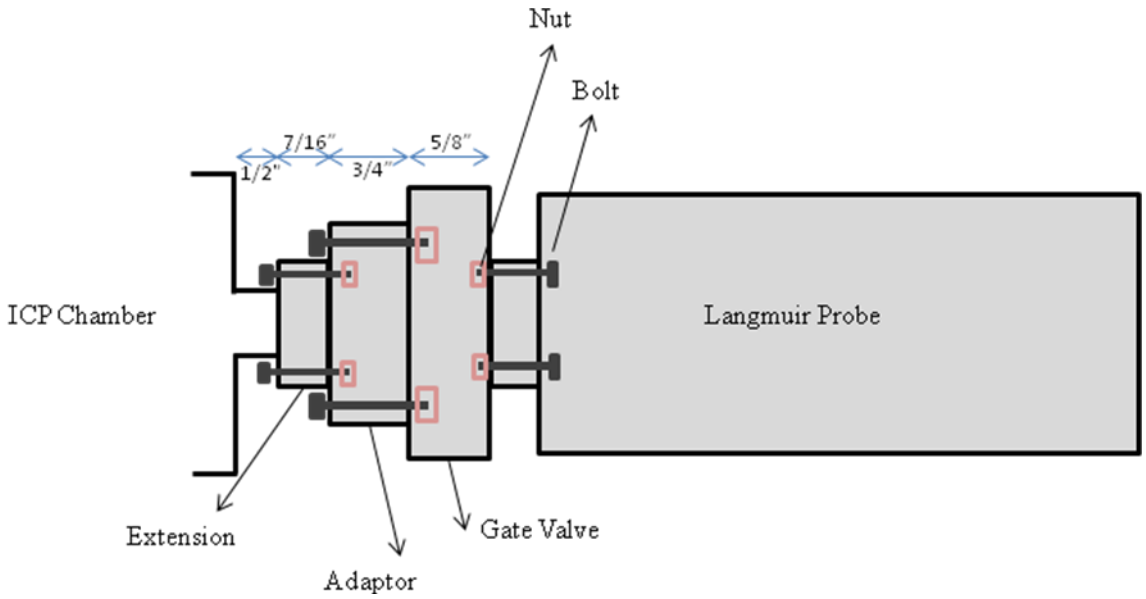

Figure 17: Schematic of Langmuir Probe System showing connection of components.

2. Find a stand to support the Langmuir probe main body.

II. Probe Operation and Data Collection

This section details how to set up and perform scans for plasma analysis.

1. Check that the etcher system is at base pressure. Then slowly open the Langmuir probe gate valve. If the Langmuir probe housing has been isolated for a long time, a significant amount of gas may have accumulated in the Langmuir probe bellow and the pressure in the chamber will rise once the gate valve seal has been cracked open. Slowly opening the valve will help protect the etcher main chamber turbo pump.
2. Turn on the Langmuir probe and z-drive electronics units and warm up for 30 minutes before acquiring data.
3. Open the ESP soft program on the diagnostics computer.
4. With the gate valve is open, advance the probe into the main chamber by selecting Probe → Z-Stage, then entering the desired insertion distance (in cm) in the Park position prompt, then selecting "Move Now" and "Ok". (parking the probe tip at the center of the main chamber requires a position of 26-27 cm)
5. Set the desired parameters for acquisition by selecting Probe → Edit, and then inputting all desired parameters.
6. Once a plasma is struck, an data can be acquired by selecting Probe → Run, then entering the amount of acquisitions, naming the file, and selecting "Start".

III. Probe Tip Replacement

This section details how to uninstall the Langmuir probe from the vacuum chamber and replace the probe tip

1. Home the z-drive and close the manual gate valve connecting the Langmuir probe house from the main chamber.
2. Remove screws holding the outer housing to the z-drive chassis, then take off the outer housing.
3. Disconnect the cables connecting the back end of the 2 ¾" CF flange (the end that the probe is attached to on the inside), then, while holding the flange (and probe) in place, remove the bolts connecting the CF flange to the bellow valve.
4. While *carefully* and *firmly* holding the bellow valve in place with one hand, and holding the

CF flange/probe in the other, advance the z-drive forward in small (~2 cm) increments until the probe can be safely removed from the bellow. It is *very important* to secure the bellow valve while doing this as when it is compressed it will want to spring out sideways! Allowing this to happen could damage the fragile bellow weldings and cause a leak.

5. Replace the probe tip using gloves and clean tongs.
6. To replace the probe, follow this procedure in reverse order, making sure to hold the probe steady while retracting the z-stage. Colliding the probe tip with the bellow while retracting could damage the new tip!
7. Once the probe CF flange is reattached to the bellow and the housing cover is replaced, the bellow volume will have to be opened to the etcher while it is isolated from all turbopumps in order to protect them (remember the bellow volume will be at atmospheric pressure!).
8. Rough pump the chamber and then pump down with the turbopump, as instructed in the etcher system operation procedures.

A.3.4. Troubleshooting

This section details major problems occurring on the Langmuir probe and the steps taken to fix them.

Spring 2007:

It was found that some plasma conditions (e.g. BCl_3-containing chemistries) lead to rapid degradation of the collected current. This is due to deposition on the probe tip while it is idle. In order to avoid deposition on the tip and prolong the lifetime of each probe tip, the following procedures are suggested:

a. Always keep the Langmuir probe retracted into the housing with the gate valve closed for any experiments that do not require data acquisition using the Langmuir probe.
b. Keep experiments as short as possible whenever the Langmuir probe is in use(this applies to all plasma conditions!)
c. If a potentially depositing plasma chemistry will be in use, always set the "Idle Park Potential" of probe (in the Probe → Edit menu) to a high negative voltage (~-80 V) right before striking plasma, and return the idle park potential to 0 V once the plasma has been turned off. This will induce ion bombardment of the probe with the plasma on which will prevent a deposition layer from developing.

d. In addition, in the Probe → Edit menu, turn on the automatic cleaning during for data acquisition in depositing plasmas by selecting the checkbox next to “Automatic Cleaning On” as well as “20 ms clean/5 ms data acq.”, and set the “Cleaning *Potential” to a high negative voltage (~ -80 V).*

APPENDIX A.4. Optical Emission Spectrometer Operation Procedures

A.4.1 Emergency Shutdown

1. Stop the program, and no further shutdown procedure is required.

2. The modules needed to be moved are optical fibers and the S2000 module where the fibers are attached.

3. The ADC1000-USB module is used for the computer on the ECR etcher (or other computers with the software properly installed if needed).

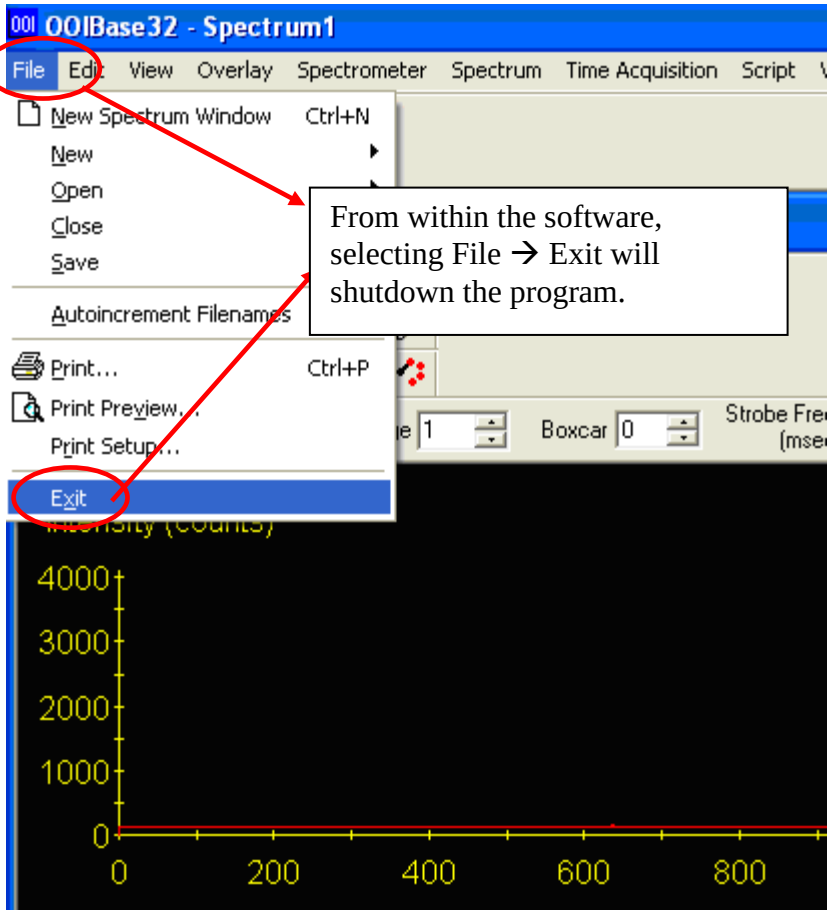

Figure 18. OES operating software

A.4.2. Schematic

The Ocean Optics S2000 System consists of 5 fiber optic cables (Labeled Master, Slave 1-4) connected to an analyzer which interfaces with a computer workstation so that data can be collected. The fiber optic cables are attached to a viewport in the ECR reactor through a machined cover held in place by screws

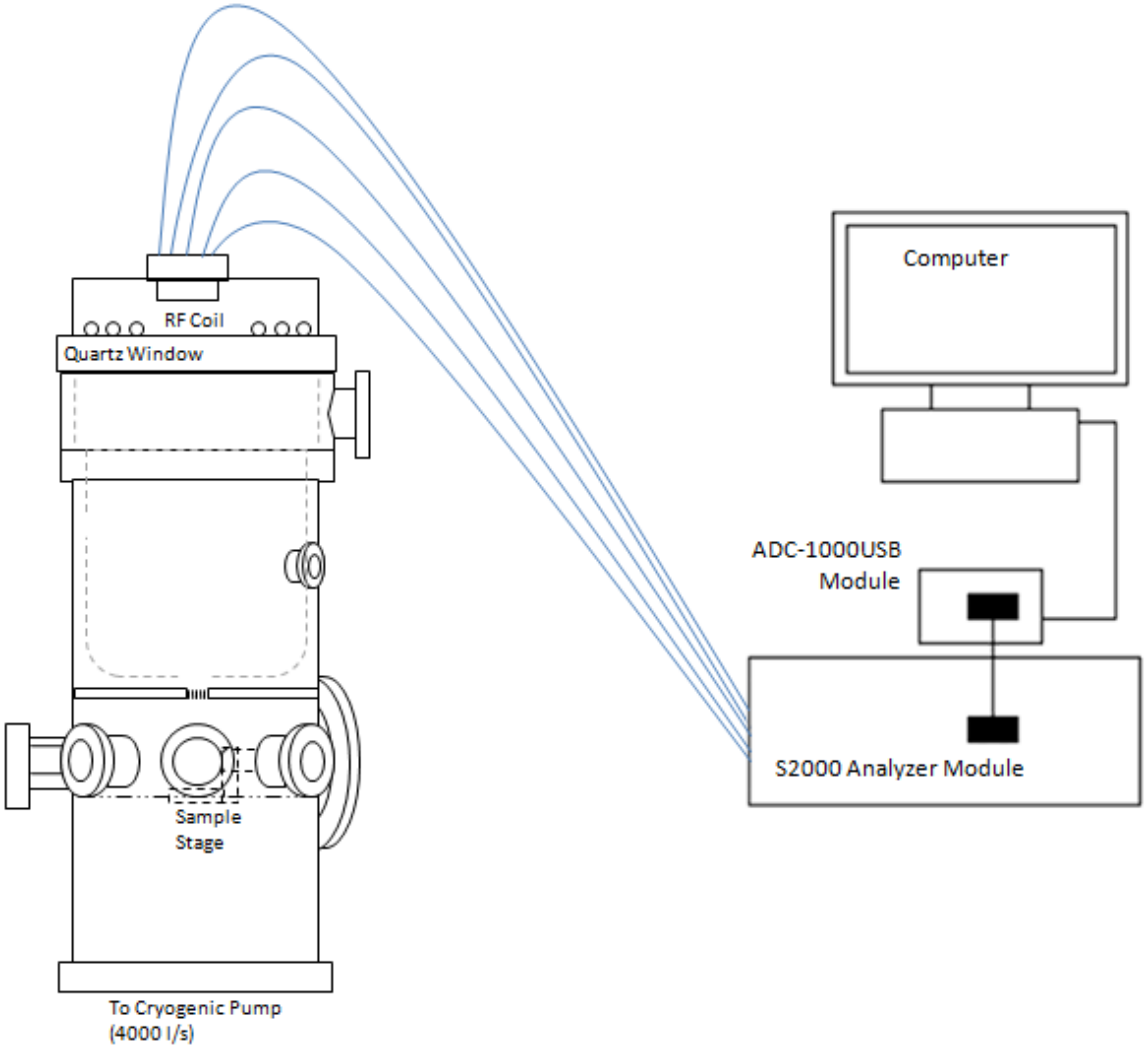

Figure 19: Schematic of Optical Emission Spectrometer showing connection of components.

A.4.3. Safety and Operating Procedures

1. Have Optical fiber and cable connections ready
    i. One end of the fiber points to the light source (plasma)
    ii. The other side of the fiber plugged into the S2000 module.
    iii. S2000 module connects to ADC1000-USB (S/N ADUD6666) converter
    iv. USB cable goes from ADC1000-USB to the computer USB port
2. Start the OOIBase 32 program
3. Load the configuration file:
    a. Go to Spectrometer → Open Configuration
    b. Load c:\Program Files\Ocean Optics\OOIBase32\Default.spec
4. Enable channels:
    a. Go to Spectrometer → Configure
    b. Select Wavelength Calibration → Spectrometer Channel
    c. For Master, Slave 1, Slave 2, Slave 3, and Slave 4: check Channel Enabled Box.
    d. Click OK
5. Set proper integration time and time of average required.

A.4.4. Wavelength Calibration Settings:

These calibrations are set in the *.spec, the file that currently loads properly is located in Jerry's directory in the main Ocean Optics\OES folder.

Settings for Each Channels

Channel	Coefficient	
Master	First Coefficient	0.09149
	Second Codfficient	-6.95276e-6
	Third Coefficient	8.21743e-11
	Intercept	195.774872
Slave 1	First Coefficient	0.08122
	Second Codfficient	-6.12735e-6
	Third Coefficient	-4.10603e-10
	Intercept	327.208588
Slave 2	First Coefficient	0.10891
	Second Codfficient	-9.05373e-6
	Third Coefficient	-3.54458e-10
	Intercept	437.932098
Slave 3	First Coefficient	0.16705
	Second Codfficient	-1.29450e-5
	Third Coefficient	-5.23387e-10
	Intercept	585.628601
Slave 4	First Coefficient	-015435
	Second Codfficient	-1.47189e-5
	Third Coefficient	-1.54958e-10
	Intercept	786.201172

APPENDIX A.5. X-ray Photoelectron Spectroscopy Operational Guidelines
A.5.1. Emergency Shutdown

1. Make sure the transfer loading arm from the tube is all the way out of the XPS chamber and then close the gate valve to the transfer tube.
2. Turn off X-ray source by pressing HV button (should be lit, light will turn off when pressed) and then STANDBY button (should be unlit, will light when pressed and OPER button to the right should become unlit). If there is time, wait for water to flow to cool the anode for ~ 1 minute and press COOLING ON button. Then, turn off the main power and chiller power.
3. Turn off energy analyzer by turning off ESCA kV and power switches on boxes from bottom to top (lens, detector, control and display)
4. Turn off software by pressing the Stop Expt/Kill Data switch until experiment stops.

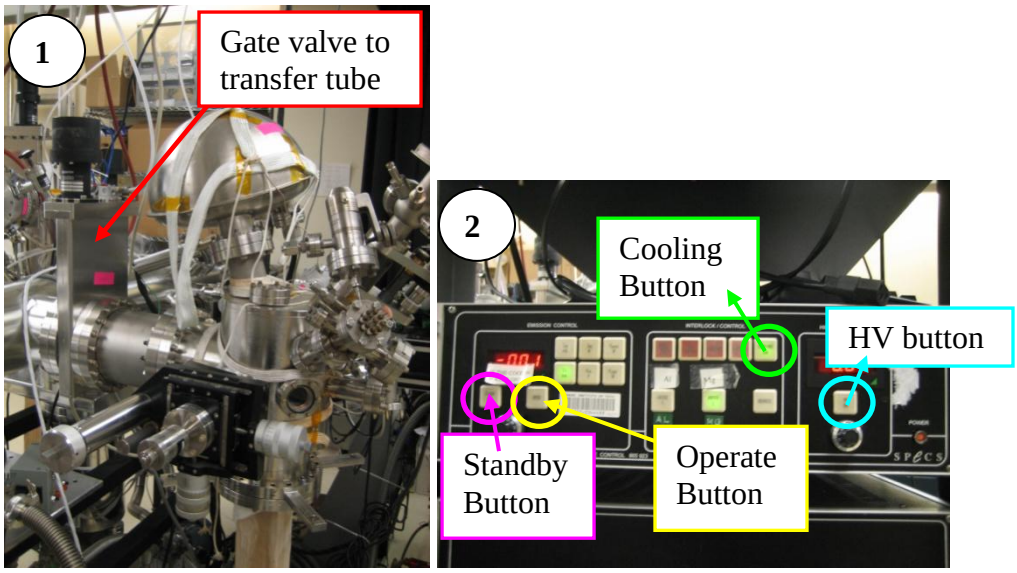

Figure 20. XPS apparatus and control panel

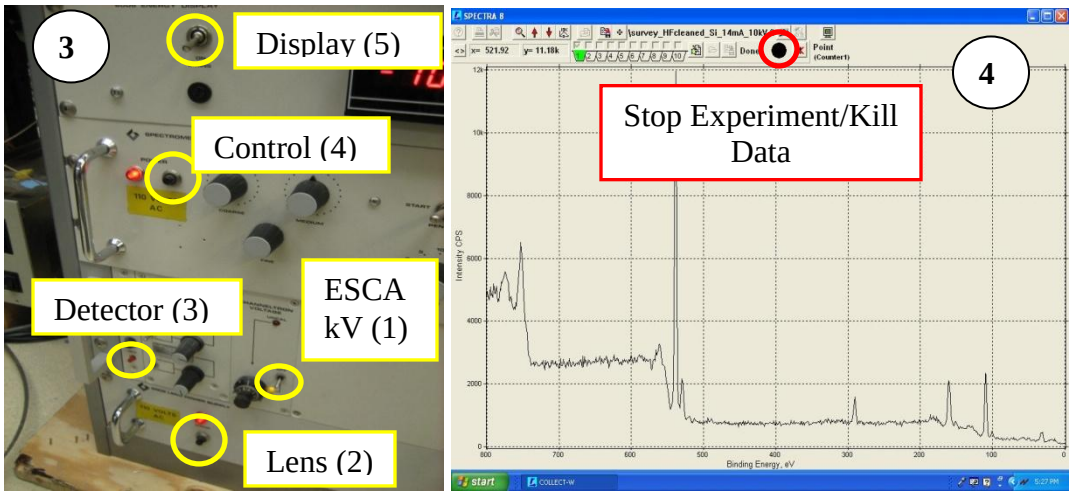

Figure 21.

A.5.2. Safety and Operating Procedures

1. Before transferring the sample, make sure the x-ray gun is backed out to a setting of about 1.5 mm on the motion manipulator (~1 cm from the Teflon spacer). Move the sample stage towards the gate valve to a setting of 1-2 on the corresponding manipulator). Lower the stage to a setting of ~4 on the corresponding manipulator. Ensure the stage is vertical. **Be careful as the stage rotates easily.**

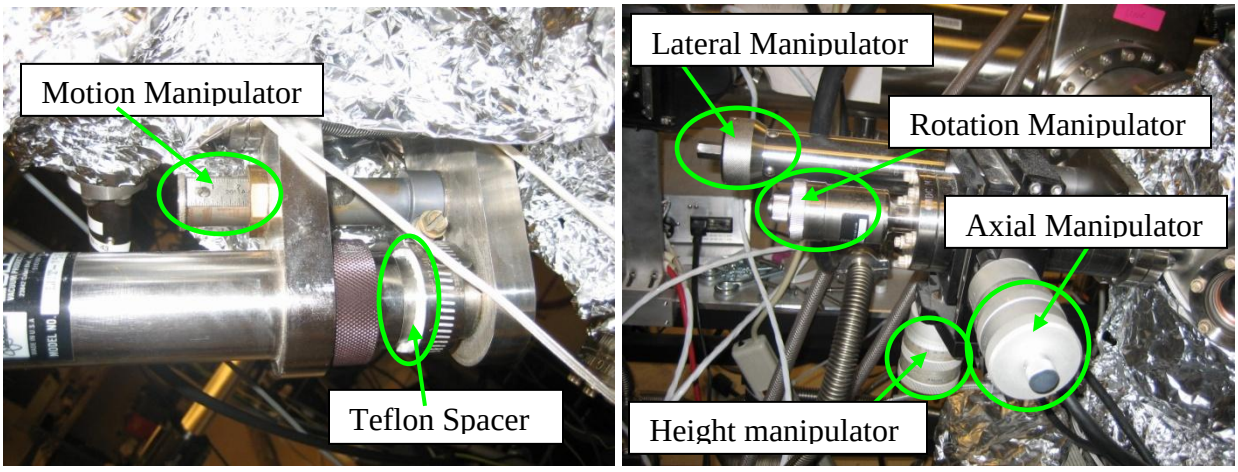

Figure 22. Sample stage manipulator

2. Check the pressure on the XPS using the ion gauge controller (base is ~1 x 10^{-9} Torr, but anything below 3 x 10^{-9} Torr is acceptable. If the pressure is above the 10^{-9} Torr range check the ion pump controller for current reading – should read ~10^{5} – 10^{6} A). Check the pressure on the TT using its ion gauge controller, pressure should be ~4 x 10^{-9} Torr (if it is higher check that the gate valve between the cryo and the TT is open, if it is not, then open it using the controller box (trace the cable to be sure)). Once both pressures are in the requisite range open the gate valve between the TT and XPS using the corresponding controller box (trace the cable if unsure).

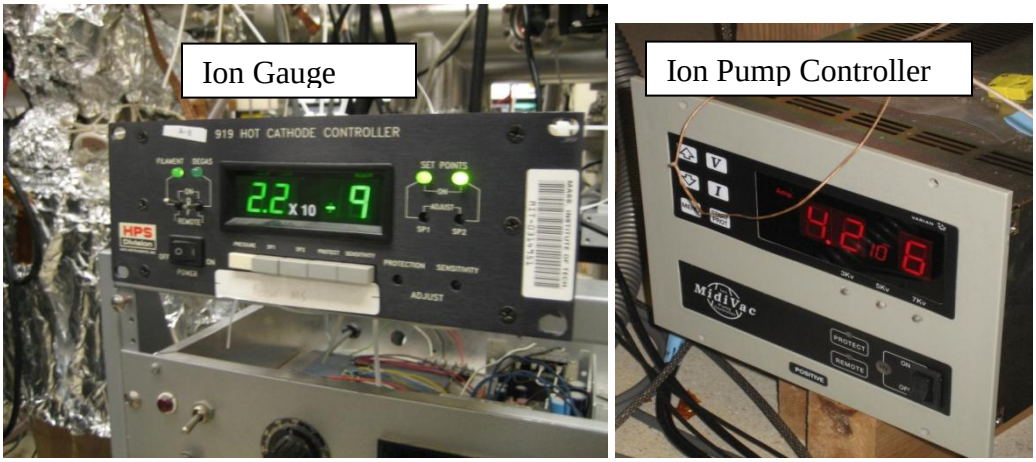

Figure 23. XPS pressure gauge

3. Slide the transfer arm into the tube **slowly**, checking the viewport occasionally to make sure that you do not collide with the stage or x-ray source. The manipulator settings on the arm should be X-setting = 5.5 (black) and Y-setting = 5 (black). Make sure the stage is aligned with the sample using the lateral manipulator (pictured in Step 1 on previous page). At this point you may have to raise the sample or lower the stage to provide the necessary vertical clearance. Lower the sample onto the stage. You may have to lower the loading arm to a Y-setting of 3-4 in order to remove the fork from the sample – slowly pull out the fork and after each small movement, increase the Y-setting slightly to avoid excessive straining. Retract the fork completely, being cautious to clear the transfer cart, and close the gate valve between the tube and the XPS.

4. Move the sample stage closer to the source and move source in until it is about 0.25 cm away from the Teflon spacer. Select the angle theta, which is the angle between the sample surface and the detector axis, using the rotational control - 240° corresponds to a 90° take off angle and 270° to a 60° take-off angle.

5. Move x-ray source closer if desired and adjust the stage position using the various manipulators until you are satisfied that the beam will illuminate the sample. Check the pressure in the XPS chamber – it should be at or below 3 x 10^{-9} Torr. Turn on the analyzer by turning on the switches labeled in the left picture below – from top to bottom: Display, Control, Detector, Lens, then ESCA kV. Turn on the x-ray source by pressing the power switch on the Control Unit. Press "Cooling On" (this should result in the button beginning to blink with a green light) and then turn on the NESLAB HX-75 Chiller (This should result in the green light becoming steady). Select an anode by pressing the corresponding button (selection will result in the button being illuminated by a green light). At this point none of the Interlock Buttons should be lit red. If they are seek assistance from a senior lab member or cautiously check all connections from electronics to the unit.

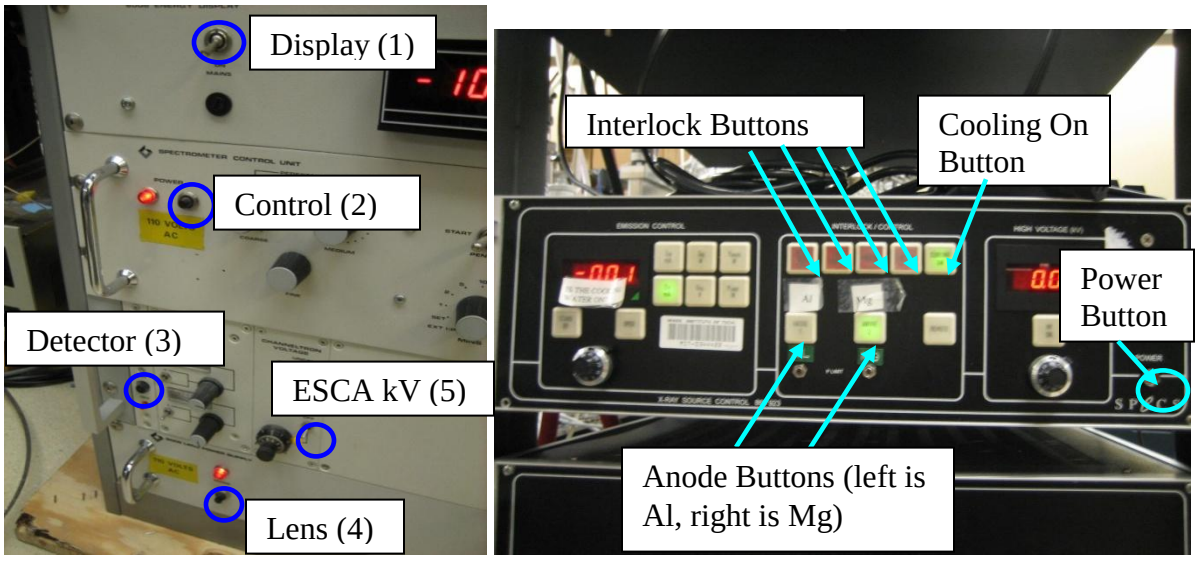

Figure 24. XPS control panel

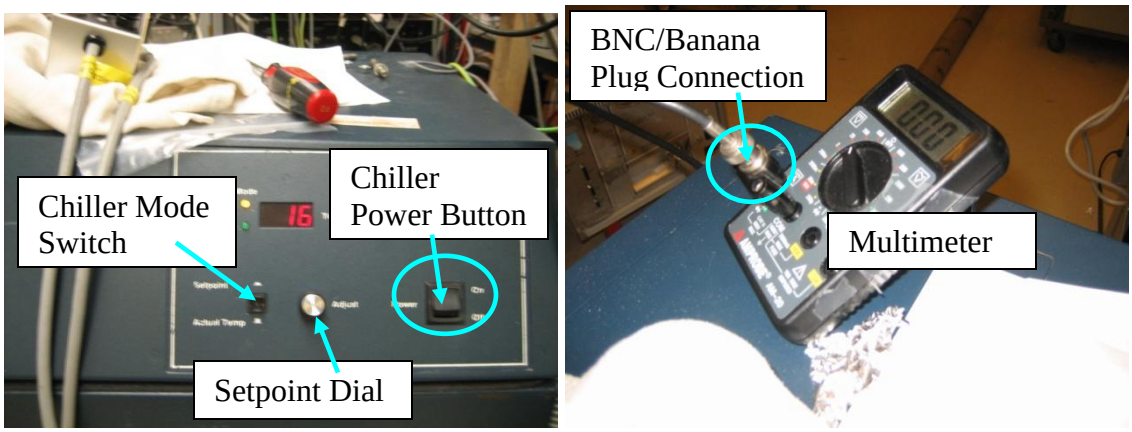

Figure 25. XPS chiller control panel and grounding test by multimeter

Check the chiller setpoint by pushing in the chiller mode switch. This should read 17 degrees. If it has changed adjust the setpoint dial while keeping the mode switch depressed. Check the flow rate by plugging in the BNC/Banana Plug connection to the multimeter. When set to measure DC Voltage the multimeter should give a reading of over 3.4 V. All the electronics to warm up for 10 minutes before running an experiment.

6. Launch the software program SPECTRA by double clicking the icon labeled SPECTRA in the center of the desktop. To save time before the experiment begins you can define your regions (survey, detailed, etc) by clicking the Edit Region Info Button. Also confirm that the software is configured for the anode you selected in Step 5, by clicking the Tools Button, then clicking “Setup Card” in the menu that pops up. In the dialogue box that pops up you can select either Mg (1253.6 eV) or Al (1486.6 eV) in the Excitation field.

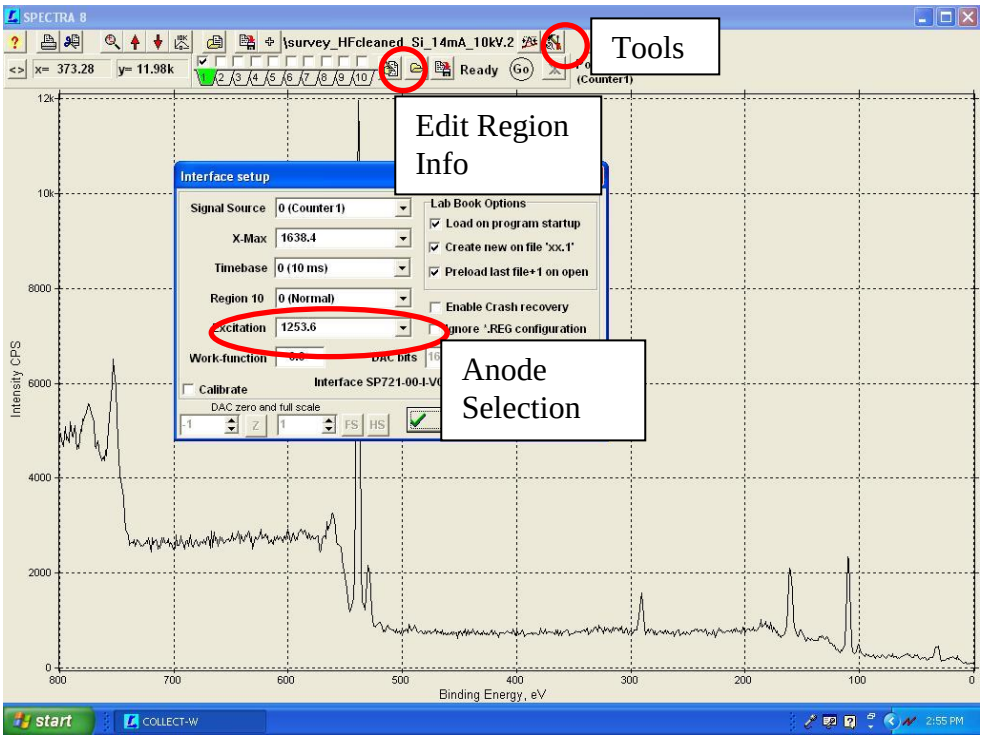

Figure 26. Set up in the XPS software

7. Once the electronics have warmed up, check that the Spectrometer Control Unit is set to COMP mode and that the Energy Selector corresponds to the Binding Energy (BE) of the anode you selected earlier in Step 5.

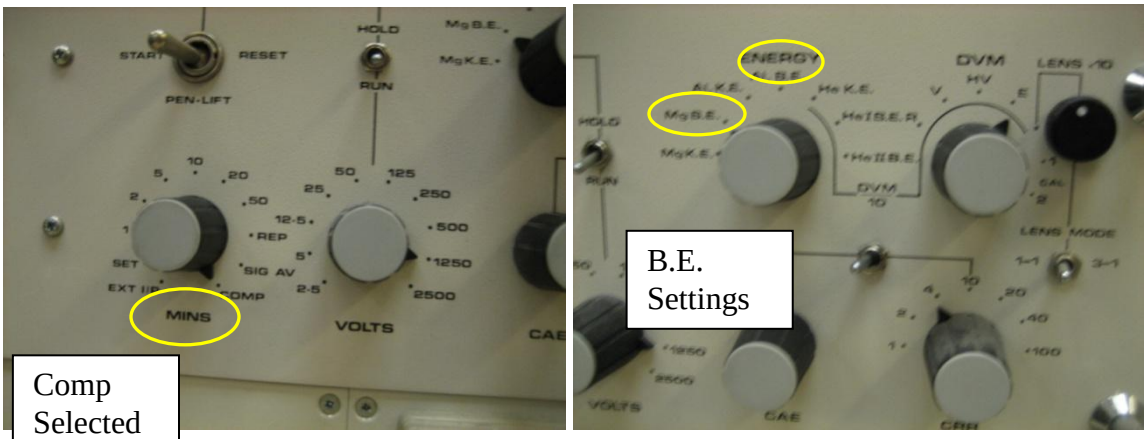

Figure 27. XPS control panel

8. Press the "I_{FIL}" button on the X-Ray Souce Control Unit, which should light up green. Press the "Stand By" button (display should change to 2.91 A) and monitor the pressure in the chamber, which will rise to as high as 2 x 10^{-8} Torr, but should decrease quickly. When it has returned to 10^{-9} Torr, press the "HV on" button and adjust the dial so that the display reads ~4.00 – 5.00 kV. Monitor the pressure, which should still be in the 10^{-9} range (Note: These values are for Mg anode, Al may be higher). Press the "Oper" button, the value of I_{FIL} should rise to ~ 3.6 A and the light should blink briefly before becoming steady again. Press the "I_E" button (should light up green) and use the left and right dials to gradually increase the I_E and HV values to the desired reading (14 mA for I_E and 10 kV for HV are standard, 18 mA for I_E and 12 kV are maximum for Mg anode, 14 kV can be used for Al anode). In the SPECTRA window press the circular button marked "Go" to the right of the Edit Regions Button.

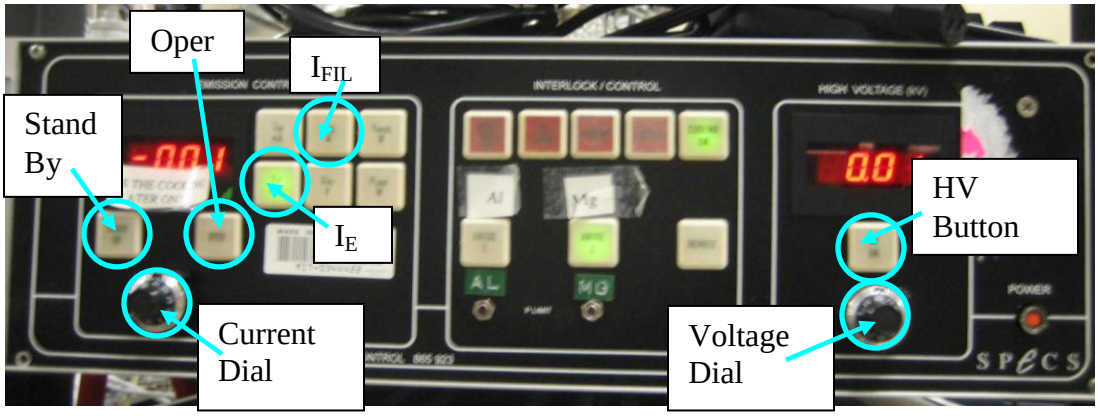

Figure 28. XPS control panel

9. Once the scans are finished, ramp down the HV and I_E values by turning down the dials slowly until they are at about 4 kV and 5 mA respectively, then Press "Oper" (the light should go off and the "Standby" button should light up. Press "HV" (the light should go off), then press "Standby" (the light should go off. If you are going to do more scans but the pressure has increased significantly over the course of your run, the system can be left in this state while it pumps down. If the pressure has not increased significantly, you can adjust the region info and then run more scans at your discretion without having to turn off the HV/I_E switches.

If you will not run anymore scans, leave the “Cooling On” button on to let the anode cool down for ~5-10 minutes. Press “Cooling On”, then press the power switch. Turn off the chiller. Turn off the analyzer electronics by turning off ESCA kV first, then the boxes from bottom to top (in reverse order from Step 5). Remove your sample from the chamber if desired.

APPENDIX A.6. Spectroscopic Ellipsometer Operational Guidelines

A.6.1 Emergency Shutdown

1. Turn off the power of LPS-400 light source.
2. Shut off the circuit breaker of the power controller.

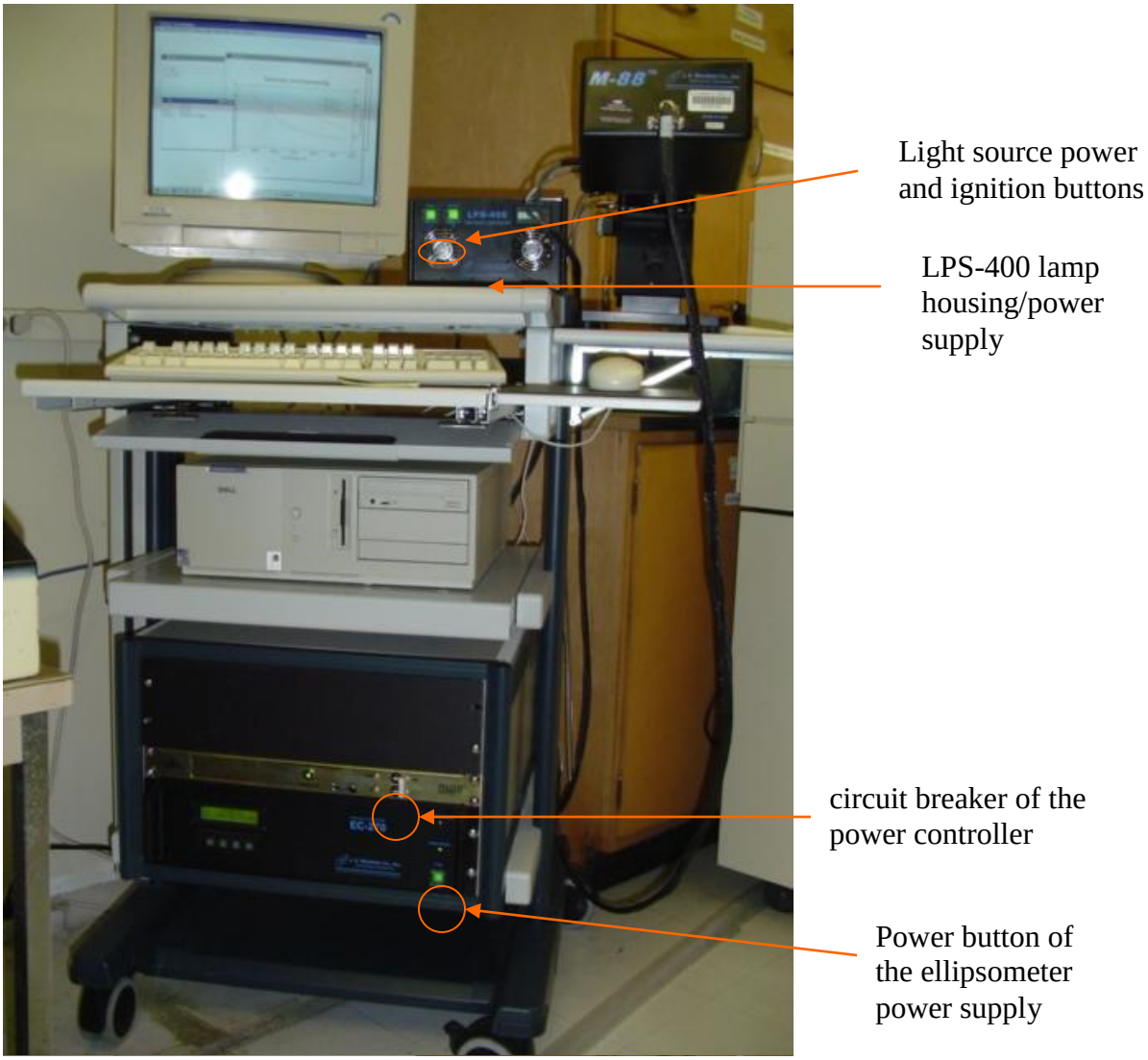

Figure 29. Ellipsometer

A.6.2. Operating Procedures

Turn-on procedure

1. Turn on the circuit breaker of the power controller.
2. Turn on the power of the ellipsometer power supply (Electronics Control Module EC-270).
3. Turn on the light source (LPS-400). Press “power” button, and **wait a few seconds**, then press “ignition” button.
4. Flip on the sign that reads “Lamp ON!”

Turn-off procedure

<For short time off>

1. Turn off the light source (LPS-400).
2. Flip on the sign that reads “Lamp OFF but Power ON!”

<For system off at the end of the day>

1. Turn off the light source (LPS-400).
2. Turn off the circuit breaker of the power controller.
3. Flip on the sign that reads “Power OFF!”

Do not leave the light source on for extended time periods.

A.6.3. Software Operation

1. Load the software (WVASE32).
2. Press “Window” on the menu bar, and select “Hardware”.
   The “Hardware” window pops up, showing a message “Status:Hardware NOT Initialized”
3. Press “Initialize”.
   You will hear motor-running sound from the ellipsometer.
4. Place your sample on the stage. Make sure the beam is hitting the area you want to probe.
5. Press “Align”. The window for alignment will pop up. Your goal is to **align the red cross to the center of the reference frame.**
6. Adjust two tuning knobs underneath the sample stage until the red cross appears on the center of the reference frame.
7. Once alignment is done, press “Esc” key on the keyboard to exit the window.
8. Press “Ellipsometric data”. A new window of “In-situ real-time scan” will appear.
9. Press “Acquire Single Scan”. Data will be collected. It takes only a second.
10. To see the graphical results, press “Window” to select “Graph”.
    It will show Ψ and Δ.
    You can see other parameters (such as ε_1, ε_2, n, k, etc.) by pressing “Type” and selecting the parameter you want to see.

To estimate layer thickness (Sequence: choose a model → fit the data)

1. Choose a model
   1) Press “Window” and select “Model”.
   2) Press “Addlayer” and select a proper material file (*.mat) for substrate.
      You can set substrate thickness to 1 mm. Contact Woolam if the material you are interested in is not in the data base.
   3) Press “Addlayer” and select a proper material file (*.mat) for each layer.
      1. For files containing *n* and *k* data (tabulated-layer file), the initial layer thickness should be reasonably close to the actual thickness. Check the “Fit” box, and press “OK”.

2. For functional files, you can fit other coefficients as well as layer thickness by checking the “Fit” boxes.

Recommended material-data file (*.mat): Files are located in C:\wvase32\mat\

Examples:

- Si: SI_JELL.mat (*n,k* data)
- SiO_2: Sio2.mat (*n,k* data)
- HfO_2: \mat\dielectr\Hfo2.mat (*n,k* data) or Hfo2_c.mat (Cauchy fit)
- ZrO_2: \ mat\dielectr\ Zro2_c.mat (Cauchy fit)
- Y_2O_3: \mat\dielectr\y2o3.mat (*n,k* data)
- SiC: \mat\semicond\sic.mat (*n,k* data)
- AlN: aln_final_nk.mat (*n,k* data) or aln_cauchy_final.mat (Cauchy fit)

2. Fit
   1) Press “Window” and select “Fit”.
   2) Press “Normal fit” several time until the result value conversed.
3. Save the data

1) Press “Experimental Data” window and go to “file” to save the data.
2) Press “Generated Data” window and go to “file” to save the data.

A.6.4. Hardware Calibration Procedure

1. Place a sample on the stage and align it.
2. Load the software (WVASE32).
3. window → hardware → calibrate
4. You will see a dialog box “Calibration Mode” with five selections, which are;

    - Normal
    - Coarse
    - Detector electronics (off sample)
    - Detector system (straight-through configuration)
    - Detector system (with calibration sample)

- “Normal” or “coarse” calibration can be performed every time the system is turned on and the data acquisition is to be carried out. However, it is not necessary to perform it unless you suspect the system is not working correctly.
- “Detector system (straight-through configuration)” calibration must be performed only once, when the instrument is first set up, and does not need to be performed every time the instrument is turned on. To perform it, please see the manufacturer’s manual.

5. For routine calibration, choose “normal” or ‘coarse” calibration, and press “OK”
6. To see the graph: window → graph

A.6.5. Installation of Compensator on Spectroscopic Ellipsometer

Follow the manual for the JA Woollam Manual Retarder to remove the input module and install compensator in between the base and the input.

Figure 30. Sample stage, light source and compensator of ellipsometer

A Si wafer with a medium thickness SiO_2 film ~260 Å should be used for calibration.

9/7/04
After the Retarder is set to "IN", be careful not to turn X and Y screws too far or they will come out and the compensator must be reassembled.

The screws should be adjusted so Psi lines up exactly and the Delta model should be shifted lower than the experimental value by 40-90deg.

Problems: On Step 10 in the manual for the JA Woollam Manual Retarder, when doing the Detector System Calibration (Calibration Sample), it finished acquiring the data. Then at Channel #87 an Error Message appeared "Error bars on calibration parameters exceed suggested limits. Verify instrument is operating properly and then repeat the straight through calibration procedure."

Solution: Increased error tolerances in the “mmx-cal.cnf” file in the WVASE32 folder. Repeated Step 10. The calibration finished. Entered delta offsets in the “hardware.cnf” file according to the manual.In “Ellipsometric Data”, the High Accuracy Mode option needs to be checked.Took data on several SiC and Si samples. Much cleaner data. Better fit. Delta is much smoother, near 90deg. Unsure if it is still very accurate for SiC…

9/29/04

Problem: Tried to measure SiC samples. Delta for the model was extremely noisy for all samples and would not fit the data.

Solution: Tried to repeat Steps 10,11. No Change.

Repeating entire calibration procedure.

Performed normal calibration (out)

Acquired dynamic data (in) and aligned psi and offset delta.

Guessed delta offset parameters in Model Options

Performed Detector System Calibration (with Calibration Sample)

DelOff1 = 78.014

DelOff2 = -1.9517e-2

A.6.7. Replacement of protection device

On March 11, 2005 the WVASE 32 program would not load. When clicking on the WVASE 32 icon on the desktop, the message "Protection Device Not Found!" was given. After contacting J.A. Woollam (phone # (402) 477-7501) and speaking to Ping He, it was determined that the protection device plugged into one of the parallel ports in the back of the computer was no longer working. J.A Woolam sent us a replacement protection device, and the WVASE 32 program is now working.

APPENDIX A.7. Transfer Tube

A.7.1. Emergency Shutdown

1. Ensure that all transfer arms are in the fully withdrawn position (i.e. they are not extended into any reactor chambers).
   Close all electrically operated gate valves on the system using the control boxes located on the transfer tube table. (In the event of a power outage, this should automatically happen). Visually inspect that this has taken place whenever possible by looking through the appropriate windows on the transfer tube. In the event that a manual gate valve is present, close it by hand.

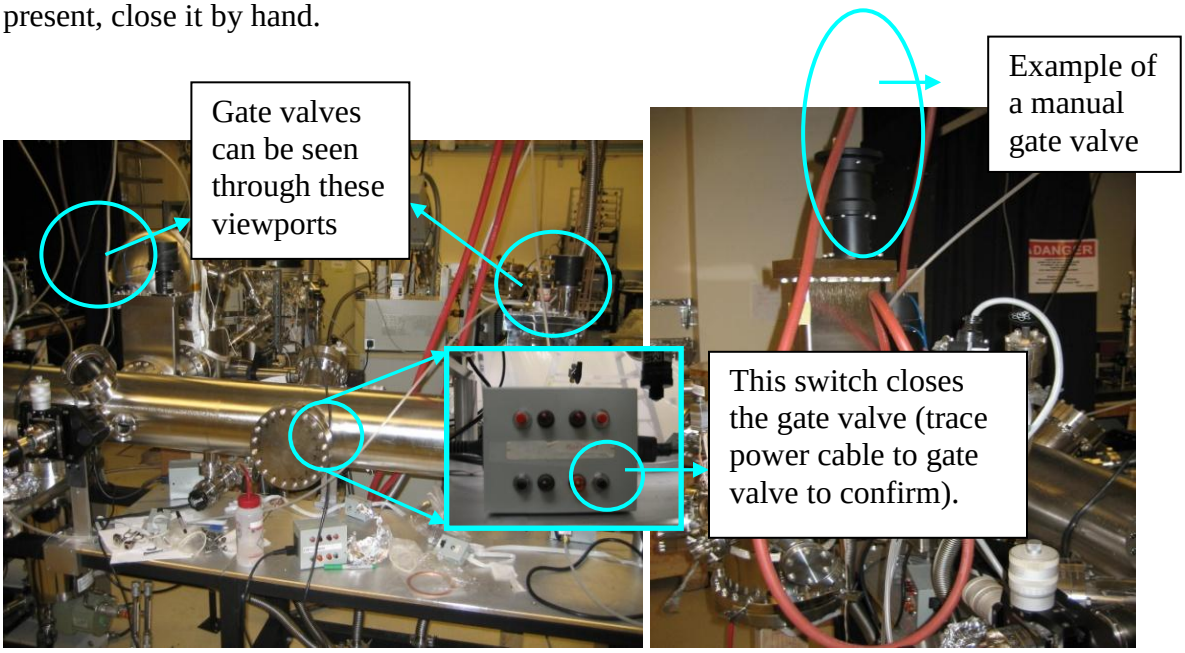

Figure 31. Windows, gate valve and gate valve controller of transfer tube

2. Press the stop button on all the turbo pump controllers (in the event of the power outage the controllers should all turn off).

Figure 32. Controller of TMP

3. If power is still available, allow the turbo pumps 10-15 minutes to wind down and then close all the roughing valves between the turbo pumps and their backing mechanical pumps. In the event of power loss close these valves immediately.

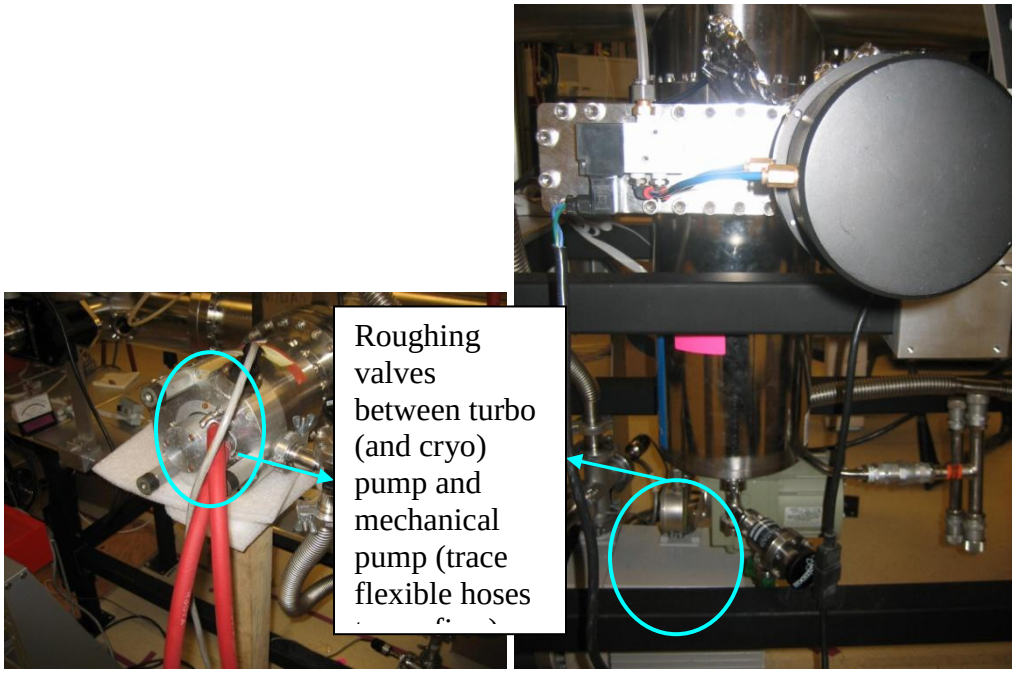

Figure 33. Roughing valve of TMP and cryopump

4. Use your discretion to turn off the mechanical pump on the tube, situated under the table.

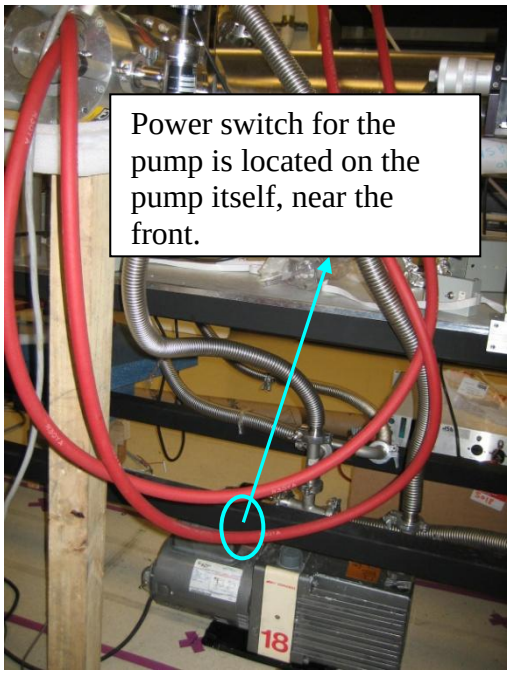

Figure 34. Mechanical pump of TMP

5. The pressure of the transfer tube is displayed on a readout/controller located on the tube table next to the loadlock (this controller monitors the loadlock and transfer tube pressure), facing the north side of the room. Monitor the pressure regularly.

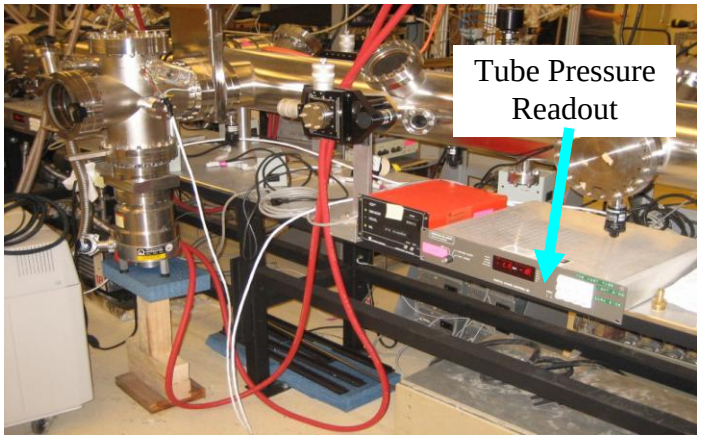

Figure 35. Ion gauge of transfer tube system

6. Double check that the gate valve above the cryopump is shut and the rough valve between the cryopump and the mechanical pump is closed (this should have been done in the previous steps). Turn off the CTI 9600 Compressor connected to the cryopump by flipping the white circuit breaker to the “off” position.

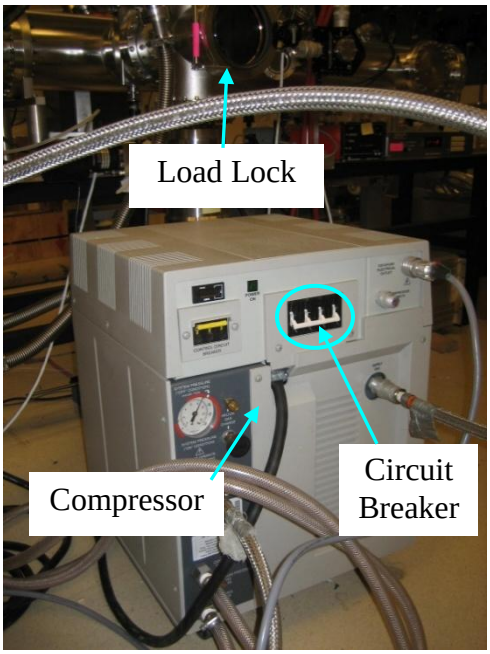

Figure 36. Compressor of cryopumps

A.7.2. Safety and Operating Procedures

Please refer to the following labeled picture when performing Steps 1 and 2.

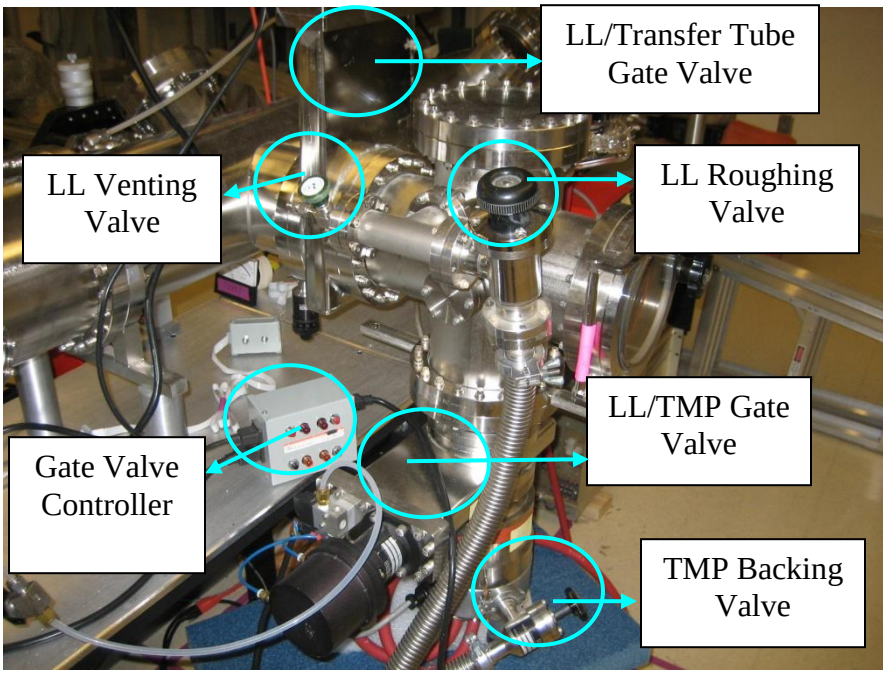

Figure 37. Component of load lock

1. To load a sample, the loadlock must first be vented. Ensure that the gate valve between the load lock and the transfer tube is CLOSED. Close the gate valve between the LL turbo and the LL. Ensure that the roughing valve between the LL and its mechanical pump is also closed. Vent the load lock by SLOWLY opening the green venting valve. Within a short time period the load lock door should open easily. Close the green venting valve. **DO NOT UNDER ANY CIRCUMSTANCES OPEN THE GATE VALVE BETWEEN THE LL AND ITS TURBO WHILE THE LOAD LOCK IS VENTED!** Place your sample holder on the pin holder inside of the load lock. If you used screws to secure your sample, ensure that the screws are facing you.

2. Close the LL door and slightly tighten the handle. Isolate the LL turbo pump and the TT turbo pump by closing the roughing valve between these pumps and their backing mechanical pump (trace the flexible hoses to confirm the pump identity). Open the roughing valve between the load lock and the mechanical pump while pressing in the door. Readjust the tightness of the screw handle, but **do not overtighten**. Verify that the LL is pumping down by checking the pressure on the thermocouple gauge attached to the mechanical pump**. Note that the turbopumps can only be isolated for ~5 minutes.**

When the pressure has dropped to ~60 mTorr, close the roughing valve to the LL, unisolate the LL and TT turbo pumps and open the gate valve to the LL turbo. Monitor the pressure using the LL ion gauge.

3. When the pressure in the LL is ~5 x 10^{-6} Torr, sample transfer is possible. In this case the pressure in the tube should be ~10^{-8} Torr. (If the loadlock pressure is ~5 x 10^{-7} Torr, then the pressure in the tube can be ~10^{-9} Torr). Accomplish this by closing the TT/Cryopump gate valve, then monitoring the pressure using the ion gauge. When the pressures are at the requisite levels open the gate valve between the LL and the transfer tube. Check for pressure spikes using the TT ion gauge**. If you are uncomfortable about transferring by yourself you may close the gate valve between the LL and its turbo pump to prevent samples from hitting the TMP if they fall.**

4. Use the transfer arm to place the sample holder onto the cart (recommended settings are on the transfer arm, but exercise caution when carrying out this operation). Try to ensure that the tines of the loading fork extend past the edge of the sample holder nearest to you. **Also remember that the arm cannot be lifted to its maximum value if it is near the limit of its lateral extension. Make adjustment in small increments, consistently checking to ensure that nothing is strained.** Retract the transfer arm completely and close the LL/TT gate valve.

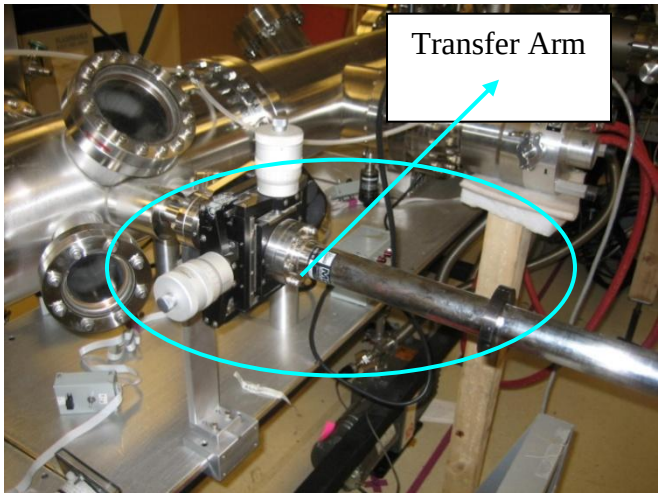

Figure 38. Transfer arm on the transfer tube

5. Use the motor control situated at the eastern end of the tube to move the cart to the desired chamber. **If the cart is having problems moving, closing the gate valve between the tube and its turbo pump often rectifies this situation, as well as the gate valve between the tube and its cryopump. However, remember to reopen the valves after moving the cart into place.** Once in place, close the gate valve between the transfer tube and its cryo pump, then open the gate valve to the transfer tube. Use the transfer arm to lift the sample holder off the cart and place it into the chamber. Retract the arm completely and then close the chamber/TT gate valve before reopening the TT/Cryopump gate valve.

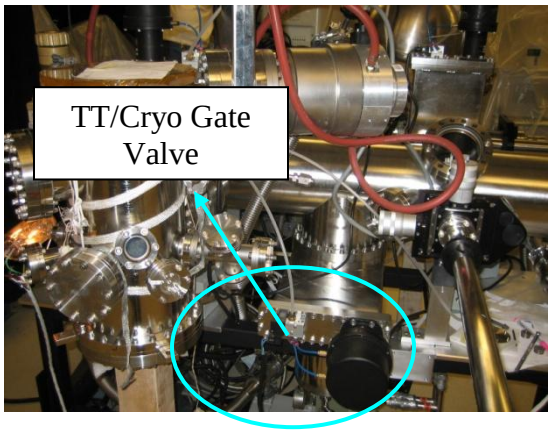

Figure 39. Gate valve of cryopump to transfer tube

6. To transfer samples from chambers to the transfer tube, first make sure the experiment has been fully halted (i.e. there is no gas flow, plasma, etc.) and that the chamber has been pumped down to its base pressure for ~15-30 minutes. Close the TT/Cryo gate valve first, then open the chamber/TT gate valve. Use the transfer arm to remove the sample from the chamber and place it into the transfer cart. Retract the transfer arm completely, close the chamber/TT gate valve and then reopen the TT/Cryo gate valve.

APPENDIX B. Translating Mixed Model Code

HfO_2 Source File

This is the source file for hafnium oxide etching in chlorine plasmas. Parameters are defined here, as well as the overall mass balance equations describing the etch/deposition process.

```
MODEL HfO2_Cl2
PARAMETER
# Sticking coefficient parameter of neutrals
S_Cl_on_Hf              AS REAL
S_Cl_on_O               AS REAL
# Sticking coefficient parameter of ions (set to unity without charging)
S_Cl_i                  AS REAL
S_Cl2_i                 AS REAL
f_thre_fac              AS REAL

# Sputtering Yield coefficient
Y_Hf_by_Cl_i           AS REAL
Y_Hf_by_Cl2_i          AS REAL
Y_O_by_Cl_i            AS REAL
Y_O_by_Cl2_i           AS REAL
Y_Cl_by_Cl_i           AS REAL
Y_Cl_by_Cl2_i          AS REAL
Y_Hf_by_Ar_i           AS REAL
Y_O_by_Ar_i            AS REAL
Y_Cl_by_Ar_i           AS REAL

# Rate for vacancy creation due to ion bombardment
B_V_Cl_i               AS REAL
B_V_Cl2_i               AS REAL
B_V_Ar_i               AS REAL
# Ion enhanced reaction coefficient
B_HfCl2                 AS REAL
B_HfCl3                 AS REAL
B_HfCl4                 AS REAL
B_Cl2                   AS REAL
B_O2                     AS REAL
B_OCl                   AS REAL

# Surface recombination coefficient
A_Cl_Cl               AS REAL
A_Cl_Cl_i             AS REAL
A_O_Cl                AS REAL
A_O_Cl_i              AS REAL

# Densification Reaction Coefficient
B_d_V_by_Cl            AS REAL
B_d_V_by_Cl2           AS REAL
B_d_V_by_Ar            AS REAL

# Annihilation Reaction Coefficient
B_Hf_V                 AS REAL
B_O_V                  AS REAL
B_Cl_V                 AS REAL
```

```
# Thermal Reaction Coefficient
m_Cl                    AS REAL

# Neutral composition from the plasma impinging on the surface
G_Cl_Frac               AS REAL

# Ion composition from the plasma impinging on the surface
G_Cl_i                  AS REAL
G_Cl2_i                 AS REAL
G_Ar_i                  AS REAL

# Ratio of total neutral species to total ion species
N2I                     AS REAL

VARIABLE
# Surface concentration variables
X_Hf        AS Concentration
X_O            AS Concentration
X_Cl        AS Concentration
X_V            AS Concentration

# Real incoming fluxes
G_Cl        AS Concentration
#G_Cl2        AS Concentration

# Nearest neighbor probabilities
J_Hf_Hf        AS Concentration
J_Hf_O        AS Concentration
J_Hf_Cl        AS Concentration
J_Hf_V        AS Concentration
J_Cl_Cl        AS Concentration
J_Cl_V        AS Concentration
J_O_O        AS Concentration
J_O_V        AS Concentration
J_O_Cl        AS Concentration


# Reaction rates for adsorption of neutrals
R_A_V_by_Cl_i, R_A_V_by_Cl2_i, R_A_V_by_Ar_i, R_A_Cl_on_Hf, R_A_Cl_on_O
AS Reaction_Rate

# Reaction rates for adsorption of ions
R_A_Cl2_i, R_A_Cl_i
AS Reaction_Rate

# Physical Sputtering Reaction Rate
R_S_Hf_by_Cl_i, R_S_Cl_by_Cl_i, R_S_Hf_by_Cl2_i, R_S_Cl_by_Cl2_i,
R_S_O_by_Cl_i, R_S_O_by_Cl2_i
AS Reaction_Rate

R_S_Hf_by_Ar_i, R_S_O_by_Ar_i, R_S_Cl_by_Ar_i
AS Reaction_Rate

# Ion Enhanced Chemical Reaction Rates
R_E_HfCl2, R_E_HfCl3, R_E_HfCl4, R_E_Cl2, R_E_O2, R_E_OCl, R_an_V,
R_E_thermal
```

```
AS Reaction_Rate

# Densification Reactions:
R_d_V_by_Cl, R_d_V_by_Cl2, R_d_V_by_Ar
AS Reaction_Rate

#Recombination
R_R_Cl_Cl, R_R_Cl_Cl_i, R_R_O_Cl, R_R_O_Cl_i
AS Reaction_Rate

# Related to total of each species:
R_A_V, R_E_V, R_E_Hf, R_A_Cl, R_E_Cl, R_E_O
AS Reaction_Rate

R_Yield, R_A_tot, R_E_tot
AS Reaction_Rate

SET

EQUATION

# Real Neutral Flux
G_Cl  = G_Cl_Frac  * N2I;

# Effective bond concentration calculations
J_Hf_Hf = 0 ;
J_Hf_O  = (4*X_Hf*2*X_O)/(4*X_Hf+2*X_O+X_Cl+X_V);
J_Hf_Cl = (4*X_Hf*1*X_Cl)/(4*X_Hf+2*X_O+X_Cl+X_V);
J_Hf_V  = (4*X_Hf*1*X_V)/(4*X_Hf+2*X_O+X_Cl+X_V);
J_Cl_Cl = (1*X_Cl*1*X_Cl)/(2*(4*X_Hf+2*X_O+X_Cl+X_V));
J_Cl_V  = (1*X_Cl*1*X_V)/(4*X_Hf+2*X_O+X_Cl+X_V);
J_O_O   = 0 ;
J_O_V   = (2*X_O*1*X_V)/(4*X_Hf+2*X_O+X_Cl+X_V);
J_O_Cl  = (2*X_O*1*X_Cl)/(4*X_Hf+2*X_O+X_Cl+X_V);

# Reactions related to adsorption
R_A_Cl_i         = S_Cl_i  * G_Cl_i  * f_thre_fac;
R_A_Cl2_i        = S_Cl2_i * G_Cl2_i * f_thre_fac;
R_A_Cl_on_Hf     = S_Cl_on_Hf  *  G_Cl  *  J_Hf_V;
R_A_Cl_on_O        = S_Cl_on_O * G_Cl * J_O_V;

# Reactions for internal bond breaking to make vacancies
R_A_V_by_Cl_i  = B_V_Cl_i  *  G_Cl_i ;
R_A_V_by_Cl2_i = B_V_Cl2_i * G_Cl2_i ;
R_A_V_by_Ar_i   = B_V_Ar_i   *   G_Ar_i ;

# Physical sputtering reactions
R_S_Hf_by_Cl_i   = Y_Hf_by_Cl_i   * X_Hf * G_Cl_i  ;
R_S_O_by_Cl_i    = Y_O_by_Cl_i    * X_O  * G_Cl_i  ;
R_S_Cl_by_Cl_i   = Y_Cl_by_Cl_i   * X_Cl * G_Cl_i  ;
R_S_Hf_by_Cl2_i  = Y_Hf_by_Cl2_i  * X_Hf * G_Cl2_i ;
R_S_O_by_Cl2_i   = Y_O_by_Cl2_i   * X_O  * G_Cl2_i ;
R_S_Cl_by_Cl2_i  = Y_Cl_by_Cl2_i  * X_Cl * G_Cl2_i ;
R_S_Hf_by_Ar_i   = Y_Hf_by_Ar_i * X_Hf * G_Ar_i ;
R_S_O_by_Ar_i    = Y_O_by_Ar_i   * X_O  * G_Ar_i ;
R_S_Cl_by_Ar_i   = Y_Cl_by_Ar_i  * X_Cl * G_Ar_i ;
```

```
# Densification reactions:
R_d_V_by_Cl  = B_d_V_by_Cl  * X_V * G_Cl_i  ;
R_d_V_by_Cl2 = B_d_V_by_Cl2 * X_V * G_Cl2_i ;
R_d_V_by_Ar     = B_d_V_by_Ar * X_V * G_Ar_i ;

# Ion enhanced chemical etching reactions
R_E_HfCl2 = B_HfCl2 * (J_Hf_Cl)^2 ;
R_E_HfCl3 = B_HfCl3 * (J_Hf_Cl)^3 ;
R_E_HfCl4 = B_HfCl4 * (J_Hf_Cl)^4 ;
R_E_Cl2   = B_Cl2   *  J_Cl_Cl  ;
R_E_OCl   = B_OCl   *  J_O_Cl    ;

# Dangling Bond Annihilation Reaction and Spontaneous Reactions
R_an_V = B_Hf_V * (J_Hf_V)^2 + B_Cl_V * (J_Cl_V)^2 + B_O_V * (J_O_V)^2 ;
R_E_thermal = m_Cl * X_Hf * G_Cl                    ;

# Recombination
  R_R_Cl_Cl = A_Cl_Cl * J_Cl_V * G_Cl;
  R_R_Cl_Cl_i = A_Cl_Cl_i * J_Cl_V * G_Cl_i ;
  R_R_O_Cl = A_O_Cl * J_O_V * G_Cl ;
  R_R_O_Cl_i = A_O_Cl_i * J_O_V * G_Cl_i ;

# Change in Dangling Bonds
R_E_V  = R_A_Cl_on_Hf + R_A_Cl_on_O + 2*R_an_V + R_d_V_by_Cl + R_d_V_by_Cl2 +
R_d_V_by_Ar + R_A_Cl_i + R_A_Cl2_i + R_R_Cl_Cl + R_R_Cl_Cl_i + R_R_O_Cl_i +
R_R_O_Cl  + 2*R_E_HfCl2 + 3*R_E_HfCl3 + 4*R_E_HfCl4  ;
R_A_V  = R_A_V_by_Cl_i  + R_A_V_by_Cl2_i + R_A_V_by_Ar_i             ;
R_E_Hf = R_S_Hf_by_Cl_i + R_S_Hf_by_Cl2_i + R_S_Hf_by_Ar_i + R_E_HfCl2 +
R_E_HfCl3  + R_E_HfCl4  + R_E_thermal  ;
R_E_Cl = R_S_Cl_by_Cl_i + R_S_Cl_by_Cl2_i + R_S_Cl_by_Ar_i + 2*R_E_HfCl2 +
3*R_E_HfCl3  + 4*R_E_HfCl4  + 2*R_E_Cl2  + R_E_OCl + R_R_Cl_Cl_i + R_R_Cl_Cl
+ 4*R_E_thermal ;
R_A_Cl = R_A_Cl_i  + 2*R_A_Cl2_i  + R_A_Cl_on_Hf + R_A_Cl_on_O ;
R_E_O  = R_S_O_by_Cl_i + R_S_O_by_Cl2_i + R_S_O_by_Ar_i + 2*R_E_O2 + R_E_OCl
+ R_R_O_Cl_i + R_R_O_Cl ;

# Total summation of added or removed atoms
R_E_tot = R_E_V + R_E_Hf + R_E_O + R_E_Cl ;
R_A_tot = R_A_V + R_A_Cl          ;
R_Yield = (R_E_tot - R_A_tot)/3             ;

# Use calculated total added and removed atoms to judge whether etching or
deposition happens.
IF (R_Yield > 0.0) THEN
$X_Hf = R_Yield - R_E_Hf  ;
$X_Cl = R_A_Cl - R_E_Cl ;
$X_O  = 2*R_Yield - R_E_O  ;
$X_V  = R_A_V - R_E_V  ;

ELSE
$X_Hf = R_Yield*3*X_Hf - R_E_Hf          ;
$X_Cl = R_Yield*3*X_Cl + R_A_Cl - R_E_Cl ;
$X_O  = R_Yield*3*X_O  - R_E_O  ;
$X_V  = R_Yield*3*X_V  + R_A_V   - R_E_V  ;

END
END
```

B.1 HfO_2 Single Conditional Calculation File

This file is used together with the definitions found in the source file for a single conditional calculation of the model, e.g. estimation of etch yield and mixing layer concentration for a single value of ion energy.

```
SIMULATION SCC_HfO2_Cl2

PARAMETER
Energy            AS REAL
Angle             AS REAL
CosAngle          AS REAL
SpuAngCoeff       AS REAL
IndReacAngCoeff   AS REAL

UNIT
SingleCalc  AS HfO2_Cl2

ASK
Energy "Energy?"  ;

SET
Angle       := 0.0                          ;
CosAngle    := cos(Angle*3.1415926/180)  ;

SpuAngCoeff     := -81.7*CosAngle^5 + 224.03*CosAngle^4 - 208.19*CosAngle^3 +
67.59*CosAngle^2 - 0.711*CosAngle - 0.0242 ;

IndReacAngCoeff := exp((CosAngle - 1)*2.4) ;

WITHIN SingleCalc DO

# Incoming Flux Condition
N2I          := 50 ;
G_Cl_Frac    := 1  ;
G_Cl_i       := 0.42  ;
G_Cl2_i      := 0.53  ;
G_Ar_i       := 0.05  ;

# Sticking coefficient of neutral species
S_Cl_on_Hf   := 0.04  ;
S_Cl_on_O  := 0.6  ;

# Sticking coefficient of ions, set to unity without surface charging.
S_Cl_i       := 1     ;
S_Cl2_i      := 1  ;
f_thre_fac   := IF (Energy>15) THEN 1 ELSE 0 END ;



# Sputtering yield coefficients
Y_Hf_by_Cl_i  := IF (0.153*(SQRT(Energy) - 3.772)>0) THEN 0.153*(SQRT(Energy)
- 3.772)*SpuAngCoeff ELSE 0.0 END ;
```

```
Y_Cl_by_Cl_i  := IF (0.045*(SQRT(Energy) - 5.112)>0) THEN 0.045*(SQRT(Energy)
- 5.112)*SpuAngCoeff ELSE 0.0 END ;
Y_O_by_Cl_i   := IF (0.015*(SQRT(Energy) - 6.408)>0) THEN 0.015*(SQRT(Energy)
- 6.408)*SpuAngCoeff ELSE 0.0 END ;
Y_Hf_by_Cl2_i := IF (0.206*(SQRT(Energy) - 4.102)>0) THEN 0.206*(SQRT(Energy)
- 4.102)*SpuAngCoeff ELSE 0.0 END ;
Y_Cl_by_Cl2_i := IF (0.055*(SQRT(Energy) - 6.218)>0) THEN 0.055*(SQRT(Energy)
- 6.218)*SpuAngCoeff ELSE 0.0 END ;
Y_O_by_Cl2_i  := IF (0.018*(SQRT(Energy) - 7.863)>0) THEN 0.018*(SQRT(Energy)
- 7.863)*SpuAngCoeff ELSE 0.0 END ;
Y_Hf_by_Ar_i := IF (0.156*(SQRT(Energy) - 3.796)>0) THEN 0.156*(SQRT(Energy)
- 3.796)*SpuAngCoeff ELSE 0.0 END ;
Y_Cl_by_Ar_i := IF (0.045*(SQRT(Energy) - 5.280)>0) THEN 0.045*(SQRT(Energy)
- 5.280)*SpuAngCoeff ELSE 0.0 END ;
Y_O_by_Ar_i  := IF (0.015*(SQRT(Energy) - 6.634)>0) THEN 0.015*(SQRT(Energy)
- 6.634)*SpuAngCoeff ELSE 0.0 END ;

# Vacancy creation due to ion bombardment
 B_V_Cl_i   := IF (Energy>10.0) THEN 2.25*(SQRT(Energy)-
SQRT(10.0))*SpuAngCoeff ELSE 0.0 END ;
 B_V_Cl2_i   := IF (Energy>19.0) THEN 2.12*(SQRT(Energy)-
SQRT(19.0))*SpuAngCoeff ELSE 0.0 END ;
 B_V_Ar_i      := IF (Energy>39.0) THEN 1.7*(SQRT(Energy)-
SQRT(39.0))*SpuAngCoeff ELSE 0.0 END ;

# Densification Reaction Coefficients
B_d_V_by_Cl  := IF (Energy>20) THEN 2.17*(SQRT(Energy)-SQRT(20))*SpuAngCoeff
ELSE 0.0 END ;
B_d_V_by_Cl2 := IF (Energy>19) THEN 2.06*(SQRT(Energy)-SQRT(19))*SpuAngCoeff
ELSE 0.0 END     ;
B_d_V_by_Ar  := IF (Energy>31) THEN 1.6*(SQRT(Energy)-SQRT(31))*SpuAngCoeff
ELSE 0.0 END     ;

# Annihilation Reaction Coefficients
B_Hf_V        := 0 ;
B_Cl_V        := 550 ;
B_O_V         := 0 ;


# Recombination Coefficients
A_Cl_Cl_i    := 0 ;
A_Cl_Cl      := 0.020 ;
A_O_Cl       := 0.013 ;
A_O_Cl_i     := 0 ;


# Ion enhanced reaction coefficient
B_HfCl2 := IF (Energy>67) THEN 0.4*(SQRT(Energy)-SQRT(67))*IndReacAngCoeff
ELSE 0.0 END ;
B_HfCl3 := IF (Energy>71) THEN 13.7*(SQRT(Energy)-SQRT(71))*IndReacAngCoeff
ELSE 0.0 END ;
B_HfCl4 := IF (Energy>75) THEN 22.8*(SQRT(Energy)-SQRT(75))*IndReacAngCoeff
ELSE 0.0 END ;
B_Cl2   := IF (Energy>0) THEN 6.2*(SQRT(Energy)-SQRT(0))*IndReacAngCoeff ELSE
0.0 END         ;
B_OCl   := IF (Energy>62)THEN 1.32*(SQRT(Energy)-SQRT(62))*IndReacAngCoeff
ELSE 0.0 END        ;
```

```
# Thermal reaction coeffienct
    m_Cl    := 0.00000 ;

    END


    PRESET
       WITHIN SingleCalc DO
       # identifier   default   lower  upper
    X_Hf :=     0.33    :0.00 :1.00  ;
    X_O  :=     0.67  :   0.00    :   1.00    ;
    X_Cl :=      0.00  :0.00    :   1.00    ;
    X_V  :=    0.00  :   0.00    :   1.00;
   END

 INITIAL
  WITHIN SingleCalc DO
  X_Hf = 0.33 ;
  X_O  = 0.67 ;
  X_Cl = 0.00 ;
  X_V  = 0.00 ;
 END

 SCHEDULE
  SEQUENCE
   CONTINUE FOR 300.0

 END
```

APPENDIX C: MC Feature Profile Simulation Code

1. Selections from File.cpp code

```
/*************************************************************************/
// In this function the initial particle choice is made depending on the
randomly generated number compared // to the gas fraction as indicated in the
input file. Changes were made to include gas phase species that
// were introduced due to the HfLaO film composition and potential etch
species
void Particle::initialize(int part_type,double enrgy)
{
 int j;
 type = part_type;
 energy = enrgy;
 //cout<<"in file: part type  "<<part_type<<endl;
 for(j=0;j<NO_ELEMENTS;j++) comp[j] = 0;
 switch(part_type)
 {

 //Ion species
 case 0: //Ar+
  comp[ION] = 1.0;
  no_atom = 0.0;
  break;

 case 1: // Cl+
  comp[ION] = 1.0;
  comp[CHLORINE] = 1.0;
  comp[VACANCY] = -1.0;
  no_atom = 0.0;
  break;

 case 2: // Cl2+
  comp[ION] = 1.0;
  comp[CHLORINE] = 2.0;
  comp[VACANCY] = -1.0;
  no_atom = 1.0;
  break;

 case 3: // O+
  comp[ION] = 1.0;
  comp[OXYGEN] = 1.0;
  comp[VACANCY]=-1.0;
  no_atom = 0.0;
  break;

 // Neutral Species
 case 4: // Cl
  comp[ION] = 0.0;
  comp[CHLORINE] = 1.0;
  comp[VACANCY] = -1.0;
  no_atom = 0.0;
  break;
```

```
case 5: // Cl2
 comp[ION] = 0.0;
 comp[CHLORINE] = 2.0;
 comp[VACANCY] = -1.0;
 no_atom = 1.0;
 break;

case 6: // O2
 comp[ION] = 0.0;
 comp[OXYGEN] = 2.0;
 comp[VACANCY] = -1.0;
 no_atom = 1.0;
 break;

case 7: // HfCl
 comp[ION] = 0.0;
 comp[HAFNIUM] = 1.0;
 comp[CHLORINE] = 1.0;
 comp[VACANCY] = -1.0;
 no_atom = 1.0;
 break;

case 8: // HfCl2
 comp[ION] = 0.0;
 comp[HAFNIUM] = 1.0;
 comp[CHLORINE] = 2.0;
 comp[VACANCY] = -1.0;
 no_atom = 2.0;
 break;

case 9: // HfCl3
 comp[ION] = 0.0;
 comp[HAFNIUM] = 1.0;
 comp[CHLORINE] = 3.0;
 comp[VACANCY] = -1.0;
 no_atom = 3.0;
 break;

case 10: // HfCl4
 comp[ION] = 0.0;
 comp[HAFNIUM] = 1.0;
 comp[CHLORINE] = 4.0;
 comp[VACANCY] = -1.0;
 no_atom = 4.0;
 break;

case 11: // OCl
 comp[ION] = 0.0;
 comp[OXYGEN] = 1.0;
 comp[CHLORINE] = 1.0;
 comp[VACANCY] = -1.0;
 no_atom = 1.0;
 break;

case 12: // Hf2OCl5
 comp[ION] = 0.0;
 comp[HAFNIUM] = 2.0;
```

```
   comp[OXYGEN] = 1.0;
   comp[CHLORINE] = 5.0;
   comp[VACANCY] = -8.0;
   no_atom = 7.0;
   break;

  case 13: // LaCl
   comp[ION] = 0.0;
   comp[LANTHANUM] = 1.0;
   comp[CHLORINE] = 1.0;
   comp[VACANCY] = -1.0;
   no_atom = 1.0;
   break;

  case 14: // LaOCl
   comp[ION] = 0.0;
   comp[LANTHANUM] = 1.0;
   comp[OXYGEN] = 1.0;
   comp[CHLORINE] = 1.0;
   comp[VACANCY] = -1.0;
   no_atom = 2.0;
   break;



  }
}


/*****************************************************************/
// Routine to define the feature.
// The initial feature is defined, based on the feature_option in the input
file
// Changes were made to include film compositions that were a mix of Hafnium
and Lanthanum and also
// different photoresist aspect ratios and oxide film thicknesses
void define_feature(Cell *lattice, Cell_large *lattice_large)
{
 int i, j, k;
 int flag_1;
 int feature_option = feature.init_feat;
 int count = 0;
 int count2 = 0;

 int mask_thickness, mask_width, half_mask_width, radius, oxide_thickness;
 //int half_domain = (int)((feature.max_x+1)/2);
 int half_domain = (int)(((double)(feature.max_x)+1.0)/2.0);//safer?
 double N;
 double Hf_La; // Hafnium fraction = Hf/(Hf+La)

 int top_of_feature;



 int ii;
 int step;
```

```
 double amp, freq;
 int nj, nk;
 int div;

 int center_y, center_z, wall_x;
 double zp, zn, xp, xn;
 double sqrt_num_z, sqrt_num_x;
 int num_bumps;
 double center2_y, center2_z;
 long seed_num;

 int top_surf_min_x, top_surf_max_x;
 int center_x;
 double yp, yn;
 double sqrt_num_y;
 double center2_x;

 int ni, step1, step2;

 int zero_of_wave;

 //for feature_option 17, 18, 19
 //int quarter_domain = (int)((feature.max_x+1)/4 );
 int quarter_domain = (int)(((double)(feature.max_x)+1.0)/4.0);//safer?
 int step_height, step_width, half_step_width;

 //for feature_option 20
 int order;
 double temp_xd, temp_yd, temp_zd;
 int temp_xi, temp_yi, temp_zi;


 //initial features:
 //  1) Flat surface
 cout<<"feature.max_x, y, z:     "<<feature.max_x<<" "<<feature.max_y<<"
"<<feature.max_z<<endl;
 cout<<"feature_option = "<<feature_option<<endl;

 if (menu.etch_or_dep==DEP)
 {

  //top_of_feature = 20;

  top_of_feature = 60;
 }
 else
 {
  top_of_feature = feature.max_z - 30;
 }



 if (feature_option == 1) //flat surface
 {
  for(i=0;i<=feature.max_x;i++)
  {
```

```
   for(j=0;j<=feature.max_y;j++)
   {
    for (k=0;k<=(top_of_feature);k++)
    {
     lattice[dim(i,j,k)].cell_type = RESIST;
     lattice[dim(i,j,k)].total_part =PACKET;
     lattice[dim(i,j,k)].part_in_cell[CARBON] =  PACKET;
    }
   }
  }
}
if (feature_option == 2) //flat Si surface
{
 for(i=0;i<=feature.max_x;i++)
 {
  for(j=0;j<=feature.max_y;j++)
  {
   for (k=0;k<=(top_of_feature);k++)
   {
    lattice[dim(i,j,k)].cell_type = POLY;
    lattice[dim(i,j,k)].total_part =PACKET;
    lattice[dim(i,j,k)].part_in_cell[HAFNIUM] = PACKET*0.90;
    lattice[dim(i,j,k)].part_in_cell[VACANCY] =  PACKET*0.10;
   }
  }
 }
}

if (feature_option == 3)
{

 mask_thickness = 40;
 mask_width = 40;
 half_mask_width = (int)(mask_width/2);

 // Initialize SiO2
 for (i=0;i<=feature.max_x;i++)
 {
  for (j=0;j<=feature.max_y;j++)
  {
   for (k=0;k<=top_of_feature-mask_thickness; k++)
   {
    lattice[dim(i,j,k)].cell_type = OXIDE;
    lattice[dim(i,j,k)].total_part = PACKET;
    lattice[dim(i,j,k)].part_in_cell[HAFNIUM] = PKT1_3;
    lattice[dim(i,j,k)].part_in_cell[OXYGEN] =  PKT2_3;
   }
  }
 }

 //initialize PR Mask
 for (k=(top_of_feature-mask_thickness+1);k<=top_of_feature;k++)
 {
  for (j=0;j<=feature.max_y;j++)
  {
   for (i=0;i<=feature.max_x;i++)
   {
```

```
      if ((i>=(half_domain-
half_mask_width))&&(i<(half_domain+half_mask_width)))
      {
       // Resist mask
       lattice[dim(i,j,k)].cell_type = RESIST;
       lattice[dim(i,j,k)].total_part = PACKET;
       lattice[dim(i,j,k)].part_in_cell[CARBON] =  PACKET;

      }
     }
    }
   }
  }
  if (feature_option == 4)
  {

   mask_thickness = 40;
   mask_width = 40;
   half_mask_width = (int)(mask_width/2);

   for (k=0;k<=(top_of_feature-mask_thickness);k++)
   {
    for(j=0;j<=feature.max_y;j++)
    {
     for(i=0;i<=feature.max_x;i++)
     {
      lattice[dim(i,j,k)].cell_type = POLY;
      lattice[dim(i,j,k)].total_part =PACKET;
      lattice[dim(i,j,k)].part_in_cell[HAFNIUM] = PACKET*0.90;
      lattice[dim(i,j,k)].part_in_cell[VACANCY] =  PACKET*0.10;
     }
    }
   }

   for (k=top_of_feature-mask_thickness+1;k<=(top_of_feature);k++)
   {
    for(j=0;j<=feature.max_y;j++)
    {
     for(i=0;i<=feature.max_x;i++)
     {
      if((i>=(half_domain-
half_mask_width))&&(i<(half_domain+half_mask_width)))
      {

      lattice[dim(i,j,k)].cell_type = RESIST;
      lattice[dim(i,j,k)].total_part =PACKET;
      lattice[dim(i,j,k)].part_in_cell[CARBON] =  PACKET*0.9;
      lattice[dim(i,j,k)].part_in_cell[VACANCY] =  PACKET*0.10;
      }
     }
    }

   }
  }
  if (feature_option == 5)
  {
```

```
  mask_thickness = 42;
  mask_width = 38;
  oxide_thickness= 6;
  half_mask_width = (int)(mask_width/2);

  for (k=0;k<=(top_of_feature-mask_thickness-oxide_thickness);k++)
  {
   for(j=0;j<=feature.max_y;j++)
   {
    for(i=0;i<=feature.max_x;i++)
    {
     lattice[dim(i,j,k)].cell_type = RESIST;

     lattice[dim(i,j,k)].total_part =PACKET;
     lattice[dim(i,j,k)].part_in_cell[CARBON] =  PACKET*0.99;
     lattice[dim(i,j,k)].part_in_cell[VACANCY] =  PACKET*0.01;
    }
   }
  }
  for (k=oxide_thickness+1;k<=(top_of_feature-mask_thickness);k++)
  {
   for(j=0;j<=feature.max_y;j++)
   {
    for(i=0;i<=feature.max_x;i++)
    {
     lattice[dim(i,j,k)].cell_type = OXIDE;
     lattice[dim(i,j,k)].total_part =PACKET;
     lattice[dim(i,j,k)].part_in_cell[HAFNIUM] = PKT1_3*0.90;
     lattice[dim(i,j,k)].part_in_cell[OXYGEN] =  PKT2_3*0.90;
     lattice[dim(i,j,k)].part_in_cell[VACANCY] =  PACKET*0.10;
    }
   }
  }

  for (k=top_of_feature-mask_thickness+1;k<=(top_of_feature);k++)
  {
   for(j=0;j<=feature.max_y;j++)
   {
    for(i=0;i<=feature.max_x;i++)
    {
     if((i>=(half_domain-
half_mask_width))&&(i<(half_domain+half_mask_width)))
      {

      lattice[dim(i,j,k)].cell_type = RESIST;
      lattice[dim(i,j,k)].total_part =PACKET;
      lattice[dim(i,j,k)].part_in_cell[CARBON] =  PACKET*0.9;
      lattice[dim(i,j,k)].part_in_cell[VACANCY] =  PACKET*0.10;
      }
    }
   }

  }

 }
 if (feature_option == 6) // Nathan's HfO2_Cl2 pattern dimensions
 {
```

```
   mask_thickness = 120; // mask FILM thickness
   mask_width = 20; // half on one side, half on the other side
   oxide_thickness= 40;
   half_mask_width = (int)(mask_width/2);

   for (k=0;k<=(top_of_feature-mask_thickness-oxide_thickness);k++)
//top_of_feature = 169 usually, this part defines the "substrate" that is
non-reactive (i.e. "resist")
   {
    for(j=0;j<=feature.max_y;j++)
    {
     for(i=0;i<=feature.max_x;i++)
     {
      lattice[dim(i,j,k)].cell_type = RESIST;
      lattice[dim(i,j,k)].total_part =PACKET;
      lattice[dim(i,j,k)].part_in_cell[CARBON] =  PACKET*0.99;
      lattice[dim(i,j,k)].part_in_cell[VACANCY] =  PACKET*0.01;
     }
    }
   }
   for (k=(top_of_feature-mask_thickness-
oxide_thickness+1);k<=(top_of_feature-mask_thickness);k++)  // this part
defines the HfO2 film
   {
    for(j=0;j<=feature.max_y;j++)
    {
     for(i=0;i<=feature.max_x;i++)
     {
      lattice[dim(i,j,k)].cell_type = OXIDE;
      lattice[dim(i,j,k)].total_part =PACKET;
      lattice[dim(i,j,k)].part_in_cell[HAFNIUM] = PKT1_3*1.0;
      lattice[dim(i,j,k)].part_in_cell[OXYGEN] =  PKT2_3*1.0;
     }
    }
   }

   for (k=top_of_feature-mask_thickness+1;k<=(top_of_feature);k++)
   {
    for(j=0;j<=feature.max_y;j++)
    {
     for(i=0;i<=feature.max_x;i++)
     {
      if(i<=half_mask_width ||i>=(feature.max_x-half_mask_width))
      {
      lattice[dim(i,j,k)].cell_type = RESIST;
      lattice[dim(i,j,k)].total_part =PACKET;
      lattice[dim(i,j,k)].part_in_cell[CARBON] =  PACKET*0.9;
      lattice[dim(i,j,k)].part_in_cell[VACANCY] =  PACKET*0.10;
      }
     }
    }

   }

  }
  if (feature_option == 7) // Hafnium Lanthanate
```

```
 {

   mask_thickness = 120;
   mask_width = 20;
   oxide_thickness= 40;
   Hf_La = 0.7142857; // Hafnium fraction = Hf/(Hf+La) for
Hf(0.25)La(0.10)O(0.65)
   half_mask_width = (int)(mask_width/2);

   for (k=0;k<=(top_of_feature-mask_thickness-oxide_thickness);k++)
//top_of_feature = 169 usually, this part defines the "substrate" that is
non-reactive (i.e. "resist")
   {
    for(j=0;j<=feature.max_y;j++)
    {
     for(i=0;i<=feature.max_x;i++)
     {
      lattice[dim(i,j,k)].cell_type = RESIST;
      lattice[dim(i,j,k)].total_part =PACKET;
      lattice[dim(i,j,k)].part_in_cell[CARBON] =  PACKET*0.99;
      lattice[dim(i,j,k)].part_in_cell[VACANCY] =  PACKET*0.01;
     }
    }
   }
   for (k=(top_of_feature-mask_thickness-
oxide_thickness+1);k<=(top_of_feature-mask_thickness);k++)  // this part
defines the HfO2 film
   {
    for(j=0;j<=feature.max_y;j++)
    {
     for(i=0;i<=feature.max_x;i++)
     {
      lattice[dim(i,j,k)].cell_type = OXIDE;
      lattice[dim(i,j,k)].total_part =PACKET;
      lattice[dim(i,j,k)].part_in_cell[HAFNIUM] = Hf_La*PKT1_3;
      lattice[dim(i,j,k)].part_in_cell[LANTHANUM] = (1-Hf_La)*PKT2_5*1.0;
      lattice[dim(i,j,k)].part_in_cell[OXYGEN] =  Hf_La*PKT2_3+(1-
Hf_La)*PKT3_5;
     }
    }
   }

   for (k=top_of_feature-mask_thickness+1;k<=(top_of_feature);k++)
   {
    for(j=0;j<=feature.max_y;j++)
    {
     for(i=0;i<=feature.max_x;i++)
     {
      if(i<=half_mask_width ||i>=(feature.max_x-half_mask_width))
      {
      lattice[dim(i,j,k)].cell_type = RESIST;
      lattice[dim(i,j,k)].total_part =PACKET;
      lattice[dim(i,j,k)].part_in_cell[CARBON] =  PACKET*0.9;
      lattice[dim(i,j,k)].part_in_cell[VACANCY] =  PACKET*0.10;
      }
     }
    }
```

```
   }

  }
  // Check all cells and determine if they are interface (surface) cells or
not
  // - set lattice[].if_intfc to TRUE/FALSE
  // - if it is an interface cell, call fit_surface() function to compute the
normal associated with this cell

  for(i=0; i<=feature.max_x; i++)
  {
   for(j=0; j<=feature.max_y; j++)
   {
    for(k=4; k<=feature.max_z-3; k++)
    {
     check_intfc(lattice, i, j, k);
     if (lattice[dim(i,j,k)].if_intfc==TRUE)
     {
      flag_1 = FALSE;
      fit_surface(i, j, k, lattice, flag_1);

      if (etch_info.end_flag==TRUE)
      {
       return;
      }

      if (flag_1 == TRUE)
      {
       fprintf(error_msg, "\ndefine_feature(): not enough neighboring cells
to fit the surface\n");
       cout<<"define_feature(): not enough neighboring cells to fit the
surface"<<endl; //this shouldn't happen
       fclose(error_msg);
      }
     }//close if (if_intfc==TRUE)
    }
   }
  }



  comp_set();




}

// In this function, the reaction set stoichiometry is set which has been
modified to include the new reactions from the TML code
void comp_set(void)
{
  int i, j;
```

```
for (j=0;j<NO_ELEMENTS;j++)
{
 for (i=0;i<NO_ION_REACTIONS;i++)
 {
  Ion_Rxn_Comp[i][j]=0;
 }
}

//Sputtering

//Hf by Ar+
Ion_Rxn_Comp[0][HAFNIUM]=1;
Ion_no_atom[0]=1;

//Hf by Cl+
Ion_Rxn_Comp[1][HAFNIUM]=1;
Ion_no_atom[1]=1;

//Hf by Cl2+
Ion_Rxn_Comp[2][HAFNIUM]=1;
Ion_no_atom[2]=1;

//Hf by O+
Ion_Rxn_Comp[3][HAFNIUM]=1;
Ion_no_atom[3]=1;

//La by Ar+
Ion_Rxn_Comp[4][LANTHANUM]=1;
Ion_no_atom[4]=1;

//La by Cl+
Ion_Rxn_Comp[5][LANTHANUM]=1;
Ion_no_atom[5]=1;

//La by Cl2+
Ion_Rxn_Comp[6][LANTHANUM]=1;
Ion_no_atom[6]=1;

//La by O+
Ion_Rxn_Comp[7][LANTHANUM]=1;
Ion_no_atom[7]=1;

//Cl by Ar+
Ion_Rxn_Comp[8][CHLORINE]=1;
Ion_no_atom[8]=1;

//Cl by Cl+
Ion_Rxn_Comp[9][CHLORINE]=1;
Ion_no_atom[9]=1;

//Cl by Cl2+
Ion_Rxn_Comp[10][CHLORINE]=1;
Ion_no_atom[10]=1;

//Cl by O+
Ion_Rxn_Comp[11][CHLORINE]=1;
Ion_no_atom[11]=1;
```

```
//O by Ar+
Ion_Rxn_Comp[12][OXYGEN]=1;
Ion_no_atom[12]=1;

//O by Cl+
Ion_Rxn_Comp[13][OXYGEN]=1;
Ion_no_atom[13]=1;

//O by Cl2+
Ion_Rxn_Comp[14][OXYGEN]=1;
Ion_no_atom[14]=1;

//O by O+
Ion_Rxn_Comp[15][OXYGEN]=1;
Ion_no_atom[15]=1;

//Ion Enhanced Etching

//HfCl
Ion_Rxn_Comp[16][HAFNIUM]=1;
Ion_Rxn_Comp[16][CHLORINE]=1;
Ion_no_atom[16]=2;

//HfCl2
Ion_Rxn_Comp[17][HAFNIUM]=1;
Ion_Rxn_Comp[17][CHLORINE]=2;
Ion_no_atom[17]=3;

//HfCl3
Ion_Rxn_Comp[18][HAFNIUM]=1;
Ion_Rxn_Comp[18][CHLORINE]=3;
Ion_no_atom[18]=4;

//HfCl4
Ion_Rxn_Comp[19][HAFNIUM]=1;
Ion_Rxn_Comp[19][CHLORINE]=4;
Ion_no_atom[19]=5;

//LaCl
Ion_Rxn_Comp[20][LANTHANUM]=1;
Ion_Rxn_Comp[20][CHLORINE]=1;
Ion_no_atom[20]=2;

//LaOCl
Ion_Rxn_Comp[21][LANTHANUM]=1;
Ion_Rxn_Comp[21][OXYGEN]=1;
Ion_Rxn_Comp[21][CHLORINE]=1;
Ion_no_atom[21]=3;

//O2
Ion_Rxn_Comp[22][OXYGEN]=2;
Ion_Rxn_Comp[22][CHLORINE]=0;
Ion_no_atom[22]=2;

//OCl
Ion_Rxn_Comp[23][OXYGEN]=1;
```

```
Ion_Rxn_Comp[23][CHLORINE]=1;
Ion_no_atom[23]=2;

//Cl2
Ion_Rxn_Comp[24][CHLORINE]=2;
Ion_no_atom[24]=2;

//Vacancy Creation

//V by Ar+
Ion_Rxn_Comp[25][VACANCY]=-1;
Ion_no_atom[25]=-1;

//V by Cl+
Ion_Rxn_Comp[26][VACANCY]=-1;
Ion_no_atom[26]=-1;
//V by Cl2+
Ion_Rxn_Comp[27][VACANCY]=-1;
Ion_no_atom[27]=-1;
//V by O+
Ion_Rxn_Comp[28][VACANCY]=-1;
Ion_no_atom[28]=-1;

//Densification

//d_V by Ar+
Ion_Rxn_Comp[29][VACANCY]=1;
Ion_no_atom[29]=1;

//d_V by Cl+
Ion_Rxn_Comp[30][VACANCY]=1;
Ion_no_atom[30]=1;

//d_V by Cl2+
Ion_Rxn_Comp[31][VACANCY]=1;
Ion_no_atom[31]=1;

//d_V by O+
Ion_Rxn_Comp[32][VACANCY]=1;
Ion_no_atom[32]=1;

//Annihilation
//Hf_V
Ion_Rxn_Comp[33][VACANCY]=2;
Ion_no_atom[33]=2;

//Cl_V
Ion_Rxn_Comp[34][VACANCY]=2;
Ion_no_atom[34]=2;

//O_V
Ion_Rxn_Comp[35][VACANCY]=2;
Ion_no_atom[35]=2;

// **Neutral Reaction Comp is pretty much not used ** //
for (j=0;j<NO_ELEMENTS;j++)
{
```

```
   for (i=0;i<NO_NEU_REACTIONS;i++)
   {
    Neu_Rxn_Comp[i][j]=0;
   }
  }

 Neu_Rxn_Comp[0][CARBON]=-1; // neutral adsorption
 Neu_Rxn_Comp[0][VACANCY]=+1;
 Neu_no_atom[0]=0;



}
```

2. Chemistry.cpp

```
/*************************************************************************/
// Calculates the consumption probability of the neutral species.
// For now, this is only used in the simple test for deposition of Si.
// The sticking probability is indicated in the input file.
// Changes were made to account for recombination processes and redeposition
of etch species
void find_consume_prob(int & consumed, Particle & species, Traj & traj,
Feature & feature, Cell *lattice, int & product, Cell_large *lattice_large)
{
 double x_Hf,x_La, x_O, x_Cl, x_C, x_V, tot_par;
 double J_Hf_Hf, J_Hf_Cl, J_Hf_O, J_Hf_V, J_La_La, J_La_O, J_La_Cl, J_La_V,
J_Cl_Cl, J_Cl_O, J_Cl_V, J_O_V, J_O_O, J_O_Cl, sum_J_top, sum_J_bottom,
J_V_frac;
 double A_recom_Cl_Cl; //recombination constant for Cl_Cl
 double A_recom_O_Cl; //recombination constant for O_Cl
 double factor;
 double sum_SiO2 = 0.0; // ratio of Si to O
 int order;
 int j;

 int stop;
 double Neu_yield[NO_NEU_REACTIONS];



 if (menu.if_chem==FALSE)
 {
  if (menu.etch_or_dep==DEP)//for deposition of Si particle
  {
   //Si consumed x% of the time
   factor = menu.stick_prob;
   if (ran2(&idum) < factor)
   {
    consumed = TRUE;
    consume_particle(species, traj, feature, lattice, product,
lattice_large,1.0);
    if (etch_info.end_flag==TRUE)
    {
     return;
    }
```

```
    }
    else
    {
     consumed = FALSE;
    }
   }
   else//ETCH
   {
    if (species.comp[ION]==0.0)//this is the only exception for now
(redeposition)
    {
     //same as above
     //Si consumed x% of the time - for now, just keep it 100%
     factor = menu.stick_prob;
     if (ran2(&idum) < factor)
     {
      consumed = TRUE;
      //do not consume when checking flux
      consume_particle(species, traj, feature, lattice, product,
lattice_large,1.0);
      if (etch_info.end_flag==TRUE)
      {
       return;
      }
     }
     else
     {
      consumed = FALSE;
     }
    }
    else
    {
     nrerror("species.comp[ION] cannot be > 0 in find_consume_prob()");
    }
   }
  }
  else //with chemistry
  {
   //nrerror("this option is not valid for now");
   etch_info.num_neu += 1;


   order = dim(traj.x_lat, traj.y_lat, traj.z_lat);
   Neu_rxn_yield_fn(lattice[order].total_part, lattice[order].part_in_cell,
species.comp, Neu_yield);

   find_lattice_type(order, lattice);
   check_intfc(lattice, traj.x_lat, traj.y_lat, traj.z_lat);

   tot_par =
(double)(lattice[order].part_in_cell[HAFNIUM]+lattice[order].part_in_cell[LAN
THANUM]+lattice[order].part_in_cell[OXYGEN] +
lattice[order].part_in_cell[CARBON] +
lattice[order].part_in_cell[CHLORINE]+lattice[order].part_in_cell[VACANCY]);
   x_Hf = (double)(lattice[order].part_in_cell[HAFNIUM])/tot_par;
   x_La = (double)(lattice[order].part_in_cell[LANTHANUM])/tot_par;
   x_O = (double)(lattice[order].part_in_cell[OXYGEN])/tot_par;
```

```
   x_C = (double)(lattice[order].part_in_cell[CARBON])/tot_par;
   x_Cl = (double)(lattice[order].part_in_cell[CHLORINE])/tot_par;
   x_V = (double)(lattice[order].part_in_cell[VACANCY])/tot_par;

   J_Hf_Hf = (4*x_Hf*4*x_Hf)/(2*(4*x_Hf+2*x_O+3*x_La+x_Cl+x_V));
   J_Hf_O  = (4*x_Hf*2*x_O)/(4*x_Hf+2*x_O+3*x_La+x_Cl+x_V);
   J_Hf_Cl = (4*x_Hf*1*x_Cl)/(4*x_Hf+2*x_O+3*x_La+x_Cl+x_V);
   J_Hf_V  = (4*x_Hf*1*x_V)/(4*x_Hf+2*x_O+3*x_La+x_Cl+x_V);
   J_La_La = (3*x_La*3*x_La)/(2*(4*x_Hf+2*x_O+3*x_La+x_Cl+x_V));
   J_La_O  = (3*x_La*2*x_O)/(4*x_Hf+2*x_O+3*x_La+x_Cl+x_V);
   J_La_Cl = (3*x_La*1*x_Cl)/(4*x_Hf+2*x_O+3*x_La+x_Cl+x_V);
   J_La_V  = (3*x_La*1*x_V)/(4*x_Hf+2*x_O+3*x_La+x_Cl+x_V);
   J_Cl_Cl = (1*x_Cl*1*x_Cl)/(2*(4*x_Hf+2*x_O+3*x_La+x_Cl+x_V));
   J_Cl_V  = (1*x_Cl*1*x_V)/(4*x_Hf+2*x_O+3*x_La+x_Cl+x_V);
   J_O_O   = (2*x_O*2*x_O)/(2*(4*x_Hf+2*x_O+3*x_La+x_Cl+x_V));
   J_O_V   = (2*x_O*1*x_V)/(4*x_Hf+2*x_O+3*x_La+x_Cl+x_V);
   J_O_Cl  = (2*x_O*1*x_Cl)/(4*x_Hf+2*x_O+3*x_La+x_Cl+x_V);
   J_Cl_O = J_O_Cl;

   //Recombination changed 8/14/2012
   if (species.comp[CHLORINE] > 0.0 && etch_info.etched_prod == 0)
   {

    A_recom_Cl_Cl = 0.004;
    A_recom_O_Cl = 0.002;

    lattice[order].part_in_cell[CHLORINE] -= A_recom_Cl_Cl*1.0*J_Cl_V;
    lattice[order].part_in_cell[VACANCY] -= A_recom_Cl_Cl*1.0*J_Cl_V;
    lattice[order].total_part -= A_recom_Cl_Cl*2.0*J_Cl_V;
    lattice[order].part_in_cell[OXYGEN] -= A_recom_O_Cl*1.0*J_O_V;
    lattice[order].part_in_cell[VACANCY] -= A_recom_O_Cl*1.0*J_Cl_V;
    lattice[order].total_part -= 2.0*J_O_V;
   }

   sum_J_top = J_Hf_V + J_Cl_V + J_O_V;
   sum_J_bottom = J_Hf_Hf + J_Hf_O + J_Hf_Cl + J_Hf_V + J_Cl_Cl + J_Cl_O +
J_Cl_V + J_O_V + J_O_O;
   J_V_frac = sum_J_top / sum_J_bottom;

   //Weighted sticking coefficient changed 8/14/2012!!!
   if ((lattice[order].part_in_cell[CARBON] > 20.0))
   {
    factor = 0.0;
   }
   else
if(lattice[order].part_in_cell[HAFNIUM]+lattice[order].part_in_cell[LANTHANUM
] > 0.0 )// If cell is not resist
   {
    if(species.type == 4) //Cl neutral
    {
     factor = 1.0; //changed 8/15/12
    }

    if(etch_info.etched_prod == 1)
    {
     factor = 1.0; // added by Calvin 10/11/12
    }
```

```
    else // any other species
    {
     factor = 0.0*x_Hf;
    }
   }
   else
   {
    factor = 0.0;
   }

   if (ran2(&idum) < factor)     //MODIFIED FROM THE CODE BELOW
   {
    if (total_ctr % 1000 == 0 && lattice[order].part_in_cell[CARBON] <= 1.0)
    {
    }
    consumed = TRUE;
    lattice[order].part_flux++;

//***************check the composition within the neutral
function*************************************


//*************************************************************************
*****************************
    consume_particle(species, traj, feature, lattice, product,
lattice_large,0.0);
   }
   else
   {
    consumed = FALSE;
   }



 }


}


/*********************************************************************/
// Called from "find_consume_prob()" and "find_ion_consume_prob()" if the
species is
//   consumed on the surface.
// Changes were made to account for recombination processes and redeposition
of etch species

void consume_particle(Particle & species, Traj & traj, Feature & feature,
Cell *lattice, int & product, Cell_large *lattice_large, double final_yield)
{
 int order;
 double Neu_yield[NO_NEU_REACTIONS];
 int whilecount=0;
 int neu_total_no_prod=0;
 int i,j;
 double recombine_f;
 double A_recom_Cl_Cl; //recombination constant for Cl_Cl
```

```
 double A_recom_O_Cl; //recombination constant for O_Cl
 double x_Hf, x_La, x_O, x_Cl, x_C, x_V, tot_par;
 double part[NO_ELEMENTS];
 double J_Hf_Hf, J_Hf_Cl, J_Hf_O, J_Hf_V, J_La_La, J_La_O, J_La_Cl, J_La_V,
J_Cl_Cl, J_Cl_O, J_Cl_V, J_O_V, J_O_O, J_O_Cl;



 order = dim(traj.x_lat, traj.y_lat, traj.z_lat);
 check_intfc(lattice,traj.x_lat,traj.y_lat,traj.z_lat);
 for (i = 0;i<NO_ELEMENTS;i++)
 {
  part[i] = lattice[order].part_in_cell[i];
 }

 tot_par =
(double)(lattice[order].part_in_cell[HAFNIUM]+lattice[order].part_in_cell[LAN
THANUM]+lattice[order].part_in_cell[OXYGEN] +
lattice[order].part_in_cell[CARBON] +
lattice[order].part_in_cell[CHLORINE]+lattice[order].part_in_cell[VACANCY]);
 x_Hf = (double)(lattice[order].part_in_cell[HAFNIUM])/tot_par;
 x_La = (double)(lattice[order].part_in_cell[LANTHANUM])/tot_par;
 x_O = (double)(lattice[order].part_in_cell[OXYGEN])/tot_par;
 x_C = (double)(lattice[order].part_in_cell[CARBON])/tot_par;
 x_Cl = (double)(lattice[order].part_in_cell[CHLORINE])/tot_par;
 x_V = (double)(lattice[order].part_in_cell[VACANCY])/tot_par;

 J_Hf_Hf = (4*x_Hf*4*x_Hf)/(2*(4*x_Hf+2*x_O+3*x_La+x_Cl+x_V));
 J_Hf_O  = (4*x_Hf*2*x_O)/(4*x_Hf+2*x_O+3*x_La+x_Cl+x_V);
 J_Hf_Cl = (4*x_Hf*1*x_Cl)/(4*x_Hf+2*x_O+3*x_La+x_Cl+x_V);
 J_Hf_V  = (4*x_Hf*1*x_V)/(4*x_Hf+2*x_O+3*x_La+x_Cl+x_V);
 J_La_La = (3*x_La*3*x_La)/(2*(4*x_Hf+2*x_O+3*x_La+x_Cl+x_V));
 J_La_O  = (3*x_La*2*x_O)/(4*x_Hf+2*x_O+3*x_La+x_Cl+x_V);
 J_La_Cl = (3*x_La*1*x_Cl)/(4*x_Hf+2*x_O+3*x_La+x_Cl+x_V);
 J_La_V  = (3*x_La*1*x_V)/(4*x_Hf+2*x_O+3*x_La+x_Cl+x_V);
 J_Cl_Cl = (1*x_Cl*1*x_Cl)/(2*(4*x_Hf+2*x_O+3*x_La+x_Cl+x_V));
 J_Cl_V  = (1*x_Cl*1*x_V)/(4*x_Hf+2*x_O+3*x_La+x_Cl+x_V);
 J_O_O   = (2*x_O*2*x_O)/(2*(4*x_Hf+2*x_O+3*x_La+x_Cl+x_V));
 J_O_V   = (2*x_O*1*x_V)/(4*x_Hf+2*x_O+3*x_La+x_Cl+x_V);
 J_O_Cl  = (2*x_O*1*x_Cl)/(4*x_Hf+2*x_O+3*x_La+x_Cl+x_V);
 J_Cl_O = J_O_Cl;




 //*********************************************************************
 double part_rem;
 part_rem=lattice[order].total_part;

 lattice[order].total_part =0.0;
          for (j=1;j<NO_ELEMENTS;j++)
   {
    if (lattice[order].part_in_cell[j] <=0.0)
    {
     lattice[order].part_in_cell[j] =0.1;
    }
```

```
     lattice[order].total_part +=lattice[order].part_in_cell[j];


    }


 if (menu.if_chem==TRUE)
 {
  //nrerror("this option is not valid for now");

  //neutral adsorption treated as a special
rxn************************************

  Neu_rxn_yield_fn(lattice[order].total_part, lattice[order].part_in_cell,
species.comp, Neu_yield);

  etch_info.neu_Cl_ads += convert(Neu_yield[0]);

  //update number of particles in a cell

 for (i=0;i<NO_NEU_REACTIONS;i++)
 {
  lattice[order].total_part += species.no_atom*Neu_yield[i];
  for (j=1;j<NO_ELEMENTS;j++)
  {
   lattice[order].part_in_cell[j] += species.comp[j]*Neu_yield[i];// Deposit
the species into the cell

  }
 }

          part_rem=lattice[order].total_part;
       lattice[order].total_part =0;
          for (j=1;j<NO_ELEMENTS;j++)
   {
    if (lattice[order].part_in_cell[VACANCY] <0)
    {
     lattice[order].part_in_cell[VACANCY] =0.1;
    }
    lattice[order].total_part +=lattice[order].part_in_cell[j];


   }
  if (lattice[order].total_part <= TRANSITION_ETCH)
  {
   etch_cell(traj, feature, lattice, lattice_large);
  }
  else if  (lattice[order].total_part >= PACKET+TRANSITION_DEP)
  {
   deposit_cell(traj, feature, lattice, lattice[order].total_part-PACKET,
lattice_large);
  }


 }
 else//no chemistry
 {
```

```
  //for Si deposition (+Si)
  if (menu.etch_or_dep==DEP)
  {
   if (species.comp[ION] == 0)
   {
    (lattice[order].total_part) += 1;

    (lattice[order].part_in_cell[HAFNIUM]) += 1;      // Deposit HAFNIUM to
the cell

    find_lattice_type(traj, lattice);          // Check the type of cell

    if (lattice[order].total_part >= PACKET+TRANSITION_DEP)
    {
     deposit_cell(traj, feature, lattice, lattice[order].total_part-PACKET,
lattice_large);
     if (etch_info.end_flag==TRUE)
     {
      return;
     }
    }
   }
   else
   {
    nrerror("species.comp[ION] cannot be >0 for deposition");
   }
  }//close if DEP

  //for Si etching (-Si)
  if (menu.etch_or_dep==ETCH)
  {
   if (species.comp[ION] > 0.0)
   {
    if ((feature.init_feat==1)||(feature.init_feat==2))
    {
     (lattice[order].total_part) -= final_yield;
     lattice[order].part_in_cell[HAFNIUM] -= final_yield; // Remove HAFNIUM
in the cell
     if (lattice[order].part_in_cell[HAFNIUM]  < 0.0)
     {
      cout<<"lattice[order].part_in_cell[HAFNIUM]  < 0 in
consume_particle()"<<endl;
      fprintf(error_msg, "\nlattice[order].part_in_cell[HAFNIUM]  < 0 in
consume_particle()");
      etch_info.end_flag = TRUE;
      return;
     }
    }
    else //with PR and/or ARC
    {
     if (menu.arc_h > 0)//with ARC layer
     {
      //for PR
      if (lattice[order].cell_type==RESIST)
      {
       //lower the selectivity factor once the Si etch starts
       if (save.counter >= menu.start_si_etch)
```

```
        {
         if (ran2(&idum) < menu.selectiv_2)
         {
          (lattice[order].total_part) -= final_yield;
          lattice[order].part_in_cell[CARBON] -= final_yield; // Remove
CARBON in the cell
          //RESIST should convert to POLY when only HAFNIUMs remain in the
cell
          if (lattice[order].part_in_cell[CARBON]  < 0.0)
          {
           cout<<"lattice[order].part_in_cell[CARBON]  < 0 in
consume_particle()"<<endl;
           fprintf(error_msg, "\nlattice[order].part_in_cell[CARBON]  < 0 in
consume_particle()");
           etch_info.end_flag = TRUE;
           return;
           //nrerror("lattice[order].part_in_cell[CARBON]  < 0 in
consume_particle()");
          }
         }
        }
        else//no selectivity factor before Si etch
        {
         //(lattice[order].total_part) -= 1.0;
         //lattice[order].part_in_cell[CARBON] -= 1.0; // Remove CARBON in
the cell
          (lattice[order].total_part) -= final_yield;
          lattice[order].part_in_cell[CARBON] -= final_yield; // Remove CARBON
in the cell
          //RESIST should convert to POLY when only HAFNIUMs remain in the
cell
          if (lattice[order].part_in_cell[CARBON]  < 0.0)
          {
           cout<<"lattice[order].part_in_cell[CARBON]  < 0 in
consume_particle()"<<endl;
           fprintf(error_msg, "\nlattice[order].part_in_cell[CARBON]  < 0 in
consume_particle()");
           etch_info.end_flag = TRUE;
           return;
           //nrerror("lattice[order].part_in_cell[CARBON]  < 0 in
consume_particle()");
          }
         }
        }

        //for POLY
        if (lattice[order].cell_type==POLY)
        {
         //this is called only when (save.counter >= menu.start_si_etch) (see
track_particle())

         //in POLY, only HAFNIUMs are in the cell (no mixture of HAFNIUM and
CARBON/OXYGEN)
         //(lattice[order].total_part) -= 1.0;
         //lattice[order].part_in_cell[HAFNIUM] -= 1.0; // Remove HAFNIUM in
the cell
         (lattice[order].total_part) -= final_yield;
```

```
         lattice[order].part_in_cell[HAFNIUM] -= final_yield; // Remove
HAFNIUM in the cell
         if (lattice[order].part_in_cell[HAFNIUM]  < 0.0)
         {
          cout<<"lattice[order].part_in_cell[HAFNIUM]  < 0 in
consume_particle()"<<endl;
          fprintf(error_msg, "\nlattice[order].part_in_cell[HAFNIUM]  < 0 in
consume_particle()");
          etch_info.end_flag = TRUE;
          return;
          //nrerror("lattice[order].part_in_cell[SIILICON]  < 0 in
consume_particle()");
         }
        }

        //for ARC
        if (lattice[order].cell_type==ARC)
        {
         //similarly, lower the selectivity once the Si etch starts
         if (save.counter >= menu.start_si_etch)
         {
          if (ran2(&idum) < menu.selectiv_2)//selectivity over POLY etch
          {

           if (ran2(&idum) < menu.selectiv)//selectivity over RESIST etch
           {
            //(lattice[order].total_part) -= 1.0;
            //lattice[order].part_in_cell[OXYGEN] -= 1.0; // Remove OXYGEN in
the cell
            (lattice[order].total_part) -= final_yield;
            lattice[order].part_in_cell[OXYGEN] -= final_yield; // Remove
OXYGEN in the cell

            //ARC should convert to POLY when only HAFNIUMs remain in the
cell
            if (lattice[order].part_in_cell[OXYGEN]  < 0.0)
            {
             cout<<"lattice[order].part_in_cell[OXYGEN]  < 0 in
consume_particle()"<<endl;
             fprintf(error_msg, "\nlattice[order].part_in_cell[OXYGEN]  < 0
in consume_particle()");
             etch_info.end_flag = TRUE;
             return;
             //nrerror("lattice[order].part_in_cell[OXYGEN]  < 0 in
consume_particle()");
            }
           }
          }
         }
         else
         {
          if (ran2(&idum) < menu.selectiv)//selectivity over RESIST etch
          {
           //(lattice[order].total_part) -= 1.0;
           //lattice[order].part_in_cell[OXYGEN] -= 1.0; // Remove OXYGEN in
the cell
           (lattice[order].total_part) -= final_yield;
```

```
           lattice[order].part_in_cell[OXYGEN] -= final_yield; // Remove
OXYGEN in the cell

           //ARC should convert to POLY when only HAFNIUMs remain in the cell
           if (lattice[order].part_in_cell[OXYGEN]  < 0.0)
           {
            cout<<"lattice[order].part_in_cell[OXYGEN]  < 0 in
consume_particle()"<<endl;
            fprintf(error_msg, "\nlattice[order].part_in_cell[OXYGEN]  < 0 in
consume_particle()");
            etch_info.end_flag = TRUE;
            return;
            //nrerror("lattice[order].part_in_cell[OXYGEN]  < 0 in
consume_particle()");
           }
          }
         }
        }

      }
      else//no ARC layer (selectivity of ARC over PR is not used anywhere)
      {
       //for PR
       if (lattice[order].cell_type==RESIST)
       {
        if (ran2(&idum) < menu.selectiv_2)
        {
         //(lattice[order].total_part) -= 1.0;
         //lattice[order].part_in_cell[CARBON] -= 1.0; // Remove CARBON in
the cell
          (lattice[order].total_part) -= final_yield;
          lattice[order].part_in_cell[CARBON] -= final_yield; // Remove CARBON
in the cell
          //RESIST should convert to POLY when only HAFNIUMs remain in the
cell
          if (lattice[order].part_in_cell[CARBON]  < 0.0)
          {
           cout<<"lattice[order].part_in_cell[CARBON]  < 0 in
consume_particle()"<<endl;
           fprintf(error_msg, "\nlattice[order].part_in_cell[CARBON]  < 0 in
consume_particle()");
           etch_info.end_flag = TRUE;
           return;
           //nrerror("lattice[order].part_in_cell[CARBON]  < 0 in
consume_particle()");
          }
         }
        }

       //for POLY
       if (lattice[order].cell_type==POLY)
       {
        (lattice[order].total_part) -= final_yield;
        lattice[order].part_in_cell[HAFNIUM] -= final_yield; // Remove
HAFNIUM in the cell
        if (lattice[order].part_in_cell[HAFNIUM]  < 0.0)
        {
```

```
          cout<<"lattice[order].part_in_cell[HAFNIUM]  < 0 in
consume_particle()"<<endl;
          fprintf(error_msg, "\nlattice[order].part_in_cell[HAFNIUM]  < 0 in
consume_particle()");
          etch_info.end_flag = TRUE;
          return;
          //nrerror("lattice[order].part_in_cell[SIILICON]  < 0 in
consume_particle()");
         }
        }

      }

     }//close if (menu.init_feat != 1 or 2)
     find_lattice_type(order,lattice);      //Check the type of cell
     check_intfc(lattice,traj.x_lat,traj.y_lat,traj.z_lat);

     if (lattice[order].total_part <= TRANSITION_ETCH)
     {
      etch_cell(traj, feature, lattice, lattice_large);
      if (etch_info.end_flag==TRUE)
      {
       return;
      }
     }
    }//close if (species.comp[ION] > 0)



   }//close if ETCH

 }//close if (menu.if_chem==FALSE)

}

/*****************************************************************/
// calculates the consumption probability of the ionic species based on
//   the angular dependent etching yield curve.
//Ion is consumed depending on the angular yield curve
//The amount removed from the cell is based on curvature dependence yield
curve
// Changes were made to account for recombination processes and redeposition
of etch species


void find_ion_consume_prob(int & consumed, Particle & species, Traj & traj,
Feature & feature, \
          Cell *lattice, double ion_angle, int & product, Cell_large
*lattice_large)
{

 double ang_dep_prob[NO_REACTIONS];
// double factor;
 int order;
 double remove_prob;
 double curv_dep_lim = menu.curv_dep;//new variable
```

```
 //more new variables
 double vec_b1, vec_b2, vec_b3;
 double tdx_new, tdy_new, tdz_new;
 double denom_1, beta_1;

 double final_yield;
 double temp_ang_dep_prob;

 if (menu.if_chem==TRUE)
 {
  //nrerror("this option is not valid for now");
  if ((ion_angle >= PI_2) || (lattice[dim(traj.x_lat, traj.y_lat,
traj.z_lat)].cell_type == RESIST))
  {
   consumed = FALSE;
  }
  else
  {
   consume_ion(consumed, species, traj, feature, lattice, ion_angle, product,
lattice_large);
  }

 }
 else//no chemistry
 {
  if ((ion_angle > PI_2)&&(menu.ang_dep_opt_Si!=0))
  {
   //consume every particle if there's no angular dependence (no scattering)
   consumed = FALSE;
  }
  else
  {
   //note: ang_dep_prob[0] = HAFNIUM etch
   //   ang_dep_prob[1] = PR etch
   //   and_dep_prob[2] = ARC etch
   ion_ang_dep(ion_angle, ang_dep_prob);

   order = dim(traj.x_lat, traj.y_lat, traj.z_lat);

   if (lattice[order].cell_type==POLY)
   {
    temp_ang_dep_prob = ang_dep_prob[0];
   }
   else
   {
    if (lattice[order].cell_type==RESIST)
    {
     temp_ang_dep_prob = ang_dep_prob[1];
    }
    else
    {
     if (lattice[order].cell_type==ARC)
     {
      temp_ang_dep_prob = ang_dep_prob[2];
     }
    }
   }
```

```
    if (ran2(&idum) < temp_ang_dep_prob)
    {
     consumed = TRUE;


     //curvature dependence-----------------------------------------------------
     //first, transform the trajectory using the coord matrix for this cell
     transformation(traj.dx, traj.dy, traj.dz, tdx_new, tdy_new, tdz_new, \
      lattice[order].coord);
     tdx_new = -tdx_new;
     tdy_new = -tdy_new;
     tdz_new = -tdz_new;
     vec_b1 = lattice[order].coeff_b[1];
     vec_b2 = lattice[order].coeff_b[2];
     vec_b3 = lattice[order].coeff_b[3];
     denom_1 = tdx_new*tdx_new + tdy_new*tdy_new;
     beta_1 = (vec_b1*tdx_new*tdx_new + vec_b2*tdy_new*tdy_new -
vec_b3*tdx_new*tdy_new)/denom_1;

     if (beta_1 > curv_dep_lim)
     {
      beta_1 = curv_dep_lim;
     }
     if (beta_1 < -curv_dep_lim)
     {
      beta_1 = -curv_dep_lim;
     }
     //remove_prob = (0.1+0.8*(ion_angle/PI))*(beta_1+0.5) + 0.1;

     if (beta_1 < 0.0)
     {
      remove_prob = menu.minslope*beta_1 + menu.intcpt;
     }
     else
     {
      remove_prob =  menu.intcpt +beta_1*
(menu.minslope+(2.0*ion_angle/PI)*(menu.maxslope-menu.minslope));

     }
     //------------------------------------------------------------------


     //yield depends on curvature
     final_yield = remove_prob;


     if (consumed==TRUE)
     {
      //do not consume when checking flux
      consume_particle(species, traj, feature, lattice, product,
lattice_large, final_yield);
      if (etch_info.end_flag==TRUE)
      {
       return;
      }
     }
```

```
    }//close if (ran2<ang_dep_prob)

   }
  }//close if (menu.if_chem==FALSE)*********************************
}

/*****************************************************************/
// In this function, the ion species are consumed and a reaction etch yield
based on the TML reaction set // is calculated, the number of particles
etched are removed from the cell
// Changes were made to account for recombination processes and redeposition
of etch species

void consume_ion(int & consumed, Particle & species, Traj & traj, Feature &
feature, Cell *lattice, \
      double angle, int & product, Cell_large *lattice_large)
{
 int order;
 double part_rem;
 int  ion_etch_prod[MAX_ION_PROD];
 int element_needed, max_element, max_element_prod;
 double ion_ang_dep_prob[NO_ION_REACTIONS], wt_factor[NO_ION_REACTIONS],
Ion_yield[NO_ION_REACTIONS];
 double alpha=1.0, alpha_up=0.0, alpha_down=0.0;
 double amount_etched=0.0;
 //  double frac_neg_V;
 int whilecount=0;
 int ion_total_no_prod=0;
 int i,j;
 int f_thre_fac;
 double recombine_f ;
 double A_recom_Cl_Cl; //recombination constant for Cl_Cl
 double A_recom_O_Cl; //recombination constant for O_Cl
 double x_Hf, x_La, x_O, x_Cl, x_C, x_V, tot_par;
 double part[NO_ELEMENTS];
 double J_Hf_Hf, J_Hf_Cl, J_Hf_O, J_Hf_V,J_La_La, J_La_O, J_La_Cl, J_La_V,
J_Cl_Cl, J_Cl_O, J_Cl_V, J_O_V, J_O_O, J_O_Cl;



 //for curv dependence
 double curv_dep_lim;
 double curv_dep_factor;
 double vec_b1, vec_b2, vec_b3;
 double tdx_new, tdy_new, tdz_new;
 double denom_1, beta_1;

 int stop;


 // Determine if the ion can induce any etching reaction
 order=dim(traj.x_lat, traj.y_lat, traj.z_lat);

 ion_ang_dep(angle, ion_ang_dep_prob);
 weigh(wt_factor);
 for (i = 0;i<NO_ELEMENTS;i++)
```

```
 {
  part[i] = lattice[order].part_in_cell[i];
 }

 if (total_ctr % 100 == 0 && lattice[order].part_in_cell[CARBON] <= 1.0)
 {
  //printf("\nIn Consume Ion HAFNIUM \n\tAfter Start:
%f",lattice[order].part_in_cell[HAFNIUM]);
 }
 tot_par =
(double)(lattice[order].part_in_cell[HAFNIUM]+lattice[order].part_in_cell[LAN
THANUM]+lattice[order].part_in_cell[OXYGEN] +
lattice[order].part_in_cell[CARBON] +
lattice[order].part_in_cell[CHLORINE]+lattice[order].part_in_cell[VACANCY]);
 x_Hf = (double)(lattice[order].part_in_cell[HAFNIUM])/tot_par;
 x_La = (double)(lattice[order].part_in_cell[LANTHANUM])/tot_par;
 x_O = (double)(lattice[order].part_in_cell[OXYGEN])/tot_par;
 x_C = (double)(lattice[order].part_in_cell[CARBON])/tot_par;
 x_Cl = (double)(lattice[order].part_in_cell[CHLORINE])/tot_par;
 x_V = (double)(lattice[order].part_in_cell[VACANCY])/tot_par;

 J_Hf_Hf = (4*x_Hf*4*x_Hf)/(2*(4*x_Hf+2*x_O+3*x_La+x_Cl+x_V));
 J_Hf_O  = (4*x_Hf*2*x_O)/(4*x_Hf+2*x_O+3*x_La+x_Cl+x_V);
 J_Hf_Cl = (4*x_Hf*1*x_Cl)/(4*x_Hf+2*x_O+3*x_La+x_Cl+x_V);
 J_Hf_V  = (4*x_Hf*1*x_V)/(4*x_Hf+2*x_O+3*x_La+x_Cl+x_V);
 J_La_La = (3*x_La*3*x_La)/(2*(4*x_Hf+2*x_O+3*x_La+x_Cl+x_V));
 J_La_O  = (3*x_La*2*x_O)/(4*x_Hf+2*x_O+3*x_La+x_Cl+x_V);
 J_La_Cl = (3*x_La*1*x_Cl)/(4*x_Hf+2*x_O+3*x_La+x_Cl+x_V);
 J_La_V  = (3*x_La*1*x_V)/(4*x_Hf+2*x_O+3*x_La+x_Cl+x_V);
 J_Cl_Cl = (1*x_Cl*1*x_Cl)/(2*(4*x_Hf+2*x_O+3*x_La+x_Cl+x_V));
 J_Cl_V  = (1*x_Cl*1*x_V)/(4*x_Hf+2*x_O+3*x_La+x_Cl+x_V);
 J_O_O   = (2*x_O*2*x_O)/(2*(4*x_Hf+2*x_O+3*x_La+x_Cl+x_V));
 J_O_V   = (2*x_O*1*x_V)/(4*x_Hf+2*x_O+3*x_La+x_Cl+x_V);
 J_O_Cl  = (2*x_O*1*x_Cl)/(4*x_Hf+2*x_O+3*x_La+x_Cl+x_V);
 J_Cl_O = J_O_Cl;

  //recombine_f = ran2(&idum);
 recombine_f = 1;

 if (species.comp[CHLORINE] > 0.0)
 {

  A_recom_Cl_Cl = 0;
  A_recom_O_Cl = 0;

  lattice[order].part_in_cell[CHLORINE] -= A_recom_Cl_Cl*1.0*J_Cl_V;
  lattice[order].part_in_cell[VACANCY] -= A_recom_Cl_Cl*1.0*J_Cl_V;
  lattice[order].total_part -= A_recom_Cl_Cl*2.0*J_Cl_V;
  lattice[order].part_in_cell[OXYGEN] -= A_recom_O_Cl*1.0*J_O_V;
  lattice[order].part_in_cell[VACANCY] -= A_recom_O_Cl*1.0*J_Cl_V;
  lattice[order].total_part -= 2.0*J_O_V;
 }

 Ion_rxn_yield_fn(lattice[order].total_part,lattice[order].part_in_cell,
species.comp, species.energy, Ion_yield);
```

```
 for (i=0;i<NO_ION_REACTIONS;i++)
 {
  alpha_up += Ion_yield[i]*wt_factor[i]*ion_ang_dep_prob[i];
  alpha_down += Ion_yield[i];
 }

 alpha = alpha_up/alpha_down ;

 if (ran2(&idum) > alpha)
 {
  consumed = FALSE;
 }
 else
 {
  consumed = TRUE;
  lattice[order].ion_flux++;

  etch_info.alpha = alpha;  //used in consume_particle to adjust N2I ratio
  //cout<<"angle "<<angle<<" alpha "<<alpha<<endl;


     //*average composition on a broad
area***********************************

  if (total_ctr % 100 == 0 && lattice[order].part_in_cell[CARBON] <= 1.0)
  {
   //printf("\n\tBefore Avg: %f",lattice[order].part_in_cell[HAFNIUM]);
  }
  ////comment start here
  average_comp(traj, lattice);
  traj.z_lat-=1;
  average_comp(traj,lattice);
  traj.z_lat  +=1;
  average_comp(traj,lattice);

  traj.x_lat  -=1;
  average_comp(traj,lattice);
  traj.x_lat +=2;
  average_comp(traj,lattice);
  traj.x_lat  -=1;


  traj.y_lat-=1;
  average_comp(traj,lattice);
  traj.y_lat  +=2;
  average_comp(traj,lattice);
  traj.y_lat  -=1;
  average_comp(traj,lattice);
  //comment end here


  traj.z_lat+=1;
  average_comp(traj,lattice);
  traj.z_lat  -=1;
  average_comp(traj,lattice);
```

```
   //**************************************

   part_rem=lattice[order].total_part;
   lattice[order].total_part =0;
          for (j=1;j<NO_ELEMENTS;j++)
    {
     if (lattice[order].part_in_cell[j] <=0.0)
     {

      lattice[order].part_in_cell[j] =0.1;
     }
     lattice[order].total_part +=lattice[order].part_in_cell[j];


    }
   Ion_rxn_yield_fn(lattice[order].total_part,lattice[order].part_in_cell,
species.comp, species.energy, Ion_yield);

   //***************check the composition within the neutral



   //threshold adjustment factor, for ion incorporation


   f_thre_fac = ( species.energy > 15 ? 1 : 0);
   lattice[order].total_part = 0.0;
   for (i=1;i<NO_ELEMENTS;i++)
   {
    lattice[order].part_in_cell[i] += f_thre_fac * species.comp[i]*cos(angle)
; // cos(angle) is the sticking probability of Cl+ and Cl2+
    lattice[order].total_part += lattice[order].part_in_cell[i];
   }
  //pause;

   //curvature dependence-----------------------------------------------------
   //first, transform the trajectory using the coord matrix for this cell
   transformation(traj.dx, traj.dy, traj.dz, tdx_new, tdy_new, tdz_new, \
    lattice[order].coord);
   tdx_new = -tdx_new;
   tdy_new = -tdy_new;
   tdz_new = -tdz_new;
   vec_b1 = lattice[order].coeff_b[1];
   vec_b2 = lattice[order].coeff_b[2];
   vec_b3 = lattice[order].coeff_b[3];
   denom_1 = tdx_new*tdx_new + tdy_new*tdy_new;
   beta_1 = (vec_b1*tdx_new*tdx_new + vec_b2*tdy_new*tdy_new -
vec_b3*tdx_new*tdy_new)/denom_1;

   curv_dep_lim = menu.curv_dep;//largest coefficient

   if (beta_1 > curv_dep_lim)
   {
    beta_1 = curv_dep_lim;
   }
   if (beta_1 < -curv_dep_lim)
   {
```

```
    beta_1 = -curv_dep_lim;
   }


   if (beta_1 < 0.0)
   {
    curv_dep_factor = menu.minslope*beta_1 + menu.intcpt;
   }
   else
   {
    curv_dep_factor =  menu.intcpt +
beta_1*(menu.minslope+(2.0*angle/PI)*(menu.maxslope-menu.minslope));
   }

   for (i=0;i<NO_ION_REACTIONS;i++)
   {
    //etch_info.ion_rxn_stat[i] += Ion_yield[i] * ion_ang_dep_prob[i];
    lattice[order].total_part -= Ion_yield[i] * ion_ang_dep_prob[i] *
Ion_no_atom[i]/alpha*curv_dep_factor;
    amount_etched += Ion_yield[i] * ion_ang_dep_prob[i] *
Ion_no_atom[i]/alpha*curv_dep_factor;

    for (j=1;j<NO_ELEMENTS;j++)
    {

     lattice[order].part_in_cell[j] -= Ion_yield[i] * ion_ang_dep_prob[i] *
Ion_Rxn_Comp[i][j]/alpha*curv_dep_factor;
     etch_info.etch_prod[j] += Ion_yield[i] * ion_ang_dep_prob[i] *
Ion_Rxn_Comp[i][j]/alpha*curv_dep_factor;

    }

   }

   // Artificial Limit to max # of vacancies
   //if (lattice[order].part_in_cell[VACANCY] > 5.0)
   //{
   // lattice[order].total_part -= (lattice[order].part_in_cell[VACANCY] -
5.0);
   // lattice[order].part_in_cell[VACANCY] = 5.0;
   //}
   lattice[order].total_part =0.0;
   for (j=1;j<NO_ELEMENTS;j++)
   {
    if (lattice[order].part_in_cell[j] <=0.0)
    {

     lattice[order].part_in_cell[j] =0.01;
    }
    lattice[order].total_part +=lattice[order].part_in_cell[j];


   }

   if (total_ctr % 100 == 0 && lattice[order].part_in_cell[CARBON] <= 1.0)
   {
    //printf("\n\tBefore Dec: %f\n",lattice[order].part_in_cell[HAFNIUM]);
```

```
   }

   part_rem = lattice[order].total_part;

   if (part_rem <= TRANSITION_ETCH)
   {
    etch_cell(traj, feature, lattice, lattice_large);
   }
   else if (part_rem >= PACKET+TRANSITION_DEP)
   {
    deposit_cell(traj, feature, lattice, part_rem-PACKET, lattice_large);

   }
  }
}


/*****************************************************************/
// this routine calculates the angular dependence of the various
// etching yields.

void ion_ang_dep(double angle, double ion_ang_dep_prob[])
{
 //double val0;
 double val1, val2;
 //double val3, val4, val5, val6, val7, val8, val9, val10, val11, val12;
 //double angle_2, angle_3, angle_4;
 double cosine, cosine2, cosine3, cosine4, cosine5, cosine6, cosine7;
 int i;
 double angle_deg;

 cosine = cos(angle);
 cosine2 = cosine*cosine;
 cosine3 = cosine2*cosine;
 cosine4 = cosine3*cosine;
 cosine5 = cosine4*cosine;
 cosine6 = cosine5*cosine;
 cosine7 = cosine6*cosine ;


 val1 = DMAX(0.0,-81.7*cosine5 + 224.03*cosine4 - 208.19*cosine3 +
67.59*cosine2 - 0.711*cosine - 0.0242);// Sputter, Densification, and Vacancy
Generation
 val2 = exp((cosine - 1)*2.4); // for ion enhanced etching



 for(i=0; i<NO_ION_REACTIONS; i++)
 {
  ion_ang_dep_prob[i] = val1/2.077757132; // 2.077757132 is the normalization
constant
 }
 for(i=16; i<25; i++)
 {
  ion_ang_dep_prob[i] = val2;
 }
}
```

```
/*********************************************************************/
// this routine takes care of the composition dependence by calculating
// suitable weight_factors before determining the total etching yield
// when an ion striked the surface. the sputtering yields of all
// products are proportional to their relative concentrations while the
// ion-enhanced etching yields depend on the fraction of C and Si on
// surface since they are part of the chlorinated products formed
// (e.g. SiCl4 and CCl4).
// this routine is called from "consume_ion()".

void weigh(double wt_factor[NO_ION_REACTIONS])
{
 double val1;
 int i;

 for (i=0; i<NO_ION_REACTIONS; i++)
  wt_factor[i] = 1;

 //val1 = 1/3.2; // the maximum value of YP's phsical sputtering curve
 val1=1; //changed by Calvin 10/11/12, it is already normalized in
ion_ang_dep_prob()
 wt_factor[0] = val1 ;
 wt_factor[1] = val1 ;
 wt_factor[2] = val1 ;
 wt_factor[3] = val1 ;


}




/*********************************************************************/
// this routine calculates the energy dependence of the various
// etching and sputtering yields. the ion-enhanced etching yields
// are dependent on the extent of chlorination and both physical
// sputtering and ion-enhanced etching yields depend on the ion
// energy(in a square-root fashion) and the threshold energy
// (specified in input_1.dat).
// this routine is called from etch() which in turn is called from
// "consume_ion()".

// ref: energy_depend
// Changes were made to include the TML reaction set

void Ion_rxn_yield_fn(double tot_par, double part[], double
comp[NO_ELEMENTS], double enrgy, double Ion_yield[NO_ION_REACTIONS])
{
 double x_Hf, x_La, x_O, x_Cl, x_C, x_V;
 double J_Hf_Hf, J_Hf_Cl, J_Hf_O, J_Hf_V, J_La_La, J_La_O, J_La_Cl, J_La_V,
J_Cl_Cl, J_Cl_O, J_Cl_V, J_O_V, J_O_O, J_O_Cl;

 //double x_Hf, x_O, x_C, x_F, x_V;
 //double J_O_V, J_C_V, J_Hf_V,J_C_O, J_C_F,J_O_F, J_O_O,J_F_F, J_Si_F,J_Hf_O
;
```

```
 double tot_bond;
 double calc_IY = 0.0;

 int i;


 for (i=0;i<NO_ION_REACTIONS;i++)
 {
  Ion_yield[i] = 0.0;
 }

 tot_par = (double)(part[HAFNIUM]+part[LANTHANUM]+part[OXYGEN] + part[CARBON]
+ part[CHLORINE]+part[VACANCY]);
 x_Hf = (double)(part[HAFNIUM])/tot_par;
 x_La = (double)(part[LANTHANUM])/tot_par;
 x_O = (double)(part[OXYGEN])/tot_par;
 x_C = (double)(part[CARBON])/tot_par;
 x_Cl = (double)(part[CHLORINE])/tot_par;
 x_V = (double)(part[VACANCY])/tot_par;

 J_Hf_Hf = (4*x_Hf*4*x_Hf)/(2*(4*x_Hf+2*x_O+3*x_La+x_Cl+x_V));
 J_Hf_O  = (4*x_Hf*2*x_O)/(4*x_Hf+2*x_O+3*x_La+x_Cl+x_V);
 J_Hf_Cl = (4*x_Hf*1*x_Cl)/(4*x_Hf+2*x_O+3*x_La+x_Cl+x_V);
 J_Hf_V  = (4*x_Hf*1*x_V)/(4*x_Hf+2*x_O+3*x_La+x_Cl+x_V);
 J_La_La = (3*x_La*3*x_La)/(2*(4*x_Hf+2*x_O+3*x_La+x_Cl+x_V));
 J_La_O  = (3*x_La*2*x_O)/(4*x_Hf+2*x_O+3*x_La+x_Cl+x_V);
 J_La_Cl = (3*x_La*1*x_Cl)/(4*x_Hf+2*x_O+3*x_La+x_Cl+x_V);
 J_La_V  = (3*x_La*1*x_V)/(4*x_Hf+2*x_O+3*x_La+x_Cl+x_V);
 J_Cl_Cl = (1*x_Cl*1*x_Cl)/(2*(4*x_Hf+2*x_O+3*x_La+x_Cl+x_V));
 J_Cl_V  = (1*x_Cl*1*x_V)/(4*x_Hf+2*x_O+3*x_La+x_Cl+x_V);
 J_O_O   = (2*x_O*2*x_O)/(2*(4*x_Hf+2*x_O+3*x_La+x_Cl+x_V));
 J_O_V   = (2*x_O*1*x_V)/(4*x_Hf+2*x_O+3*x_La+x_Cl+x_V);
 J_O_Cl  = (2*x_O*1*x_Cl)/(4*x_Hf+2*x_O+3*x_La+x_Cl+x_V);
 J_Cl_O = J_O_Cl;

 ////////////////////////////////////////////////////////////////////
 // New Ion reaction yield functions below for HfO2_Cl2 code 9/18/12 //
 ////////////////////////////////////////////////////////////////////

 //Physical Sputtering

 // Hf by blank
 Ion_yield[0] = DMAX(0.0, x_Hf*0.156*(sqrt(enrgy)-3.796)); // by Ar+
 Ion_yield[1] = DMAX(0.0, x_Hf*0.153*(sqrt(enrgy)-3.772)); // by Cl+
 Ion_yield[2] = DMAX(0.0, x_Hf*0.206*(sqrt(enrgy)-4.102)); // by Cl2+
 Ion_yield[3] = 0.0; // by O+

 // La by blank
 Ion_yield[4] = DMAX(0.0, x_La*0.0133*(sqrt(enrgy)-3.89)); // by Ar+
 Ion_yield[5] = DMAX(0.0, x_La*0.013*(sqrt(enrgy)-3.840)); // by Cl+
 Ion_yield[6] = DMAX(0.0, x_La*0.017*(sqrt(enrgy)-4.320)); // by Cl2+
 Ion_yield[7] = 0.0; // by O+

 // Cl by blank
 Ion_yield[8] = DMAX(0.0, x_Cl*0.045*(sqrt(enrgy)-5.280)); // by Ar+
 Ion_yield[9] = DMAX(0.0, x_Cl*0.045*(sqrt(enrgy)-5.112)); // by Cl+
 Ion_yield[10] = DMAX(0.0, x_Cl*0.055*(sqrt(enrgy)-6.218)); // by Cl2+
```

```
 Ion_yield[11] = 0.0; // by O+

 // O by blank
 Ion_yield[12] = DMAX(0.0, x_O*0.015*(sqrt(enrgy)-6.634)); // by Ar+
 Ion_yield[13] = DMAX(0.0, x_O*0.015*(sqrt(enrgy)-6.408)); // by Cl+
 Ion_yield[14] = DMAX(0.0, x_O*0.018*(sqrt(enrgy)-7.863)); // by Cl2+
 Ion_yield[15] = 0.0; // by O+

 //Ion Enhanced Etching
 Ion_yield[15] = 0.0; // HfCl
 Ion_yield[17] = 0.0; // HfCl2
 Ion_yield[18] = DMAX(0.0, pow(J_Hf_Cl,3.0)*2.7*(sqrt(enrgy)-sqrt(71.0))); //
HfCl3
 Ion_yield[19] = DMAX(0.0, pow(J_Hf_Cl,4.0)*4.8*(sqrt(enrgy)-sqrt(75.0))); //
HfCl4
 Ion_yield[20] = DMAX(0.0, J_La_Cl*1.52*(sqrt(enrgy)-sqrt(85.0))); // LaCl
 Ion_yield[21] = DMAX(0.0, J_La_Cl*J_La_O*3.46*(sqrt(enrgy)-sqrt(73.0))); //
LaOcl
 Ion_yield[22] = 0.0; // O2
 Ion_yield[23] = DMAX(0.0, J_O_Cl*0.28*(sqrt(enrgy)-sqrt(62.0))); // OCl
 Ion_yield[24] = DMAX(0.0, J_Cl_Cl*1.7*(sqrt(enrgy)-sqrt(0.0))); // Cl2

 // Vacancy Generation
 Ion_yield[25] = DMAX(0.0, 1.1*(sqrt(enrgy)-sqrt(39.0))); // by Ar+
 Ion_yield[26] = DMAX(0.0, 1.64*(sqrt(enrgy)-sqrt(28.0))); // by Cl+
 Ion_yield[27] = DMAX(0.0, 1.44*(sqrt(enrgy)-sqrt(27.0))); // by Cl2+
 Ion_yield[28] = 0.0; // by O+

 // Densification
 Ion_yield[29] = DMAX(0.0, 1.12*(sqrt(enrgy)-sqrt(31.0))); // by Ar+
 Ion_yield[30] = DMAX(0.0, 1.97*(sqrt(enrgy)-sqrt(2.0))); // by Cl+
 Ion_yield[31] = DMAX(0.0, 1.79*(sqrt(enrgy)-sqrt(19.0))); // by Cl2+
 Ion_yield[32] = 0.0; // by O+

 // Annihilation
 Ion_yield[33] = 0.0; // Hf_V
 Ion_yield[34] = 0.0; // Cl_V
 Ion_yield[35] = 0.0; // O_V

 if (part[CARBON] >= 20.0)
 {
  for (i=0;i<NO_ION_REACTIONS;i++)
  {
   Ion_yield[i] = 0.0;
  }
 }

}

// This function calculates the neutral reaction yield
void Neu_rxn_yield_fn(double tot_par, double part[], double
comp[NO_ELEMENTS], double Neu_yield[NO_NEU_REACTIONS])
{
 double x_Hf, x_La, x_O, x_Cl, x_C, x_V;
 double J_Hf_Hf, J_Hf_Cl, J_Hf_O, J_Hf_V, J_La_La, J_La_O, J_La_Cl, J_La_V,
J_Cl_Cl, J_Cl_O, J_Cl_V, J_O_V, J_O_O, J_C_V, J_O_Cl;
 //double x_Hf, x_O, x_C, x_F, x_V;
```

```
 //double J_O_V, J_C_V, J_Hf_V;
 double tot_bond;

 int i;
 //int runtime_neu_yield;
 //time_t start, end;


 //start = time(NULL);

 for (i=0;i<NO_NEU_REACTIONS;i++)
 {
  Neu_yield[i] = 0.0;
 }

 tot_par = (double)(part[HAFNIUM]+part[LANTHANUM]+part[OXYGEN] + part[CARBON]
+ part[CHLORINE]+part[VACANCY]);
 x_Hf = (double)(part[HAFNIUM])/tot_par;
 x_La = (double)(part[LANTHANUM])/tot_par;
 x_O = (double)(part[OXYGEN])/tot_par;
 x_C = (double)(part[CARBON])/tot_par;
 x_Cl = (double)(part[CHLORINE])/tot_par;
 x_V = (double)(part[VACANCY])/tot_par;

 J_Hf_Hf = (4*x_Hf*4*x_Hf)/(2*(4*x_Hf+2*x_O+3*x_La+x_Cl+x_V));
 J_Hf_O  = (4*x_Hf*2*x_O)/(4*x_Hf+2*x_O+3*x_La+x_Cl+x_V);
 J_Hf_Cl = (4*x_Hf*1*x_Cl)/(4*x_Hf+2*x_O+3*x_La+x_Cl+x_V);
 J_Hf_V  = (4*x_Hf*1*x_V)/(4*x_Hf+2*x_O+3*x_La+x_Cl+x_V);
 J_La_La = (3*x_La*3*x_La)/(2*(4*x_Hf+2*x_O+3*x_La+x_Cl+x_V));
 J_La_O  = (3*x_La*2*x_O)/(4*x_Hf+2*x_O+3*x_La+x_Cl+x_V);
 J_La_Cl = (3*x_La*1*x_Cl)/(4*x_Hf+2*x_O+3*x_La+x_Cl+x_V);
 J_La_V  = (3*x_La*1*x_V)/(4*x_Hf+2*x_O+3*x_La+x_Cl+x_V);
 J_Cl_Cl = (1*x_Cl*1*x_Cl)/(2*(4*x_Hf+2*x_O+3*x_La+x_Cl+x_V));
 J_Cl_V  = (1*x_Cl*1*x_V)/(4*x_Hf+2*x_O+3*x_La+x_Cl+x_V);
 J_O_O   = (2*x_O*2*x_O)/(2*(4*x_Hf+2*x_O+3*x_La+x_Cl+x_V));
 J_O_V   = (2*x_O*1*x_V)/(4*x_Hf+2*x_O+3*x_La+x_Cl+x_V);
 J_O_Cl  = (2*x_O*1*x_Cl)/(4*x_Hf+2*x_O+3*x_La+x_Cl+x_V);
 J_Cl_O = J_O_Cl;



 // Added by Calvin 9/28/10, neutral reaction yield depends on sticking coeff
and bond conc.
 if ((comp[CHLORINE]==1.0)&&(comp[CARBON]==0.0)&&(comp[HAFNIUM]==0.0)) //Cl
NEUTRAL
 {
  Neu_yield[0] = 0.001 * J_Hf_V + 0.002 * J_La_V + 0.3 * J_O_V  ; // changed
9/18/12
  //Neu_yield[0] = 1.0;
 }
 else if ((comp[OXYGEN] == 1.0)&&(comp[CARBON]==0.0)&&(comp[HAFNIUM]==0.0))
 {
  Neu_yield[0] = 0.0 * J_Hf_V + 0.0 * J_O_V ;
 }
 else if (etch_info.etched_prod ==1) // added by Calvin 10/11/12
 {
```

```
   Neu_yield[0] = 0.001 * J_Hf_V + 0.002 * J_La_V + 0.3 * J_O_V  ; // added by
Calvin 10/12/12 to be like Cl neutrals
   //Neu_yield[0] = 1.0;
  }
  else  //CXFY, C, CO
  {
   Neu_yield[0] = 0.0* J_O_V;
  }

  // if cell contains more than 20 carbon particles, neutrals do not react
  if (part[CARBON] >= 20.0)
  {
   Neu_yield[0] = 0.0;
  }
}
```

BIBLIOGRAPHY

Abrams, C. F. and D. B. Graves (1998). "Energetic ion bombardment of SiO2 surfaces: Molecular dynamics simulations." Journal Of Vacuum Science & Technology A **16**(5): 3006-3019.

Abrams, C. F. and D. B. Graves (1999). "Molecular dynamics simulations of Si etching by energetic CF3+." Journal Of Applied Physics **86**(11): 5938-5948.

Agarwal, A. and M. J. Kushner (2009). "Plasma atomic layer etching using conventional plasma equipment." Journal Of Vacuum Science & Technology A **27**(1): 37-50.

Ahn, S.-E., M.-J. Lee, et al. (2008). "Write current reduction in transition metal oxide based resistance-change memory." Advanced Materials **20**(5): 924-+.

Alshareef, H. N., M. Quevedo-Lopez, et al. (2006). "Work function engineering using lanthanum oxide interfacial layers." Applied Physics Letters **89**(23).

Amorim, J., H. S. Maciel, et al. (1991). "High-Density Plasma Mode Of An Inductively Coupled Radio-Frequency Discharge." Journal Of Vacuum Science & Technology B **9**(2): 362-365.

Arunachalam, V., S. Rauf, et al. (2001). "Integrated multi-scale model for ionized plasma physical vapor deposition." Journal of Applied Physics **90**(1): 64-73.

Aston, F. W. (1920). "Isotopes and atomic weights." Nature **105**: 617-619.

Athavale, S. D. and D. J. Economou (1995). Molecular dynamics simulation of atomic layer etching of silicon. Proceedings of the 41st National Symposium of the American Vacuum Society, Denver, Colorado (USA), AVS.

Athavale, S. D. and D. J. Economou (1996). "Realization of atomic layer etching of silicon." Journal Of Vacuum Science & Technology B **14**(6): 3702-3705.

Badenes, G., R. Rooyackers, et al. (2000). "A new dummy-free shallow trench isolation concept for mixed-signal applications." Journal Of The Electrochemical Society **147**(10): 3827-3832.

Balooch, M., M. Moalem, et al. (1996). "Low-energy Ar ion-induced and chlorine ion etching of silicon." Journal of Vacuum Science & Technology A: Vacuum, Surfaces, and Films **14**(1): 229-233.

Barin, I. and O. Knacke (1973). Thermochemical properties of inorganic substances. Berlin; New York, Springer-Verlag.

Barone, M. E. and D. B. Graves (1995). "MOLECULAR-DYNAMICS SIMULATIONS OF DIRECT REACTIVE ION ETCHING OF SILICON BY FLUORINE AND CHLORINE." Journal of Applied Physics **78**(11): 6604-6615.

Barone, M. E. and D. B. Graves (1996). "Molecular dynamics simulations of plasma-surface chemistry." Plasma Sources Science & Technology **5**(2): 187-192.

Barone, M. E., T. O. Robinson, et al. (1996). "Molecular dynamics simulations of direct reactive ion etching: Surface roughening of silicon by chlorine." Ieee Transactions On Plasma Science **24**(1): 77-78.

Blauer, J. and M. Farber (1963). "Heat of Formation and Entropy of (BOCl)[sub 3]." The Journal of Chemical Physics **39**(1): 158-160.

Booth, J. P., O. Joubert, et al. (1991). "Oxygen atom actinometry reinvestigated: Comparison with absolute measurements by resonance absorption at 130 nm." Journal of Applied Physics **69**(2): 618-626.

Booth, J. P. and N. Sadeghi (1991). "Oxygen and fluorine atom kinetics in electron cyclotron resonance plasmas by time-resolved actinometry." Journal of Applied Physics **70**(2): 611-620.

Buttari, D., S. Heikman, et al. (2002). Digital etching for highly reproducible low damage gate recessing on AlGaN/GaN HEMTs. High Performance Devices, 2002. Proceedings. IEEE Lester Eastman Conference on.

Byoung Hun, L., R. Choi, et al. (2000). Characteristics of TaN gate MOSFET with ultrathin hafnium oxide (8 Å-12 Å). Electron Devices Meeting, 2000. IEDM Technical Digest. International.

Cardinaud, C., M.-C. Peignon, et al. (2000). "Plasma etching: principles, mechanisms, application to micro- and nano-technologies." Applied Surface Science **164**(1-4): 72.

Cavallotti, C., E. Pantano, et al. (2005). "Multiscale simulation of silicon film growth." Crystal Research And Technology **40**(10-11): 958-963.

Chae, H., S. A. Vitale, et al. (2003). "Silicon dioxide etching yield measurements with inductively coupled fluorocarbon plasmas." Journal of Vacuum Science & Technology A: Vacuum, Surfaces, and Films **21**(2): 381-387.

Chae, H., S. A. Vitale, et al. (2003). "Silicon dioxide etching yield measurements with inductively coupled fluorocarbon plasmas." Journal of Vacuum Science & Technology A **21**(2): 381-387.

Chang, J. P., A. P. Mahorowala, et al. (1998). Plasma-surface kinetics and feature profile evolution in chlorine etching of polysilicon. International workshop on basic aspects of nonequilibrium plasmas interacting with surfaces (BANPIS"97), Shirahama, Wakayama (Japan), AVS.

Chang, J. P. and H. H. Sawin (1997). "Kinetic study of low energy ion-enhanced polysilicon etching using Cl, Cl-2, and Cl+ beam scattering." Journal Of Vacuum Science & Technology A-Vacuum Surfaces And Films **15**(3): 610-615.

Chang, J. P. and H. H. Sawin (2001). "Molecular-beam study of the plasma-surface kinetics of silicon dioxide and photoresist etching with chlorine." Journal of Vacuum Science & Technology B **19**(4): 1319-1327.

Chen, J. H., W. J. Yoo, et al. (2004). "Investigation of etching properties of HfO based high-K dielectrics using inductively coupled plasma." Journal Of Vacuum Science & Technology A **22**(4): 1552-1558.

Chen, R. and S. F. Bent (2006). "Chemistry for positive pattern transfer using area-selective atomic layer deposition." Advanced Materials **18**(8): 1086-+.

Chen, W., X. Q. Liu, et al. (2006). "Fabrication and characterization of novel cross point structures for molecular electronic integrated circuits." Journal Of Vacuum Science & Technology B **24**(6): 3217-3220.

Cheng, C. C., K. V. Guinn, et al. (1994). "IN-SITU PULSED LASER-INDUCED THERMAL-DESORPTION STUDIES OF THE SILICON CHLORIDE SURFACE-LAYER DURING SILICON ETCHING IN HIGH-DENSITY PLASMAS OF CL2 AND CL2/O2 MIXTURES." Journal Of Vacuum Science & Technology A-Vacuum Surfaces And Films **12**(5): 2630-2640.

Choi, J. H., Y. Mao, et al. (2011). "Development of hafnium based high-k materials-A review." Materials Science & Engineering R-Reports **72**(6): 97-136.

Chu, Y.-H., L. W. Martin, et al. (2008). "Electric-field control of local ferromagnetism using a magnetoelectric multiferroic." Nature Materials **7**(6): 478-482.

Coburn, J. W. and M. Chen (1980). "Optical emission spectroscopy of reactive plasmas: A method for correlating emission intensities to reactive particle density." Journal of Applied Physics **51**(6): 3134-3136.
Cruden, B. A., M. V. V. S. Rao, et al. (2002). "Neutral gas temperature estimate in CF[sub 4]/O[sub 2]/Ar inductively coupled plasmas." Applied Physics Letters **81**(6): 990-992.
Cui, J. P., Y. Z. He, et al. (2000). "Temperature measurement of reflected shock wave by using chemical indicator." Acta Mechanica Sinica **16**(1): 63-69.
Dagostino, R., F. Cramarossa, et al. (1981). "Spectroscopic Diagnostics Of Cf4-O2 Plasmas During Si And Sio2 Etching Processes." Journal Of Applied Physics **52**(3): 1259-1265.
Dalton, T. J., J. C. Arnold, et al. (1993). "MICROTRENCH FORMATION IN POLYSILICON PLASMA-ETCHING OVER THIN GATE OXIDE." Journal of the Electrochemical Society **140**(8): 2395-2401.
Dennard, R. H., Gaenssle.Fh, et al. (1974). "DESIGN OF ION-IMPLANTED MOSFETS WITH VERY SMALL PHYSICAL DIMENSIONS." Ieee Journal of Solid-State Circuits **SC 9**(5): 256-268.
Dimoulas, A., G. Vellianitis, et al. (2004). "La2Hf2O7 high-kappa gate dielectric grown directly on Si(001) by molecular-beam epitaxy." Applied Physics Letters **85**(15): 3205-3207.
Ding, J. and N. Hershkowitz (1996). "Symmetric rate model for fluorocarbon plasma etching of SiO2." Applied Physics Letters **68**(12): 1619-1621.
Dittmer, G. and U. Niemann (1987). "EVALUATION OF THERMODYNAMIC DATA ON ZIRCONIUM AND HAFNIUM HALIDES AND OXYHALIDES BY MEANS OF TRANSPORT EXPERIMENTS." Philips Journal of Research **42**(1): 15-40.
Doliska, A., A. Vesel, et al. (2012). "Interaction between model poly(ethylene terephthalate) thin films and weakly ionised oxygen plasma." Surface and Interface Analysis **44**(1): 56-61.
Donnelly, R. G. and T. S. King (1978). "Surface composition and surface cluster size distribution of Cu-Ni alloys via a monte carlo method." Surface Science **74**(1): 89-108.
Donnelly, V. M., D. L. Flamm, et al. (1984). "Anisotropic Etching Of Sio2 In Low-Frequency Cf4/O2 And Nf3/Ar Plasmas." Journal Of Applied Physics **55**(1): 242-252.
Donnelly, V. M. and M. V. Malyshev (2000). "Diagnostics of inductively coupled chlorine plasmas: Measurements of the neutral gas temperature." Applied Physics Letters **77**(16): 2467.
Donnelly, V. M. and M. J. Schabel (2002). "Spatially resolved electron temperatures, species concentrations, and electron energy distributions in inductively coupled chlorine plasmas, measured by trace-rare gases optical emission spectroscopy." Journal of Applied Physics **91**(10): 6288.
Doyle, B. S., S. Datta, et al. (2003). "High performance fully-depleted tri-gate CMOS transistors." Ieee Electron Device Letters **24**(4): 263-265.
Ellingham, H. (1944). "Transactions and Communications." Journal of the Society of Chemical Industry **63**(5): 125-160.
Flamm, D. L., V. M. Donnelly, et al. (1983). "BASIC CHEMISTRY AND MECHANISMS OF PLASMA-ETCHING." Journal of Vacuum Science & Technology B **1**(1): 23-30.
Fracassi, F. and J. W. Coburn (1986). "Quartz Crystal Microbalance Studies of the Plasma-Assisted Etching of Polyimide and Tungsten Thin Films." MRS Online Proceedings Library **68**: null-null.
Frankwicz, P., L. Gardner, et al. (2012). "Reduction of Greenhouse Gas Emissions by Metal Interconnect Etch Process Optimization." ECS Transactions **41**(34): 1-7.

Frenklach, M. (1998). "Simulation of surface reactions." Pure And Applied Chemistry **70**(2): 477-484.
Glassner, A., L. Argonne National, et al. (1957). The thermochemical properties of the oxides, fluorides, and chlorides to 2500^0 K. [Lemont, Ill.], Argonne National Laboratory.
Greer, F., J. W. Coburn, et al. (2000). "Vacuum beam studies of photoresist etching kinetics." Journal Of Vacuum Science & Technology A-Vacuum Surfaces And Films **18**(5): 2288-2294.
Guha, S., V. K. Paruchuri, et al. (2007). "Examination of flatband and threshold voltage tuning of HfO 2 /TiN field effect transistors by dielectric cap layers." Applied Physics Letters **90**(9).
Gulbrans.Ea (1970). "THERMOCHEMISTRY AND OXIDATION OF REFRACTORY METALS AT HIGH TEMPERATURE." Corrosion **26**(1): 19-&.
Gulbrans.Ea and S. A. Jansson (1972). "HIGH-TEMPERATURE OXIDATION, REDUCTION, AND VOLATILIZATION REACTIONS OF SILICON AND SILICON-CARBIDE." Oxidation of Metals **4**(3): 181-&.
Guo, W., B. Bai, et al. (2009). "Mixing-layer kinetics model for plasma etching and the cellular realization in three-dimensional profile simulator." Journal Of Vacuum Science & Technology A **27**(2): 388-403.
Guo, W. and H. H. Sawin (2009). "Review of profile and roughening simulation in microelectronics plasma etching." Journal of Physics D-Applied Physics **42**(19).
Hagström, S., C. Nordling, et al. (1964). "Electron spectroscopy for chemical analyses." Physics Letters **9**(3): 235.
Haynes, W. M. (2011). CRC handbook of chemistry and physics. Boca Raton, Fla.; London, CRC ; Taylor & Francis [distributor].
Heinecke, R. A. H. (1975). "Control Of Relative Etch Rates Of Sio2 And Si In Plasma Etching." Solid-State Electronics **18**(12): 1146-1147.
Helmer, B. A. and D. B. Graves (1998). "Molecular dynamics simulations of Ar+ and Cl+ impacts onto silicon surfaces: Distributions of reflected energies and angles." Journal Of Vacuum Science & Technology A-Vacuum Surfaces And Films **16**(6): 3502-3514.
Helot, M., T. Chevolleau, et al. (2006). "Plasma etching of HfO2 at elevated temperatures in chlorine-based chemistry." Journal of Vacuum Science & Technology A **24**(1): 30-40.
Hisamoto, D., W. C. Lee, et al. (2000). "FinFET - A self-aligned double-gate MOSFET scalable to 20 nm." Ieee Transactions On Electron Devices **47**(12): 2320-2325.
Ho, M. Y., H. Gong, et al. (2002). "Suppressed crystallization of Hf-based gate dielectrics by controlled addition of Al2O3 using atomic layer deposition." Applied Physics Letters **81**(22): 4218-4220.
Hoang, J., C. C. Hsu, et al. (2008). "Feature profile evolution during shallow trench isolation etch in chlorine-based plasmas. I. Feature scale modeling." Journal Of Vacuum Science & Technology B **26**(6): 1911-1918.
Hopwood, J. (1992). "Review of inductively coupled plasmas for plasma processing." Plasma Sources Science and Technology **1**(2): 109.
Hsu, C. C., J. W. Coburn, et al. (2006). "Etching of ruthenium coatings in O-2- and Cl-2-containing plasmas." Journal Of Vacuum Science & Technology A **24**(1): 1-8.
Hsu, C. C., J. Hoang, et al. (2008). "Feature profile evolution during shallow trench isolation etch in chlorine-based plasmas. II. Coupling reactor and feature scale models." Journal Of Vacuum Science & Technology B **26**(6): 1919-1925.

Hsu, C. C., M. J. Titus, et al. (2007). "Measurement and modeling of time- and spatial-resolved wafer surface temperature in inductively coupled plasmas." Journal Of Vacuum Science & Technology A **25**(3): 607-614.
Hubbard, K. J. and D. G. Schlom (1996). "Thermodynamic stability of binary oxides in contact with silicon." Journal of Materials Research **11**(11): 2757-2776.
Hwang, W. S., J. H. Chen, et al. (2005). "Investigation of etching properties of metal nitride/high-k gate stacks using inductively coupled plasma." Journal Of Vacuum Science & Technology A **23**(4): 964-970.
Iwakawa, A., T. Nagaoka, et al. (2008). "Molecular Dynamics Simulation of Si Etching by Off-Normal Cl+ Bombardment at High Neutral-to-Ion Flux Ratios." Japanese Journal Of Applied Physics **47**(11): 8560-8564.
Izyumskaya, N., Y. Alivov, et al. (2009). "Oxides, Oxides, and More Oxides: High- Oxides, Ferroelectrics, Ferromagnetics, and Multiferroics." Critical Reviews in Solid State and Materials Sciences **34**(3-4): 89-179.
Jia, C. and J. Berakdar (2009). "Multiferroic oxides-based flash memory and spin-field-effect transistor." Applied Physics Letters **95**(1).
Jung, K. B., H. Cho, et al. (1999). "Relative merits of Cl-2 and CO/NH3 plasma chemistries for dry etching of magnetic random access memory device elements." Journal Of Applied Physics **85**(8): 4788-4790.
Jurgensen, C. W. and E. S. G. Shaqfeh (1989). "FACTORS CONTROLLING THE ETCHING RATE AND ETCHING PROFILE IN THE O-2 REACTIVE ION ETCHING PATTERN TRANSFER STEP IN MULTILEVEL LITHOGRAPHY." Polymer Engineering and Science **29**(13): 878-881.
Karapiperis, L., D. Dubreuil, et al. (1985). "Ion beam lithography: An investigation of resolution limits and sensitivities of ion-beam exposed PMMA." Journal of Vacuum Science & Technology B: Microelectronics and Nanometer Structures **3**(1): 353-357.
Kastenmeier, B. E. E., P. J. Matsuo, et al. (1996). "Chemical dry etching of silicon nitride and silicon dioxide using CF4/O-2/N-2 gas mixtures." Journal Of Vacuum Science & Technology A-Vacuum Surfaces And Films **14**(5): 2802-2813.
Kiihamaki, J. and S. Franssila (1999). "Pattern shape effects and artefacts in deep silicon etching." Journal Of Vacuum Science & Technology A-Vacuum Surfaces And Films **17**(4): 2280-2285.
Kimura, Y., J. W. Coburn, et al. (2004). "Vacuum beam studies of fluorocarbon radicals and argon ions on Si and SiO2 surfaces." Journal of Vacuum Science & Technology A **22**(6): 2508-2516.
Kortshagen, U., N. D. Gibson, et al. (1996). "On the E - H mode transition in RF inductive discharges." Journal of Physics D: Applied Physics **29**(5): 1224.
Kota, G. P., J. W. Coburn, et al. (1998). "The recombination of chlorine atoms at surfaces." Journal Of Vacuum Science & Technology A-Vacuum Surfaces And Films **16**(1): 270-277.
Kulkarni, N. S. and R. T. DeHoff (2002). "Application of volatility diagrams for low temperature, dry etching, and planarization of copper." Journal of the Electrochemical Society **149**(11): G620-G632.
Kwon, O., B. Bai, et al. (2006). "Surface kinetics modeling of silicon and silicon oxide plasma etching. III. Modeling of silicon oxide etching in fluorocarbon chemistry using

translating mixed-layer representation." Journal Of Vacuum Science & Technology A **24**(5): 1920-1927.
Kwon, O. and H. H. Sawin (2006). "Surface kinetics modeling of silicon and silicon oxide plasma etching. II. Plasma etching surface kinetics modeling using translating mixed-layer representation." Journal Of Vacuum Science & Technology A **24**(5): 1914-1919.
Layadi, N., V. M. Donnelly, et al. (1997). "Cl-2 plasma etching of Si(100): Nature of the chlorinated surface layer studied by angle-resolved x-ray photoelectron spectroscopy." Journal of Applied Physics **81**(10): 6738-6748.
Lee, B. H., J. Oh, et al. (2006). "Gate stack technology for nanoscale devices." Materials Today **9**(6): 32-40.
Lee, C.-H., S.-H. Hur, et al. (2005). "Charge-trapping device structure of SiO[sub 2]/SiN/high-k dielectric Al[sub 2]O[sub 3] for high-density flash memory." Applied Physics Letters **86**(15): 152908.
Lee, J. S., J. W. Kim, et al. (2001). "Photo-electrochemical gate recess etching for the fabrication of AlGaN/GaN heterostructure field effect transistor." Japanese Journal Of Applied Physics Part 2-Letters **40**(3A): L198-L200.
Lee, K. T. and S. Raghavan (1999). "Etch rate of silicon and silicon dioxide in ammonia-peroxide solutions measured by quartz crystal microbalance technique." Electrochemical and Solid State Letters **2**(4): 172-174.
Levinson, J. A., E. S. G. Shaqfeh, et al. (2000). "Ion-assisted etching and profile development of silicon in molecular and atomic chlorine." Journal Of Vacuum Science & Technology B **18**(1): 172-190.
Lieberman, M. A. and A. J. Lichtenberg (2005). Principles of Plasma Discharges and Materials Processing. New York, Wiley.
Lill, T. and O. Joubert (2008). "Materials science - The cutting edge of plasma etching." Science **319**(5866): 1050-1051.
Lim, W. S., S. D. Park, et al. (2008). "Atomic layer etching of (100)/(111) GaAs with chlorine and low angle forward reflected Ne neutral beam." Surface & Coatings Technology **202**(22-23): 5701-5704.
Litvak, H. E. (1996). End point control via optical emission spectroscopy. The 3rd International Workshop on Advanced Plasma Tools for Etching, Chemical Vapor Deposition, and Plasma Vapor Deposition: Sources, Process Control, and Diagnostics, San Jose, California (USA), AVS.
Liu, J., Y. Mao, et al. (2008). "Generation of Oxide Nanopatterns by Combining Self-Assembly of S-Layer Proteins and Area-Selective Atomic Layer Deposition." Journal of the American Chemical Society **130**(50): 16908-16913.
Liu, J., R. M. Martin, et al. (2008). "Characteristics of Hf-silicate thin films synthesized by plasma enhanced atomic layer deposition." Journal of Vacuum Science & Technology A **26**(5): 1251-1257.
Lo, S. H., D. A. Buchanan, et al. (1997). "Quantum-mechanical modeling of electron tunneling current from the inversion layer of ultra-thin-oxide nMOSFET's." Ieee Electron Device Letters **18**(5): 209-211.
Lucklum, R. and P. Hauptmann (2001). "Thin film shear modulus determination with quartz crystal resonators: a review." Proceedings of the 2001 IEEE International Frequncy Control Symposium and PDA Exhibition (Cat. No.01CH37218): 408-418.

Lymberopoulos, D. P. and D. J. Economou (1993). "Fluid Simulations Of Radio-Frequency Glow-Discharges - 2-Dimensional Argon Discharge Including Metastables." Applied Physics Letters **63**(18): 2478-2480.
Mahorowala, A. P. and H. H. Sawin (2002). "Etching of polysilicon in inductively coupled Cl-2 and HBr discharges. II. Simulation of profile evolution using cellular representation of feature composition and Monte Carlo computation of flux and surface kinetics." Journal of Vacuum Science & Technology B **20**(3): 1064-1076.
Mahorowala, A. P. and H. H. Sawin (2002). "Etching of polysilicon in inductively coupled Cl[sub 2] and HBr discharges. III. Photoresist mask faceting, sidewall deposition, and microtrenching." Journal of Vacuum Science & Technology B: Microelectronics and Nanometer Structures **20**(3): 1077-1083.
Malyshev, M. V. and V. M. Donnelly (2000). "Diagnostics of chlorine inductively coupled plasmas. Measurement of electron temperatures and electron energy distribution functions." Journal of Applied Physics **87**(4): 1642.
Malyshev, M. V. and V. M. Donnelly (2001). "Diagnostics of inductively coupled chlorine plasmas: Measurement of electron and total positive ion densities." Journal of Applied Physics **90**(3): 1130.
Malyshev, M. V., V. M. Donnelly, et al. (2000). "Diagnostic studies of aluminum etching in an inductively coupled plasma system: Determination of electron temperatures and connections to plasma-induced damage." Journal of Vacuum Science & Technology A: Vacuum, Surfaces, and Films **18**(3): 849-859.
Marchack, N. and J. P. Chang (2011). "Perspectives in nanoscale plasma etching: what are the ultimate limits?" Journal of Physics D-Applied Physics **44**(17).
Marchack, N. and J. P. Chang (2012). "Chemical Processing of Materials on Silicon: More Functionality, Smaller Features, and Larger Wafers." Annual Review of Chemical and Biomolecular Engineering **3**(1): 235-262.
Martin, L. W., Y. H. Chu, et al. (2010). "Advances in the growth and characterization of magnetic, ferroelectric, and multiferroic oxide thin films." Materials Science & Engineering R-Reports **68**(4-6): III-133.
Martin, R. M., H.-O. Blom, et al. (2009). "Plasma etching of Hf-based high-k thin films. Part II. Ion-enhanced surface reaction mechanisms." Journal of Vacuum Science & Technology A: Vacuum, Surfaces, and Films **27**(2): 217.
Martin, R. M. and J. P. Chang (2009). "Plasma etching of Hf-based high-k thin films. Part I. Effect of complex ions and radicals on the surface reactions." Journal of Vacuum Science & Technology A: Vacuum, Surfaces, and Films **27**(2): 209.
Martin, R. M. and J. P. Chang (2009). "Plasma etching of Hf-based high-k thin films. Part III. Modeling the reaction mechanisms." Journal of Vacuum Science & Technology A: Vacuum, Surfaces, and Films **27**(2): 224.
Matsui, J., N. Nakano, et al. (2001). "The effect of topographical local charging on the etching of deep-submicron structures in SiO2 as a function of aspect ratio." Applied Physics Letters **78**(7): 883-885.
Mayne, K. I. (1952). "MASS SPECTROMETRY." Reports on Progress in Physics **15**: 24-48.
McKeown, D. (1961). "NEW METHOD FOR MEASURING SPUTTERING IN REGION NEAR THRESHOLD." Review of Scientific Instruments **32**(2): 133-&.

Mistry, K., C. Allen, et al. (2007). "A 45 nm logic technology with high-k+metal gate transistors, strained silicon, 9 Cu interconnect layers, 193 nm dry patterning, and 100% Pb-free packaging." 2007 IEEE International Electron Devices Meeting - IEDM '07.

Miyoshi, Y., Z. L. Petrovic, et al. (2002). "Transition between capacitive and inductive mode in inductively coupled plasma observed by emission computerized tomography." Ieee Transactions On Plasma Science **30**(1): 130-131.

Mogab, C. J., A. C. Adams, et al. (1978). "Plasma Etching Of Si And Sio2 - Effect Of Oxygen Additions To Cf4 Plasmas." Journal Of Applied Physics **49**(7): 3796-3803.

Molodetsky, I., A. Navrotsky, et al. (2000). "Energetics of X-ray-amorphous zirconia and the role of surface energy in its formation." Journal of Non-Crystalline Solids **262**(1-3): 106-113.

Mott-Smth, H. M. and I. Langmuir (1926). "The theory of collectors in gaseous discharges." Physical Review **28**(4): 0727-0763.

Murto, R. W., M. I. Gardner, et al. (2003). "Challenges in gate stack engineering." Solid State Technology **46**(10): 43-+.

Nixon, W. C. (1971). "General Principles Of Scanning Electron Microscopy." Philosophical Transactions Of The Royal Society Of London Series B-Biological Sciences **261**(837): 45-&.

O'Sullivan, C. K. and G. G. Guilbault (1999). "Commercial quartz crystal microbalances - theory and applications." Biosensors & Bioelectronics **14**(8-9): 663-670.

Oehrlein, G. S. and H. L. Williams (1987). "Silicon Etching Mechanisms In A Cf4/H2 Glow-Discharge." Journal Of Applied Physics **62**(2): 662-672.

Oehrlein, G. S., Y. Zhang, et al. (1994). "Fluorocarbon High-Density Plasmas .2. Silicon Dioxide And Silicon Etching Using Cf4 And Chf3." Journal Of Vacuum Science & Technology A-Vacuum Surfaces And Films **12**(2): 333-344.

Ohta, H., A. Iwakawa, et al. (2008). "An interatomic potential model for molecular dynamics simulation of silicon etching by Br+-containing plasmas." Journal Of Applied Physics **104**(7).

Oiseth, S. K., A. Krozer, et al. (2004). "Ultraviolet light treatment of thin high-density polyethylene films monitored with a quartz crystal microbalance." Journal of Applied Polymer Science **92**(5): 2833-2839.

Oldham, W. G., A. R. Neureuther, et al. (1980). "A GENERAL SIMULATOR FOR VLSI LITHOGRAPHY AND ETCHING PROCESSES .2. APPLICATION TO DEPOSITION AND ETCHING." Ieee Journal of Solid-State Circuits **15**(4): 520-524.

Ono, K. and M. Tuda (1997). Profile evolution during cold plasma beam etching of silicon.

Osher, S. and J. A. Sethian (1988). "FRONTS PROPAGATING WITH CURVATURE-DEPENDENT SPEED - ALGORITHMS BASED ON HAMILTON-JACOBI FORMULATIONS." Journal of Computational Physics **79**(1): 12-49.

Ostrikov, K. (2007). "Plasma Nanoscience: From Nature's Mastery to Deterministic Plasma-Aided Nanofabrication." Plasma Science, IEEE Transactions on **35**(2): 127.

Park, H. B., B. Ju, et al. (2009). "Performance and reliability improvement of HfSiON gate dielectrics using chlorine plasma treatment." Applied Physics Letters **94**(4).

Pourbaix, M. (1976). "SOME APPLICATIONS OF POTENTIAL-PH DIAGRAMS TO STUDY OF LOCALIZED CORROSION." Journal of the Electrochemical Society **123**(2): C25-C36.

Ragnarsson, L. A., V. S. Chang, et al. (2007). "Achieving conduction band-edge effective work functions by La2O3 capping of hafnium silicates." Ieee Electron Device Letters **28**(6): 486-488.
Rauf, S., T. Sparks, et al. (2007). "A molecular dynamics investigation of fluorocarbon based layer-by-layer etching of silicon and SiO2." Journal Of Applied Physics **101**(3).
Rittersma, Z. M., J. C. Hooker, et al. (2006). "Characterization of field-effect transistors with La2Hf2O7 and HfO2 gate dielectric layers deposited by molecular-beam epitaxy." Journal of Applied Physics **99**(2).
Robertson, J. (2000). "Band offsets of wide-band-gap oxides and implications for future electronic devices." Journal of Vacuum Science & Technology B **18**(3): 1785-1791.
Robertson, J. (2006). "High dielectric constant gate oxides for metal oxide Si transistors." Reports on Progress in Physics **69**(2): 327-396.
Rossnagel, S. M. and R. S. Robinson (1983). "MONTE-CARLO MODEL OF TOPOGRAPHY DEVELOPMENT DURING SPUTTERING." Journal Of Vacuum Science & Technology A-Vacuum Surfaces And Films **1**(2): 426-429.
Sauerbrey, G. (1959). "Verwendung Von Schwingquarzen Zur Wagung Dunner Schichten Und Zur Mikrowagung." Zeitschrift Fur Physik **155**(2): 206-222.
Scott, J. F. (2007). "Data storage - Multiferroic memories." Nature Materials **6**(4): 256-257.
Sha, L. and J. P. Chang (2003). "Plasma etching selectivity of ZrO[sub 2] to Si in BCl[sub 3]/Cl[sub 2] plasmas." Journal of Vacuum Science & Technology A: Vacuum, Surfaces, and Films **21**(6): 1915-1922.
Sha, L. and J. P. Chang (2004). "Plasma etching of high dielectric constant materials on silicon in halogen chemistries." Journal Of Vacuum Science & Technology A **22**(1): 88-95.
Sha, L., B. O. Cho, et al. (2002). "Ion-enhanced chemical etching of ZrO2 in a chlorine discharge." Journal Of Vacuum Science & Technology A-Vacuum Surfaces And Films **20**(5): 1525-1531.
Sha, L., R. Puthenkovilakam, et al. (2003). "Ion-enhanced chemical etching of HfO2 for integration in metal-oxide-semiconductor field effect transistors." Journal Of Vacuum Science & Technology B **21**(6): 2420-2427.
Shamiryan, D., M. Baklanov, et al. (2009). "Selective Removal Of High-K Gate Dielectrics." Chemical Engineering Communications **196**(12): 1475-1535.
Shang, L., S. A. Campbell, et al. (1994). "The Development Of An Anisotropic Si Etch Process Selective To Gexsi1-X Underlayers." Journal Of The Electrochemical Society **141**(2): 507-510.
Shenton, M. J. and G. C. Stevens (2001). "Surface modification of polymer surfaces: atmospheric plasma versus vacuum plasma treatments." Journal Of Physics D-Applied Physics **34**(18): 2761-2768.
Siegbahn, K., E. F. Barnett, et al. (1972). "Electron Spectroscopy With Monochromatized X-Rays." Science **176**(4032): 245-&.
Simpson, W. C. and J. A. Yarmoff (1996). "Fundamental studies of halogen reactions with III-V semiconductor surfaces." Annual Review Of Physical Chemistry **47**: 527-554.
Slaughter, J. M. (2009). Materials for Magnetoresistive Random Access Memory. Annual Review of Materials Research. Palo Alto, Annual Reviews. **39:** 277-296.
Stafford, L., S. J. Pearton, et al. (2006). "Influence of ion mixing on the energy dependence of the ion-assisted chemical etch rate in reactive plasmas." Journal Of Applied Physics **100**(6).

Steinbruchel, C. (1983). "Langmuir Probe Measurements On Chf3 And Cf4 Plasmas - The Role Of Ions In The Reactive Sputter Etching Of Sio2 And Si." Journal Of The Electrochemical Society **130**(3): 648-655.
Steinbruchel, C. (1989). "Universal Energy-Dependence Of Physical And Ion-Enhanced Chemical Etch Yields At Low Ion Energy." Applied Physics Letters **55**(19): 1960-1962.
Stout, P. J., S. Rauf, et al. (2006). "Modeling dual inlaid feature construction." Journal of Vacuum Science & Technology B **24**(3): 1344-1352.
Sugiyama, T., T. Matsuura, et al. (1997). "Atomic-layer etching of Ge using an ultraclean ECR plasma." Applied Surface Science **112**: 187-190.
Tamirisa, P. A., G. Levitin, et al. (2007). "Plasma etching of copper films at low temperature." Microelectronic Engineering **84**(1): 105-108.
Thompson, S. E., M. Armstrong, et al. (2004). "A logic nanotechnology featuring strained-silicon." Ieee Electron Device Letters **25**(4): 191-193.
Thompson, S. E., R. S. Chau, et al. (2005). "In search of "forever," continued transistor scaling one new material at a time." Ieee Transactions on Semiconductor Manufacturing **18**(1): 26-36.
Ushakov, S. V., C. E. Brown, et al. (2004). "Effect of La and Y on crystallization temperatures of hafnia and zirconia." Journal of Materials Research **19**(3): 693-696.
van Dijk, J., G. M. W. Kroesen, et al. (2009). "Plasma modelling and numerical simulation." Journal Of Physics D-Applied Physics **42**(19): 19301, 19301-19314.
Vasenkov, A. V., X. Li, et al. (2004). "Properties of c-C4F8 inductively coupled plasmas. II. Plasma chemistry and reaction mechanism for modeling of Ar/c-C4F8/O-2 discharges." Journal Of Vacuum Science & Technology A **22**(3): 511-530.
Ventzek, P. L. G., R. J. Hoekstra, et al. (1994). "2-DIMENSIONAL MODELING OF HIGH PLASMA-DENSITY INDUCTIVELY-COUPLED SOURCES FOR MATERIALS PROCESSING." Journal of Vacuum Science & Technology B **12**(1): 461-477.
Veprek, S. (1972). "Statistical-Model Of Chemical Reactions In Nonisothermal Low-Pressure Plasma." Journal Of Chemical Physics **57**(2): 952-959.
Vitale, S. A., H. Chae, et al. (2001). "Silicon etching yields in F-2, Cl-2, Br-2, and HBr high density plasmas." Journal of Vacuum Science & Technology A **19**(5): 2197-2206.
Wallace, R. M. and G. D. Wilk (2003). "High-kappa dielectric materials for microelectronics." Critical Reviews In Solid State And Materials Sciences **28**(4): 231-285.
Wang, X. P., M. F. Li, et al. (2006). "Physical and electrical characteristics of high-kappa gate dielectric Hf(1-x)LaxOy." Solid-State Electronics **50**(6): 986-991.
Wang, X. P., H. Y. Yu, et al. (2007). "Wide V-fb and V-th tunability for metal-gated MOS devices with HfLaO gate dielectrics." Ieee Electron Device Letters **28**(4): 258-260.
Werbaneth, P. and J. Almerico (2000). "Observations on the chemistry and physics of STI etch in Cl-2-Ar plasmas." Solid State Technology **43**(12): 87-+.
Wilk, G. D., R. M. Wallace, et al. (2000). "Hafnium and zirconium silicates for advanced gate dielectrics." Journal of Applied Physics **87**(1): 484-492.
Wilk, G. D., R. M. Wallace, et al. (2001). "High-kappa gate dielectrics: Current status and materials properties considerations." Journal of Applied Physics **89**(10): 5243-5275.
Wu, C. H., B. F. Hung, et al. (2007). "High-temperature stable HfLaON p-MOSFETs with high-work-function Ir3Si gate." Ieee Electron Device Letters **28**(4): 292-294.
Yamamoto, Y., K. Kita, et al. (2006). "Structural and electrical properties of HfLaOx films for an amorphous high-k gate insulator." Applied Physics Letters **89**(3).

Yeo, Y. C., T. J. King, et al. (2002). "Direct tunneling leakage current and scalability of alternative gate dielectrics." Applied Physics Letters **81**(11): 2091-2093.
Yeon, C. K. and H. J. You (1998). "Deep-submicron trench profile control using a magnetron enhanced reactive ion etching system for shallow trench isolation." Journal Of Vacuum Science & Technology A-Vacuum Surfaces And Films **16**(3): 1502-1508.
Yinon, J. and F. S. Klein (1971). "The quadrupole and its applications in vacuum technology and mass spectrometry." Vacuum **21**(9): 379-383.
Yu, H. Y., N. Wu, et al. (2002). "Thermal stability of (HfO2)(x)(Al2O3)(1-x) on Si." Applied Physics Letters **81**(19): 3618-3620.
Zamani, D., M. Keswani, et al. (2012). "Dynamics of Interactions Between HF and Hafnium Oxide During Surface Preparation of High-K Dielectrics." IEEE Transactions on Semiconductor Manufacturing **25**(3): 511-515515.
Zau, G. C. H. and H. H. Sawin (1992). "Effects Of O2 Feed Gas Impurity On Cl2 Based Plasma-Etching Of Polysilicon." Journal Of The Electrochemical Society **139**(1): 250-256.
Zekonyte, J., V. Zaporojtchenko, et al. (2005). "Investigation of the drastic change in the sputter rate of polymers at low ion fluence." Nuclear Instruments & Methods in Physics Research Section B-Beam Interactions with Materials and Atoms **236**: 241-248.
Zhang, D. and M. J. Kushner (2000). "Surface kinetics and plasma equipment model for Si etching by fluorocarbon plasmas." Journal Of Applied Physics **87**(3): 1060-1069.